OUKA
The University of Osaka
Institutional Knowledge Archive

Title	Study on the Infection Prevention Performance of Floor-Supply Displacement Ventilation System Combined with Local Exhaust Ventilation in Healthcare Facilities
Author(s)	吉原, 隼
Citation	大阪大学, 2026, 博士論文
Version Type	VoR
URL	https://doi.org/10.18910/105479
rights	
Note	

The University of Osaka Institutional Knowledge Archive : OUKA

https://ir.library.osaka-u.ac.jp/

The University of Osaka

Doctoral Dissertation

Study on the Infection Prevention Performance of Floor-Supply Displacement Ventilation System Combined with Local Exhaust Ventilation in Healthcare Facilities

Jun Yoshihara

November 2025

Department of Architectural Engineering,
Graduate School of Engineering,
The University of Osaka, Japan

ABSTRACT

This study aimed to contribute to the design of advanced ventilation systems for healthcare facilities, where precise indoor airflow control is critical for infection prevention. The research systematically evaluated the combined performance of Local Exhaust Ventilation (LEV) and Floor-Supply Displacement Ventilation (FSDV) as an effective strategy to reduce airborne infection risk during close-distance conversations. Using a combination of computational fluid dynamics (CFD), full-scale experiments, and microscopic observations, the effects of ventilation type, hood configuration, airflow rate, and contaminant phase (gas or particle) on infection risk and indoor cleanliness were comprehensively investigated.

The results demonstrated that FSDV produced the most stable and calm displacement airflow among the tested systems, with contaminant removal efficiency increasing with ventilation rate. When combined with LEV, exhaled air was effectively captured even at moderate ventilation rates (6–12 ACH), maintaining extremely low infection risk throughout the room. Under high ventilation conditions (50 ACH), gas-based assessments estimated higher infection risks than particle-based evaluations, representing a conservative, safety-side estimation. Furthermore, under FSDV airflow, the particle resuspension rate ranged from 10^{-8} to 10^{-4} h^{-1}, significantly lower than resuspension caused by human walking on typical floors.

This study provides scientific insights into the optimal design of LEV and FSDV systems and contributes to establishing ventilation design guidelines that balance airborne infection control and energy efficiency in healthcare facilities and other high-cleanliness environments. Future work should include transient analyses and field verification to deepen understanding of FSDV and LEV performance and to clarify the relationship between their implementation cost and practical effectiveness.

List of Contents

ABSTRACT i

List of Contents iii

I. Abbreviations vii

II. Nomenclature x

1 Introduction 1

1.1 Background 1

1.2 Literature Review 4

1.2.1 COVID-19 Transmission Mechanisms 4

1.2.2 Ventilation Strategies for Airborne Infection Control 5

1.2.3 Ventilation Requirements in Medical Facilities 6

1.2.4 Local Exhaust Ventilation (LEV) and Personal Exhaust Ventilation (PEV) 8

1.2.5 Floor-Supply Displacement Ventilation (FSDV) 9

1.2.6 Particle Resuspension and Research Trends 10

1.3 Research Objectives and Scope 11

1.4 Structure of the Thesis 13

2 CFD Analysis of Local Exhaust Ventilation for Close-Contact Conversation 15

2.1 Purpose of the Chapter 15

2.2 Methodology of Exhalation Measurements 16

2.2.1 Measurement of Exhaled Air Velocity During Japanese Speech 16

2.2.2 Measurement of Exhaled Air Volume During Japanese Speech 18

2.3 Methodology of CFD Analysis 19

2.3.1 Analysis Conditions 19

2.3.2 Simulation Cases 23

2.3.3 Hood Capture Performance Assessment in CFD 25

2.3.4 Infection Risk Assessment from Tracer Gas in CFD 26

2.3.5 Calculation of SVE5 28

2.4 Results 29

2.4.1 Measurement Results of Exhaled Air during Talking 29

2.4.2 CFD Simulation Results 33

2.5 Discussion 42

2.5.1 Comparison with Previous Studies and Limitations of the Exhaled air Measurements and Steady-State CFD 42

2.5.2 Influence of Convergence and Human Thermal Plume on CFD Accuracy.....43
2.5.3 Significance and Future Potential of FSDV and LEV Introduction.....46
2.6 Conclusion 47

3 Experimental Evaluation of Different Underfloor Air-Distribution Systems without LEV.....50

3.1 Purpose of the Chapter.....50
3.2 Methodology.....51
3.2.1 Experimental Facilities 51
3.2.2 Tracer Gas Generation Method for Exhaled Human Breath Simulation.....57
3.2.3 Experimental Cases and Procedures 58
3.2.4 Normalization of Tracer Gas Concentration and Temperature.....61
3.2.5 Contaminant Removal Efficiency in the Breathing Zone 62
3.3 Results and discussions.....62
3.3.1 Vertical Distribution of Tracer Gas Concentration.....62
3.3.2 Contaminant Removal Efficiency in the Breathing Zone 65
3.3.3 Vertical Distribution of Air Temperature.....66
3.3.4 Summary of Key Findings 69
3.4 Conclusion 70
3.5 Appendix 3-A: Measurement of Ventilation Rate in the Test Chamber with Different Tracer Gas Release Points 72

4 Experimental Evaluation of LEV Performance under Different Ventilation Systems 74

4.1 Purpose of the Chapter.....74
4.2 Methodology.....75
4.2.1 Experimental Facilities 75
4.2.2 Tracer Gas Generation Method for Speaking Exhalation Simulation.....79
4.2.3 Experimental Cases and Procedures 80
4.2.4 Normalization of Tracer Gas Concentration 81
4.2.5 Hood Capture Performance Assessment in Experiment.....82
4.2.6 Infection Risk Assessment from Tracer Gas in Experiment.....82
4.3 Results and discussions.....84
4.3.1 Vertical Distribution of Tracer Gas Concentration.....84
4.3.2 Hood Capture Efficiency.....86
4.3.3 Infection Risk for the Opponent Person.....87
4.3.4 Summary of Key Findings 88
4.4 Conclusion 90

5 Experimental Investigation of LEV and Ventilation System Performance Using Tracer Gas and Simulated Saliva at High Ventilation Rates 92

5.1 Purpose of the Chapter 92
5.2 Methodology 94
5.2.1 Experimental Cases and Facilities 94
5.2.2 Conditions of Exhalation Generation 97
5.2.3 Measurement Points and Experimental Procedures 98
5.2.4 Normalization of Tracer Gas Concentration 101
5.2.5 Hood Capture Performance Assessment in Experiment 101
5.2.6 Infection Risk Assessment from Particles in Experiment 101
5.3 Results 103
5.3.1 Results from CO_2 Gas Concentration Measurements 103
5.3.2 Results from Artificial Saliva Particles 107
5.3.3 Infection Probability Estimated from Tracer Gas and Particle Concentrations 110
5.4 Discussion 112
5.4.1 Summary of Key Findings 112
5.4.2 Comparison with Previous Studies 113
5.4.3 Limitations 114
5.4.4 Implications for Future Work 116
5.5 Conclusion 117
5.6 Appendix 5-A: Nebulizer Performance Measurement 119

6 Experimental Study on Airflow-Induced Particle Resuspension under FSDV Conditions 122

6.1 Purpose of the Chapter 122
6.2 Methodology 123
6.2.1 Experimental Procedures and Facilities 123
6.2.2 Particle Dispersion on Carpet 126
6.2.3 Parameters and Experimental Cases 129
6.2.4 Calculation of Resuspension Rate 131
6.3 Results 134
6.3.1 Time Series of Indoor Particle Concentration 134
6.3.2 Resuspension Rate 139
6.3.3 Close-Up Images of the Carpet 141
6.4 Discussion 143
6.4.1 Estimation of Particle Behavior after Resuspension 143
6.4.2 Summary of Key Findings 145

6.4.3 Comparison with Previous Studies 147
6.4.4 Limitations and Implications for Future Work 148
6.5 Conclusion 149
6.6 Appendix 6-A: Validation of Uniform Particle Distribution 151
6.7 Appendix 6-B: Temperature and Relative Humidity during the Experiments 154

7 General Conclusions 155

7.1 Summary of Each Chapter 155
7.2 Overall Conclusions and Future Perspectives 158
7.3 List of Publications (Original paper) 162

ACKNOWLEDGEMENT 164

REFERENCES i

I. Abbreviations

Abbreviations

Infectious Diseases

COVID-19	Coronavirus disease 2019
SARS-CoV-2	Severe acute respiratory syndrome coronavirus 2

Ventilation Systems and Diffusers

LEV	Local exhaust ventilation
FSDV	Floor-supply displacement ventilation
MV	Mixing ventilation
DV	Displacement ventilation
IJV	Impinging jet ventilation
UFAD	Underfloor air distribution system
PV	Personal ventilation
PEV	Personal exhaust ventilation
OTV	Occupant targeted ventilation
SFD	Swirling flow-type floor diffuser
HFD	Horizontal flow-type floor diffuser
CD	Ceiling diffuser

Building Air-Conditioning Systems

HVAC	Heating, ventilation, and air conditioning
AHUs	Air-handling systems
OHU	Outdoor air-handling unit
OA	Outdoor air
EA	Exhaust air
SA	Supply air

RA	Return air
HEPA	High-efficiency particulate air filter
CAV	Constant air volume

Organizations

WHO	World Health Organization
NIID	Japan's National Institute of Infectious Diseases
REHVA	Federation of European Heating, Ventilation and Air Conditioning Associations
HEAJ	Health Engineering Association of Japan
CDC	Centers for Disease Control and Prevention
ASHRAE	American Society of Heating, Refrigerating and Air-Conditioning Engineers
SHASE	The Society of Heating, Air-Conditioning and Sanitary Engineers of Japan
AIJ	Architectural Institute of Japan

Others

ACH	Air changes per hour
CFD	Computational fluid dynamics
LRN	Low-Reynolds-number
PET	Polyethylene terephthalate
RNA	Ribonucleic acid
SVE5	Scale for ventilation efficiency 5
PID	Proportional-Integral-Derivative control
SD	Standard deviation
AVE	Average
CO_2	Carbon dioxide
He	Helium
EDIS	Expiratory droplet investigation system
AIIRs	Airborne infection isolation rooms

ATD	Arizona test dust
RH	Relative humidity
AH	Absolute humidity
CASBEE	Comprehensive assessment system for built environment efficiency

II. Nomenclature

The nomenclature used in this dissertation is summarized below in the order of its appearance in each chapter. Symbols that have already been defined in previous chapters are omitted.

Symbols	Description	Units
Chapter 2		
β	Vertical exhalation angle	[°]
$v_{x\,i}$	Instantaneous velocity components along the X axes (10 Hz)	[m/s]
v_{y_i}	Instantaneous velocity components along the Y axes (10 Hz)	[m/s]
$v_{z\,i}$	Instantaneous velocity components along the Z axes (10 Hz)	[m/s]
$\bar{\beta}$	Mean vertical exhalation angle	[°]
$\lvert\bar{v}\rvert$	Mean velocity magnitude	[m/s]
n_e	Number of elements used for the mean value calculation	[-]
$\overline{V_b}$	Mean exhaled air volume per minute	[L/min]
V_{PET}	Total volume of air collected in the PET bag after one minute of reading	[L]
T_m	Measurement duration (1 minute in all cases)	[min]
k	Turbulent kinetic energy	[m^2/s^2]
ε	Turbulent energy dissipation rate	[m^2/s^3]
U	Mean velocity	[m/s]
I	Turbulence intensity	[-]
C_μ	Model coefficient (C_μ=0.09)	[-]
L	Turbulence length scale	[m]
Q_h	Hood exhaust flow rate	[m^3/h]
H_h	Hood-head distance	[mm]
P_h	Hood horizontal position	[mm]
Q	Total ventilation rate	[m^3/h]
η	Hood capture efficiency	[-]

C_h	Tracer gas concentration in the hood exhaust air	[-]
Q_{ce}	Ceiling exhaust flow rate	[m^3/h]
C_{ce}	Tracer gas concentration in the ceiling exhaust air	[-]
C_{SA}	Tracer gas concentration in the supply air	[-]
P	Probability of infection for a susceptible individual	[-]
n	Number of infectious quanta inhaled	[quanta]
C	Number of new infections	[-]
S_0	Initial number of susceptible individuals	[-]
C_{avg}	Time-averaged quanta concentration in the room	[quanta/m^3]
Q_b	Volumetric breathing rate of an occupant	[m^3/h]
D	Exposure duration	[h]
q	Quanta emission rate	[quanta/h]
n_{dc}	Total number of quanta inhaled by doctor (non-infected person)	[quanta]
$C_{q,dc}$	Quanta concentration in front of the doctor's (non-infected person's) mouth	[quanta/m^3]
Q_{dc}	Breathing rate of the doctor (non-infected person)	[m^3/h]
t_{ex}	Exposure time during which the doctor (non-infected person) inhales air containing quanta concentration $C_{q,dc}$	[h]
$C'_{g,dc}$	Normalized tracer gas concentration in front of the doctor's mouth relative to the perfectly mixed concentration	[-]
$C_{g,dc}$	Local tracer gas concentration at the doctor's mouth	[-]
$C_{g,pm}$	Tracer gas concentration under perfectly mixed conditions	[-]
SVE 5(x)	Contribution ratio of the exhaust opening air to be exhausted at a point (x)	[-]
n_o	Name (or identifier) of the air outlet	[-]
$C'(x, n_o)$	Concentration at position x obtained by solving the concentration transport equation in the reverse time direction under the clean initial conditions and n_o inlet concentration $C_0(n_o)$	[-]
$C_0(n_o)$	Contaminant concentration with the contaminant generation q (m^3/h) from the air outlet named n_o (flow rate of $n_0 = Q(n_o)$)	[-]
M	Contaminant generation rate	[m^3/h]
$Q(n_o)$	Airflow rate through the exhaust outlet n_o	[m^3/h]

Chapter 3

T_{EA}	Exhaust air temperature	[°C]
T_{SA}	Supply air temperature	[°C]
W_i	Internal heat generation	[W]
C_p	Specific heat capacity of air	[J/kg·K]
ρ_a	Air density	[kg/m³]
Q_e	Ventilation rate in experiment (exhaust flow rate)	[m³/h]
$t_{\text{gas,tot}}$	Total tracer gas generation time (CO_2 + He) for each ventilation rate	[min]
$t_{\text{gas,wait}}$	Duration of waiting for the tracer gas concentration steady state	[min]
C'_{CO_2}	Normalized CO_2 concentration rise	[-]
$C_{CO_2,p}$	Measured CO_2 concentration at a point p	[-]
$C_{CO_2,SA}$	CO_2 concentration in the supply air	[-]
$C_{CO_2,EA}$	CO_2 concentration in the exhaust air	[-]
ΔT	Temperature rise	[K]
T_p	Measured temperature at a point p	[°C]
ε_{OZ}	Contaminant removal efficiency averaged in the occupied zone	[-]
$\langle C_{CO_2,OZ} \rangle$	Average CO_2 concentration in the occupied zone	[-]
Q_m	Measured ventilation rate	[m³/h]
M_{CO_2}	CO_2 generation rate	[m³/h]

Chapter 4

$C_{CO_2,h}$	CO_2 concentration in the exhaust air from the local exhaust hood	[-]
Q_{LO}	Exhaust flow rates of the linear outlet	[m³/h]
$C_{CO_2,LO}$	CO_2 concentration in the exhaust air from the linear outlet	[-]
$C'_{CO_2,dc}$	Normalized CO_2 concentration rise in front of the doctor's mouth	[-]
$C_{CO_2,dc}$	CO_2 concentration in front of the doctor's mouth	[-]
$t_{P\%}$	Time until the infection probability reached P%	[h]
$t_{5\%}$	Time until the infection probability reached 5%	[h]

Chapter 5

Q_{pc}	Sampling flow rate of the particle counter	[m³/h]
V_{dp}	Total volume of particles detected in front of the doctor's mouth divided by the measurement time	[m³/h]
V_{ep}	Total generated particle volume divided by the emission duration	[m³/h]
M_{ab}	Masses of artificial saliva solution in the nebulizer generator chamber before emission	[g]
M_{aa}	Masses of artificial saliva solution in the nebulizer generator chamber after emission	[g]
ρ_{aa}	Density of artificial saliva after evaporation	[g/m³]
ρ_{ab}	Density of artificial saliva before evaporation	[g/m³]
R_c	Compositional ratio of artificial saliva after evaporation to that before evaporation	[-]
R_d	Particle diameter ratio after evaporation to before evaporation	[-]

Chapter 6

e_s (T)	Saturation vapor pressure	[hPa]
T	Dry-bulb temperature	[K]
A_1-A_6	Empirical constants (reported by Hyland and Wexler (1983) [1])	[-]
e	Water vapor pressure	[hPa]
RH	Relative humidity	[%]
AH	Absolute humidity	[g/m^3]
r_j	Resuspension rate (coefficient) for each particle size range j	[h^{-1}]
R_j	Resuspension amount per unit time for size range j	[g/h]
L_j	Deposited particle mass on the carpet (i.e., particle loading) for size range j	[g]
α	Conversion factor accounting for the total resuspension amount (210.2, 157.7, and 52.6 for v_f = 0.040, 0.030, and 0.010 m/s)	[-]
$N'_{pc,i,j}$	Number of particles measured at time step i for size range j, with the 10-minute average value prior to operator entry subtracted	[-]
V_j	Representative particle volume for size range j	[m^3]
ρ_p	Particle density (2.83 for Ryukakusan)	[g/m^3]
Δt	Duration of each time step (constant within each test case; 6 s for flow rates of 1000, 850, and 750 m³/h, and 12 s for 250 m³/h)	[s]
n	Total number of time steps (total number of data points)	[-]

Q_{ca}	Airflow volume per 500 × 500 mm air-permeable carpet tile	[m^3/h]
Q_{pc}	Suction flow rate of particle counter (0.170)	[m^3/h]
$N_{pc,i,j}$	Number of particles measured at time step *i* for size range *j*	[-]
$\overline{N_{pcb,J}}$	Average number of particles measured during the 10 minutes before operator entry, for size range *j*	[-]
V_r	Room volume (20.06)	[m^3]
Q_e	Exhaust airflow rate	[m^3/h]
L_{total}	Total applied mass of particles on the carpet (1.000 ± 0.003)	[g]
f_p	Mass fraction of test particles in each particle size class	[–]
m_p	Mass of a single particle	[kg]
F_D	Aerodynamic drag force acting on a particle	[N]
F_G	Gravitational force acting on a particle	[N]
C_D	Drag coefficient	[–]
A_p	Projected cross-sectional area of a particle (= πD_p^2 / 4)	[m^2]
ρ_f	Air density	[kg/m^3]
v_r	Relative velocity between the particle and the surrounding airflow (the surrounding airflow was assumed to be zero when calculating v_g)	[m/s]
Re_p	Particle Reynolds number (= $\rho_f D_p v_r / \mu$)	[-]
D_p	Particle diameter	[m]
μ	Dynamic viscosity of air	[Pa·s]
v_g	Terminal settling velocity of a particle under gravity	[m/s]
g	Gravitational acceleration (9.81)	[m/s^2]
v_u	Area-averaged supply air velocity in FSDV	[m/s]
A_c	Floor area of the test chamber, including non–flow-through panels	[m^2]
t_c	Estimated time required for a particle to reach the ceiling (outlet)	[s]
H_c	Ceiling height of the chamber	[m]
SD_p	Standard deviation of the mass increase among the 25 Petri dishes	[g]
CV	Coefficient of variation (SD_p / Average)	[-]

1 Introduction

1.1 Background

Since the outbreak of the novel coronavirus disease (COVID-19) in late 2019, the importance of ventilation as a fundamental strategy for controlling airborne infection has been re-emphasized worldwide. Numerous studies have demonstrated that airborne transmission, caused by droplets and droplet nuclei released during speaking, coughing, or breathing, plays a dominant role in the spread of respiratory infections. In particular, medical facilities—where frequent close-contact interactions between patients and healthcare workers are unavoidable—require advanced airflow management to ensure both infection control and thermal comfort.

As shown in **Figure 1-1**, one promising countermeasure is the application of a local exhaust ventilation (LEV) system near the respiratory emission source. When an infected person exhales or coughs, droplets and droplet nuclei are released into the surrounding air and can remain suspended for long periods. By capturing these contaminants immediately after emission, LEV systems can substantially reduce exposure concentrations around non-infected persons. Because the location of the emission source (the patient) is easily identifiable in consultation or examination rooms, LEV represents a rational and effective approach for airborne infection control in such environments.

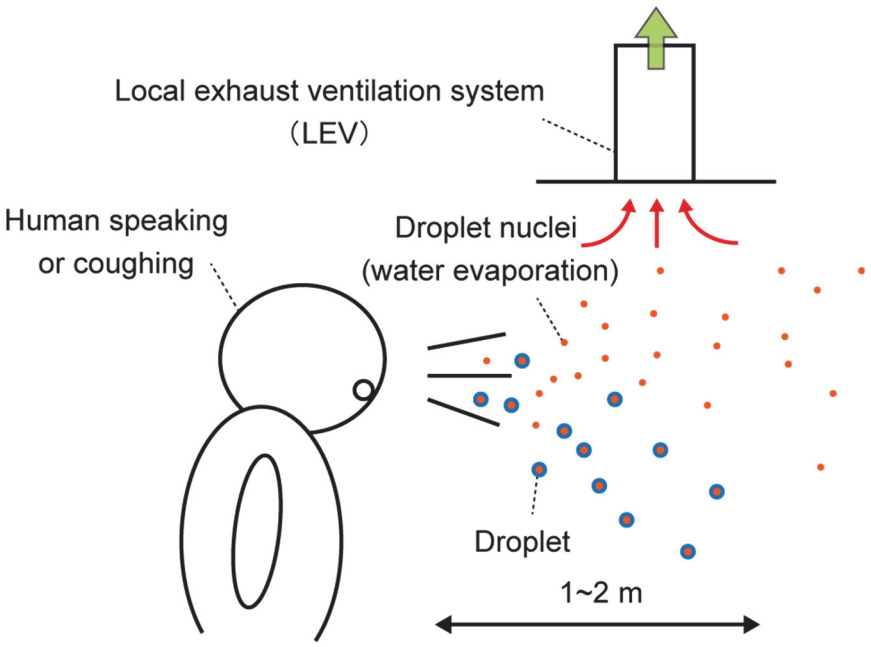


Figure 1-1. Concept of applying a local exhaust ventilation (LEV) system for airborne infection control

However, the performance of LEV is highly influenced by the surrounding airflow field. Among various ventilation methods, floor-supply displacement ventilation (FSDV) is particularly compatible with LEV because it provides a wide supply area and low outlet velocity, creating calm, upward airflow that minimizes interference with local exhaust capture.

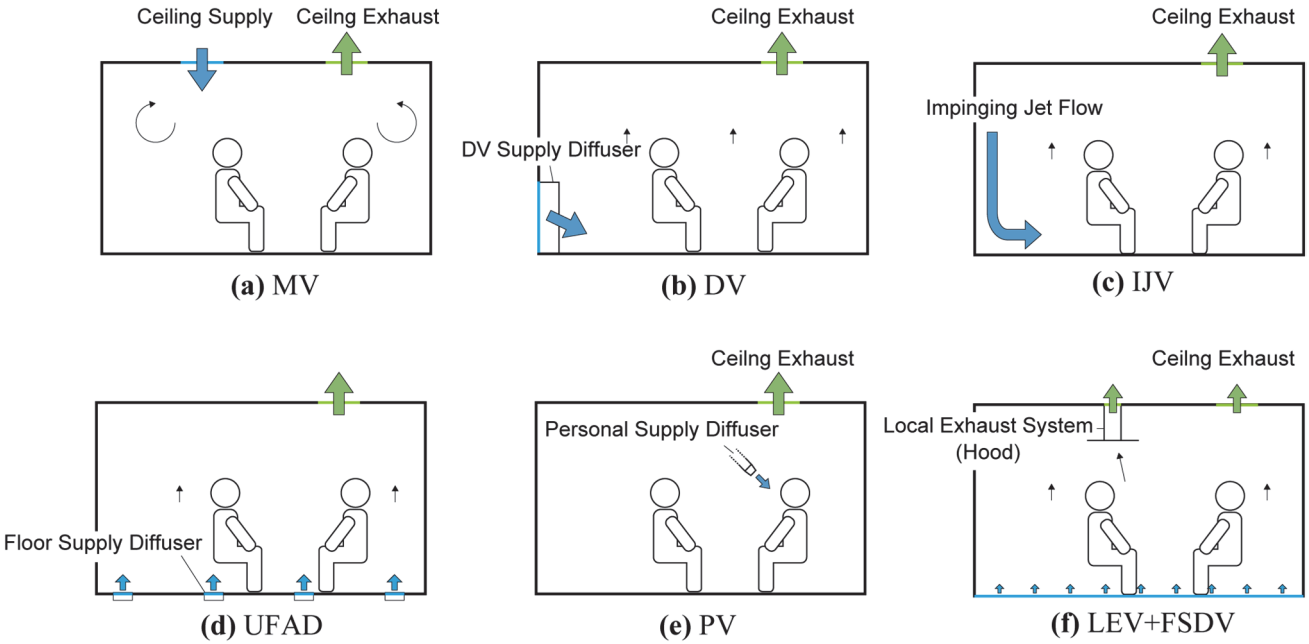


Figure 1-2. Various ventilation methods used in indoor environments such as offices, meeting rooms, and consulting rooms (close-distance conversation): (a) Mixing Ventilation (MV), (b) Displacement Ventilation

(DV), (c) Impinging Jet Ventilation (IJV), (d) Underfloor Air Distribution (UFAD), (e) Personal Ventilation (PV), and (f) the proposed combined system of Local Exhaust Ventilation (LEV) and Floor-Supply Displacement Ventilation (FSDV).

Figure 1-2 compares several typical air distribution systems—mixing ventilation (MV), displacement ventilation (DV), impinging jet ventilation (IJV), underfloor air distribution (UFAD), and personal ventilation (PV)—together with the proposed LEV + FSDV configuration. While conventional systems such as MV or IJV promote uniform mixing or high air velocity, they tend to disperse exhaled contaminants more widely. In contrast, displacement-type systems such as DV and FSDV can transport exhaled air upward through the thermal plume of the human body, reducing horizontal diffusion and improving indoor air quality near the breathing zone.

Despite these advantages, the adoption of FSDV in medical facilities has been limited due to concerns regarding particle resuspension from the floor surface. Dust or droplet particles that have settled on the floor may be re-entrained into the air by the upward supply airflow or by human walking. However, as illustrated in **Figure 1-3**, almost no quantitative data are available concerning resuspension phenomena under FSDV conditions. This lack of evidence has led to a perception that FSDV may be unsuitable for clean or clinical environments—an assumption not yet supported by experimental verification.

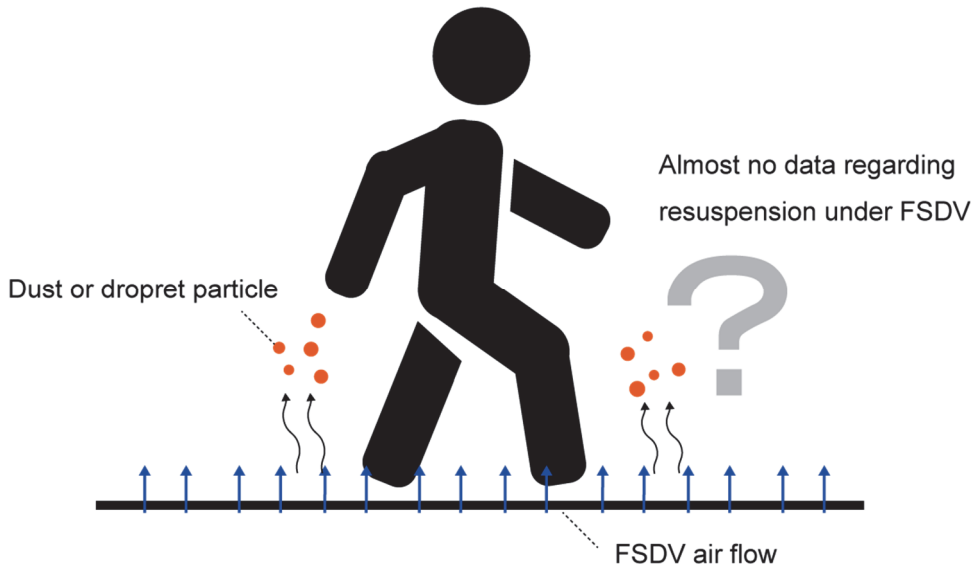


Figure 1-3. Conceptual illustration of particle resuspension under FSDV conditions.

Therefore, this study aims to clarify both the infection-risk reduction potential of LEV systems combined

with various ventilation configurations and the airflow-induced resuspension behavior of particles under FSDV conditions. Through systematic CFD analyses and controlled experiments, the thesis seeks to provide fundamental knowledge and design guidance for the effective use of LEV and FSDV in spaces where airborne infection prevention is critical, such as hospitals, clinics, and meeting environments.

1.2 Literature Review

1.2.1 COVID-19 Transmission Mechanisms

Since the onset of the COVID-19 pandemic in late 2019, extensive research has been conducted to clarify the transmission routes of the severe acute respiratory syndrome coronavirus 2 (SARS-CoV-2). Recent studies have established that airborne transmission—through droplet nuclei and small droplets that behave as aerosols—is one of the major infection pathways of COVID-19[2–4].

Evidence from outbreak investigations and experimental studies has demonstrated that aerosolized viral particles can remain suspended in the air for extended periods and contribute to secondary infections at distances beyond conventional social distancing ranges [5,6]. According to the World Health Organization (WHO) publication “Coronavirus disease (COVID-19): How is it transmitted?” (December 2021) [7], SARS-CoV-2 spreads primarily through close-contact interactions, such as face-to-face conversations, where infectious particles can be transmitted via short-range airborne or droplet routes. The WHO also highlighted that infections can occur in poorly ventilated and crowded indoor environments, where aerosols accumulate over time. Similarly, Japan’s National Institute of Infectious Diseases (NIID) has emphasized the need for effective ventilation strategies to mitigate transmission in confined and insufficiently ventilated rooms [8]. These statements collectively underscore that airborne transmission is a principal route of SARS-CoV-2 infection, and ventilation plays a crucial role in mitigating this risk.

The size and aerodynamic behavior of emitted particles are key to understanding airborne transmission. The WHO defines droplets as particles larger than 5 μm, which typically settle within 1–2 m due to gravity, whereas droplet nuclei smaller than 5 μm can remain suspended and travel long distances with airflow [9]. However, this boundary differs from that used in aerosol science. Tang et al. [10] summarized the differing perspectives among clinicians, aerosol scientists, and the public regarding the terminology of droplets and aerosols. From an aerosol scientist’s viewpoint, particles even larger than 5 μm may remain airborne over considerable distances depending on the local airflow conditions [11,12]. This emphasizes that airflow character-

istics—including velocity, direction, and turbulence—directly influence the risk of airborne infection indoors.

In summary, the accumulated evidence indicates that airborne transmission through small particles and droplet nuclei is a dominant infection pathway for SARS-CoV-2, especially in indoor environments with inadequate ventilation. Consequently, controlling airflow and improving ventilation design are recognized as fundamental strategies for infection prevention. However, the relationship between ventilation rates and infection risk varies substantially depending on specific environmental conditions, and current evidence remains limited; therefore, further research is required. In Chapters 2, 4, and 5 of this thesis, the relationship between ventilation rates and infection risk during close-range conversations is quantified.

1.2.2 Ventilation Strategies for Airborne Infection Control

To mitigate airborne transmission, ventilation plays a vital role by removing infectious aerosols from the breathing zone and diluting contaminated indoor air [4]. Various ventilation strategies have been developed to achieve both thermal comfort and infection control, as summarized in **Figure 1-2**. These include mixing ventilation (MV), displacement ventilation (DV), impinging jet ventilation (IJV), underfloor air distribution (UFAD), floor-supply displacement ventilation (FSDV), and personalized or local exhaust systems (PV, LEV). Each system exhibits distinct airflow characteristics that influence how exhaled contaminants are dispersed and removed.

The most common approach is mixing ventilation (MV) (**Fig. 1-2a**), also known as an overhead system, where both air supply and exhaust diffusers are located at the ceiling level. MV maintains nearly uniform air conditions by vigorous mixing; however, it can also promote the widespread distribution of exhaled aerosols. Li et al. [6] reported that poor ventilation (1 L/s per person) contributed to long-range airborne transmission in a restaurant outbreak. Zhang et al. [13] demonstrated that although HVAC mixing enhances circulation, vortices near walls and corners may trap aerosols for extended periods. These findings indicate that MV, while common, may not adequately prevent airborne transmission in high-risk settings such as consulting rooms.

Displacement ventilation (DV) (**Fig. 1-2b**) supplies conditioned air near the floor and exhausts it at the ceiling, forming a unidirectional upward airflow aligned with the human thermal plume. This stratified flow limits horizontal dispersion and creates a calm airflow field that helps reduce droplet-nuclei spread [14–16]. Bhagat et al. [17] showed that DV effectively improved air quality and reduced infection risk in hospitals. However, Wei et al. [18] noted that DV alone may not mitigate short-range transmission, emphasizing the

complementary use of personalized ventilation (PV) or local exhaust systems (LEV) near emission sources.

Impinging jet ventilation (IJV) (**Fig. 1-2c**) is a semi-displacement method that uses high-momentum jets directed toward the floor, where they spread radially before rising with buoyancy. Rajaratnam [19] first characterized its flow behavior, and subsequent studies, such as those by Yamasawa et al. [20], analyzed the effects of jet momentum and internal heat generation on cooling and ventilation performance. Although IJV offers good stratification, its practical effectiveness for infection control has not been sufficiently evaluated.

Underfloor air distribution (UFAD) (**Fig. 1-2d**) supplies conditioned air through diffusers embedded in a raised floor. Properly designed UFAD can improve ventilation efficiency and occupant comfort while reducing energy use [21–23]. Loudermilk [24] highlighted that UFAD ensures supply air reaches occupants directly and isolates heat gains above the occupied zone. Studies by Cheong et al. [25] and Nao et al. [26] demonstrated that UFAD can lower infection risk compared with MV, but the effect depends strongly on airflow rate and diffuser placement. Thus, the air change rate may be a more dominant factor than ventilation type in determining infection control performance.

On the other hand, Melikov et al. defined Occupant Targeted Ventilation (OTV) as ventilation that prioritizes health and comfort for individual and group occupants and non-uniform air distribution [27]. From this perspective, PV is a type of OTV, and the system in this study (**Figure 1-2f)** can also be considered a type of OTV.

In summary, although research findings related to aerosol transmission exist for each ventilation method, comparative studies conducted under identical conditions remain limited, highlighting the need for further investigation. In this thesis, Chapters 4 and 5 compare different underfloor air-distribution systems with a ceiling-supply system and evaluate the resulting indoor contaminant concentration distributions and associated infection risks.

1.2.3 Ventilation Requirements in Medical Facilities

In medical facilities where contact with infectious patients is likely, advanced and precisely controlled ventilation systems are required to minimize airborne infection risks. International and domestic guidelines—including those from REHVA, the Health Engineering Association of Japan (HEAJ), and the Centers for Disease Control and Prevention (CDC)—clearly define ventilation requirements for different types of medical spaces. For example, airborne infection isolation rooms (AIIRs) and protective isolation units often require

extremely high ventilation rates, reaching up to 50 air changes per hour (ACH), depending on the purpose and risk level of the room. These values are far greater than those in ordinary offices or residential buildings, highlighting the unique design challenges in healthcare ventilation.

The fundamental requirement for preventing airborne transmission is to maintain sufficient outdoor air supply per person to dilute and remove infectious aerosols [2–4,28]. However, beyond the total ventilation rate, the airflow pattern and distribution system are equally important. Conventional ceiling diffuser (CD) systems promote mixing throughout the entire space, which can inadvertently distribute exhaled contaminants. In contrast, displacement ventilation (DV) or floor-supply displacement ventilation (FSDV) systems are more suitable for minimizing exposure, as they promote stratified airflow, carrying exhaled air and bioeffluents upward and away from the breathing zone [15,27,29–31]. This vertical flow, aligned with the human thermal plume, allows contaminated air to be exhausted efficiently while supplying cleaner air to the occupied zone.

Nonetheless, the performance of DV and FSDV strongly depends on operational conditions. If the ventilation volume is insufficient, the thermal stratification interface may descend into the breathing zone, reducing effectiveness and increasing exposure risk [18,26]. Proper control of supply temperature, diffuser placement, and airflow velocity is therefore essential. When designed and operated appropriately, studies have shown that DV and FSDV can significantly reduce airborne infection risks and improve indoor air quality in healthcare settings [17,32] cilities demand high ventilation rates and carefully designed airflow management systems to ensure infection control. Among available systems, displacement-based ventilation—particularly FSDV—offers a promising approach for achieving both thermal comfort and effective contaminant removal under high-ventilation conditions typical of consulting rooms and isolation spaces. However, according to the hospital design guidelines (HEAS-02-2022), unidirectional airflow systems assume ceiling supply with floor or wall exhaust and are not recommended for susceptible patient rooms, as the improvement in survival probability is considered insufficient relative to the associated costs [33]. Moreover, despite the strong potential of unidirectional upward airflow—from floor supply to ceiling exhaust—for mitigating infection risks, this configuration has not been adequately considered in existing guidelines. Therefore, further accumulation of evidence is required to clarify the advantages of floor-supply systems in reducing infection risk. In Chapters 2, 4, and 5 of this thesis, the infection-risk reduction performance of floor-supply ventilation is investigated.

1.2.4 Local Exhaust Ventilation (LEV) and Personal Exhaust Ventilation (PEV)

Local Exhaust Ventilation (LEV) systems were originally developed for industrial applications to protect workers from hazardous gases, fumes, and dust by capturing contaminants directly at the source [34]. LEV has been widely applied in factories, laboratories, and commercial kitchens, where hood-type exhaust devices—such as tapered, flanged, or flat designs—effectively remove pollutants before they disperse into the surrounding environment. These systems are based on the principle of source control, which is now being reconsidered as a promising strategy for infection prevention in indoor environments.

In parallel, Personal Exhaust Ventilation (PEV)—also referred to as Personalized Exhaust (PE) or Personalized Ventilation (PV)—was developed to provide localized control of the air immediately around an occupant. PV systems typically supply clean air near the breathing zone to improve comfort and reduce exposure to contaminants, and have been introduced in offices, classrooms, and vehicles [35,36]. Building on this concept, Yang et al. [37] compared PV and PE systems and demonstrated that PE, which captures exhaled air directly at the source, is more effective for airborne infection control than supplying air from personalized nozzles. However, their study did not fully examine the influence of overall ventilation rates or background airflow on system performance.

While LEV shares the same source-capture principle as PEV, its applications in infection control environments—particularly in close-contact situations such as consulting rooms—remain limited and insufficiently documented. Only a few studies, such as those by Allison et al. [38], have investigated LEV performance for removing dental aerosols and droplets. However, systematic evaluations under speech or coughing conditions are still lacking. Moreover, the aerodynamic interaction between LEV and surrounding airflow fields—such as those created by displacement or floor-supply ventilation systems—has not yet been quantitatively clarified.

In summary, both PEV and LEV have significant potential for controlling airborne transmission by capturing droplets and droplet nuclei at the source. Yet, their effectiveness in realistic medical and conversational settings has not been systematically investigated. This study therefore focuses on experimentally evaluating the performance of LEV under close-distance conversational conditions, aiming to establish its applicability as a practical infection control measure in medical facilities.

1.2.5 Floor-Supply Displacement Ventilation (FSDV)

Floor-supply displacement ventilation (FSDV) is a variant of displacement ventilation (DV) characterized by its large air supply surface area and low supply air velocity, creating a calm and stable airflow field. The system distributes conditioned air uniformly from the entire floor surface through perforated metal panels or air-permeable carpets, which helps maintain extremely low horizontal air velocities within the occupied zone. This configuration minimizes local drafts and promotes a stratified flow field similar to that of conventional DV but with greater flow uniformity.

FSDV was first investigated by Akimoto et al. (1997) [39] as an advanced form of underfloor air distribution (UFAD). Their research demonstrated that FSDV can achieve high levels of thermal comfort due to its weak draft sensation and stable vertical temperature gradient [32,40]. Compared with UFAD, which relies on discrete diffusers, FSDV provides a smoother and more uniform upward flow, making it particularly suitable for environments that require calm and clean air distribution, such as hospitals, laboratories, and clean rooms.

Subsequent studies have highlighted several advantages of FSDV. Its large supply area enables a very low outlet velocity at a given ventilation rate, thereby reducing turbulence intensity and limiting the lateral spread of exhaled contaminants. Furthermore, the system's upward displacement pattern aligns with the natural human thermal plume, effectively transporting airborne pollutants and heat away from the breathing zone. These characteristics suggest that FSDV can serve as an ideal background ventilation system for local exhaust devices (LEV) and other source-control measures.

However, despite its promising potential, practical applications of FSDV remain limited. There are concerns related to its high initial installation cost, the difficulty of cleaning water spills, possible thermal draft discomfort due to strong vertical temperature gradients, and the resuspension of settled particles from the floor surface. In particular, while FSDV has often been perceived as unfavorable in medical settings because of potential dust resuspension, empirical data validating or quantifying this phenomenon are scarce. Most of these concerns have been based on assumptions rather than experimental evidence. Therefore, it is essential to systematically investigate the aerodynamic and environmental behaviors associated with FSDV. In Chapter 3 of this thesis, the contaminant removal performance of FSDV is compared with various ventilation systems.

1.2.6 Particle Resuspension and Research Trends

Numerous studies have investigated particle resuspension phenomena, addressing both microscopic mechanisms and macroscopic human-induced processes. Research in this field generally falls into two categories: (1) microscale studies, which focus on the fundamental physical forces governing adhesion and detachment—such as aerodynamic drag, adhesion, and electrostatic interactions—and (2) mac
roscale studies, which examine resuspension caused by human activities such as walking, cleaning, or mechanical vibration [40–44].

Field measurements in offices and residences have provided valuable insights into the sources and spatial distribution of airborne particles. These studies have shown that fine particles (< 2 μm) primarily originate from outdoor air infiltration, while coarse particles (2–10 μm) are largely generated by resuspension due to human activity, even in spaces equipped with filtration systems [40–47]. Chamber-based experiments have been used to clarify the effects of parameters such as floor material, relative humidity, and walking intensity. Although results vary among studies [48,49], the overall trend indicates that resuspension is higher on carpeted surfaces than on hard flooring and increases under low humidity conditions [50–53]. In addition to adult walking, research has also examined infant crawling behavior, revealing significantly higher exposure levels in infants' breathing zones—emphasizing the public health importance of understanding resuspension mechanisms [54,55].

At the microscopic level, several studies have explored the influence of particle size, surface type, and deposition morphology on resuspension dynamics. These works have revealed that resuspension differs substantially between single-layer and multilayer deposits, suggesting complex detachment mechanisms dependent on surface roughness and adhesive forces [43,56,57]. However, most existing research has been conducted under ceiling-supply or horizontal airflow conditions, or in small-scale wind tunnel environments. These conditions differ substantially from the upward airflow field characteristic of floor-supply displacement ventilation (FSDV).

To date, quantitative data on particle resuspension under FSDV conditions remain extremely limited. Only a few studies, such as that by Kiyosuke et al. [58], have reported potential resuspension during walking in FSDV environments. However, their findings mainly describe temporal concentration responses without providing quantitative metrics such as resuspension rates or fractions. Consequently, there is a clear need for systematic experimental evaluation of resuspension phenomena under FSDV airflow, even in the absence of human movement, to better understand the interaction between upward displacement flow, humidity, and ad-

hesive forces.

Therefore, this study focuses on airflow-induced particle resuspension under FSDV conditions, aiming to establish fundamental data that will support the safe and effective implementation of FSDV in medical and cleanroom environments. This topic is addressed in Chapter 6.

1.3 Research Objectives and Scope

As discussed in Section 1.2, ventilation plays a crucial role in mitigating airborne infection risks, particularly in healthcare environments. However, current knowledge regarding the relationship between ventilation rates and infection risk during close-contact conversations remains limited, and further research is needed to inform the selection of appropriate ventilation strategies. Although several studies have examined infection risks associated with individual ventilation methods, few have evaluated multiple systems under identical laboratory conditions. Furthermore, despite the potential of floor-supply ventilation to provide superior infection-control performance, it has not been considered in hospital design guidelines due to the scarcity of available evidence and the lack of prior implementation cases. Therefore, this study focuses on understanding the relationship between ventilation methods and infection risk during close-contact conversations in indoor settings such as consulting rooms and meeting spaces. The primary objective is to clarify the effectiveness of local exhaust ventilation (LEV) systems and various air-distribution strategies, thereby providing scientific guidance for designing infection-conscious ventilation systems in healthcare facilities.

The application of LEV for infection control remains relatively unexplored; thus, this study provides one of the first systematic and comprehensive investigations into its effectiveness and operational conditions. In addition, the study evaluates the performance of floor-supply displacement ventilation (FSDV) both as a stand-alone ventilation method and in combination with LEV.

FSDV is expected to inherently reduce airborne infection risks due to its calm upward airflow field, and comparing its performance with other floor-supply systems contributes valuable insights for understanding its distinct advantages.

The specific objectives and scope of this research are summarized as follows:

(1) Measurement of exhalation characteristics and fundamental CFD analysis (Chapter 2)

Exhaled air velocity and flow rate during speech were measured for Japanese adults. Based on these data, CFD simulations were conducted to analyze the effects of LEV exhaust flow rate, position, height, and overall room ventilation rate on contaminant capture performance.

(2) Comparative evaluation of different underfloor air-distribution systems without LEV (Chapter 3)
Three floor-based air distribution systems—FSDV, horizontal flow-type floor diffusers (HFD), and swirling flow-type floor diffusers (SFD)—as well as a ceiling diffuser (CD) were experimentally compared in terms of contaminant removal efficiency and thermal comfort. These results provide foundational data for HVAC designers selecting ventilation strategies.

(3) Experimental evaluation of the combined effects of LEV and air distribution systems (Chapter 4)
Building upon the CFD and experimental results from Chapters 2 and 3, the combined effects of LEV and different air distribution systems (FSDV, HFD, SFD, CD) were examined experimentally by varying the ventilation rate, and the corresponding reduction in infection risk was evaluated.

(4) Comparison of infection risks based on gas and particle behavior (Chapter 5)
Under high ventilation conditions (1000 m^3/h = 50 ACH), the dispersion and infection risk of exhaled contaminants were evaluated by comparing gaseous tracer (CO_2, representing droplet nuclei) and artificial saliva particles (representing droplets). Studies that directly compare gas and particle behavior are rare, and this provides valuable insight into infection transmission mechanisms.

(5) Quantitative evaluation of airflow-induced particle resuspension under FSDV conditions (Chapter 6)
Given that FSDV forms a calm airflow field, concerns exist regarding potential particle resuspension from floor surfaces. This chapter experimentally quantifies particle resuspension under FSDV by varying supply velocity and relative humidity, presenting novel data that have not been reported in previous studies.

Collectively, these investigations aim to establish a scientific basis for selecting appropriate ventilation configurations and implementing LEV systems to reduce airborne infection risks in medical and general indoor environments.

1.4 Structure of the Thesis

This dissertation is organized into seven chapters, as outlined below.

Chapter 1: Introduction

Provides the research background, reviews previous studies, and outlines the research objectives and scope.

Chapter 2: CFD Analysis of Local Exhaust Ventilation for Close-Contact Conversation

Presents CFD analyses based on experimentally measured exhalation characteristics, examining how LEV exhaust flow rate, position, and room ventilation rate affect contaminant capture performance.

Chapter 3: Experimental Evaluation of Different Underfloor Air-Distribution Systems without LEV

Compares the contaminant removal and thermal comfort performance of four ventilation systems (FSDV, HFD, SFD, CD) to clarify their fundamental ventilation characteristics.

Chapter 4: Experimental Evaluation of LEV Performance under Different Ventilation Systems

Experimentally investigates the combined effects of LEV and various ventilation systems (FSDV, HFD, SFD, CD) by varying ventilation rates, and evaluates their infection risk reduction performance.

Chapter 5: Experimental Investigation of LEV and Ventilation System Performance Using Tracer Gas and Simulated Saliva at High Ventilation Rates

Examines the behavior of droplets and droplet nuclei under high ventilation conditions (50 ACH), comparing infection risk assessments based on tracer gas and particle measurements.

Chapter 6: Airflow-Induced Particle Resuspension under FSDV Conditions

Quantifies airflow-induced resuspension of deposited particles under FSDV by varying humidity and velocity, elucidating particle behavior in calm airflow environments.

Chapter 7: General Conclusions

Integrates the findings from all chapters, discusses design implications for infection risk reduction, and proposes guidelines for the practical implementation of LEV and FSDV systems in built environments.

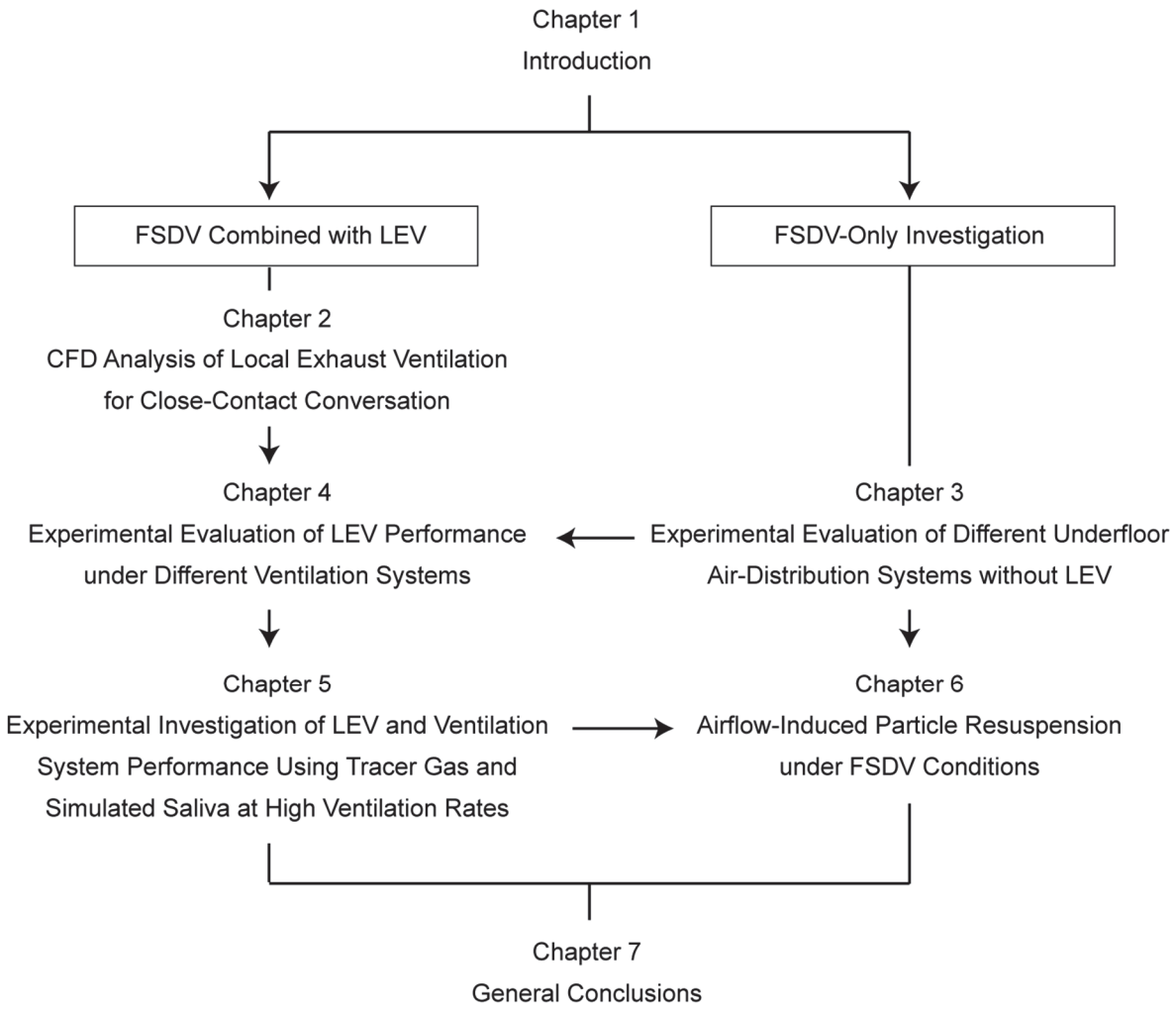


Figure 1-4. Overall structure of this thesis.

2 CFD Analysis of Local Exhaust Ventilation for Close-Contact Conversation

2.1 Purpose of the Chapter

This chapter focuses on a computational fluid dynamics (CFD) analysis of a combined ventilation system consisting of local exhaust ventilation (LEV) and floor-supply displacement ventilation (FSDV). The objective is to clarify the airflow field and contaminant removal characteristics around occupants during close-distance conversation, which serves as a fundamental reference for the full-scale experiments presented in Chapter 4 and 5.

An overview of the CFD analysis parameters and geometric configurations used in this study is shown in **Figure 2-1**. To evaluate the influence of LEV on contaminant capture and dispersion, three parameters were varied: (1) hood flow rate (Q_h), (2) vertical distance between the hood and the patient's head (H_h), and (3) horizontal position of the hood relative to the patient's mouth (P_h). The tested ventilation flow rates ranged from 120 to 1,000 m³/h (equivalent to 6–50 air changes per hour, ACH), covering both typical and intensive ventilation conditions as suggested by international guidelines.

The CFD analysis was performed under steady-state conditions using boundary conditions based on the measured properties of exhaled airflow during Japanese conversation. This dataset was obtained experimentally in a preliminary study to represent realistic exhalation behavior specific to Japanese phonetic patterns.

The results of this chapter provide a quantitative understanding of the interaction between LEV and FSDV under various configurations, and form the basis for the experimental design and infection risk assessments discussed in Chapters 4 and 5.

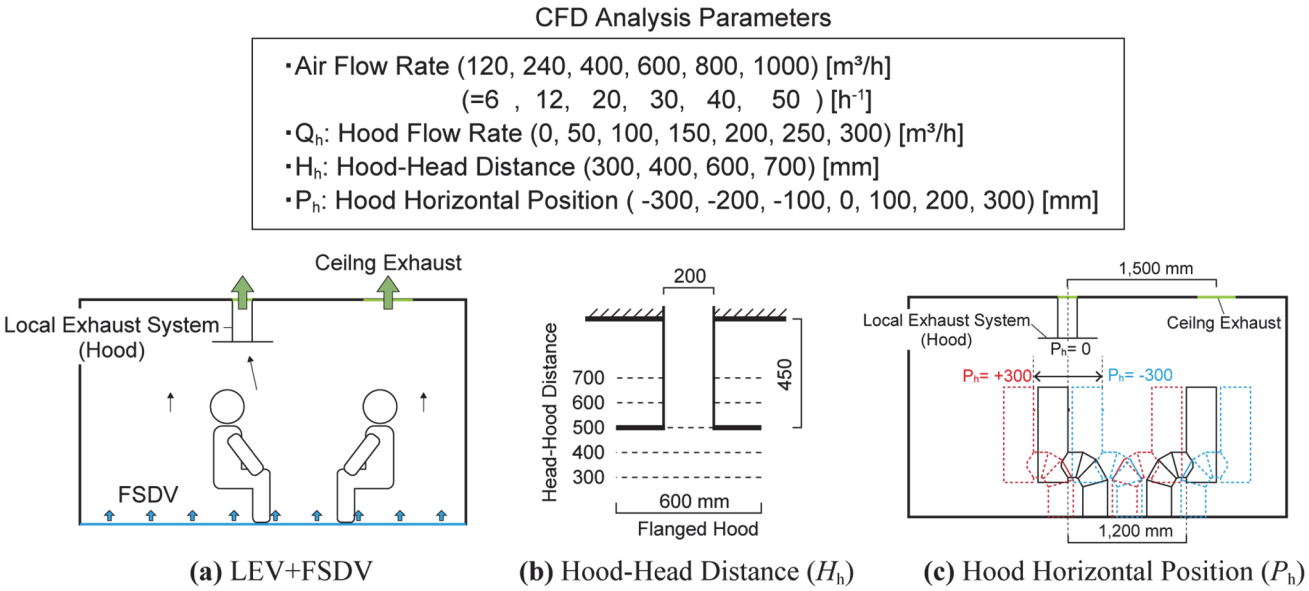


Figure 2-1. Schematic diagram of CFD analysis parameters: (a) Ventilation configuration (LEV + FSDV). (b) Hood–head vertical distance (H_h). (c) Hood horizontal position (P_h).

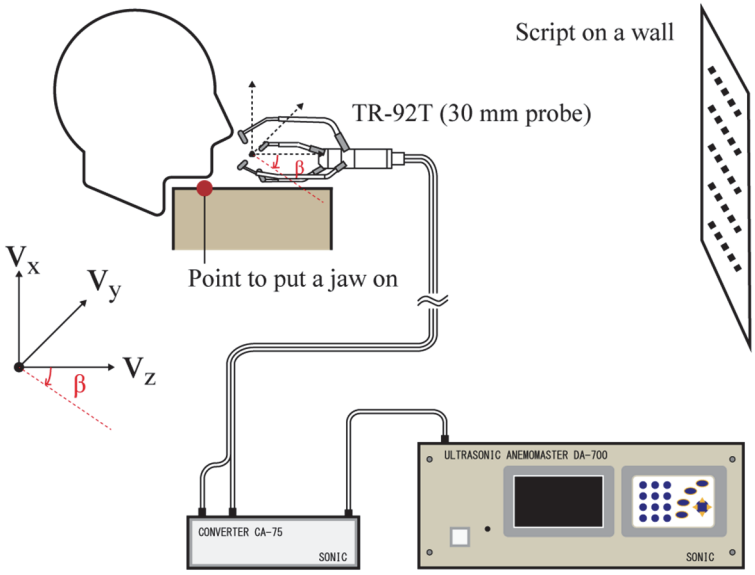
2.2 Methodology of Exhalation Measurements

2.2.1 Measurement of Exhaled Air Velocity During Japanese Speech

This measurement was conducted in January 2022 to obtain realistic exhalation characteristics for use as boundary conditions in the CFD analysis. The experiment aimed to measure the velocity of exhaled air during speech under controlled conditions.

An ultrasonic anemometer (Sonic Corporation, model DA-700) equipped with a TR-92T probe (diameter 30 mm) was used, as illustrated in **Figure 2-2**. The TR-92T probe measures the mean velocity components along the X, Y, and Z axes within a 30 mm sensing region at a sampling frequency of 10 Hz.

During the experiment, subjects read the same Japanese script displayed on a wall for one minute, and each trial was repeated three times. The script consisted of a general Japanese article about COVID-19, selected to represent natural conversational speech, as shown in **Figure 2-2b**. Each subject placed their chin on a fixed support to maintain a constant distance between the mouth and the probe, as shown in **Figure 2-2a**. They were instructed to read the script as if conversing with a person standing approximately 1.5 m in front of them.



Converter CA-75 Ultrasonic anemometer model DA-700 (Sonic corporation)

(a)

新型コロナウイルス感染症（COVID-19）は、SARS-CoV-2 ウイルスによって引き起こされる感染症です。COVID-19 によって起こる症状のほとんどは 軽度から中等度であり、特別な治療を受けずに回復します。 しかし、中には重症化して医療機関での治療が必要になることもあります。
ウイルスは、感染者が咳やくしゃみをする、話す、歌う、息をするときに、 小さな液体の粒子となって口や鼻から拡散する可能性があります。 この粒子は、大きな呼吸器飛沫から小さなエアロゾルまでさまざまです。
COVID-19 感染者の近くにいるときにウイルスを吸い込んだり、 汚染された物に触れてから自分の目、鼻、口に触れたりすると、 ウイルスに感染する可能性があります。
このウイルスは、屋内や人が多い環境で拡散しやすくなります。 (V: Breath Potition)

(b)

Figure 2-2. Setting of velocity measurement from talking: (a) Schematic diagram of the velocity measurement system. (b) The script subjects read.

Six subjects (three males and three females, aged 21–24, average age 22.5 years) from Osaka University participated in the measurement. The measured velocity components were used to calculate the vertical exhalation angle β_i [°] and total exhalation speed $|v_i|$ [m/s] using Eqs. (2-1) and (2-2):

$$\beta_i = \tan^{-1}\left(\frac{-v_{x_i}}{v_{z_i}}\right) \quad (2-1)$$

$$|v_i| = \sqrt{v_{x_i}^2 + v_{y_i}^2 + v_{z_i}^2} \quad (2-2)$$

where v_{x_i} , v_{y_i}, and v_{z_i} are the instantaneous velocity components along the X, Y, and Z axes (10 Hz) [m/s].

The mean vertical angle $\bar{\beta}$ and mean velocity magnitude $|\bar{v}|$ for each 60-second measurement were calculated using Eqs. (2-3) and (2-4), respectively:

$$\bar{\beta} = \frac{1}{n_e}\sum_{i=1}^{n_e}\left\{tan^{-1}\left(\frac{-v_{x_i}}{v_{z_i}}\right)\right\} \quad (2-3)$$

$$|\bar{v}| = \frac{1}{n_e}\sum_{i=1}^{n_e}\sqrt{v_{x_i}^2 + v_{y_i}^2 + v_{z_i}^2} \quad (2-4)$$

where n_e is the number of elements used for the mean value calculation [-].

2.2.2 Measurement of Exhaled Air Volume During Japanese Speech

The experimental setup is illustrated in **Figure 2-3**. The total volume of exhaled air was measured using a mask, a check valve, and a polyethylene terephthalate (PET) bag. Each subject read the same Japanese script (shown in **Figure 2-2b**) while wearing a custom-made mask whose edges were sealed with rubber to prevent leakage. The exhaled air passed through a silicone tube into the PET bag. A one-way check valve was installed in the middle of the tube to prevent the reverse flow of air from the bag.

Subjects were allowed to remove the mask for normal breathing between trials. After donning the mask again, they resumed reading the script for one minute. Upon completion, the accumulated air volume in the PET bag was measured using a dry gas meter (SINAGAWA Co., Ltd.), as shown in **Figure 2-3**.

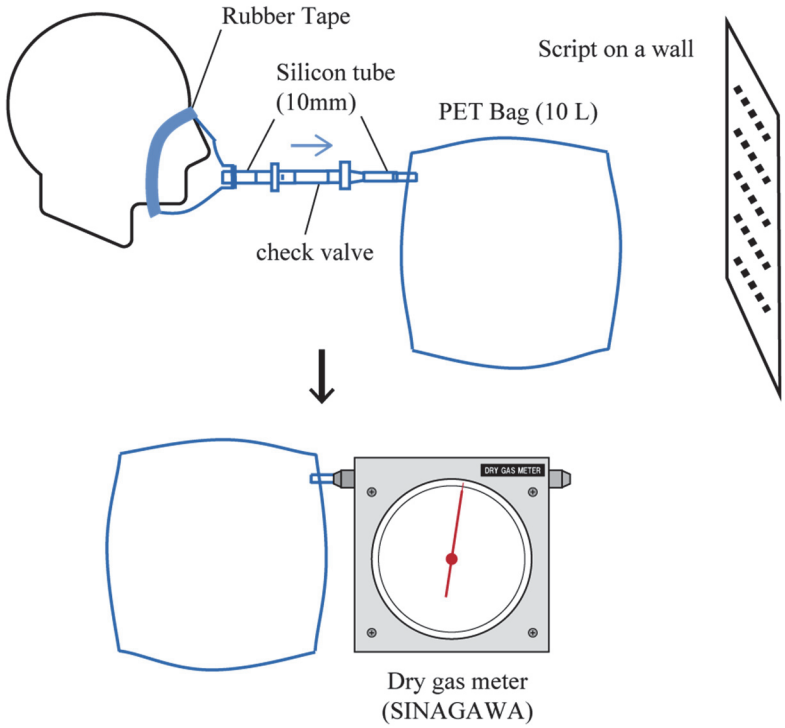


Figure 2-3. Schematic diagram of the volume measurement from talking

The same six subjects (three males and three females, aged 21–24) participated in this experiment. Each subject performed the test three times, and the mean exhaled air volume per minute was calculated using Eq. (2-5):

$$\overline{V_b} = \frac{V_{PET}}{T_m} \qquad (2-5)$$

where $\overline{V_b}$ is the mean exhaled air volume per minute [L/min], V_{PET} is the total volume of air collected in the PET bag after one minute of reading [L], and T_m is the measurement duration (1 minute in all cases) [min].

2.3 Methodology of CFD Analysis

2.3.1 Analysis Conditions

This study employed computational fluid dynamics (CFD) to simulate airflow and contaminant transport during a medical consultation scenario. The overall CFD modeling procedure is summarized in **Table 2-1**. The analysis was conducted under steady-state conditions, with 3,000 iterations, ensuring convergence below 10^{-4}

for all cases. The validity of this convergence criterion is discussed in Chapter 4.2.

Table 2-1

CFD method.

CFD code	STREAM ver 2021
Turbulence model	Standard k-ε model (Steady State)
Algorithm	SIMPLE
Discretization scheme for advection	QUICK
Number of cycles	3,000

The analysis domain, representing a consultation room, measured 2.4 × 3.8 × 2.2 m (20.064 m³), as illustrated in **Figure 2-4**. A patient and a doctor were modeled as seated, facing each other at a mouth-to-mouth distance of 1,200 mm, simulating close-distance conversation. It was assumed that the patient was infected with SARS-CoV-2 but was unaware of the infection, and thus both individuals conversed without masks.

Tracer gas was emitted solely from the patient's mouth, with the same density as air, to represent droplet nuclei generated during speech. This modeling assumption follows previous findings by Morawska et al. [59], who reported that the peak droplet diameter from speech is below 0.8 μm, and Ai et al. [60], who demonstrated that particles smaller than 3–5 μm exhibit aerodynamic behavior similar to gaseous contaminants. Accordingly, the droplet nuclei emitted from speech were assumed to behave as passive scalars, enabling simulation using tracer gas.

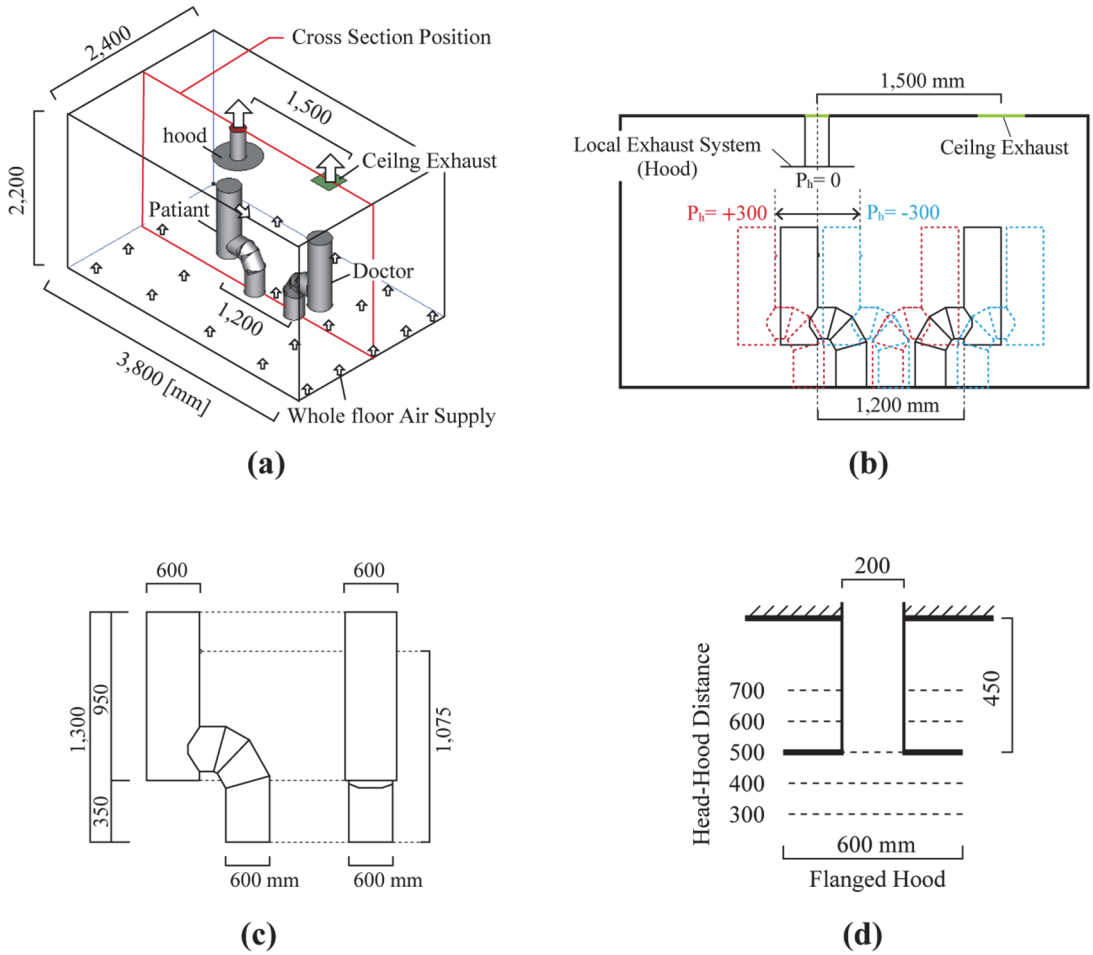


Figure 2-4. Details of CFD analysis settings: (a) Analysis room (Case A, basic condition); (b) Cross section of the consulting room and definition of the hood horizontal position (P_h); (c) Details of the human model; (d) Details of the local exhaust ventilation (hood).

The boundary conditions applied in the CFD analysis are summarized in **Table 2-2**. The velocity, flow rate, and exhalation angle of the tracer gas were based on the experimental results described in this study, with their validity discussed in Section 2.5.1. The tracer gas temperature was set to 32°C [61], and its molecular diffusivity was 1.41×10^{-5} m²/s, corresponding to the value of CO_2 [62]. The sensible heat generation from both the patient and doctor models was set to 75 W [63]. Although radiative heat transfer was initially considered, all human sensible heat (75 W) was assigned to the first computational cell adjacent to the human surface because the wall temperature was fixed and surface heat generation was applied only to the human model. Consequently, the intensity of the thermal plume may be slightly overestimated.

The geometry of the human models was based on the thermal manikin developed at the University of Osaka, as shown in **Figure 2-4c**. The supply air was introduced from the entire floor area at 20°C, assuming a

neutral (non-heating/non-cooling) thermal condition. All walls were treated as thermally insulated, with heat transfer coefficients determined according to ASHRAE Standard 140-2017 [64], as listed in **Table 2-2**.

Table 2-2.
Boundary conditions for CFD analysis.

Analys volume Number of mesh First mesh distance from each wall		2.4 (x)×3.8 (y)×2.2 (z) = 20.064 m³ 106(x)×183(y)×126 (z) = 2,444,148 100 mm
Wall condition	Thermal	Ceiling: 20 ℃, 0.957 W/(m^{2}K) Wall: 20 ℃, 3.048 W/(m^{2}K) Floor: 20 ℃, 4.018 W/(m^{2}K)
Heat generation		75 W × 2 people
Tracer gas emission (doctor mouth)		Diffusivity : 1.41 × 10^{-5} m^2/s (CO_2) Dencity: 1.17 kg/m^3 (Air) Specific heat: 1007 J/kg·K (Air) Thermal conductivity: 0.026 (Air) Temperature: 32 ℃ Flow rate: 5.21 L/min Velocity: 0.30 m/s Vertical Angle (β): -11.9 ° Size: 17.04 × 17.04 mm^2
Supply air temperature		20 ℃
Ceiling Exhaust Boundary Condition		Natural outlet

The turbulent kinetic energy (k) and turbulent dissipation rate (ε) at the inlets were calculated using Eqs. (2-6) and (2-7):

$$k = \frac{3}{2}(U \times I)^2 \qquad (2-6)$$

$$\varepsilon = C_\mu^{3/4} \frac{k^{1/2}}{L} \qquad (2-7)$$

where U is the mean velocity [m/s], I is the turbulence intensity [-], C_μ is the model coefficient (C_μ=0.09) [-], and L is the turbulence length scale [m]. The corresponding inlet boundary conditions are summarized in **Table 2-3**.

Table 2-3.

Boundary conditions for CFD analysis. (k and ε).

	I (-)	L (m)	Flow rate (m^3/h)	A (m^2)	v (m/s)	k (m^2/s^2)	ε (m^2/s^3)
Patient mouth	1.00E-01	1.70E-03	0.313	2.90E-04	0.300	1.35E-03	4.78E-03
Floor	1.00E-02	1.00E-02	120.1	9.12	3.66E-03	2.01E-09	1.48E-12
	1.00E-02	1.00E-02	240.5	9.12	7.32E-03	8.05E-09	1.19E-11
	1.00E-02	1.00E-02	401.0	9.12	1.22E-02	2.24E-08	5.50E-11
	1.00E-02	1.00E-02	601.6	9.12	1.83E-02	5.04E-08	1.86E-10
	1.00E-02	1.00E-02	802.2	9.12	2.44E-02	8.96E-08	4.40E-10
	1.00E-02	1.00E-02	1000.0	9.12	3.05E-02	1.39E-07	8.53E-10

The ventilation configuration consisted of floor-supply air (OA) and two exhaust routes: a local exhaust ventilation (LEV) hood positioned directly above the patient, and ceiling exhaust outlets for balancing the overall room airflow rate, as illustrated in **Figure 2-4**. The hood had a flanged design, which demonstrated high capture efficiency under crossflow conditions according to Komori et al. [65]. The computational grid employed a structured mesh consisting of 2,444,148 cells (106 × 183 × 126). The first grid spacing from the wall was 100 mm, while that near the human surface was 10 mm. The mesh independence and validity of these parameters are discussed in Chapter 2.5.2

2.3.2 Simulation Cases

To evaluate the effects of combining a local exhaust hood (LEV) with an underfloor air-supply displacement ventilation (FSDV) system, four major parameters were investigated: (1) hood flow rate (Q_h), (2) hood height (vertical hood–head distance, H_h), (3) horizontal hood position (P_h), and (4) overall ventilation rate (ACH). These parameters and their ranges are summarized in **Table 2-4**, and the corresponding geometric configurations are illustrated in **Figure 2-6**.

To examine the influence of hood installation, a case without a hood was also included, represented by a hood flow rate of Q_h = 0 m^3/h in **Table 2-4**. The base condition was defined as Q_h = 100 m^3/h, H_h = 500 mm, and P_h = 0 mm, where P_h = 0 mm indicates that the center of the hood is located directly above the patient's mouth (see **Figure 2-6**). Each parameter was varied individually from this base condition, while all other conditions were held constant. When the horizontal hood position (P_h) was changed, both the patient and doctor

models were shifted to maintain a constant distance between the hood and the ceiling exhaust outlet.

Table 2-4.
Details of each simulation cases.

Case Name	Paremeter	Floor-Supply Flow Rate (m^3/h) (Air Change Rate (ACH))	Q_h: Hood Flow Rate (m^3/h)	H_h: Hood-Head Distance (mm)	P_h: Hood Horizontal Position (mm)
Case A-0	(Basic Condition)	1000 m^3/h (50 ACH)	100	500	0
Case A-1	Q_h (m^3/h)		50, 150, 200, 250, 300		
Case A-2	H_h (mm)		100	300, 400, 600, 700	
Case A-3	P_h (mm)			500	-300, -200, -100, 100, 200, 300
Case B-0	(Basic Condition)	120 m^3/h (6 ACH)	100	500	0
Case B-1	Q_h (m^3/h)		50, 75, 120		
Case B-2	H_h (mm)		100	300, 400, 600, 700	
Case B-3	P_h (mm)			500	-300, -200, -100, 100, 200, 300
Case C	Air Change Rate	120, 240, 401, 602, 802, 1,000 (6, 12, 20, 30, 40, 50)	100	500	0
Case D	Air Change Rate	120, 240, 401, 602, 802, 1,000 (6, 12, 20, 30, 40, 50)	-	500	0

All CFD simulation cases were classified into four groups—Case A, Case B, Case C, and Case D—according to their specific objectives and boundary conditions, as summarized below:

Case A: Effect of Hood Parameters under High Ventilation Conditions (Q = 1,000 m³/h, 50 ACH).
The purpose of Case A was to evaluate the influence of each hood parameter (Q_h, H_h, P_h) under high-ventilation conditions. The floor-supply air (SA) flow rate was fixed at 1,000 m³/h (50 ACH), and the hood parameters were systematically varied. At this ventilation rate, the average room air velocity was approximately 0.03 m/s, which exceeds the terminal settling velocity of 10 μm droplets (0.003 m/s) [66]. Therefore, these conditions were expected to effectively remove both droplets and droplet nuclei through ventilation. According to Yamanaka et al., the WHO guideline for healthcare settings (12 ACH) corresponds to a ventilation rate of approximately 1,302 m³/h for a standard room size of 6 × 6.7 × 2.7 m³ [67,68]. Since the number of infectious quanta (n) in the Wells–Riley model depends on ventilation rate (Eqs. (2-11) and (2-12)), the parameter variation based on airflow rate was considered essential. In addition, the experimental chamber used for the

full-scale tests in Chapters 5 had a fixed maximum ventilation capacity of 1,000 m³/h, which was adopted as the upper limit in this study.

Case B: Effect of Hood Parameters under Typical Consultation Room Conditions (Q = 120 m³/h, 6 ACH). The purpose of Case B was to evaluate the influence of each hood parameter under standard ventilation conditions for consultation rooms. The floor-supply airflow rate was fixed at 120 m³/h (6 ACH), corresponding to the recommended range for healthcare environments (6–12 ACH) by REHVA [69]. Each hood parameter (Q_h, H_h, and P_h) was varied from the base condition as shown in **Table 2-4**.

Case C: Effect of Overall Ventilation Rate with Hood Installed (Q_h = 100 m³/h)
The purpose of Case C was to investigate the effect of ventilation rate while keeping the hood parameters constant (Q_h = 100 m³/h, H_h = 500 mm, P_h = 0 mm). The overall room ventilation rate was varied from 6 to 50 ACH by adjusting the floor-supply airflow rate between 120 and 1,000 m³/h, as listed in **Table 2-4**.

Case D: Comparison of Hood and No-Hood Conditions across Ventilation Rates
Case D was designed to directly compare the effects of installing a hood at each ventilation rate. The hood was removed (Q_h = 0 m³/h) to serve as a control condition corresponding to Case C, as shown in **Table 2-4**.

In total, 43 CFD simulations were conducted: Case A: 17 conditions, Case B: 14 conditions, Case C: 6 conditions, and Case D: 6 conditions.

2.3.3 Hood Capture Performance Assessment in CFD

To evaluate the contaminant removal performance of the local exhaust hood, the hood capture efficiency (η) was used as a primary indicator. The capture efficiency represents the proportion of tracer gas captured by the hood relative to the total amount exhausted from the room and is calculated using Eq. (2-8):

$$\eta = \frac{Q_h(C_h - C_{SA})}{Q_h(C_h - C_{SA}) + Q_{ce}(C_{ce} - C_{SA})} \quad (2-8)$$

where Q_h is the hood exhaust flow rate [m³/h], C_h is the tracer gas concentration in the hood exhaust air [-], Q_{ce} is the ceiling exhaust flow rate [m³/h], C_{ce} is the tracer gas concentration in the ceiling exhaust air [-], and

C_{SA} is the tracer gas concentration in the supply air [-]. In this simulation, C_{SA}= 0.

The hood capture efficiency (η) quantitatively expresses the fraction of contaminants directly captured by the hood relative to the total amount removed through both exhaust routes. It primarily depends on the flow rate ratio between the hood and the ceiling exhaust, as well as the aerodynamic interaction between the hood and the surrounding flow field.

While η provides a useful measure of the hood's local capture performance, it does not fully represent the overall infection control capability of the ventilation system. Therefore, to comprehensively evaluate contaminant dispersion and infection risk within the occupied zone, spatial concentration distributions were also analyzed using the CFD results.

2.3.4 Infection Risk Assessment from Tracer Gas in CFD

The Wells–Riley model, originally proposed by Wells [70] and later refined by Riley et al. [71], was employed to estimate the airborne infection risk associated with the studied ventilation system. The Wells–Riley model is a classical probabilistic model that describes the transmission of airborne infectious diseases in enclosed spaces. The fundamental equation of the model is given by Eq. (2-9):

$$P = 1 - e^{-n} \tag{2-9}$$

where P is the probability of infection for a susceptible individual, and n is the number of infectious quanta inhaled. This relationship indicates that one quanta corresponds to the infectious dose that results in 63.2% infection probability among exposed individuals.

The infection probability can also be expressed as Eq. (2-10)

$$P = \frac{C}{S_0} \tag{2-10}$$

where C is the number of new infections, S_0 is the initial number of susceptible individuals.

Because the quantity of virus particles required to infect 63.2% of exposed individuals varies by disease type and viral strain, each pathogen requires an individual assessment. For example, for SARS-CoV-1, dose–response models based on animal experiments have been employed to determine this value [72].

The Wells–Riley model defines the relationship between quanta emission and exposure through Eqs. (2-11) and (2-12), as presented by REHVA [69]:

$$n = C_{avg} Q_b D \quad (2-11)$$

$$C_{avg} = \frac{q}{Q} \quad (2-12)$$

where n is the total number of quanta inhaled [quanta], C_{avg} is the time-averaged quanta concentration in the room [quanta/m³], Q_b is the volumetric breathing rate of an occupant [m³/h], D is the exposure duration [h], q is the quanta emission rate [quanta/h], and Q is the total ventilation rate [m³/h].

Because C_{avg} is derived under the assumption of steady-state and perfectly mixed airflow, the Wells–Riley model inherently assumes a uniform distribution of infectious particles in the indoor environment.

Despite its simplicity, several uncertainties remain in estimating the infection probability *P*. The quanta emission rate (q) depends primarily on the viral load in respiratory fluids (RNA copies/mL), which can vary by seven orders of magnitude (10^4–10^{11}) depending on the individual and the variant strain [73]. Moreover, the duration of exposure (*D*) for healthcare workers, such as physicians, is often variable and difficult to define precisely, since actual consultation times differ widely even within a single day. Therefore, the infection probability cannot be directly calculated without assuming specific values for Q_b and *D*.

To address these limitations and enable direct comparison among ventilation configurations, this study introduces a localized infection risk indicator based on the quanta concentration in front of the doctor's mouth. The total number of quanta inhaled by the doctor (non-infected person) is calculated as follows (Eq. (2-13)):

$$n_{dc} = C_{q,dc} Q_{dc} t_{ex} \quad (2-13)$$

where n_{dc} is the total number of quanta inhaled by doctor (non-infected person) [quanta], $C_{q,dc}$ is the quanta concentration in front of the doctor's (non-infected person's) mouth [quanta/m³], Q_{dc} is the breathing rate of the doctor (non-infected person) [m³/h], and t_{ex} is the exposure time during which the doctor (non-infected person) inhales air containing quanta concentration $C_{q,dc}$ [h].

The local quanta concentration $C_{q,dc}$ [quanta/m³] was estimated using Eqs. (2-14) and (2-15):

$$C_{q,dc} = \frac{q}{Q} \cdot C'_{g,dc} \quad (2-14)$$

$$C'_{g,dc} = \frac{C_{g,dc}}{C_{g,pm}} \quad (2-15)$$

where $C_{q,dc}$ is the quanta concentration in front of the doctor's mouth [quanta/m³], $C'_{g,dc}$ is the normalized tracer gas concentration in front of the doctor's mouth relative to the perfectly mixed concentration [-], $C_{g,dc}$ is the local tracer gas concentration at the doctor's mouth [-], and $C_{g,pm}$ is the tracer gas concentration under perfectly mixed conditions [-].

It was assumed that the spatial distribution of quanta follows the same pattern as that of the tracer gas concentration, since the droplet nuclei generated from speech exhibit gas-like aerodynamic behavior at small diameters (≤ 5 μm). Therefore, $C_{g,dc}$ represents the local concentration relative to the ideal well-mixed condition. The quanta emission rate (q) was set to 42 quanta/h, corresponding to light activity with speaking, based on the values recommended by REHVA [69] and the experimental data of Buonanno et al. [73]. The breathing rate of the doctor Q_{dc} was assumed to be 5.21 L/min (= 3.13 × 10^{-4} m³/s ≈ 1.13 m³/h), as obtained from the experimental measurements in this chapter (see **Table 2-8**).

2.3.5 Calculation of SVE5

To quantitatively evaluate the contribution of each air outlet to the contaminant removal process, the SVE5 (Scale for Ventilation Efficiency 5) index proposed by Kobayashi et al. [74] was employed. SVE5 represents the local contribution ratio of each exhaust outlet to the removal of contaminants at a specific position in the room. The SVE5 value at a point x is defined by Eq. (2-15):

$$SVE\,5(x) = \frac{C'(x, n_o)}{C_0(n_o)} \quad (2-15)$$

where n_o denotes the name (or identifier) of the air outlet. $C'(x, n_o)$ represents the tracer gas concentration at position x, which is obtained by solving the concentration transport equation in the reverse-time direction under clean initial conditions, with a unit concentration imposed at the exhaust outlet n_o. $C_0(n_o)$ is the reference concentration at the exhaust outlet, defined by Eq. (2-16):

$$C_0(n_o) = \frac{M}{Q(n_o)} \quad (2-16)$$

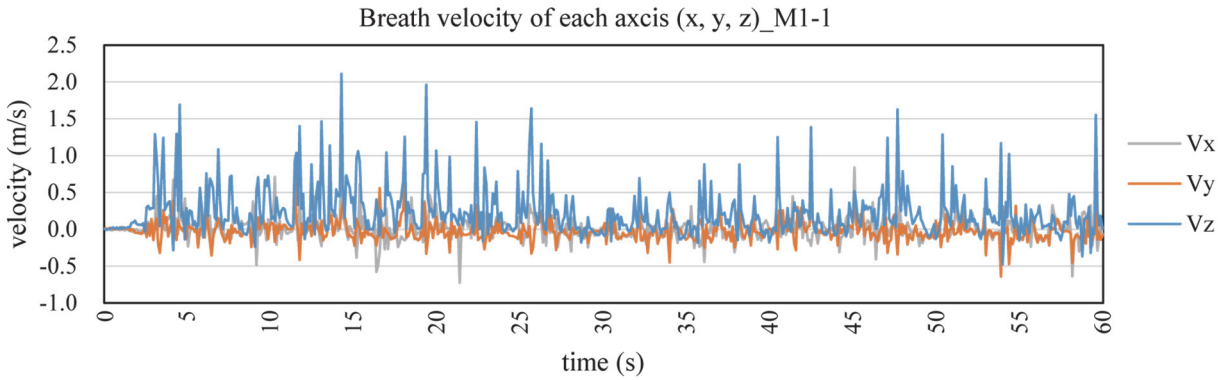
where M is the contaminant generation rate [m³/h], and $Q(n_o)$ is the airflow rate through the exhaust outlet n_o [m³/h].

The SVE5(x) value thus expresses how effectively the airflow from a particular exhaust outlet contributes to contaminant removal at a given location. Higher SVE5 values indicate that a larger portion of the local contaminants are removed through the specific exhaust outlet, while lower values imply weaker coupling between the local airflow field and the corresponding exhaust path. This method is particularly useful for analyzing multi-exhaust ventilation systems, such as those combining a local exhaust hood and a ceiling exhaust, as in the present study.

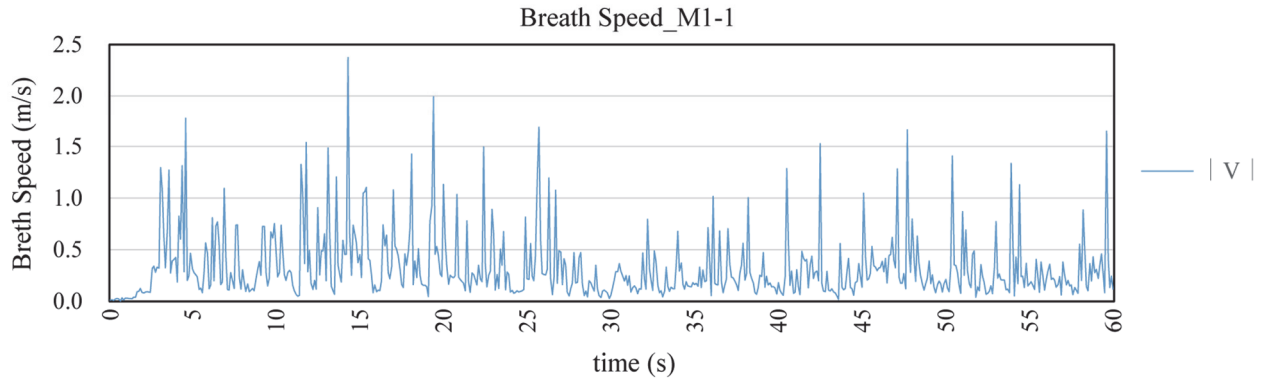
2.4 Results

2.4.1 Measurement Results of Exhaled Air during Talking

Figure 2-5 presents a representative time series of the exhaled air velocity measured during speech (one randomly selected male subject). The vertical component of velocity (v_z) was identified as the dominant element of exhaled airflow. The time variation of v_z closely followed the rhythm of natural conversation throughout the one-minute measurement period. Several sharp peaks were observed in the velocity profile, likely corresponding to plosive sounds such as /p/ and /t/, which are known to generate higher expiratory momentum [75].



(a) Exhaled air velocity components along each axis (x, y, z) for one male subject (1 minute, 10 Hz).



(b) Magnitude of exhaled air speed for the same measurement (1 minute, 10 Hz).

Figure 2-5. Measurement results of exhaled air velocity during Japanese speech: (a) Exhaled air velocity components along each axis (x, y, z) for one male subject (1 minute, 10 Hz). (b) Magnitude of exhaled air speed for the same measurement (1 minute, 10 Hz).

The results of the mean exhaled air velocity $|\bar{v}|$ [m/s] for all subjects are summarized in **Table 2-5**. The mean values were calculated using Eq. (2-4) based on one-minute measurements. Negative velocity values, corresponding to inhalation phases, were excluded from the averaging process. Therefore, only elements where v_z >0 (n_d= 7,604) were used for the final calculation. The overall mean exhalation velocity across all subjects was 0.30 m/s, which was subsequently adopted as the boundary condition for CFD analysis (see **Table 2-2**).

Table 2-5.

Summarization of the breath speed: $|\bar{v}|$ [m/s] of each measurement (one minute, and three times for each of the six subjects). The data using calculation mean value is only v_z>0.

	Male	Female	
M (F) 1-1	0.36	0.45	
M (F) 1-2	0.34	0.52	**Max**
M (F) 1-3	0.28	0.49	
M (F) 2-1	0.19	0.17	
M (F) 2-2	0.24	0.17	**min**
M (F) 2-3	0.42	0.17	
M (F) 3-1	0.28	0.19	
M (F) 3-2	0.31	0.21	
M (F) 3-3	0.36	0.23	Total Average [m/s]
Average	0.31	0.29	0.30

Table 2-6 presents the vertical breath angle β [°] shown in **Figure 2-2**, which was calculated by varying the number of sampling elements $n_e$as defined in Eq. (2-3). In Eq. (2-2), when the vertical velocity component v_z is small (e.g., $v_z < 0.1$or $v_z < 0.05$), β tends to be overestimated. Therefore, calculations were performed while adjusting $n_e$according to the magnitude of v_z.

Table 2-6.

Summarizes the vertical breath angle: β [°], calculated by each element selection.

elements selection	β (°)	n_e
all	6.5	10,800
$v_z \geqq 0$	17.8	7,604
$v_z \geqq 0.05$	15.3	5,771
$v_z \geqq 0.1$	13.4	4,294
$v_z \geqq 0.5$	11.9	839

The total number of sampled data points was 10,800 (10 Hz sampling for one minute, repeated three times for each of the six subjects), of which 839 data points satisfied $v_z \geq 0.5$. Since elements with greater momentum are more representative of the true exhalation direction, only these were used to estimate an accurate mean angle. Consequently, a vertical breath angle β of 11.9° was adopted as the boundary condition for

the CFD simulation, as listed in **Table 2-2**. The mean values of β, calculated using only elements satisfying $v_z \geq 0.5$, are summarized in **Table 2-7**.

Table 2-7.
Summarization of the vertical breath angle: β [°]. The data using the calculation for mean value is only v_z>0.5.

	Male	Female	
M (F) 1-1	5.50	25.8	**Max**
M (F) 1-2	2.98	25.0	
M (F) 1-3	7.78	22.4	
M (F) 2-1	12.5	-10.6	**min**
M (F) 2-2	12.5	2.97	
M (F) 2-3	20.2	-4.89	
M (F) 3-1	17.3	7.48	
M (F) 3-2	16.7	18.6	
M (F) 3-3	17.3	14.3	Total Average [°]
Average	12.5	11.2	11.9

The results of exhaled air volume measurements are summarized in **Table 2-8**, calculated using Eq. (2-5). As shown in **Fig. 2-3**, the exhaled air was collected in a PET bag through a mask system during a one-minute reading of the Japanese script. The mean exhaled air volume among all participants was 5.21 L/min, and this value was also adopted as a CFD boundary condition (**Table 2-2**).

Table 2-8.
Summarization of breath volume measurement: (V_b) [L/min]. (one minute, and three times for each of the six subjects).

	Male	Female	
M (F) 1-1	6.67	3.23	
M (F) 1-2	7.05	3.54	
M (F) 1-3	6.18	3.83	
M (F) 2-1	7.12	5.06	
M (F) 2-2	7.00	6.07	
M (F) 2-3	8.07 **Max**	6.59	
M (F) 3-1	4.72	2.55 **min**	
M (F) 3-2	5.02	3.02	
M (F) 3-3	4.85	3.19	Total Average [L/min]
Average	6.30	4.12	5.21

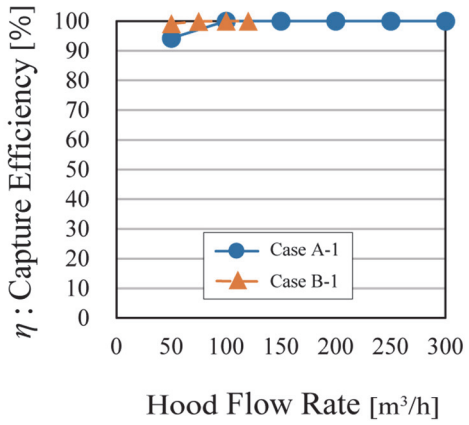
From the measured mean exhalation velocity (0.30 m/s) and volumetric flow rate (5.21 L/min), the effective mouth opening area of the patient model was estimated as 17.04 × 17.04 mm, assuming a square outlet shape. These experimentally derived parameters ensured that the CFD boundary conditions closely represented realistic human breathing during conversation.

2.4.2 CFD Simulation Results

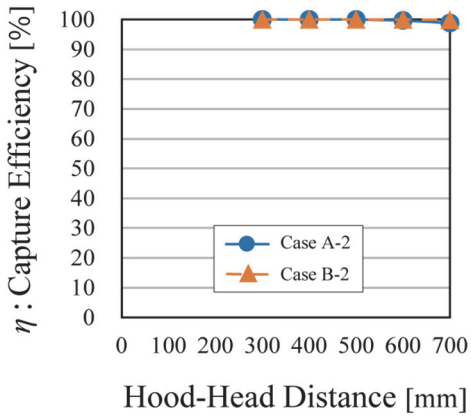
Figure 2-6 presents the calculated hood capture efficiency η [%] for Cases A, B, and C. Note that η was not defined in Case D, since no hood was installed. In **Figure 2-6a**, where the hood flow rate (Q_h) was varied, high capture efficiency values were obtained in both Case A (SA = 1,000 m³/h, 50 ACH) and Case B (SA = 120 m³/h, 6 ACH). Similarly, in **Figure 2-6b**, which examined the hood–head distance (H_h), high η values were observed across both cases. However, in **Figure 2-6c**, when the horizontal hood position (P_h) was changed, η exhibited large fluctuations in Case A, while remaining relatively stable in Case B.

These variations can be attributed to the difference in flow rate balance between the hood and the ceiling exhaust, as will be discussed later with reference to **Figure 2-13**. In **Figure 2-6d**, where the room air supply rate was varied, η remained close to 100% across all airflow conditions, indicating high overall capture performance. Overall, **Figure 2-6** demonstrates that the horizontal position of the hood plays a critical role in de-

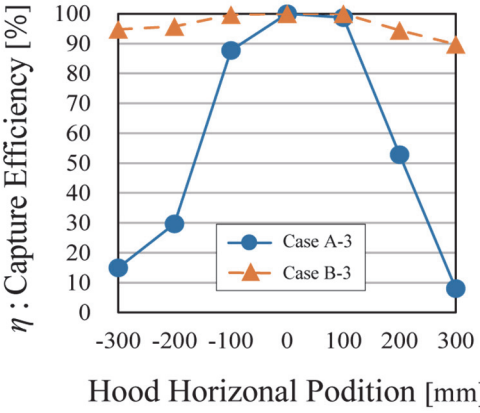
termining capture efficiency under high ventilation conditions (1,000 m³/h, 50 ACH).



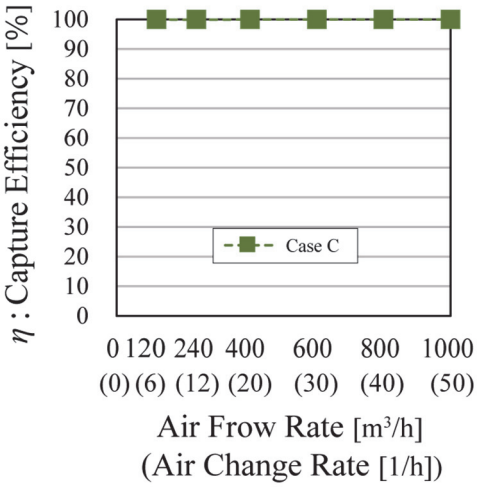
(a) Case A-1 (SA=1,000 m³/h, H_h=500 mm, P_h=0mm)
Case B-1 (SA=120 m³/h, H_h=500 mm, P_h=0mm)



(b) Case A-2 (SA=1,000 m³/h, Q_h=100 m³/h, P_h=0mm)
Case B-2 (SA=120 m³/h, Q_h=100 m³/h, P_h=0mm)



(c) Case A-3 (SA=1,000 m³/h, Q_h=100 m³/h, H_h=500 mm)
Case B-3 (SA=120 m³/h, Q_h=100 m³/h, H_h=500 mm)



(d) Case C (Q_h=100 m³/h, H_h=500 mm, P_h=0mm)

Figure 2-6. Hood capture efficiency (η) for each parameter: (a) Effect of hood flow rate (Q_h) — Case A-1 (SA = 1,000 m³/h, H_h = 500 mm, P_h = 0 mm) and Case B-1 (SA = 120 m³/h, H_h = 500 mm, P_h = 0 mm). (b) Effect of hood–head distance (H_h) — Case A-2 (SA = 1,000 m³/h, Q_h = 100 m³/h, P_h = 0 mm) and Case B-2 (SA = 120 m³/h, Q_h = 100 m³/h, P_h = 0 mm). (c) Effect of horizontal hood position (P_h), Case A-3 (SA = 1,000 m³/h, Q_h = 100 m³/h, H_h = 500 mm) and Case B-3 (SA = 120 m³/h, Q_h = 100 m³/h, H_h = 500 mm). (d) Effect of total air flow rate (SA) — Case C (Q_h = 100 m³/h, H_h = 500 mm, P_h = 0 mm).

As discussed in Section 2.2.3, the exhaust route of tracer gas is a more meaningful indicator for infection risk than η alone. **Figures 2-7** through **2-13** summarize the CFD results of tracer gas concentration and airflow

patterns.

・**Figure 2-7** shows the normalized tracer gas concentration in front of the doctor's mouth ($C'_{g,dc}$), representing local exposure potential, for Cases A–D.

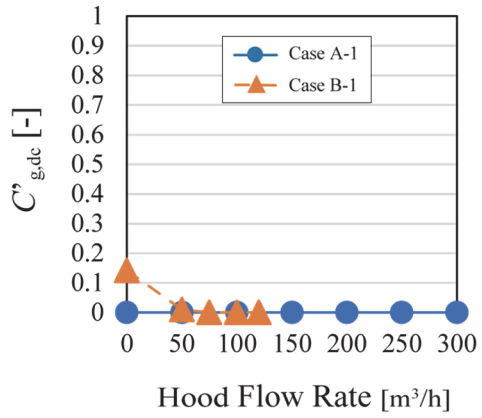
・**Figure 2-8** illustrates the relationship between capture efficiency η and $C'_{g,dc}$.

・**Figures 2-9** and **2-10** show the spatial quanta concentration distributions [quanta/m³].

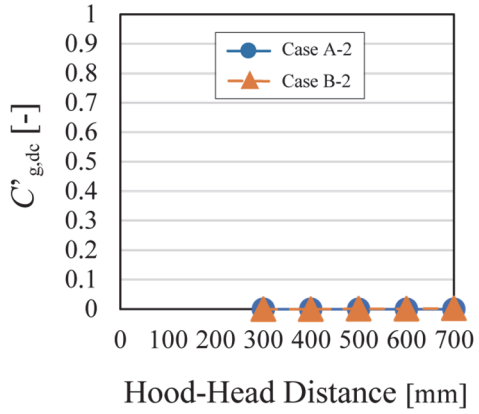
・**Figures 2-11–2-13** depict the contribution ratio of the hood to total exhaust flow, quantified by SVE5.

In the SVE5 plots, red regions (SVE5 = 1) indicate areas where air is exhausted entirely through the hood, while blue regions (SVE5 = 0) correspond to airflow exhausted through the ceiling outlet.

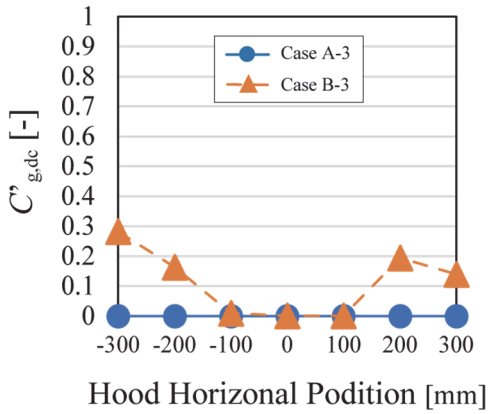
In **Figure 2-7a–b** and **Figure 2-8a, b, d, e,** $C'_{g,dc}$ remained extremely low, suggesting minimal infection potential ($C'_{g,dc}$ <10^{-25} in Case A, $C'_{g,dc}$ <10^{-3} in Case B), except when the hood was not used. However, as shown in Figures **2-7c** and **2-8c, f**, the horizontal hood position had a marked effect in Case B, contrary to the modest influence observed in the capture efficiency (**Figure 2-6c**).



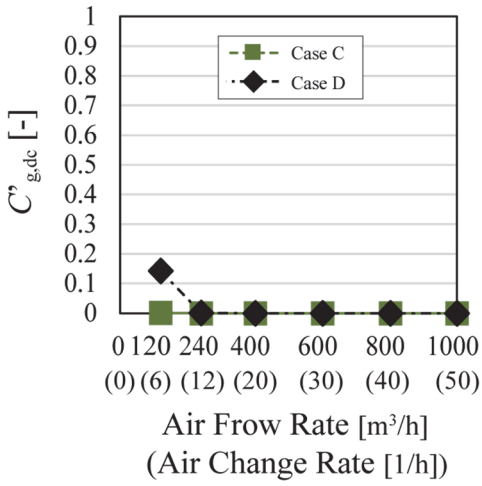
(a) Case A-1 (SA=1,000 m³/h, H_h=500 mm, P_h=0mm)
Case B-1 (SA=120 m³/h, H_h=500 mm, P_h=0mm)



(b) Case A-2 (SA=1,000 m³/h, Q_h=100 m³/h, P_h=0mm)
Case B-2 (SA=120 m³/h, Q_h=100 m³/h, P_h=0mm)



(c) Case A-3 (SA=1,000 m³/h, Q_h=100 m³/h, H_h=500 mm)
Case B-3 (SA=120 m³/h, Q_h=100 m³/h, H_h=500 mm)



(d) Case C (Q_h=100 m³/h, H_h=500 mm, P_h=0mm)
Case D (No hood)

Figure 2-7. The results of the tracer gas concentration in front of the doctor's mouth normalized by perfect mixing concentration $C'_{g,dc}$ [-] in Cases A, B, C, and D: (a) Case A-1 (SA = 1000 m3/h, H_h = 500 mm, P_h = 0 mm); Case B-1 (SA = 120 m^3/h, H_h = 500 mm, P_h = 0 mm). (b) Case A-2 (SA = 1000 m3/h, Q_h = 100 m^3/h, P_h = 0 mm); Case B-2 (SA = 120 m^3/h, Q_h = 100 m^3/h, P_h = 0 mm). (c) Case A-3 (SA = 1000 m^3/h, Q_h = 100 m^3/h, H_h = 500 mm); Case B-3 (SA = 120 m^3/h, Q_h = 100 m^3/h, H_h = 500 mm). (d) Case C (Q_h = 100 m^3/h, H_h = 500 mm, P_h = 0 mm); Case D (no hood).

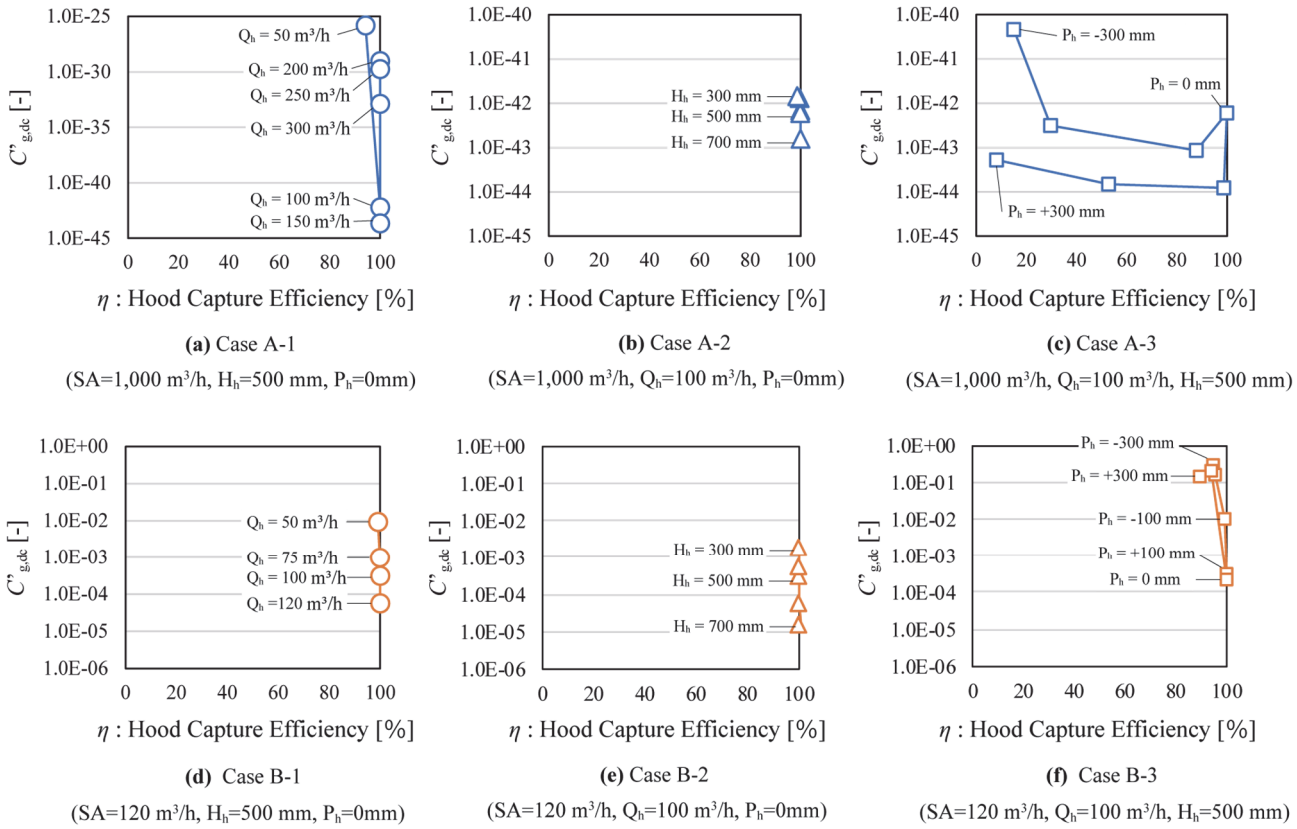


Figure 2-8. The relationship between hood capture efficiency η [%] and the tracer gas concentration in front of the doctor's mouth normalized by perfect mixing concentration $C'_{g,dc}$ [-] in Cases A and B. (a) Case A-1 (SA = 1000 m^3/h, H_h = 500 mm, P_h = 0 mm). (b) Case A-2 (SA = 1000 m^3/h, Q_h = 100 m^3/h, P_h = 0 mm). (c) Case A-3 (SA = 1000 m^3/h, Q_h = 100 m^3/h, H_h = 500 mm). (d) Case B-1 (SA = 120 m^3/h, H_h = 500 mm, P_h = 0 mm). (e) Case B-2 (SA = 120 m^3/h, Q_h = 100 m^3/h, P_h = 0 mm). (f) Case B-3 (SA = 120 m^3/h, Q_h = 100 m^3/h, H_h = 500 mm).

Flow visualizations in **Figure 2-9a–g** demonstrate that, even at a mean room velocity of only 0.03 m/s (corresponding to SA = 1,000 m³/h), a strong upward displacement flow developed under high ventilation (Case A). This upward flow carried a small amount of leaked tracer gas directly to the ceiling exhaust, bypassing the doctor's breathing zone—a pattern also visible in **Figures 2-12a–g**. In contrast, in Case B (SA = 120 m³/h), the weaker momentum allowed leaked tracer gas to remain near the hood and re-enter the capture zone (**Figures 2-9h–n** and **2-12h–n**). This resulted in a higher apparent η, but also increased exposure near the doctor's mouth, as shown in **Figure 2-8f**.

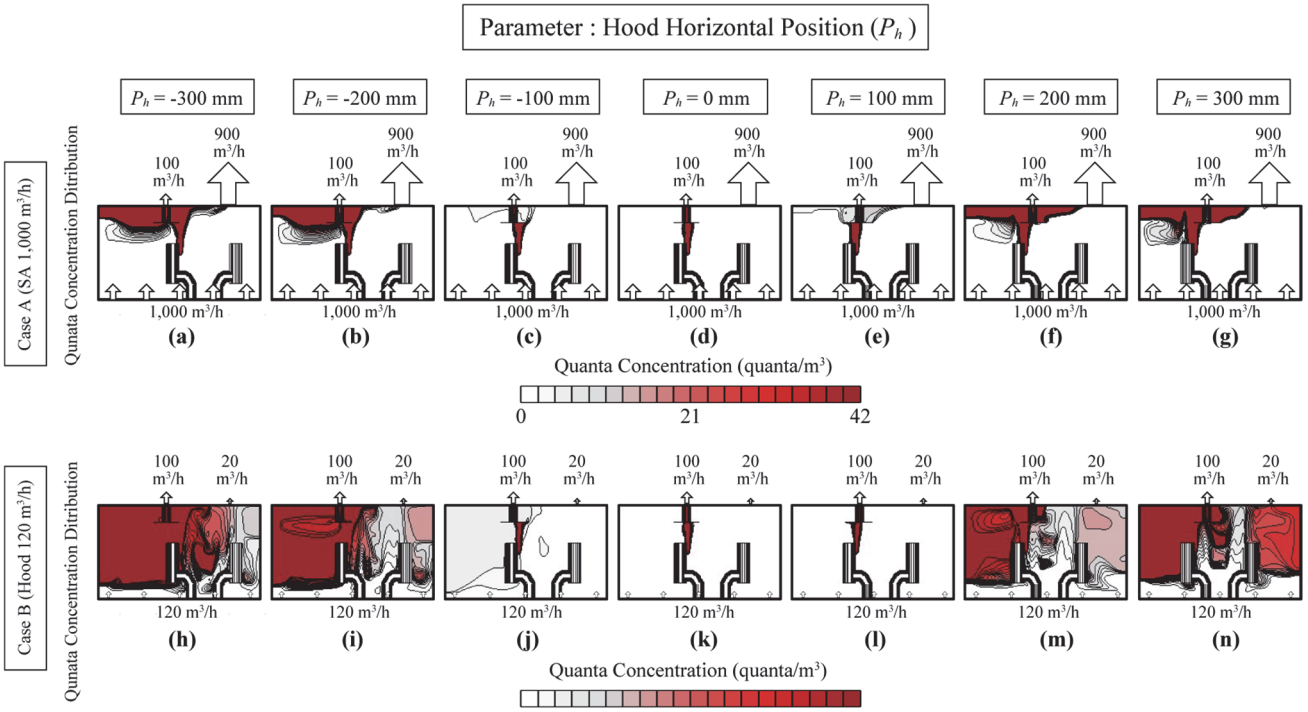


Figure 2-9. Quanta concentration distribution [quanta/m³] for different hood horizontal positions (comparison between Case A (a–g): SA = 1,000 m³/h and Case B (h–n): SA = 120 m³/h). The hood horizontal positions are as follows: (a,h) P_h = −300 mm, (b, i) P_h = −200 mm, (c, j) P_h = −100 mm, (d, k) P_h =0 mm, (e, l) P_h = +100 mm, (f, m) P_h = +200 mm, and (g, n) P_h = +300 mm.

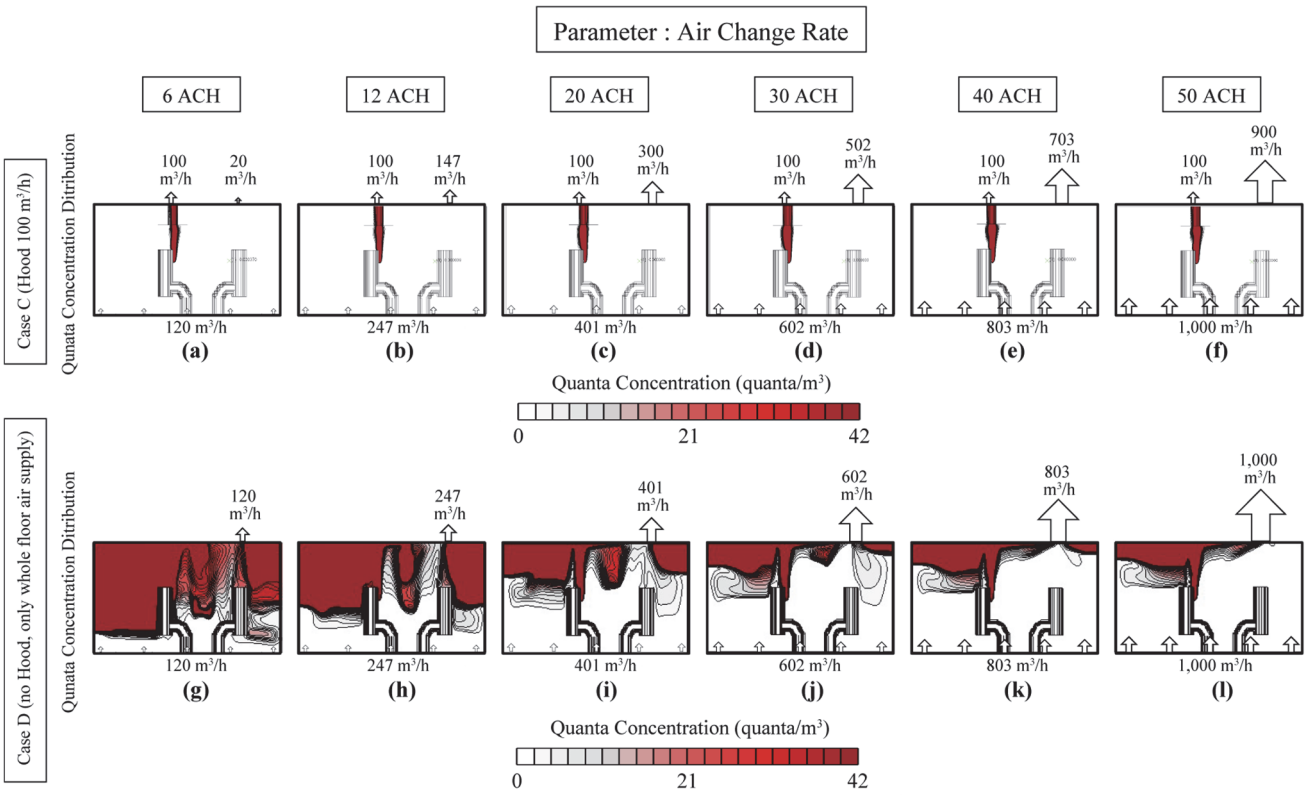


Figure 2-10. Quanta concentration distribution [quanta/m³] for different air change rates (ACH): Comparison

between Case C (a–f, hood = 100 m³/h) and Case D (g–l, no hood). The air change rates and corresponding supply air volumes are as follows: (a, g) 6 ACH (120 m³/h); (b, h) 12 ACH (240 m³/h); (c, i) 20 ACH (400 m³/h); (d, j) 30 ACH (600 m³/h); (e, k) 40 ACH (800 m³/h); (f, l) 50 ACH (1,000 m³/h).

As shown in **Figure 2-11**, increasing the hood flow rate enlarged the red (SVE5 = 1) region in both Case A and Case B, indicating a greater portion of the patient's exhaled air being directly captured. However, in **Figure 2-12**, lateral hood displacement (±200 mm) prevented full coverage of the patient's mouth area in Case A, while complete coverage was maintained in Case B. These findings confirm that hood flow rate is the dominant factor governing capture performance, but the balance of flow rates between the hood and ceiling exhaust strongly affects capture efficiency when the horizontal offset between the hood and patient's mouth increases. In **Figure 2-7d**, $C'_{g,dc}$ remained low across all ventilation rates (6–50 ACH) when the hood flow rate was fixed at 100 m³/h ($C'_{g,dc}$ = 1.07×10^{-4} in 6 ACH, $C'_{g,dc}$ = 6.05×10^{-43} in 50 ACH). Even without a hood (Case D), $C'_{g,dc}$ remained low at high air supply rates, except for the lowest condition of SA = 120 m³/h, where $C'_{g,dc}$= 4.96×10^{-2}.

Figures **2-10a–f** show tracer gas concentration distributions for Case C (hood = 100 m³/h) under varying ventilation rates, while **Figures 2-10g–l** show the corresponding distributions for Case D (no hood). Comparison between Cases C and D clearly demonstrates the hood's effectiveness, particularly at 6 ACH (120 m³/h), which corresponds to the minimum ventilation rate recommended by REHVA [69] for consultation rooms. Under these low-flow conditions, the hood reduced exposure significantly, lowering $C_{q,dc}$ from 4.96×10^{-2} quanta/ m^3 (no hood) to 1.07×10^{-4} quanta/ m^3 (with hood).

Consequently, it can be concluded that the floor-supply displacement ventilation (FSDV) system alone provides sufficient protection for the doctor when the ventilation rate exceeds 240 m³/h (12 ACH). However, under low ventilation rates (≤120 m³/h, 6 ACH), the addition of a local exhaust hood (100 m³/h) is highly effective in further reducing infection risk.

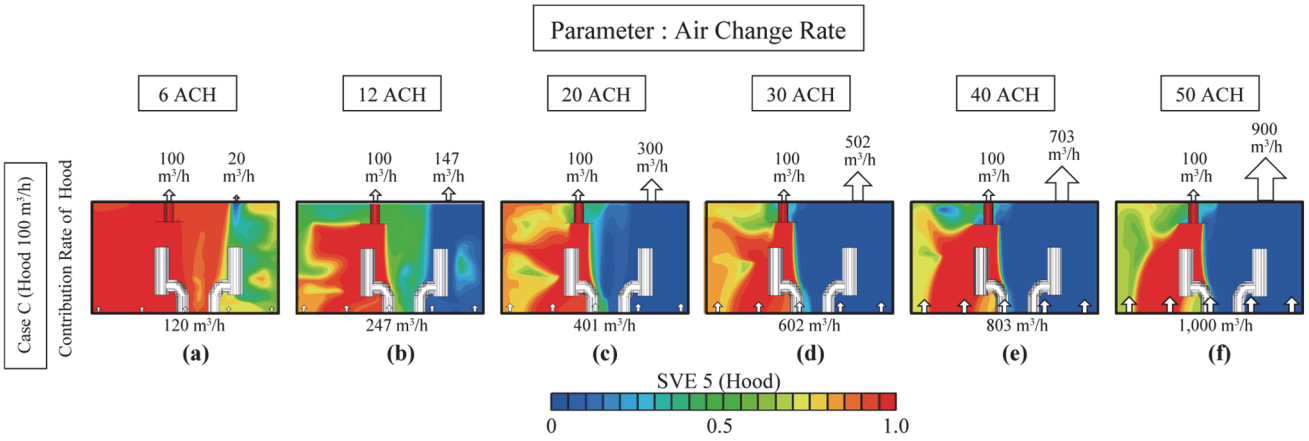


Figure 2-11. Contribution rate of the hood calculated by SVE 5 for different air change rates (Case C, parameter: air change rate/supply airflow rate). The air change rates and corresponding supply air volumes are as follows: (a) 6 ACH (120 m³/h); (b) 12 ACH (240 m³/h); (c) 20 ACH (400 m³/h); (d) 30 ACH (600 m³/h); (e) 40 ACH (800 m³/h); (f) 50 ACH (1,000 m³/h).

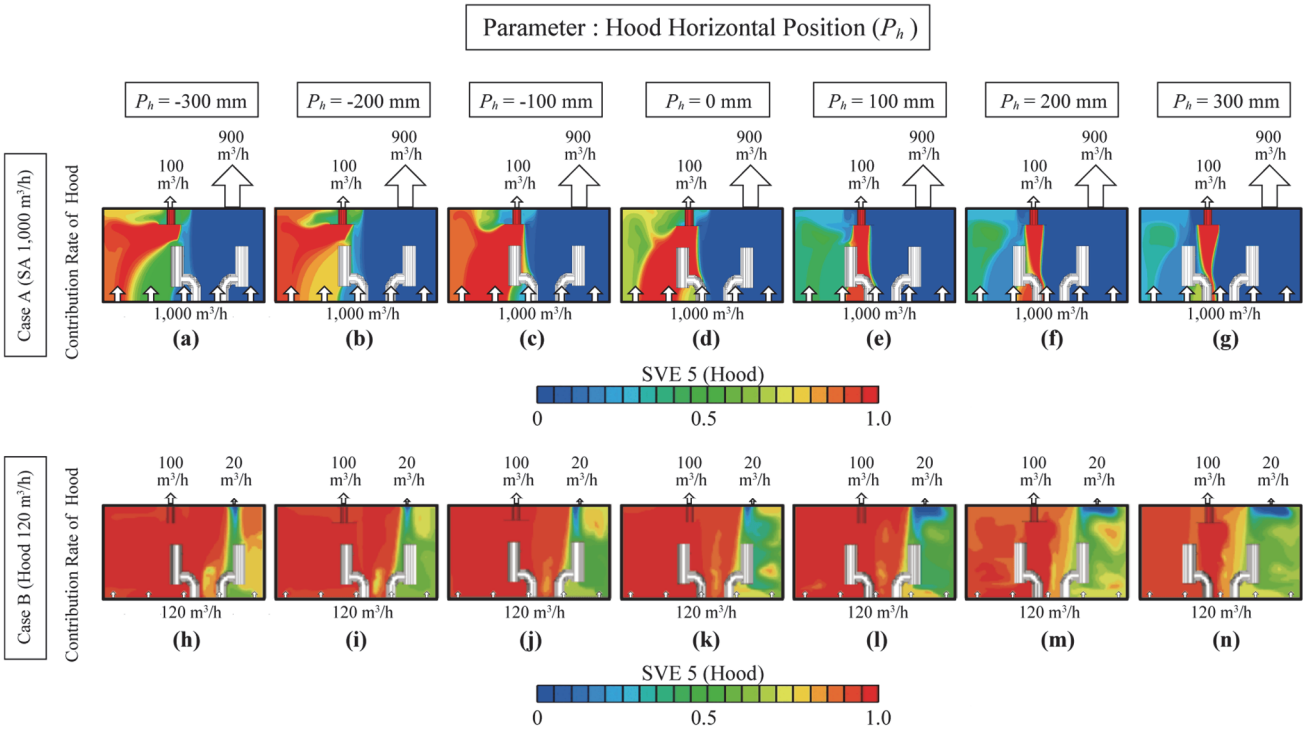


Figure 2-12. Contribution rate of the hood calculated by SVE 5 for different hood horizontal positions (comparison between Case A (a–g) and Case B (h–n)). The hood horizontal positions are as follows: (a, h) P_h = −300 mm, (b, i) P_h = −200 mm, (c, j) P_h = −100 mm, (d, k) P_h =0 mm, (e, l) P_h = +100 mm, (f, m) P_h = +200 mm, and (g, n) P_h = +300 mm.

Figure 2-13 illustrates the spatial distribution of SVE5 for different airflow rates. As the total airflow rate increased, the difference between the hood and ceiling exhaust flows became more pronounced, leading to stronger SVE5 gradients. In **Figure 2-13a** (SA = 120 m³/h), a large red area indicates that most contaminants near the patient were captured by the hood, while the blue area around the doctor shows clean airflow supplied from below. This configuration—where the red zone covers the patient's mouth and the blue zone encompasses the doctor's breathing zone—represents the optimal separation of exhaust routes for minimizing cross-contamination. Thus, the flow rate balance between the hood and other exhaust paths is a key parameter controlling the extent of the capture region and the overall reduction in infection risk.

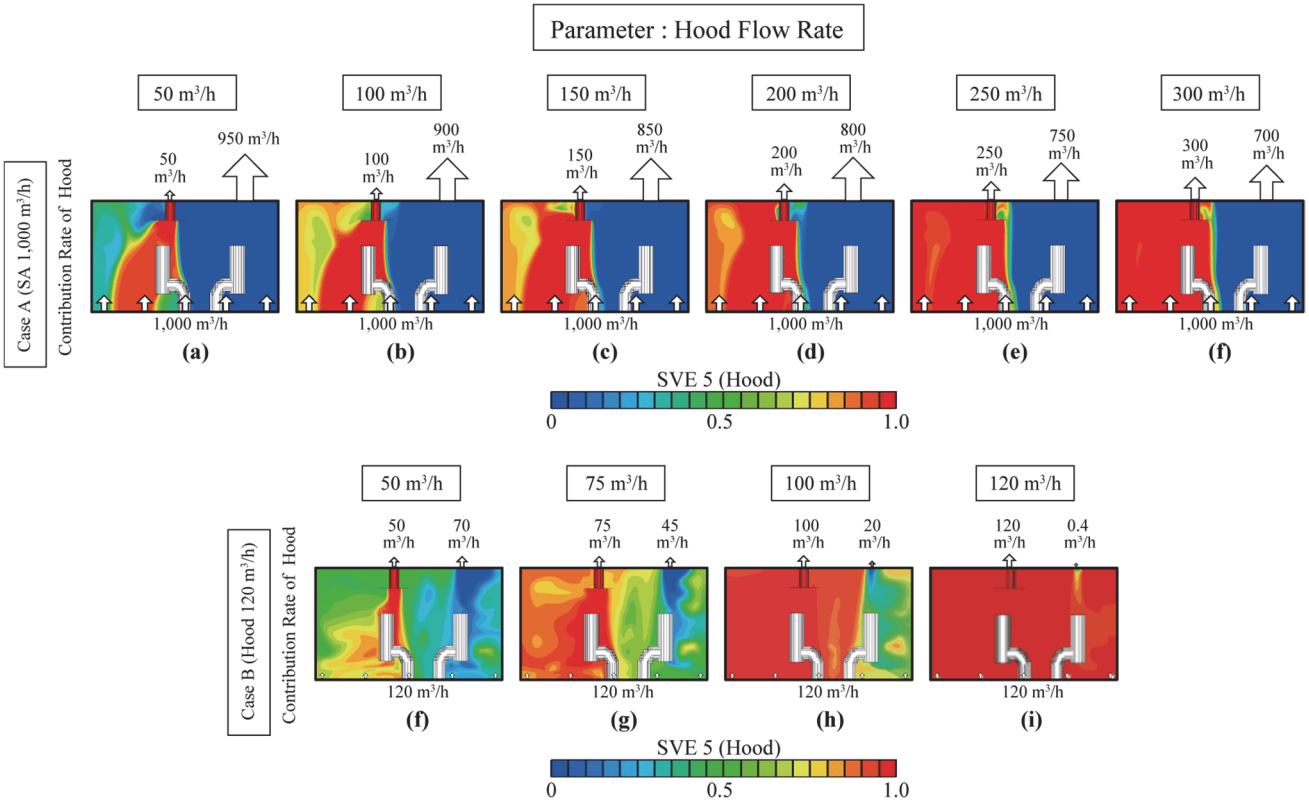


Figure 2-13. Contribution rate of the hood calculated by SVE 5 for different hood flow rates (comparison between Case A (a–f) and Case B (g–i), parameter: hood flow rate). The hood flow rates are as follows: (a, f) Q_h=50 m³/h; (g) Q_h=75 m³/h; (b, h) Q_h=100 m³/h; (i) Q_h=120 m³/h; (c) Q_h=150 m³/h; (d) Q_h=200 m³/h; (e) Q_h=250 m³/h; (f) Q_h=300 m³/h.

2.5 Discussion

2.5.1 Comparison with Previous Studies and Limitations of the Exhaled air Measurements and Steady-State CFD

In the measurement of exhaled air velocity during speech, an average value of 0.30 m/s was obtained. This result is smaller than the average initial air velocities reported in previous studies, such as 4.07 m/s for males by Kwon et al. [49] and 3.9 m/s by Chao et al. [50]. This discrepancy can be attributed to methodological differences. The previous studies mainly focused on pulse emissions—that is, instantaneous velocity peaks occurring during the pronunciation of plosive sounds—whereas the present study aimed to reproduce the average flow conditions during continuous conversation for steady-state CFD analysis. In addition, the ultrasonic anemometer (Sonic Corporation, DA-700 with TR-92T 30 mm probe) measured the mean velocity within a 30 mm sensing volume for each axis. Since this sensing diameter is larger than the typical mouth opening during speech, the actual local peak velocity could be somewhat higher than the measured value of 0.30 m/s.

For the exhaled air volume, an average value of 5.21 L/min was obtained. Although this value is smaller than that reported by Gupta et al. [75] (10.48 ± 0.76 L/min for males, body surface area 1.8 m^2), the difference likely arises from the measurement methodology. In this study, the total air volume collected in a PET bag over one minute of speech was used to compute the average exhalation rate according to Eq. (2-5). This approach did not explicitly account for the ratio of speaking to breathing time within that minute. Therefore, if the actual speaking time were considered, the estimated value would be somewhat higher than 5.21 L/min. Despite the smaller magnitude, the results are consistent in order of scale and exhibit inter-individual variability comparable to that reported in previous research. Consequently, this deviation does not significantly affect the validity of the CFD boundary conditions or the overall conclusions of the study.

The mouth size of the patient model was set to 17.04 × 17.04 mm (2.90 cm^2), determined from the measured exhalation velocity (0.30 m/s) and volume (5.21 L/min). This value is slightly smaller than the mean mouth opening area reported by Gupta et al. [75] (1.80 ± 0.03 cm^2). The averaged values from all subjects were applied as CFD boundary conditions, as summarized in **Table 2-1**.

Regarding the CFD modeling of exhalation, a steady-state simulation was adopted, neglecting the temporal variations in exhalation and inhalation that occur during actual speech. Previous CFD studies have examined exhalation [76,77], inhalation [78,79], or both [80,81]. For instance, Villafruela et al. [77] compared

three different boundary conditions—one time-dependent and two constant—in an unsteady-state simulation. They found that using a constant mean velocity tended to overestimate both the horizontal penetration distance and vertical rise of the exhaled jet compared with the time-dependent case, which better represented real speech. Accordingly, in this study, the steady-state simulation focusing solely on exhalation likely overestimates the volume of exhaled air reaching the doctor's breathing zone. While this may not perfectly represent actual respiratory behavior, it provides a conservative estimate that avoids underestimating infection risk.

Furthermore, because this study required simulating a large number of cases (43 in total) to evaluate the effects of multiple parameters, the use of steady-state conditions was a practical compromise between computational efficiency and physical realism. Nonetheless, the simplification represents one of the main limitations of this study. For more precise modeling of close-proximity conversations, incorporating time-dependent or transient CFD analysis of exhalation would be an important subject for future work.

2.5.2 Influence of Convergence and Human Thermal Plume on CFD Accuracy

To verify the convergence of the CFD simulations, analyses up to 10,000 iterations were conducted for Case A-0 and Case B-0, which represent the baseline conditions with supply airflow rates of 1,000 m³/h and 120 m³/h, respectively. Although the relative residuals of all governing equations dropped below 10^{-4} early in the computation, slight variations in tracer gas concentrations at the hood, ceiling exhaust, and in front of the doctor's mouth ($C'_{g,dc}$) continued until the end of 10,000 iterations. Similar convergence behavior was observed in all simulation cases.

To evaluate the order of variation in $C'_{g,dc}$ across iterations, the average, standard deviation (SD), and their ratio (SD/AVE) for $C'_{g,dc}$ and η were calculated for the intervals between 2,001–3,000 and 9,001–10,000 iterations, as summarized in **Table 2-8**. Case B-3 (Ph = –300 mm) was selected for detailed analysis because it showed the highest $C'_{g,dc}$ among all cases. The results in **Table 2-8** indicate that η values were consistent between 2,001–3,000 and 9,001–10,000 iterations across all three examined cases. While the SD/AVE of $C'_{g,dc}$ for 2,001–3,000 iterations ranged between 19.5% and 37.2%, this fluctuation was larger than the difference in average $C'_{g,dc}$ between 2,001–3,000 and 9,001–10,000 iterations (64.1–90.8% of the ratio). This finding suggests that the variability of $C'_{g,dc}$ within the 2,001–3,000 iteration range exceeded the mean difference caused by extending the iteration number. Therefore, a computation length of 3,000 iterations was adopted for all subsequent analyses of $C'_{g,dc}$ and η, as it provided sufficient convergence while reducing computation time and cost.

Table 2-9.
The summarization of the average, standard deviation, their rate of $C'_{g,dc}$, and η calculated from 2,001 to 3,000 cycles and from 9,001 to 10,000 cycles in standard k-ε turbulence model.

Model	Standard k-ε tublence model				Standard k-ε tublence model			
Cycles for AVE, SD, and η	**2,001~3,000 cycles**				**9,001~10,000 cycles**			
	$AVE(C'_{g,dc})$	$SD(C'_{g,dc})$	$SD/AVE(C'_{g,dc})$	η (%)	$AVE(C'_{g,dc})$	$SD(C'_{g,dc})$	$SD/AVE(C'_{g,dc})$	η (%)
Case A-0 (SA=1,000 m3/h)	1.88E-41	3.66E-42	1.95E-01	99.97	2.07E-41	4.40E-42	2.13E-01	100.00
Case B-0 (SA=120 m3/h)	1.61E-04	5.99E-05	3.72E-01	100.00	2.51E-04	3.31E-05	1.32E-01	100.00
Case B-3 (P_h=-300mm)	1.81E-01	4.18E-02	2.31E-01	94.74	2.25E-01	7.11E-02	3.16E-01	94.84

To assess the influence of the human thermal plume and mesh resolution, simulations were conducted using both the standard k–ε turbulence model and the low-Reynolds-number (LRN) model under Case B-0, where the low mean airflow velocity (0.004 m/s) enhances the effect of buoyant plumes. As summarized in **Table 2-9**, the first mesh spacing from the human body was 10 mm, yielding an average y^+ value of 7.3 for the standard k–ε model. Although this y^+ is smaller than the optimal range for the standard k–ε model ($y^+ > 30$), it results from the generally low mean velocity in the room—0.030 m/s for 1,000 m³/h and 0.004 m/s for 120 m³/h—calculated from the total flow rate divided by the floor area.

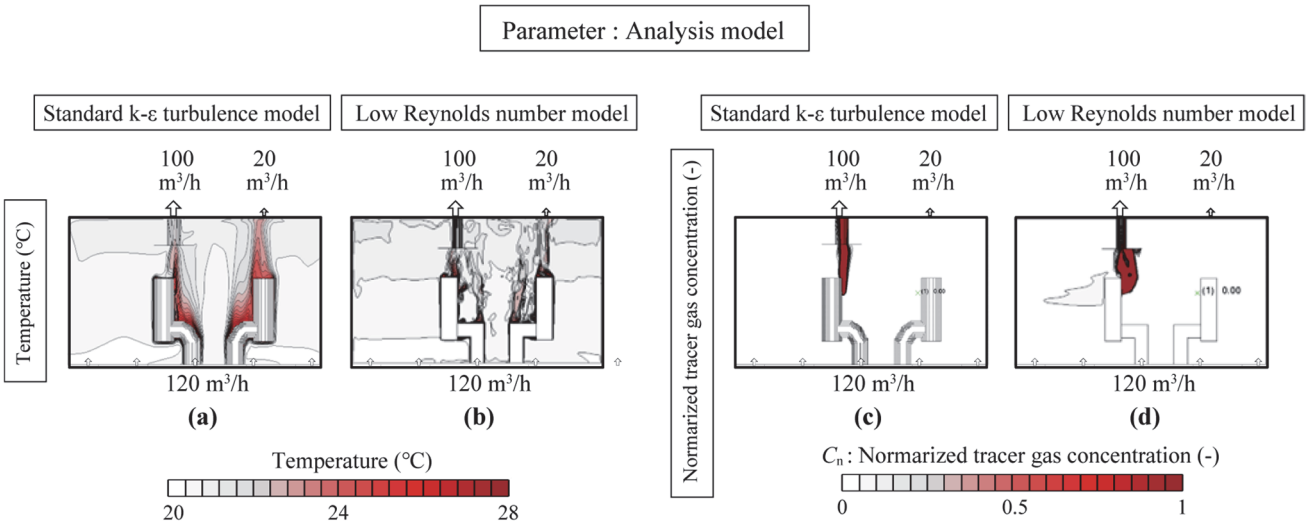


Figure 2-14. Comparison of thermal and tracer gas distributions simulated using the standard k–ε turbulence model (3,000 cycles) and the low Reynolds number model (20,000 cycles) in Case B-0: (a) Temperature distribution by the standard k–ε turbulence model; (b) Temperature distribution by the low Reynolds number

model; (c) Tracer gas concentration distribution by the standard k–ε turbulence model; (d) Tracer gas concentration distribution by the low Reynolds number model.

As shown in **Figure 2-14a** and **Figure 2-14b**, the standard k–ε model appears to slightly overestimate the intensity of the human thermal plume compared with the low-Reynolds-number model, despite the low y^+ value. Nevertheless, the calculated $C'_{g,dc}$ and η values presented in **Table 2-10** agreed closely between the two turbulence models, indicating that the plume modeling had a negligible influence on the results. While the low-Reynolds-number model is generally recognized as more accurate for predicting buoyancy-driven plumes, its significantly higher computational cost renders it impractical for multi-case parametric studies. Consequently, the standard k–ε turbulence model was deemed adequate for comparative analyses among cases, as the differences in $C'_{g,dc}$ and η between the two models remained small in Case B-0 (see **Table 2-10**).

Table 2-10.

The comparison of the average, standard deviation, their rate of $C'_{g,dc}$, and η between the standard k-ε turbulence model and the low Reynolds number mode in Case B-0.

Model	**Standard k-ε tublence model**				**Low Reynolds number model**			
Toatal Mesh	2,444,148				32,460,912			
First mesh	Wall: 100 mm Around human model: 10 mm				Wall: 0.5 mm Around human model: 0.5 mm			
Average of y+	Wall: 11.6 Around human model: 7.3				Wall: 0.18, Around human model: 0.45			
Cycles for AVE, SD, and η	2,001~3,000				15,001~20,000			
	$AVE(C'_{g,dc})$	$SD(C'_{g,dc})$	$SD/AVE(C'_{g,dc})$	η (%)	$AVE(C'_{g,dc})$	$SD(C'_{g,dc})$	$SD/AVE(C'_{g,dc})$	η (%)
Case B-0 (SA=120 m3/h)	1.61E-04	5.97E-05	3.71E-01	100	1.42E-04	1.87E-04	1.32E+00	99.72

Finally, the hood capture efficiency (η) was determined from the averaged tracer gas concentrations at the hood and ceiling exhaust between 2,001–3,000 iterations for the standard k–ε model and between 15,001–20,000 iterations for the low-Reynolds-number model.

2.5.3 Significance and Future Potential of FSDV and LEV Introduction

Regarding the estimation of infection risk, the CFD simulation results summarized in **Figure 2-7** revealed that a considerable risk of airborne transmission remained under low ventilation conditions, particularly at a supply airflow rate (SA) of 120 m³/h (6 ACH). This finding indicates that even when complying with the REHVA-recommended ventilation rate of 6–12 ACH, a susceptible person may still be exposed to infectious aerosols during close-distance conversations (1.2 m). This result is consistent with REHVA's statement that general ventilation improvements alone do not effectively mitigate transmission via close contact or short-range airborne routes [69]. Under such low-ventilation conditions (SA = 120 m³/h, 6 ACH), the installation of a local exhaust hood proves effective, provided that it is positioned at an appropriate distance from the patient's mouth—for instance, at Q_h = 100 m³/h, H_h = 500 mm, and P_h = ±100 mm—as demonstrated by the simulation results.

The CFD analysis further showed that the normalized tracer gas concentration in front of the doctor's mouth ($C'_{g,dc}$) remained relatively low across the entire range of supply airflow rates from 120 to 1,000 m³/h, regardless of the presence or absence of a hood, except under the lowest ventilation condition (SA = 120 m³/h, where $C'_{g,dc} = 4.96\times10^{-2}$). These results do not imply that the introduction of a hood is unnecessary. Rather, they highlight its broader functional and operational advantages. In a centralized air-handling unit (AHU) system, ceiling exhaust air can be safely reused as return air (RA) if the local exhaust ventilation (LEV) system effectively captures the majority of contaminated exhaled air from the source. This mechanism can substantially reduce the requirement for excessive outdoor air supply, which is typically used to dilute infectious aerosols, thereby contributing to energy efficiency and sustainable ventilation design.

In summary, combining FSDV with LEV enables both localized contaminant removal and overall energy-efficient operation. While high ventilation rates can achieve sufficient dilution, they also increase energy demand. Conversely, the strategic placement of an LEV hood above the contaminant source provides an effective means of minimizing airborne transmission risk at lower ventilation rates. Therefore, the proposed FSDV + LEV system represents a promising approach for healthcare facilities and other indoor environments requiring both infection control and energy conservation.

2.6 Conclusion

In this chapter, the performance of a combined local exhaust ventilation (LEV) and floor-supply displacement ventilation (FSDV) system was investigated through steady-state computational fluid dynamics (CFD) analysis. The study also incorporated experimental measurements of exhaled air velocity, volume, and angle during Japanese speech to establish realistic boundary conditions.

The main findings of this chapter are summarized as follows:

Exhaled Air Measurements Dualing Japanese Speech

・The measured mean exhalation velocity was 0.30 m/s, calculated using only data points with positive vertical velocity components ($v_z > 0$). To ensure sufficient momentum for accurate estimation of the exhalation angle, only data with $v_z \geq 0.5$ were used, resulting in a mean vertical angle of 11.9°. The mean exhaled air volume during speech was 5.21 L/min, which, together with the velocity data, determined a model mouth opening size of 17.0 × 17.0 mm (2.90 cm²). These parameters were applied as CFD boundary conditions.

Effect of Hood Flow Rate and Exhaust Balance

・The hood flow rate (Q_h) was identified as the most influential parameter governing the capture efficiency (η). The balance between the hood and ceiling exhaust flow rates significantly affected the capture performance, particularly when the horizontal hood position (P_h) relative to the patient's mouth was varied. Maintaining a proper balance between exhaust routes ensured stable and effective contaminant removal.

Airflow Distribution and Contaminant Capture

・For infection risk reduction, it was essential to separate the exhaust flow paths of the patient's exhaled air and the doctor's breathing zone. As demonstrated in **Figure 2-13a**, this was achieved when the hood's capture region (red area, SVE 5 = 1) covered the patient's mouth, and the ceiling exhaust region (blue area, SVE 5 = 0) corresponded to the doctor's breathing zone. Proper airflow management via hood and exhaust balancing was therefore crucial to preventing cross-contamination.

Infection Risk Reduction by Hood Installation

・The CFD analysis showed that the FSDV alone could maintain a sufficiently low infection risk for supply

airflow rates above 240 m³/h (12 ACH). However, at lower ventilation rates (120 m³/h, 6 ACH), the FSDV alone was insufficient. In such conditions, introducing an LEV hood directly above the patient's head effectively reduced the quanta concentration in front of the doctor's mouth ($C_{q,dc}$) from 4.96×10^{-2} quanta/ m^3 (no hood) to 1.07×10^{-4} quanta/ m^3 (with hood, Q_h = 100 m³/h), substantially lowering the doctor's infection risk during close-distance conversation.

Energy Efficiency and System Integration

・By introducing 100 m³/h of exhaust airflow through a hood (LEV) positioned above the patient's head, the quanta concentration in front of the doctor's mouth ($C_{q,dc}$) is maintained at 1.07×10^{-4} quanta/m³ even at a ventilation rate of 6 ACH. Although this value is slightly higher than that observed at 50 ACH ($C_{q,dc} = 6.05 \times 10^{-43}$ quanta/m³), it still represents a comparably low infection risk. These findings indicate that implementing the hood could contribute to energy conservation by allowing a reduction in the overall ventilation rate.

・In centralized air-handling systems (AHUs), air from the ceiling exhaust can be safely reused as return air (RA) if the LEV captures a large portion of the patient's exhaled contaminants. This reduces the need for high outdoor air ventilation rates typically required for infection control and can therefore contribute to energy conservation and sustainable HVAC design.

Limitations and Future Work

Despite the promising results, several limitations of this study must be acknowledged:

・CFD Validation: The current findings are based solely on CFD simulations. Future experimental validation under controlled full-scale conditions is necessary to confirm the numerical results.

・Parameters (Variables): In this study, the exhaust flow rate of the hood (LEV), the hood height, and the horizontal position of the hood were selected as parameters to examine its detailed performance. However, factors such as the distance between the doctor and the patient and the exhalation velocity are also expected to significantly influence infection-risk assessment, particularly when reproducing close-range conversations in a consultation room.

・Droplet Modeling: The study modeled droplet nuclei as passive scalar tracers. The influence of large droplets, which may pose a higher infection risk for COVID-19, was not explicitly considered.

・Steady-State Simplification: The CFD simulations modeled only exhalation under steady-state conditions, neglecting the time-dependent alternation of inhalation and exhalation during speech. Although this assump-

tion may overestimate infection risk, future studies should employ transient or time-dependent CFD analyses for higher accuracy.

・Turbulence Modeling: While the low-Reynolds-number (LRN) model provides higher accuracy for buoyant plume simulation, the standard k–ε model was adopted to balance computational cost. The comparison in Case B-0 (**Table 2-9**) indicated minimal differences in $C'_{g,dc}$ and η between the two models, supporting the adequacy of the chosen approach for comparative studies.

The results confirm that combining LEV with FSDV significantly enhances both contaminant removal efficiency and infection control performance, particularly in low-ventilation environments such as consulting rooms. Beyond infection control, this hybrid system offers energy-saving potential through reduced dependence on outdoor air ventilation. Consequently, the FSDV + LEV configuration represents a practical and efficient ventilation design strategy for hospitals, cleanrooms, and other high-performance indoor environments.

3 Experimental Evaluation of Different Underfloor Air-Distribution Systems without LEV

3.1 Purpose of the Chapter

This chapter aims to evaluate and compare the performance of three floor-supply air distribution systems—floor-supply displacement ventilation (FSDV), horizontal flow-type diffuser (HFD), and swirling flow-type diffuser (SFD)—in terms of indoor contaminant concentration and thermal comfort. The local exhaust ventilation (LEV) system was not applied in this study; thus, the primary objective was to clarify the intrinsic ventilation performance of each air distribution system.

To simulate exhaled human breath, a tracer gas was generated from the mouths of two simplified thermal manikins through a sponge material, enabling a passive diffusion-based emission. The experimental concept and parameters are illustrated in **Figure 3-1**. For comparison, a conventional ceiling diffuser (CD) with a cooling-cone setting (anemostat type) was included, resulting in a total of four air distribution systems tested. The airflow rate was varied in four stages (120–480 m^3/h) for each system, and the steady-state tracer gas concentration and temperature distributions were measured. The ventilation performance was then assessed based on the contaminant removal efficiency in the breathing zone and the vertical temperature difference.

Previous studies have investigated individual floor-supply systems, yet experimental comparisons among multiple floor-supply types under identical conditions remain limited. Therefore, the data obtained in this study provide valuable and fundamental information for selecting and designing floor-supply air distribution systems in practical applications.

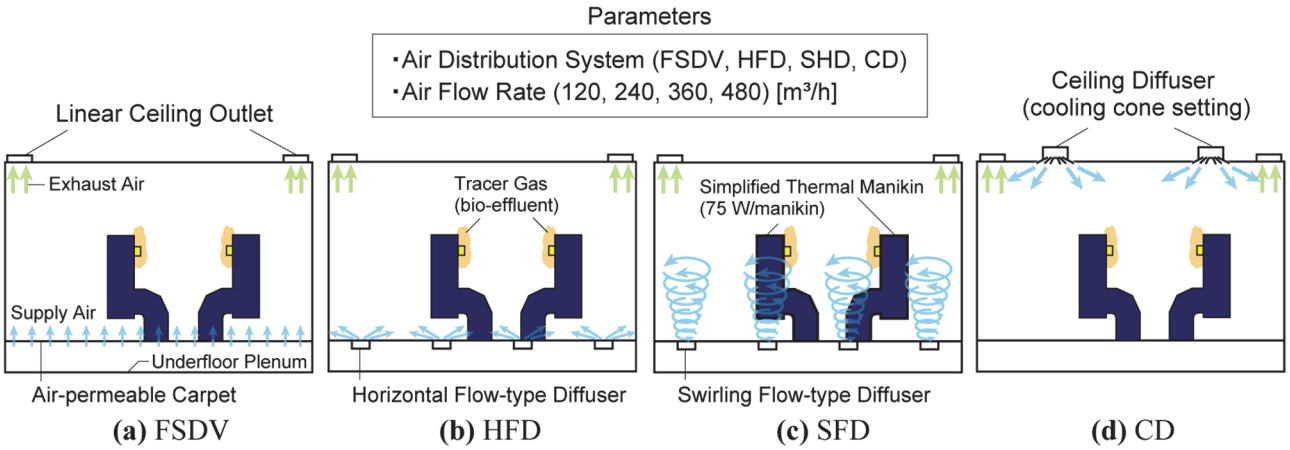


Figure 3-1. Conceptual diagram of the experimental setup and air distribution systems: (a) floor-supply displacement ventilation (FSDV), (b) horizontal flow-type diffuser (HFD), (c) swirling flow-type diffuser (SFD), and (d) ceiling diffuser (CD) (anemostat type with a cooling-cone setting).

3.2 Methodology

3.2.1 Experimental Facilities

The experiments were conducted at the University of Osaka between December 2023 and January 2024. The plan, sectional, and isometric views of the experimental facility are shown in **Figure 3-2**. The facility consists of two zones: the test chamber, which serves as the main experimental space, and its surrounding auxiliary space. The test chamber has internal dimensions of 3,800 mm × 2,400 mm × 2,200 mm and includes a 300 mm-high underfloor plenum. Air is supplied either through the underfloor plenum or via ceiling anemostat diffusers (KUKEN Kogyo, C2 type, 200 mm φ). Exhaust air is removed through two linear exhaust outlets (KUKEN Kogyo, VLT-3 type, 1,000 mm wide) installed on the ceiling.

A constant air volume (CAV) unit (Kyoritsu Air Tec Inc, CAV-FW type, 250 mm φ, equipped with a windmill-type velocity sensor) was used to control the airflow rate at 1,000 m³/h for supply and 990 m³/h for exhaust, maintaining the chamber at a slightly positive pressure. The cleanroom-type ventilation system was designed to achieve a cleanliness level of approximately Class 10,000. Outside air introduced from the outdoor air-handling unit (OHU) passes through a HEPA filter, and a portion of the supply air is bypassed to the exhaust duct to fine-tune the actual flow rate supplied to the chamber (see **Figure 3-2b**).

The supply-air temperature was controlled using an OHU and a reheating coil. The air temperature downstream of the reheating coil was monitored and adjusted to the target value with an accuracy of 0.1 °C.

This system controls only the supply-air temperature and does not compensate based on the indoor air temperature. Since the surrounding space was not equipped with a dedicated temperature control system, four portable electric heaters and small fans were used to maintain a uniform thermal environment.

An isometric view of the test chamber is shown in **Figure 3-2c**. The chamber represents a small room occupied by two persons, containing two simplified thermal manikins, two chairs, and a gas heater used to warm the tracer gas. Because the experiments were conducted during the same period as those described in Chapter 4, a local exhaust hood was present near the ceiling, but was not operated in this experiment. The simplified manikins were designed with reference to Magnus et al. [82], with partial modifications. Each manikin consisted of a steel cylindrical trunk connected to elbow-shaped legs made of the same material. Heating cables were wound around the surface and covered with 100 % cotton fabric. The heat generation rate was set to 75 W per manikin, and the distance between the front surfaces of the two trunks was 1,200 mm, representing a typical face-to-face configuration.

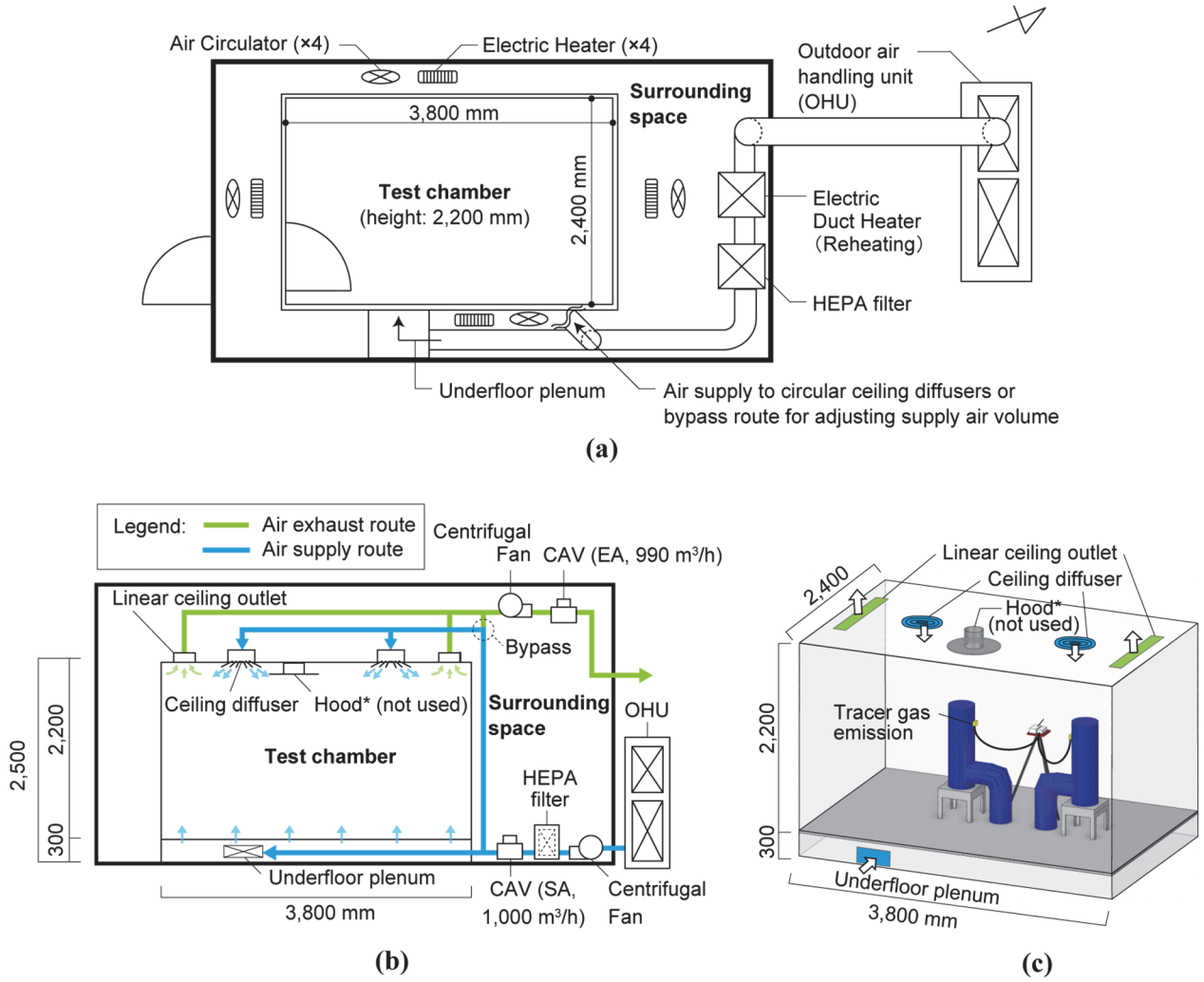


Figure 3-2. Configuration of the test chamber and air distribution system used for the exhaled human breath simulation experiment: (a) Overview of the air circulation system, (b) airflow supply and exhaust routes, and (c) three-dimensional schematic of the test chamber.

Note: The ceiling hood was installed for the experiments described in Chapter 4, but was not used in this experiment.*

Figure 3-3 shows the arrangement of the air diffusers and the measurement points in the test chamber. The measurements were conducted for contaminant (CO_2) concentration and air temperature.

In the case of FSDV, the entire floor was not used as a supply surface; some areas were covered with non-perforated panels (light gray areas in **Figure 3-3a**). The positions of the perforated panels used for air supply are indicated by the dark gray areas in the figure. A total of 40 air-permeable carpet tiles (each 500 × 500 mm) were installed.

In the HFD, six diffusers were evenly distributed; in the SFD, four diffusers; and in the CD, two diffusers were installed. The number of diffusers was selected so that, under the maximum ventilation rate of 480 m³/h,

the airflow rate per diffuser did not exceed the rated value specified by the manufacturer (KUKEN Kogyo). Consequently, under lower ventilation rates, the airflow rate per diffuser was below the rated capacity in some cases (**Table 3-1**). For the HFD and SFD conditions, the air-permeable carpet was removed, and the perforated floor panels were sealed with vinyl sheets and tape to prevent unintended air leakage from areas other than the diffusers (light gray areas in **Figures 3-2b** and **c**).

The CO_2 concentration and air temperature in the room were measured using five vertical poles (Pa–Pe). To minimize the direct influence of supply airflow and to evaluate the overall characteristics of the indoor environment, the pole positions were adjusted depending on the air distribution system. The measurement heights on the vertical poles are shown in **Figures 3-3e** and **f**. CO_2 concentration was measured using a CO_2 recorder (RTR-576, T&D Corporation), and air temperature was measured using T-type thermocouples. A total of six measurement points in the vertical direction for CO_2 and seventeen for temperature were established.

The measurement points for wall surface temperature are shown in **Figures 3-3g** and **h**. Measurements were conducted at corresponding positions on both the inner and outer wall surfaces, and additional points were installed at the center of the short-side exterior wall. On the inner wall surfaces, 30 points in total were measured: 18 on the long walls and 12 on the short walls. On the outer wall surfaces, 12 points for wall temperature and 4 points for air temperature (one at the center of each wall) were measured.

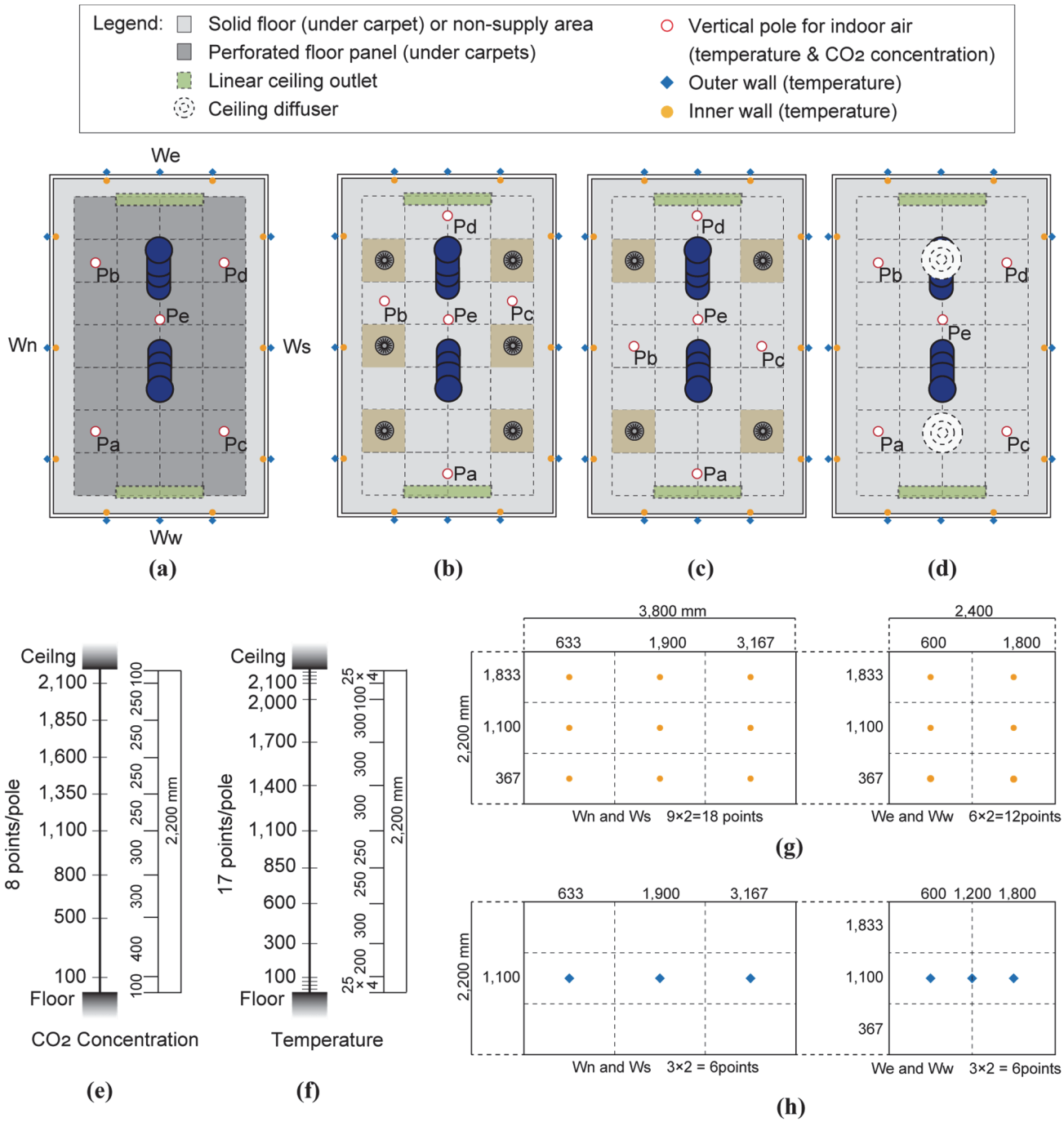


Figure 3-3. Layout of air diffusers and measurement points for each air distribution system: (a) floor-supply displacement ventilation (FSDV), (b) horizontal flow-type diffuser (HFD), (c) swirling flow-type diffuser (SFD), and (d) ceiling diffuser (CD). (d) vertical poles for measuring CO_2 concentration. (e) vertical poles for measuring indoor air temperature. (f) measurement points for the temperature of the inner walls (We and Ww, Wn, and Ws). (g) measurement points for the temperature of the outer walls (We and Ww, Wn, and Ws).

Figure 3-4 illustrates the detailed configurations of each underfloor air distribution (UFAD) system. As shown in **Figure 3-2**, air supplied to the 300 mm-high underfloor plenum is delivered into the room through

panels and either carpets or diffusers, depending on the ventilation system.

In the FSDV (floor-supply displacement ventilation) system, the supply air passes through a perforated metal panel and then through an air-permeable carpet before entering the occupied zone. The details of the air-permeable carpet and the perforated panel are shown in **Figure 3-5**. The carpet has a high- and low-loop pile structure, consisting of a nylon 6 surface and a glass fiber and polyester nonwoven backing. According to measurements conducted by the author, the open-area ratio of the perforated panel is approximately 4.5%.

In the HFD (horizontal flow-type diffuser) system, the supply air is discharged nearly horizontally through slits. A wooden panel with the same dimensions as the perforated panel was fabricated, and the diffusers were embedded into it. To prevent undesirable air leakage, all other openings were sealed with a vinyl sheet and tape, as shown in the light gray areas of **Figures 3-2b** and **3-2c**. The system was designed so that the horizontal jet spreads across the floor and subsequently forms a displacement flow pattern through the balance with the thermal plume generated by the manikins.

In the SFD (swirling flow-type diffuser) system, the supply air is introduced into the underfloor plenum and then discharged into the room through four swirling diffusers. Each diffuser was mounted on a wooden panel similar to that used for the HFD setup. Because the swirling diffusers generate strong momentum and highly turbulent airflow, they are expected to enhance air mixing in the room, similar to the airflow pattern of the ceiling diffuser (CD).

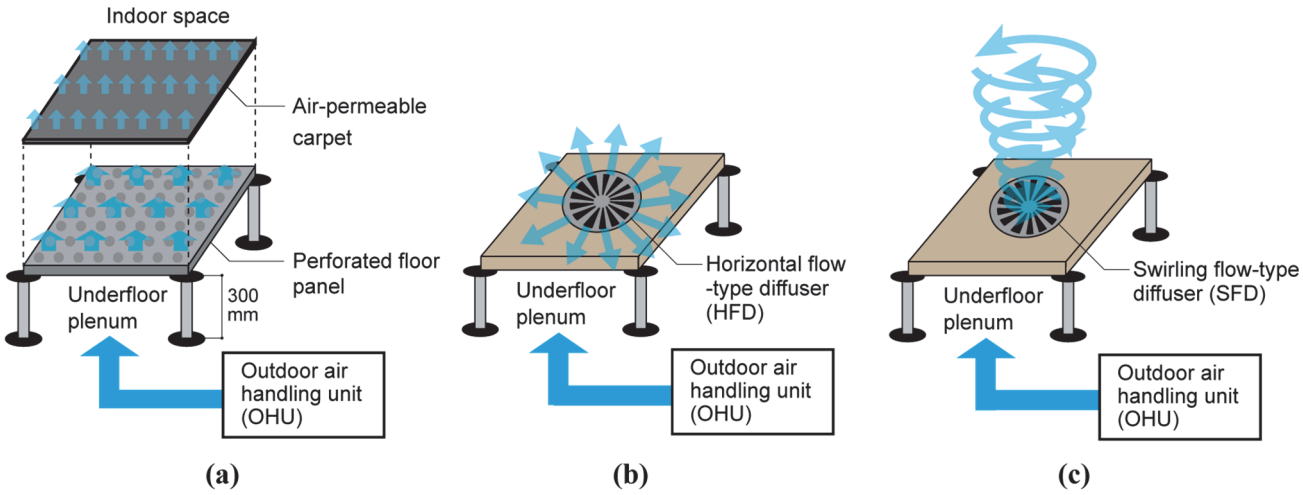


Figure 3-4. Detailed configurations of floor-supply air diffusers in each underfloor air distribution (UFAD) system: (a) air-permeable carpet type for floor-supply displacement ventilation (FSDV), (b) horizontal flow-type diffuser (HFD) and (c) swirling flow-type diffuser (SFD).

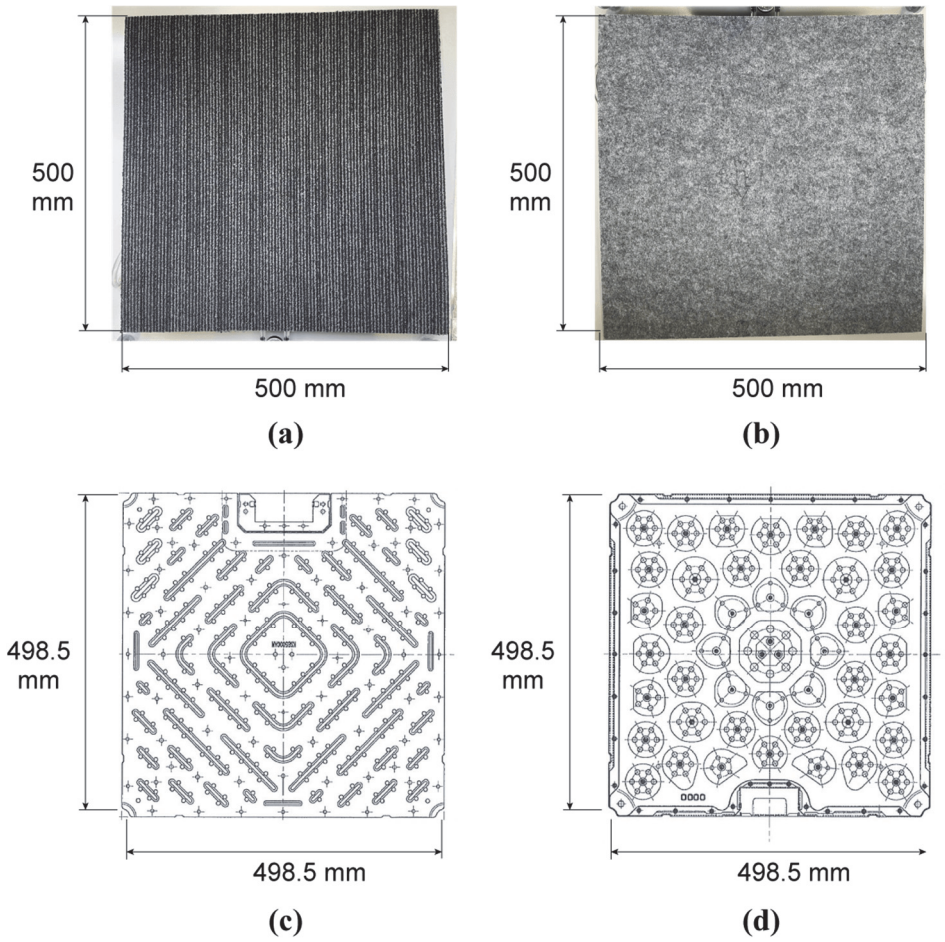


Figure 3-5. Details of the air-permeable carpet and perforated floor panel used for the floor-supply displacement ventilation (FSDV) system: (a) front side of the air-permeable carpet (material: Nylon 6), (b) back side of the air-permeable carpet (material: glass fiber and polyester nonwoven), (c) front side of the perforated floor panel, and (d) back side of the perforated floor panel.
Note: (c) and (d) are excerpts from the completion drawing of the perforated steel floor panel (Model: KSB500CAN) provided by Daidan Corporation (2022).

3.2.2 Tracer Gas Generation Method for Exhaled Human Breath Simulation

Tracer gas simulating exhaled human breath was released from two thermal manikins. Although the tracer was emitted from the mouth, its behavior under seated conditions is considered largely comparable to that of general bio-effluent released from the human body. An overview of the generation system is shown in **Figure 3-6**. To achieve a density close to that of air, carbon dioxide (CO_2) and helium (He) were mixed at a volumetric ratio of 5:3, yielding a total flow rate of 7 L/min (CO_2 : He = 4.38 : 2.62 L/min). The flow rate was precisely controlled using a mass flow controller (Fujikin, FCS-T1000L series). The mixed gas was heated by a gas

heater and passed through a thermally insulated vinyl tube before being exhaled through a sponge located at the mouth position of each manikin (1,100 mm above the floor). The gas heater consisted of a stainless-steel tube incorporating a heating element and thermocouple, with PID control implemented through a dedicated temperature controller. During the experiment, the heater was thermally insulated to maintain the gas outlet temperature at approximately 30–35 °C (measured with T-type thermocouples), with the heater temperature set to 80 °C.

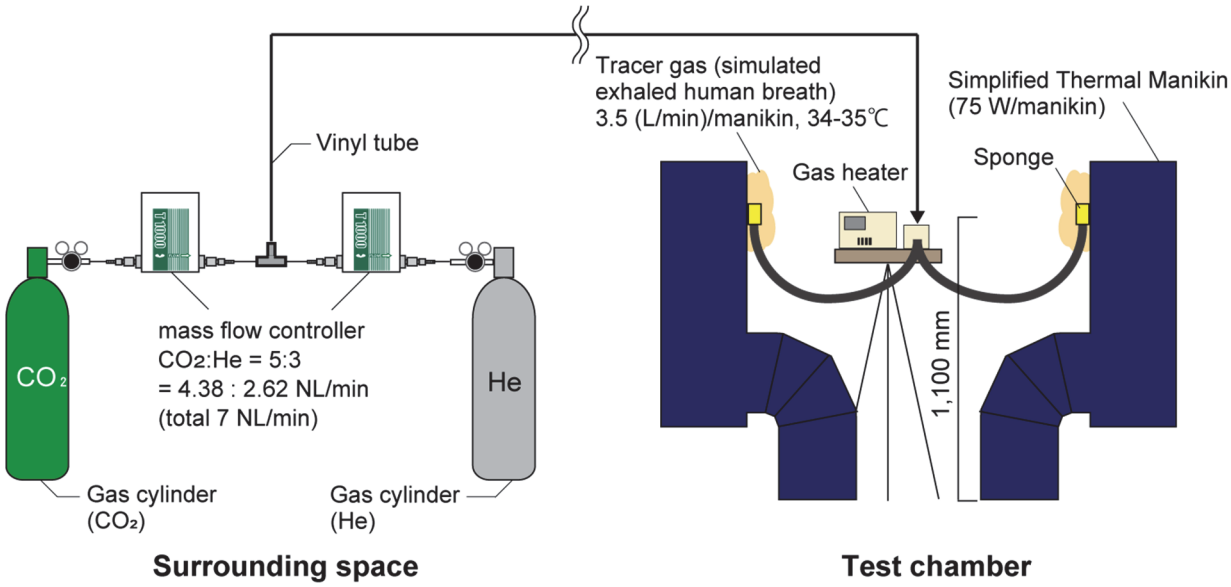


Figure 3-6. Experimental setup for tracer gas generation used in the exhaled human breath simulation.

3.2.3 Experimental Cases and Procedures

The experimental conditions are summarized in **Table 3-1**. A total of 16 cases were tested, combining four air distribution systems (FSDV, HFD, SFD, and CD) with four airflow rates of 120, 240, 360, and 480 m³/h. The airflow rates were selected based on the recommended air change rates for consultation rooms (6–12 h^{-1}) specified by REHVA [69], and extended beyond this range to evaluate the fundamental performance characteristics of each system. Although the conditions with 18 and 24 h^{-1} exceed typical values for general occupied spaces, such ventilation rates are within the range commonly applied to industrial or cleanroom environments when including recirculated air.

The number of diffusers was determined such that the standard flow rate range per diffuser by the manufacturer (Kyoritsu Air Tec Inc.) would not be exceeded under the maximum flow rate of 480 m³/h. The same

number of diffusers was used across all conditions, and only the total airflow rate was varied. As a result, the cases marked with an asterisk (*) in **Table 3-1** indicate conditions where the airflow per diffuser was below the standard rated flow described in the manufacturer's catalog.

As shown in **Figure 3-2**, the chamber was designed to maintain a slightly positive pressure, with the supply and exhaust airflow rates controlled at 1,000 and 990 m³/h, respectively, using CAV units. To verify experimental accuracy, the leakage airflow was measured for each air distribution system and flow rate, and the results are summarized in **Appendix 3-A**. As a result, in this study, the ventilation rate was adjusted based on the measured exhaust airflow rate, which was determined by releasing tracer gas directly below the exhaust outlet. Accordingly, throughout Chapters 3, 4, and 6, the term "ventilation rate" refers to this exhaust-based ventilation rate used as the reference value for all analyses.

Table 3-1.
Experimental conditions for each air distribution system.

Air distribution system	Air flow rate [m³/h] (Air change rate [h^{-1}])	Flow rate per diffuser [m³/h]	Standard flow rate range per diffuser [m³/h]
Floor-supply displacement ventilation (FSDV)	120(6), 240(12), 360(18), 480(24)	-	-
Horizontal flow-type diffuser (HFD)×6	120(6), 240(12), 360(18), 480(24)	20*, 40* ,60, 80	45-90
Swirling flow-type diffuser (SFD)×4	120(6), 240(12), 360(18), 480(24)	30*, 60*, 90, 120	90-150
Ceiling diffuser (CD)×2	120(6), 240(12), 360(18), 480(24)	60*, 120*, 180, 240	135-480

∗ : Below standard flow rate range per diffuser [m^3/h].

Table 3-2 summarizes the supply and exhaust air temperatures for each ventilation condition. During the experiments, an ideal adiabatic condition was assumed, with the supply air temperature fixed at 20 °C and no heat transmission through the chamber walls. Because of heat generation from the manikins and the gas heaters, the room was treated as a cooling load condition. As shown in Figure 3-2a, the temperature of the surrounding space was adjusted using four portable electric heaters and four small circulation fans.
The theoretical temperature difference between the exhaust and supply air under each ventilation rate was calculated using Eq. (3-1):

$$T_{EA} - T_{SA} = \frac{W_i}{C_p \cdot \rho_a \cdot Q} \qquad (3-1)$$

where T_{EA} is the exhaust air temperature [°C], T_{SA} is the supply air temperature [°C], W_i is the internal heat generation [W] (= 180), C_p is the specific heat capacity of air [J/kg·K] (= 1006), ρ_a is the air density [kg/m³] (= 1.2), and Q is the total ventilation rate [m³/s].

The total internal heat generation W_i was defined as 180 W, consisting of 150 W from the two manikins and 30 W from the gas heater and other measuring instruments, as determined by a wattmeter. The theoretical exhaust air temperatures calculated from Eq. (3-1), along with the measured values, are presented in **Table 3-2**. During the experiments, these theoretical exhaust air temperatures were used as target reference values, and the temperature of the surrounding space was fine-tuned by adjusting the electric heaters.

Table 3-2.
Experimental conditions of tracer gas generation and temperature difference between supply and exhaust air for each air flow rate.

Air flow rate [m³/h]	$t_{gas,tot}$ [min]	$t_{gas,wait}$ [min]	T_{SA} [°C]	T_{EA} [°C]	T_{EA}-T_{SA} [°C]
120	50	35	20	24.47	4.47
240	35	20	20	22.24	2.24
360	30	15	20	21.49	1.49
480	30	15	20	21.12	1.12

$t_{gas,tot}$: total tracer gas generation time (CO_2 + He) for each ventilation rate
$t_{gas,wait}$: waiting time required for the tracer gas concentration to stabilize

The experimental schedule is shown in **Figure 3-7**. First, the temperature of the surrounding space was adjusted using portable electric heaters, and the system was allowed to reach a steady thermal state. After the temperature stabilized, a tracer gas mixture (CO_2 + He) was released for a fixed duration, and measurements continued until the indoor concentration reached a steady state. The waiting time required for the tracer gas concentration to stabilize is defined as $t_{gas,wait}$, which varied depending on the ventilation rate. These waiting times for each ventilation condition are summarized in **Table 3-2**. The steady-state CO_2 concentration and air temperature used in the analyses presented in Section 3.3 were obtained by averaging the data during the final 15 minutes and 20 minutes, respectively, after steady conditions were achieved.

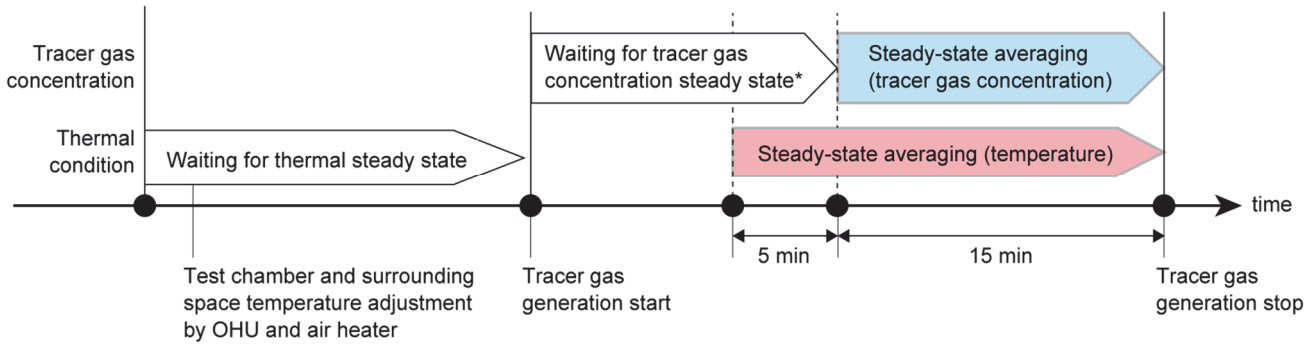


Figure 3-7. Experimental procedure and timing chart for the tracer gas measurement.
Note: The duration of waiting for the tracer gas concentration steady state ($t_{gas,wait}$) depends on the air flow rate, as shown in Table 3-2.

3.2.4 Normalization of Tracer Gas Concentration and Temperature

The contaminant concentration was evaluated using the normalized CO_2 concentration rise (C'_{CO_2}), defined by Eq. (3-2), which expresses the relative increase in CO_2 concentration based on the exhaust concentration as a reference.

$$C'_{CO_2} = \frac{C_{CO_2,p} - C_{CO_2,SA}}{C_{CO_2,EA} - C_{CO_2,SA}} \quad (3-2)$$

where $C_{CO_2,p}$ is the measured CO_2 concentration at a point p, $C_{CO_2,SA}$ is the CO_2 concentration in the supply air, and $C_{CO_2,EA}$ is the CO_2 concentration in the exhaust air. All values represent the time-averaged concentrations under steady-state conditions.

The air temperature was evaluated using the temperature rise (ΔT), which represents the difference between the local temperature and the supply air temperature, as given by Eq. (3-3).

$$\Delta T = T_p - T_{SA} \quad (3-3)$$

where T_p is the measured temperature at a point p, and T_{SA} is the temperature of the supply air.

3.2.5 Contaminant Removal Efficiency in the Breathing Zone

To evaluate air quality within the occupied zone, the average normalized concentration and the contaminant removal efficiency in the occupied zone ($\varepsilon_{\mathrm{OZ}}$) were calculated [83,84]. The contaminant removal efficiency represents the ratio between the tracer gas concentration rise in the exhaust air and the average concentration rise within the occupied zone, as expressed in Eq. (3-4). A higher value of $\varepsilon_{\mathrm{OZ}}$ indicates more effective removal of contaminants from the occupied zone without unnecessary dispersion. Under perfectly mixed conditions, the room-averaged concentration equals the exhaust concentration, resulting in $\varepsilon_{\mathrm{OZ}}$ = 1. Therefore, values greater than 1 indicate better contaminant removal performance than that of a perfectly mixed condition. It should be noted that the term "efficiency" in this context refers to the effectiveness of contaminant removal without dispersion into the occupied zone, rather than the speed or rate of removal.

$$\varepsilon_{\mathrm{OZ}} = \frac{C_{CO_2,EA} - C_{CO_2,SA}}{\langle C_{CO_2,OZ} \rangle - C_{CO_2,SA}} \qquad (3-4)$$

where $\varepsilon_{\mathrm{OZ}}$ is the contaminant removal efficiency averaged in the occupied zone [-], $C_{CO_2,EA}$ is the CO_2 concentration in the exhaust air, $C_{CO_2,SA}$ is the CO_2 concentration in the supply air, and $\langle C_{CO_2,OZ} \rangle$ is the average CO_2 concentration in the occupied zone. The occupied zone was defined as the region below 1,800 mm from the floor, and the average CO_2 concentration $\langle C_{CO_2,OZ} \rangle$ was calculated using measurements at heights of 100, 500, 800, 1,100, 1,350, and 1,600 mm.

3.3 Results and discussions

3.3.1 Vertical Distribution of Tracer Gas Concentration

Figure 3-8 presents the vertical distributions of the room-averaged tracer gas concentration for each air distribution system and air change rate. The normalized concentration was calculated using Eq. (3-2). Since only small variations were observed among the pole positions, the results were averaged over four poles (Pa–Pd), excluding Pe located between the manikins, to represent the overall room condition.

First, the results for each air distribution system are discussed based on **Figures 3-8a–d**.
For the reference system, the ceiling diffuser (CD), the normalized concentration remained close to 1.0 under all conditions, indicating a well-mixed airflow. Even when the diffuser flow rate was below its rated capacity

(120–240 m^3/h), the airflow pattern was nearly that of complete mixing. At higher flow rates (360–480 m^3/h), the normalized concentration slightly exceeded 1.0, which may be attributed to underestimation of the exhaust concentration due to air leakage.

In the floor-supply displacement ventilation (FSDV) system, a distinct concentration boundary layer was consistently formed above 1,500 mm, indicating effective displacement ventilation. Among the four systems tested, FSDV achieved the lowest overall concentration, suggesting the most efficient removal of contaminants without spreading them throughout the room.

The horizontal flow-type diffuser (HFD) also exhibited displacement ventilation characteristics with a clear boundary layer; however, as the airflow rate increased, the normalized concentration within the occupied zone tended to rise. This behavior is likely due to the relatively small chamber size and the high air change rates (18–24 h^{-1}), where the short diffuser spacing (approximately 1,000 mm) caused adjacent air jets to interact and generate stronger turbulence.

The swirling flow-type diffuser (SFD) showed typical mixed-ventilation characteristics at rated flow conditions (360–480 m^3/h). At the lower flow rate of 120 m^3/h, below the rated capacity, the turbulence intensity decreased, and the airflow pattern approached that of displacement ventilation.

Next, **Figures 3-8e–h** compare the air distribution systems at each airflow rate. As the ventilation rate increased, the characteristic differences among the systems became more evident. At the lowest airflow rate (120 m^3/h, corresponding to approximately six air changes per hour), all three floor-supply systems exhibited similar displacement ventilation performance. Overall, the trend in average concentration was FSDV < HFD < SFD < CD.

Both FSDV and HFD generated displacement-type flow fields, but FSDV achieved this with the lowest supply velocity. As a result, for the same ventilation rate, FSDV provided a calmer airflow environment and minimized the diffusion of contaminants originating from occupants. This advantage became increasingly pronounced as the airflow rate increased.

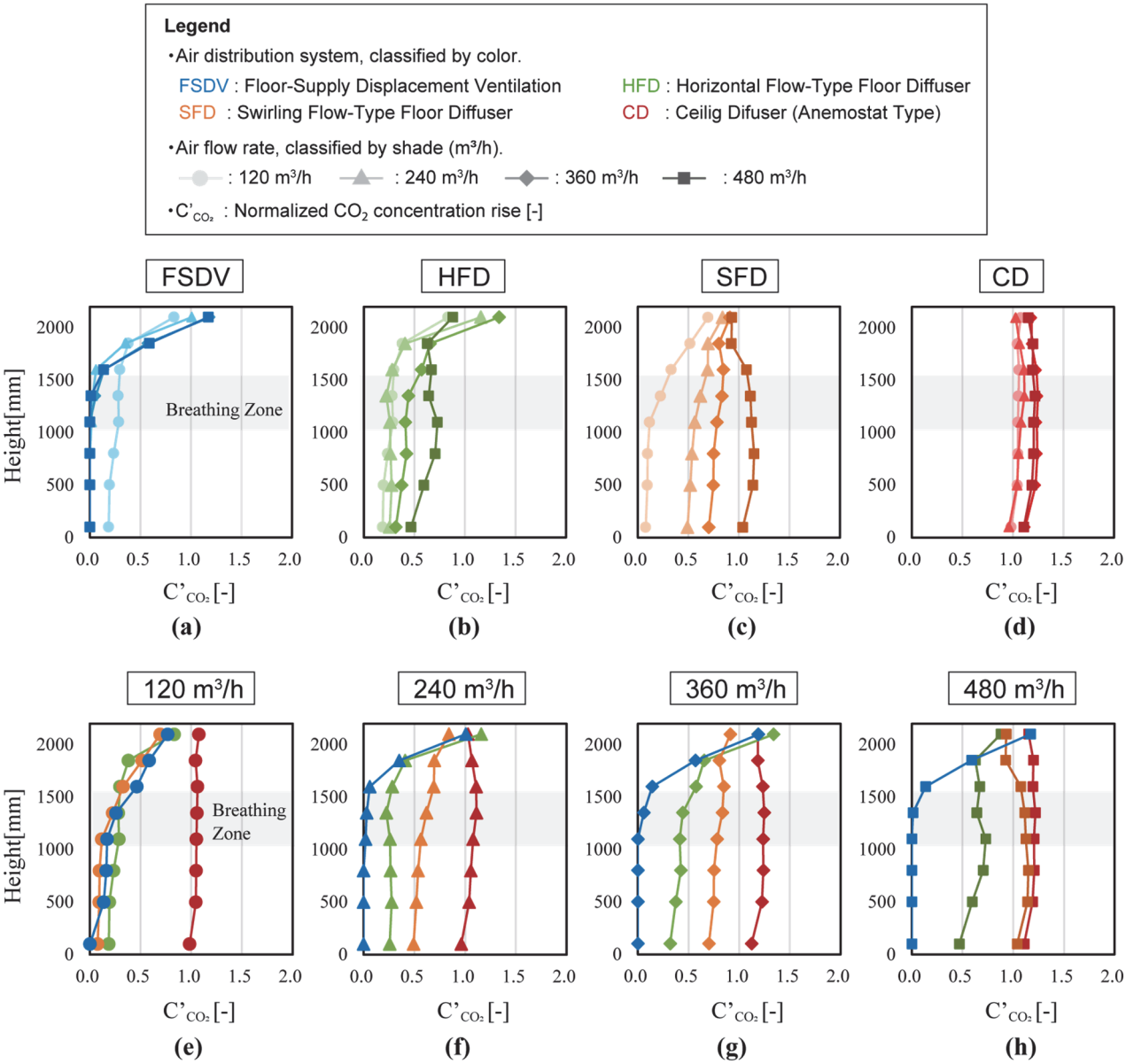


Figure 3-8. Vertical profiles of normalized CO_2 concentration rise (C'_{CO_2}) averaged over poles a–d for each air distribution system and air flow rate. (a)–(d) show comparisons among the air distribution systems: (a) floor-supply displacement ventilation (FSDV), (b) horizontal flow-type diffuser (HFD), (c) swirling flow-type diffuser (SFD), and (d) ceiling diffuser (CD). (e)–(h) show comparisons among air flow rates: (e) 120 m³/h, (f) 240 m³/h, (g) 360 m³/h, and (h) 480 m³/h

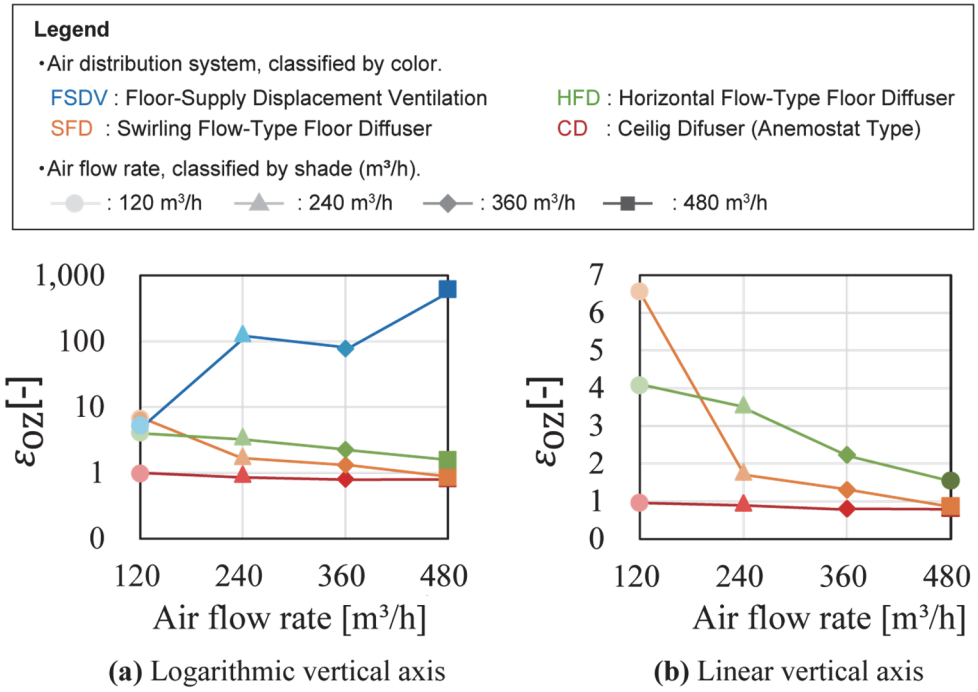
3.3.2 Contaminant Removal Efficiency in the Breathing Zone

Figure 3-9 presents the calculated contaminant removal efficiency in the occupied zone (ε_{OZ}), which allows a detailed comparison of the performance of each air distribution system within the occupied zone.
It should be noted that the term "efficiency" in this context refers to the effectiveness of removing contaminants from the occupied zone without their dispersion, rather than the speed or rate of removal.

For the reference system (CD), ε_{OZ} remained approximately 1.0 across all ventilation rates. This is consistent with the results in **Figure 3-8**, where a well-mixed airflow pattern was observed, confirming that the evaluation index functions correctly under mixed ventilation conditions.

For all three floor-supply systems (FSDV, HFD, and SFD), ε_{OZ} exceeded 1.0, indicating higher removal performance compared with mixed ventilation. In the HFD and SFD systems, ε_{OZ} decreased inversely with increasing ventilation rate. This suggests that while higher airflow rates are effective for diluting contaminants, they also enhance turbulence and diffusion, thereby reducing the removal effectiveness from the occupied zone. In these diffuser-based systems, the magnitude of turbulent mixing plays a dominant role in determining contaminant removal performance.

In contrast, the FSDV maintained a calm, piston-flow-like airflow pattern regardless of ventilation rate, resulting in ε_{OZ} increasing with higher ventilation rates. This represents a fundamental distinction between FSDV and diffuser-based floor-supply systems. The results confirm that FSDV can maintain a stable, low-turbulence airflow field even at higher air change rates (18–24 h^{-1}), demonstrating its advantage as a highly efficient ventilation strategy for contaminant removal in occupied spaces.



(a) Logarithmic vertical axis **(b)** Linear vertical axis

Figure 3-9. Contaminant removal efficiency in the breathing zone (ε_{OZ}) for each air distribution system as a function of air flow rate: (a) Results plotted on a logarithmic vertical axis. (b) Results plotted on a linear vertical axis.

3.3.3 Vertical Distribution of Air Temperature

Figure 3-10 shows the room-averaged vertical temperature distributions for each air distribution system and air flow rate. The temperature was normalized by the difference from the supply air temperature, as defined in Eq. (3-3). Similar to the tracer gas concentration results, only minor variations were observed among the measurement poles; therefore, the average value of the five poles (Pa–Pe) was used to represent the overall indoor condition.

First, the results for each air distribution system are discussed based on **Figures 3-10a–d**. Under identical supply-air temperature conditions, the overall room temperature decreased as the ventilation rate increased. The ceiling diffuser (CD) exhibited a nearly uniform vertical temperature distribution, indicating well-mixed ventilation. Both the floor-supply displacement ventilation (FSDV) and horizontal flow-type diffuser (HFD) systems showed clear thermal stratification at all ventilation rates. However, as the airflow rate increased, the vertical temperature gradient became smaller, suggesting that the room air approached a more uniform thermal distribution. In contrast, for the swirling flow-type diffuser (SFD), temperature stratification was observed under low-flow conditions (120 and 240 m³/h), while higher flow rates produced nearly uniform temperature

fields, indicating enhanced mixing within the room.

Next, **Figures 3-10e–h** compare the results across different air flow rates. At lower flow rates (120 and 240 m³/h), all three floor-supply systems (FSDV, HFD, and SFD) exhibited similar stratified profiles, although the magnitude of the temperature gradient varied slightly among them. At higher flow rates (360 and 480 m³/h), FSDV and HFD maintained distinct thermal stratification, whereas SFD and CD produced uniform vertical temperature distributions. These results demonstrate that FSDV and HFD tend to preserve displacement-like thermal characteristics even at higher air change rates, while SFD and CD promote stronger thermal mixing.

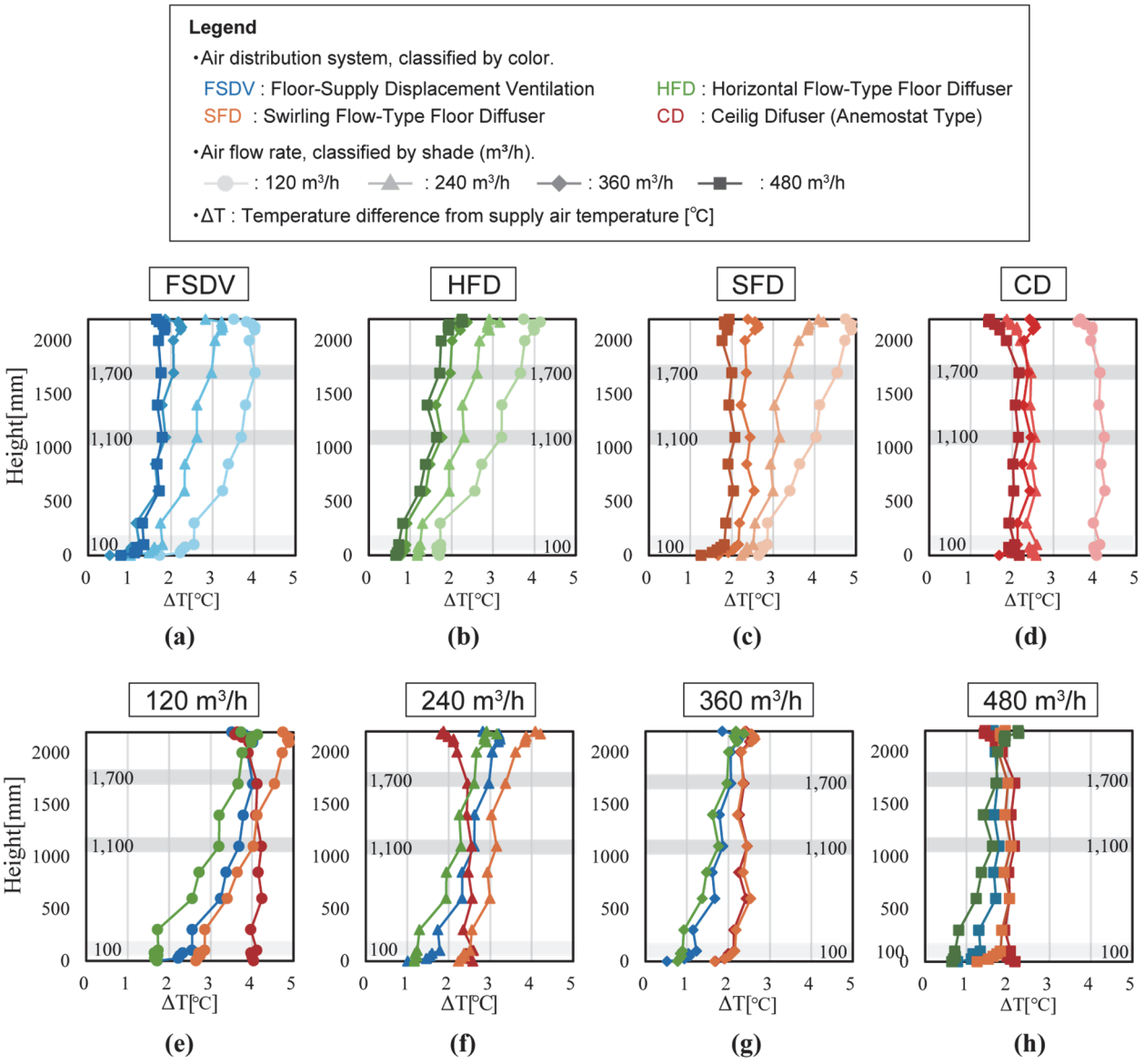
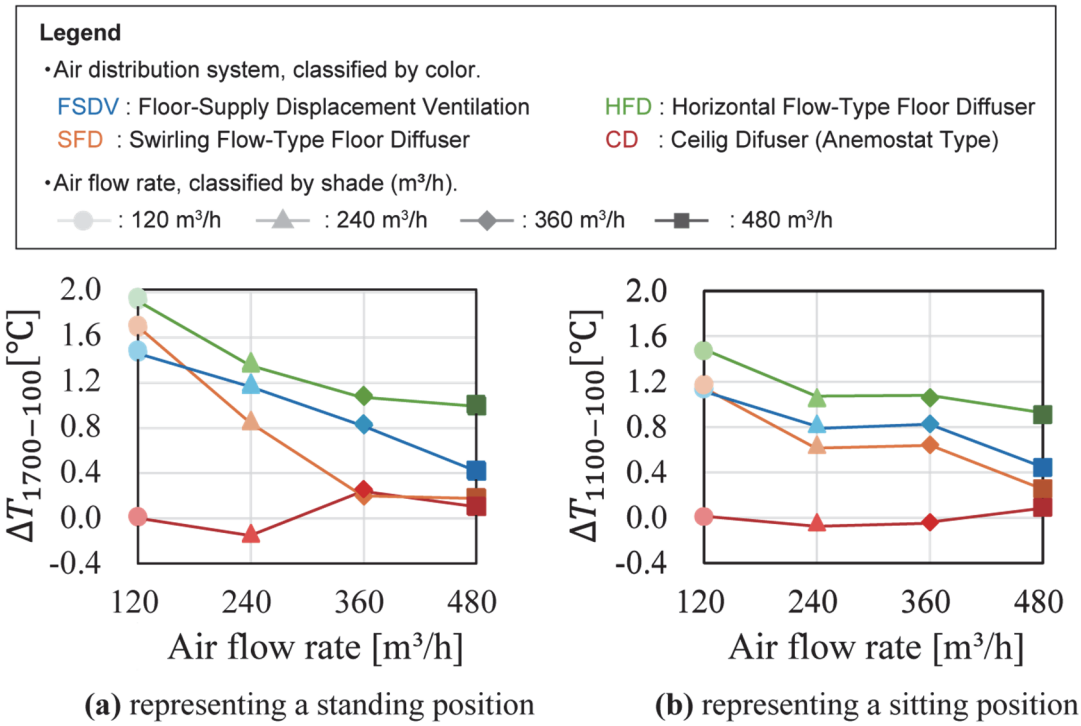


Figure 3-10. Vertical temperature profiles averaged over poles a–e for each air distribution system and air flow rate. (a)–(d) show comparisons among the air distribution systems: (a) floor-supply displacement ventila-

tion (FSDV), (b) horizontal flow-type diffuser (HFD), (c) swirling flow-type diffuser (SFD), and (d) ceiling diffuser (CD). (e)–(h) show comparisons among air flow rates: (e) 120 m³/h, (f) 240 m³/h, (g) 360 m³/h, and (h) 480 m³/h.

Figure 3-11 presents the calculated vertical temperature differences between the head and foot levels under both standing and seated conditions. The foot level was defined at a height of 100 mm above the floor, while the head level was set at 1,700 mm for the standing condition and 1,100 mm for the seated condition. Accordingly, the vertical temperature differences $\Delta T_{1700-100}$ and $\Delta T_{1100-100}$ were calculated.

The results indicate that for all floor-supply systems, the vertical temperature difference decreased as the ventilation rate increased, implying improved thermal comfort with higher airflow rates. In both standing and seated postures, the temperature difference remained within 2 °C, which satisfies the acceptable limits specified by ASHRAE Standard 55 [85] (4 °C for standing occupants and 3 °C for seated occupants).



(a) representing a standing position **(b)** representing a sitting position

Figure 3-11. Vertical temperature differences (ΔT) between upper and lower measurement heights for each air distribution system and air flow rate: (a) shows the temperature difference between 1,700 mm and 100 mm ($\Delta T_{1700\text{-}100}$), representing a standing position, and (b) shows the temperature difference between 1,100 mm and 100 mm ($\Delta T_{1100\text{-}100}$), representing a sitting position.

3.3.4 Summary of Key Findings

This section summarizes and discusses the key findings obtained from the results presented in **Figures 3-8** through **3-11**.

From the vertical concentration distributions, the airflow characteristics observed in the experiments generally matched the pre-experimental expectations. Specifically, mixed airflow fields were formed in the ceiling diffuser (CD) and swirling flow-type diffuser (SFD) systems, whereas displacement-type airflow fields were formed in the horizontal flow-type diffuser (HFD) and floor-supply displacement ventilation (FSDV) systems.

Distinct differences were observed between the CD and SFD under sub-rated airflow conditions. In the CD system, the supply airflow direction was opposite to the thermal plume generated by the human body, promoting mixing even at low airflow rates and maintaining a well-mixed airflow field. In contrast, the SFD supplied air in the same direction as the thermal plume, and thus, at low airflow rates, the airflow pattern tended to shift toward a displacement-type field. These findings suggest that when an SFD is adopted with the intention of achieving complete mixing, operating below the rated airflow may unintentionally result in a displacement-like airflow pattern.

For the HFD, the distance between diffusers was relatively short (approximately 1,000 mm), compared with typical design practice. Consequently, as the airflow rate increased, the normalized concentration in the occupied zone rose to around 0.5. This result indicates that a short diffuser spacing enhances turbulent mixing, producing a more mixed airflow field than intended. Therefore, when using an HFD to achieve displacement ventilation, sufficient diffuser spacing should be ensured to maintain the desired airflow characteristics.

Among the four ventilation systems, the FSDV exhibited the lowest average indoor contaminant concentration and the least dispersion of exhaled human breath. The distinguishing feature of the FSDV is its ability to maintain a stable, low-velocity piston flow even at high airflow rates (18–24 h^{-1}), resulting in an increase in contaminant removal efficiency with increasing ventilation rate. At the maximum airflow of 480 m^3/h, the contaminant removal efficiency of the FSDV was more than ten times higher than that of the HFD and SFD. These results demonstrate that the FSDV provides a highly efficient ventilation strategy, particularly suitable for clean environments such as factories, cleanrooms, and medical facilities.

Furthermore, the results show that in all floor-supply systems, the vertical temperature difference between the head and foot levels decreased as the ventilation rate increased, implying improved thermal comfort. In both standing and seated conditions, the vertical temperature difference remained within 2 °C, satisfying

the acceptable criteria defined in ASHRAE Standard 55 (4 °C for standing and 3 °C for seated occupants). In practice, supplying cool air from the floor can potentially cause thermal discomfort due to downdrafts; thus, designers often increase the supply air temperature while maintaining a higher airflow rate under cooling conditions. Therefore, when designing floor-supply ventilation systems, it is essential to balance the reduction in vertical temperature difference (thermal comfort) with the potential increase in contaminant dispersion resulting from higher airflow rates.

3.4 Conclusion

In this chapter, full-scale experiments were conducted on four air distribution systems—floor-supply displacement ventilation (FSDV), horizontal flow-type diffuser (HFD), swirling flow-type diffuser (SFD), and ceiling diffuser (CD)—to compare their performance in terms of contaminant removal efficiency and thermal comfort under different ventilation rates. The number of diffusers was selected such that, at the maximum airflow rate (480 m^3/h), the operating range remained within the manufacturer's recommended specification. Consequently, under low-flow conditions, some cases operated below the rated flow range. It should also be noted that the air change rate (6–24 h^{-1}) was relatively high, and the diffuser spacing was approximately 1,000 mm, which is closer than in typical design practice.

The main findings of this chapter are summarized as follows:

Airflow Characteristics and Concentration Distribution

・Mixed airflow fields were formed in the CD and SFD systems, while displacement airflow fields were observed in the HFD and FSDV systems. Among them, the FSDV exhibited the most stable vertical concentration profile regardless of airflow rate, achieving the lowest average contaminant concentration. This result confirmed that the FSDV most effectively suppressed the dispersion of exhaled human breath among all systems tested.

・Under sub-rated airflow conditions, a notable difference was observed between the CD and SFD systems. Because the CD supplies air opposite to the upward human thermal plume, mixing was promoted even at low airflow rates, maintaining a well-mixed flow field. In contrast, the SFD supplies air in the same direction as

the thermal plume, and thus a displacement-type flow pattern emerged at low airflow rates. These results suggest that when the SFD is used for complete mixing, operating below its rated airflow may unintentionally lead to a displacement-like airflow field.

Evaluation of Contaminant Removal Efficiency

・The contaminant removal efficiency, ε_{OZ}, was approximately 1 (perfect mixing) for the CD, decreased with increasing airflow rate for the HFD and SFD, and increased with airflow rate for the FSDV. Under the maximum airflow condition (480 m³/h), ε_{OZ} for the FSDV was more than ten times higher than that for the HFD and SFD, quantitatively demonstrating the superior performance of the FSDV.

Evaluation of Thermal Comfort

・In all floor-supply systems, the vertical temperature difference between the head and foot levels decreased with increasing airflow rate. In both standing and seated conditions, the temperature difference remained within 2 °C, satisfying the comfort criteria specified in ASHRAE Standard 55 [85]. These results indicate that FSDV and HFD systems can maintain thermally comfortable environments when adequate airflow is provided.

Design implications and further applications

・The FSDV maintained a stable piston flow even under high airflow conditions, achieving both high contaminant removal performance and thermal comfort. In contrast, the airflow characteristics and efficiency of HFD and SFD systems were more sensitive to airflow rate and diffuser arrangement. In the design of floor-supply systems, it is essential to balance the benefit of reduced vertical temperature difference with the potential increase in contaminant dispersion caused by higher airflow.

These findings provide fundamental data for the next chapter, which evaluates infection risk reduction performance through the combined operation of local exhaust ventilation (LEV) and general ventilation systems.

3.5 Appendix 3-A: Measurement of Ventilation Rate in the Test Chamber with Different Tracer Gas Release Points

In this experiment, the ventilation rate was controlled by adjusting the opening angle of a manual damper. During adjustment, the measured ventilation rate, calculated from the steady-state mass balance of contaminant concentration, was continuously monitored and matched to the target airflow rate.

However, as described in Section 3.2.1, the experimental chamber was designed as a cleanroom maintained under positive pressure, resulting in unavoidable air leakage to the outside. Therefore, both the supply and exhaust airflow rates were calculated based on the contaminant concentration balance expressed in Eq. (3-5), and the difference in the measured ventilation rate depending on the tracer gas release position was evaluated.

$$Q_m = \frac{M_{\mathrm{CO_2}}}{C_{\mathrm{CO_2,EA}} - C_{CO_2,SA}} \qquad (3-5)$$

where Q_m is the measured ventilation rate [m^3/h], $M_{\mathrm{CO_2}}$ is the CO_2 generation rate [m^3/h], $C_{\mathrm{CO_2,EA}}$ is the CO_2 concentration in the exhaust air [-], $C_{CO_2,SA}$ is the CO_2 concentration in the supply air.

When tracer gas was released into the supply duct, it was introduced through a pressure-measurement port located upstream of the HEPA filter, before entering the test chamber. For the floor-supply systems, the supply concentration was measured immediately below the floor diffuser, while for the ceiling-type anemostat systems, it was measured directly beneath the anemostat outlet. For the exhaust concentration measurements, tracer gas was released just below the exhaust outlet, and the concentration was monitored from a sampling port installed in the exhaust duct outside the chamber. The background CO_2 concentration in the outdoor air was measured upstream of the outdoor air handling unit (OHU).

The calculated supply and exhaust airflow rates based on the measured concentrations are shown in **Fig. 3-A-1**. The exhaust rate generally agreed well with the target value, whereas the supply rate was slightly higher, with differences of up to approximately 65 m³/h. In particular, under low ventilation conditions, the ratio of leakage flow to total ventilation increased, indicating that special attention should be given when interpreting the results under these conditions.

Because the CO_2 concentration of the leaked air from the test chamber could not be accurately deter-

mined, the ventilation rate measured by releasing tracer gas directly below the exhaust outlet was adopted as the reference value for all analyses. Specifically, the airflow rate was calculated based on a steady-state mass balance using the exhaust concentration. Accordingly, the "ventilation rate" referred to in Chapters 3, 4, and 6 represents this measured exhaust-based ventilation rate.

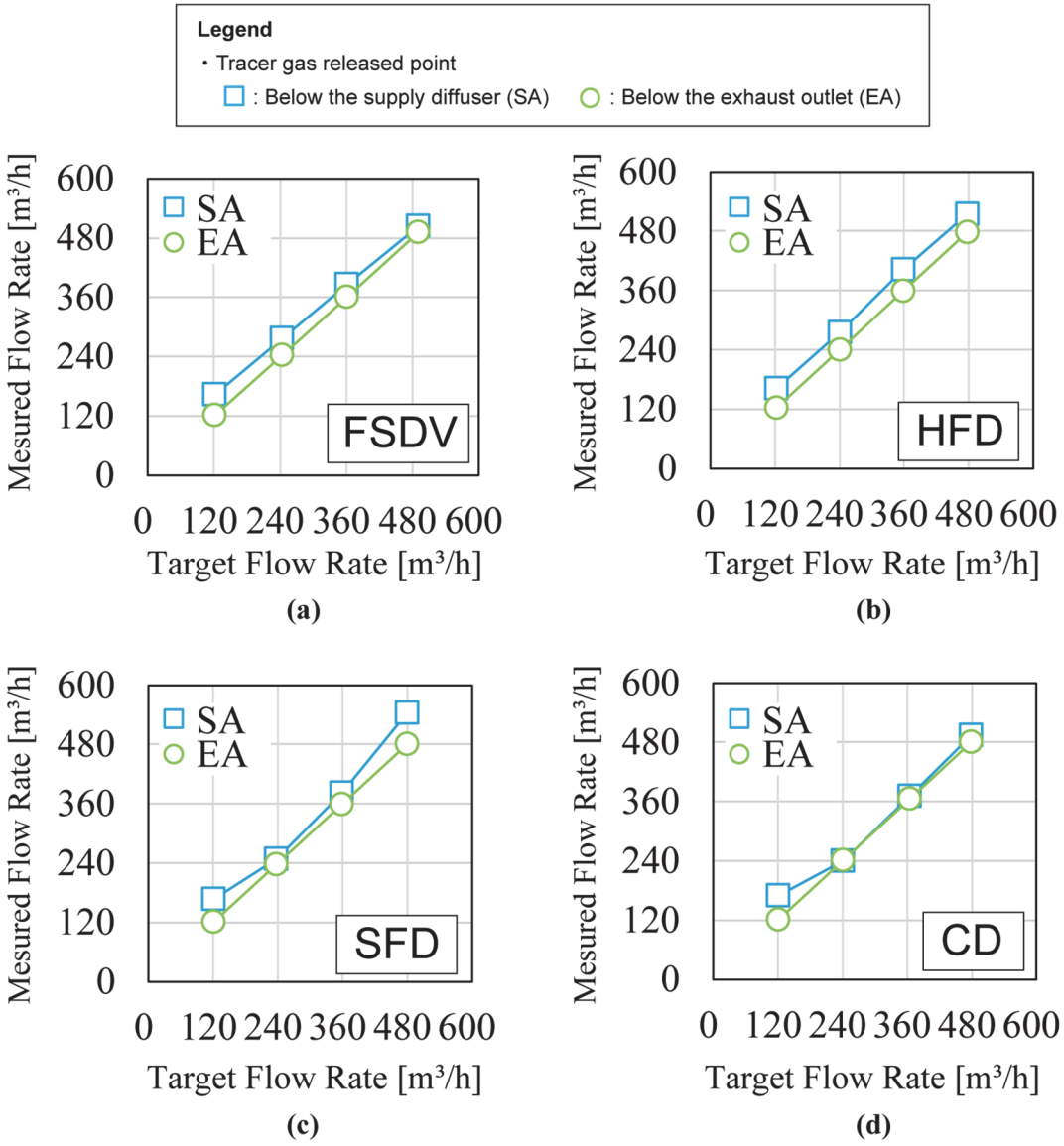


Figure 3-A-1. Ventilation rates calculated from mass balance of tracer gas concentrations, when the tracer gas was released either below the supply diffuser (SA) or below the exhaust outlet (EA): (a) floor-supply displacement ventilation (FSDV), (b) horizontal flow-type diffuser (HFD), (c) swirling flow-type diffuser (SFD), and (d) ceiling diffuser (CD).

4 Experimental Evaluation of LEV Performance under Different Ventilation Systems

4.1 Purpose of the Chapter

This chapter aims to evaluate the combined performance of local exhaust ventilation (LEV) with four different air distribution systems: floor-supply displacement ventilation (FSDV), horizontal flow-type diffuser (HFD), swirling flow-type diffuser (SFD), and a conventional ceiling diffuser (CD). The focus is on clarifying the effectiveness of LEV in suppressing airborne contaminant dispersion during face-to-face conditions under various ventilation environments. In this chapter, a detailed analysis is conducted assuming that one of the occupants in the consultation room (the patient) is infected with SARS-CoV-2, and the infection risk of the other occupant (the doctor) is quantitatively assessed.

Similar to Chapter 3, full-scale chamber experiments were conducted in which the airflow rate was varied in four stages (120–480 m^3/h) for each ventilation system. Two cases were compared: with and without LEV operation, where the hood exhaust flow rate was set to 100 m^3/h in the operated condition. A schematic diagram of the experimental concept and parameters is shown in **Figure 4-1**. The tracer gas was used to represent speech droplet nuclei. It was released from the mouth of a simplified manikin simulating a patient, at a flow rate of 5.21 L/min, velocity of 0.30 m/s, and angle of 11.9° downward from the horizontal, based on the human exhalation data obtained in Chapter 2. The steady-state tracer gas concentration distribution was measured to evaluate the hood capture efficiency, and the infection risk was estimated from the CO_2 concentration rise in front of the opponent person (doctor).

The performance of LEV systems is strongly affected by surrounding airflow patterns, which depend on the ventilation type and airflow rate. However, few studies have systematically investigated the infection-control performance of LEV under various ventilation conditions. Therefore, the experimental data obtained in this chapter provide novel and valuable insights for designing and optimizing LEV applications in medical and similar indoor environments.

The experiments in this chapter were conducted during the same period as those described in Chapter 3, with the main differences being the presence or absence of the LEV system and the tracer gas generation

method. Hence, details common to both experiments—such as chamber setup and measurement instruments—are omitted here and can be referred to in Chapter 3.

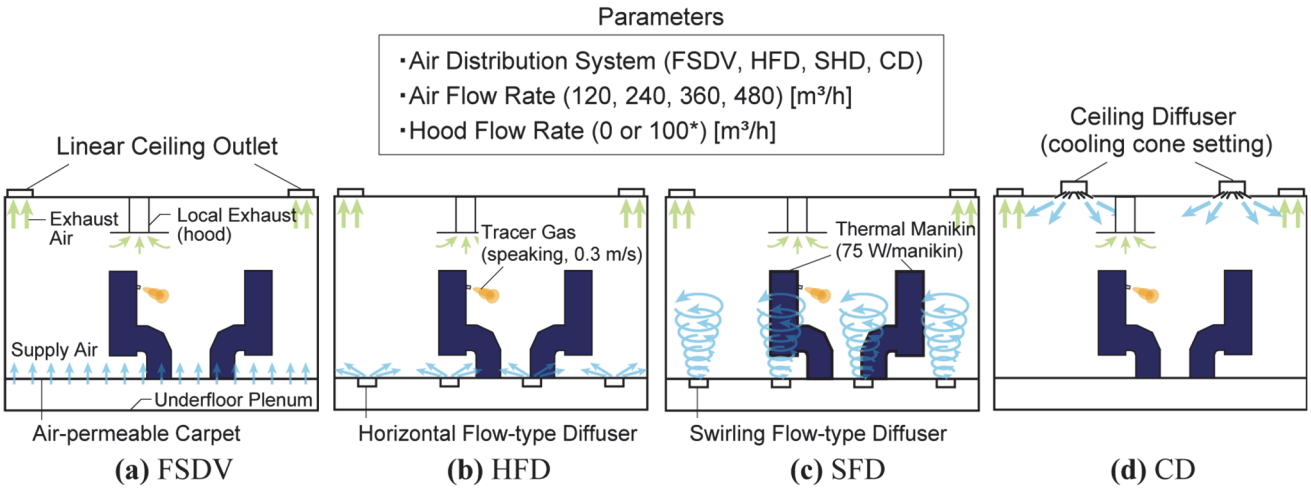


Figure 4-1. Conceptual diagram of the experimental setup and air distribution systems. (a) floor-supply displacement ventilation (FSDV), (b) horizontal flow-type diffuser (HFD), (c) swirling flow-type diffuser (SFD), and (d) ceiling diffuser (CD) with a cooling cone setting.

Note: ＊Hood flow rate was 50 m^3/h only under air flow rate 120 m^3/h condition.

4.2 Methodology

4.2.1 Experimental Facilities

The experiments were conducted at the University of Osaka between December 2023 and January 2024. The sectional and isometric views of the experimental facility are shown in **Figure 4-2**; the plan view is identical to **Figure 3-2a**. The fundamental experimental setup, including the test facility, temperature-control system, and simplified manikins, was identical to that described in Chapter 3 and is therefore not repeated here. The main differences are that a local exhaust ventilation (LEV) system was introduced to reduce the infection risk, and the exhalation velocity was controlled to reproduce more realistic speaking conditions.

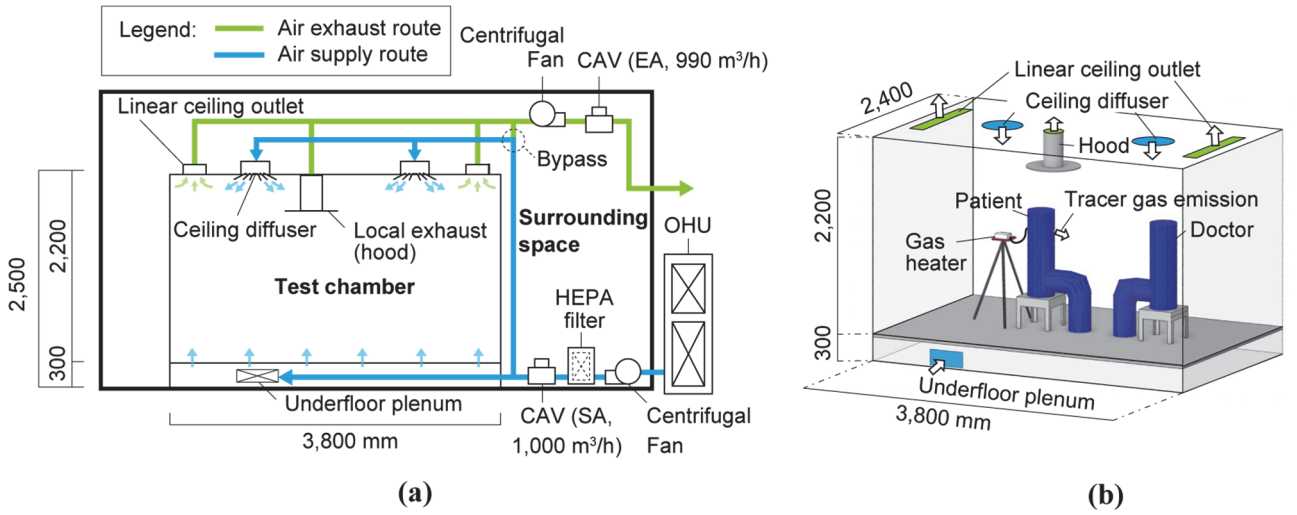


Figure 4-2. Configuration of the test chamber and air distribution system : (a) sectional view showing details of the supply and exhaust air routes with the local exhaust hood, and (b) three-dimensional schematic of the test chamber showing the face-to-face conversation setup.

Note: The plan view of the air circulation system is identical to that shown in Figure 3-2a and is therefore omitted here.

Figure 4-3 shows the configuration of the local exhaust ventilation (LEV) hood and its positional relationship with the exhalation outlet. The hood was a flanged hood with a diameter of 600 mm, identical in shape to that used in the CFD analysis presented in Chapter 2. The CFD results in Chapter 2 indicated that the relative position of the hood significantly affects its capture performance, and that locating the hood directly above the emission source (the patient) provides the most effective capture. Therefore, in this experiment, the hood was installed 500 mm above the patient's head.

The distance between the mouths of the patient (infected person) and the doctor (opponent person) was 1,200 mm. The CO_2 concentration in front of the doctor's mouth was measured using a CO_2 recorder (RTR-576, T&D Corporation) to evaluate the rise in tracer-gas concentration due to exhalation.

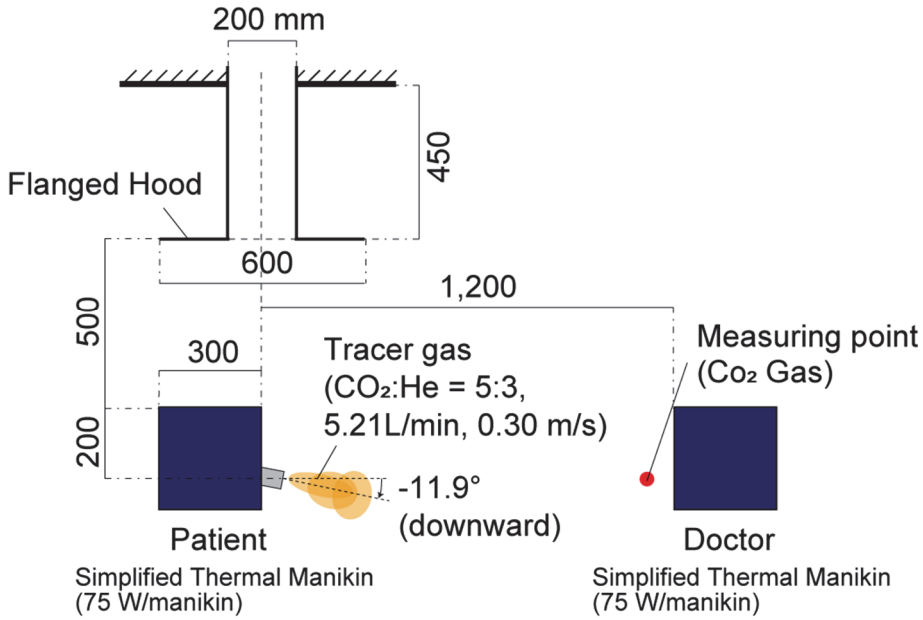


Figure 4-3. Experimental setup showing the configuration of the flanged hood, the tracer gas generation point, and the CO_2 measuring point.

Figure 4-4 shows the arrangement of the air diffusers and the measurement points for contaminant (CO_2) concentration and air temperature in the test chamber. The primary difference from **Figure 3-3** is that a local exhaust ventilation (LEV) hood was installed above the manikin representing the patient. Details of the vertical measurement poles and wall surface temperature measurements are identical to those shown in **Figures 3-3e–3-3h** and are therefore omitted here.

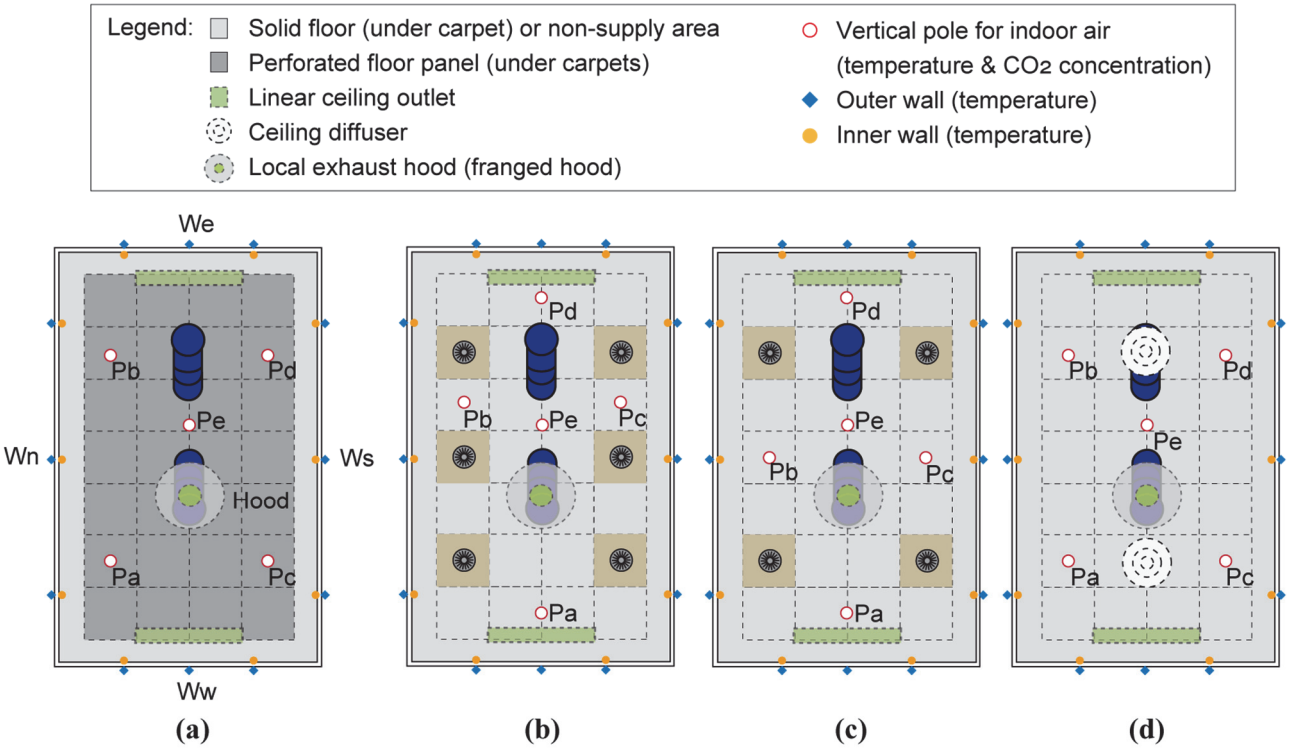


Figure 4-4. Layout of air diffusers and the local exhaust hood (flanged hood) for each air distribution system: (a) floor-supply displacement ventilation (FSDV), (b) horizontal flow-type diffuser (HFD), (c) swirling flow-type diffuser (SFD), and (d) ceiling diffuser (CD).

Note: The measurement points for vertical profiles of temperature and CO_2 concentration, as well as wall surface temperatures, were the same as in Figure 3-3 and are therefore omitted here.

Figure 4-5 shows the detailed dimensions of the simplified thermal manikins and the measurement point of tracer gas concentration in front of the doctor's mouth. The manikins were identical to those used in Chapter 3, and their materials and specifications are described in Section 3.2.1. In this chapter, one of the occupants in the consultation room (the patient) is assumed to be infected with SARS-CoV-2, and the infection risk of the other (the doctor) is evaluated. For this purpose, a CO_2 recorder (RTR-576, T&D Corporation), identical to those used for indoor CO_2 concentration measurements, was installed at the mouth position of the doctor manikin. The mouth height of the seated manikin was set at 1,100 mm above the floor, which is consistent with the height used for measuring indoor CO_2 concentration distribution.

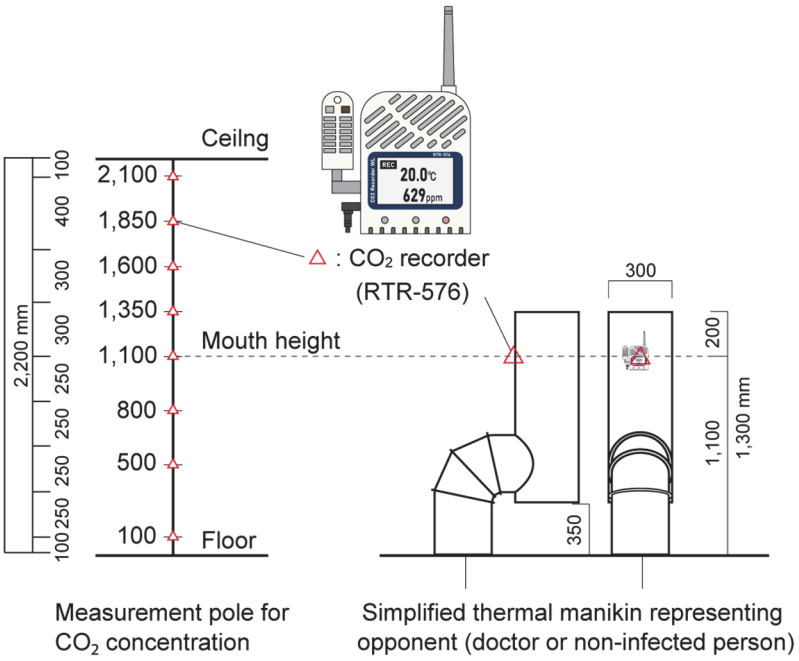


Figure 4-5. Dimensions of the simplified thermal manikin and measurement points of CO_2 concentration in front of the opponent's mouth (doctor or non-infected person).

4.2.2 Tracer Gas Generation Method for Speaking Exhalation Simulation

Tracer gas representing exhaled air during speaking (passive contaminant) was released from the manikin simulating the patient. An overview of the generation system is shown in **Figure 4-6**. The flow rate, velocity, and exhalation angle were set to reproduce the measured conditions obtained in Chapter 2 using human subjects, namely a flow rate of 5.21 L/min, a velocity of 0.30 m/s, and an angle of 11.9° downward. To match the density of air, CO_2 and He were mixed at a volumetric ratio of 5:3, giving a total flow rate of 5.21 L/min (CO_2 : He = 3.26 : 1.95 L/min). The flow rate was controlled by a mass flow controller (Fujikin, FCS-T1000L series). The mixed gas was heated by the same gas heater used in Chapter 3 and passed through a thermally insulated tube before being released from the mouth of the patient manikin (1,100 mm above the floor). The gas temperature was maintained at approximately 30–35 °C (measured with T-type thermocouples).

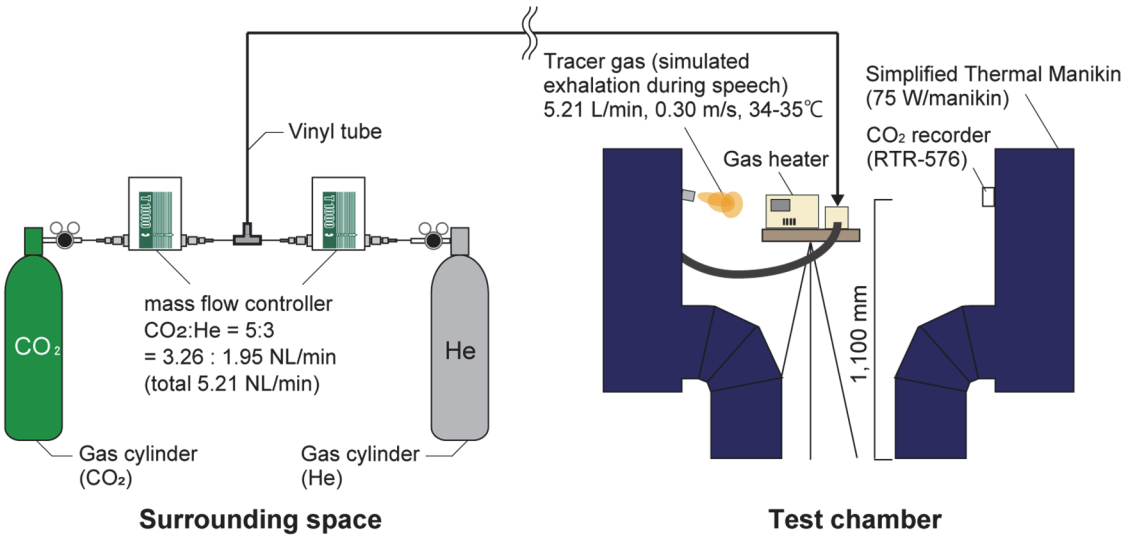


Figure 4-6. Experimental setup for tracer gas generation simulating exhalation during speech.

4.2.3 Experimental Cases and Procedures

The experimental conditions are summarized in **Table 4-1**. Similar to Chapter 3, four air distribution systems (FSDV, HFD, SFD, and CD) were tested at four airflow rates of 120, 240, 360, and 480 m³/h. For each airflow condition, two local exhaust ventilation (LEV) cases were examined — with and without hood operation (100 m³/h and 0 m³/h, respectively) — resulting in a total of 32 test cases. Air change rates of 6–12 h^{-1} correspond to the target ventilation range recommended by REHVA for consultation rooms [69].

The CFD analysis presented in Chapter 2 indicated that the relative position of the hood has a major influence on capture performance and that the hood should ideally be located above the contaminant source. Since the effect of height was found to be relatively minor, the hood height was set to 500 mm above the patient's head, representing a realistic and acoustically acceptable position. In addition, the analysis in Chapter 2 demonstrated that the airflow ratio between the hood and other ceiling exhaust outlets significantly affects capture efficiency. While the CFD model in Chapter 2 (**Figure 2-4a**) assumed a single ceiling exhaust outlet, the present experimental setup includes two linear exhaust outlets on both sides of the ceiling, providing conditions better suited to evaluate the performance of the hood alone. According to the CFD results (**Figure 2-6d**), when the room ventilation rate ranged from 120 to 480 m³/h, a hood exhaust rate of 100 m³/h achieved a capture efficiency close to 100%. Therefore, the hood exhaust rate in this experiment was set to 100 m³/h. However, for the lowest ventilation condition (120 m³/h), the hood exhaust rate was reduced to 50 m³/h due to

facility limitations, with the line-type exhaust outlets (LOs) adjusted to 70 m³/h.

As described in **Appendix 3-A**, the "ventilation rate" in this chapter refers to the exhaust airflow rate, which was determined by releasing tracer gas directly below the exhaust outlets and calculating the flow based on a steady-state mass balance.

Table 4-1.

Experimental conditions for each air distribution system with and without a local exhaust hood.

Air distribution system	Air exhaust method	Air flow rate [m³/h] (Air change rate [h^{-1}])	Flow rate per diffuser [m³/h]	Hood flow rate [m³/h]	Standard flow rate range per diffuser [m³/h]
FSDV	LO×2	120(6), 240(12), 360(18), 480(24)	-	0	-
HFD×6	LO×2	120(6), 240(12), 360(18), 480(24)	20*,40*,60,80	0	45-90
SFD×4	LO×2	120(6), 240(12), 360(18), 480(24)	30*,60*,90,120	0	90-150
CD×2	LO×2	120(6), 240(12), 360(18), 480(24)	60*,120*,180,240	0	135-480
FSDV	LO×2 + Hood	120(6), 240(12), 360(18), 480(24)	-	100**	-
HFD×6	LO×2 + Hood	120(6), 240(12), 360(18), 480(24)	20*,40*,60,80	100**	45-90
SFD×4	LO×2+ Hood	120(6), 240(12), 360(18), 480(24)	30*,60*,90,120	100**	90-150
CD×2	LO×2+ Hood	120(6), 240(12), 360(18), 480(24)	60*,120*,180,240	100**	135-480

Abbreviation: FSDV: Floor-supply displacement ventilation; HFD: Horizontal flow-type floor diffuser; SFD: Swirling flow-type floor diffuser; CD: Ceiling diffuser (anemostat type, cooling cone setting); LO: Linear ceiling outlet.

＊: Below standard flow rate range per diffuser [m^3/h].

＊＊: Hood flow rate was 50 m^3/h only when the room flow rate was 120 m^3/h (6 ACH).

4.2.4 Normalization of Tracer Gas Concentration

As in Chapter 3, the normalized concentration rise (C'_{CO_2}) was used to evaluate the spatial distribution of the tracer gas within the test chamber. This index allows quantitative comparison of the contaminant dispersion characteristics under different air distribution systems and with or without the local exhaust ventilation (LEV) system. The normalized concentration rise is defined by Eq. (4-1), which expresses the relative increase in CO_2 concentration based on the flow-weighted exhaust concentration as a reference:

$$C'_{CO_2} = \frac{C_{CO_2,p} - C_{CO_2,SA}}{\left(Q_h C_{CO_2,h} + Q_{LO} C_{CO_2,LO}\right)/Q_e - C_{CO_2,SA}} \quad (4-1)$$

where $C_{CO_2,p}$ is the measured CO_2 concentration at a point p [-], $C_{CO_2,SA}$ is the CO_2 concentration in the supply air [-], $C_{CO_2,h}$ is the CO_2 concentration in the exhaust air from the local exhaust hood [-], $C_{CO_2,LO}$ is the CO_2 concentration in the exhaust air from the linear outlet [-], Q_h is the exhaust flow rates of the local exhaust hood [m³/h], Q_{LO} is the exhaust flow rates of the linear outlet [m³/h], and Q_e is the total exhaust airflow rate [m³/h].

Here, Q_h was measured using an ultrasonic anemometer (ATZTA TRZ150-DC/5P, Aichi Tokei Denki Co., Ltd.). All values represent the time-averaged concentrations under steady-state conditions. This definition ensures that the exhaust reference concentration properly accounts for both exhaust paths by using a flow-weighted average, maintaining consistency with the mass-balance framework.

4.2.5 Hood Capture Performance Assessment in Experiment

The hood capture efficiency (η), which represents the proportion of tracer gas captured by the local exhaust hood relative to the total generated amount, was calculated using Eq. (4-2). This parameter serves as a direct indicator of the effectiveness of the hood in capturing contaminants released from the source.

$$\eta = \frac{Q_h(C_{CO_2,h} - C_{CO_2,SA})}{Q_h(C_{CO_2,h} - C_{CO_2,SA}) + Q_{LO}(C_{CO_2,LO} - C_{CO_2,SA})} \quad (4-2)$$

4.2.6 Infection Risk Assessment from Tracer Gas in Experiment

As described in Section 2.3.4, the airborne infection risk during close-distance conversation was estimated using the Wells–Riley model (Eqs. (2-9) and (2-10)), incorporating the local tracer gas concentration distribution obtained from CFD analysis. In this section, the same concept (Eq. (2-13)) is applied to the experimental results, in which CO_2 was used as a tracer gas to determine the quanta concentration in front of the doctor's (non-infected person's) mouth.

The quanta concentration in front of the doctor's (non-infected person's) mouth, $C_{q,dc}$ [quanta/m³], was calculated using Eqs. (4-3) and (4-4):

$$C_{q,dc} = \frac{q}{Q_e} \cdot C'_{CO_2,dc} \quad (4-3)$$

$$C'_{CO_2,dc} = \frac{C_{CO_2,dc} - C_{CO_2,SA}}{M_{CO_2}/Q_e} \quad (4-4)$$

where q is the quanta emission rate (42 quanta/h), Q_e is the ventilation rate (exhaust flow rate) [m^3/h], $C'_{CO_2,dc}$ is the nomarized tracer gas concentration rize in front of the doctor's mouth [-], $C_{CO_2,dc}$ is the tracer gas concentration in front of the doctor's mouth [-], and M_{CO_2} is the tracer gas (CO_2) emission rate (3.25 L/min). The steady-state average value over the final 15 minutes of each condition was used ase $C_{CO_2,dc}$.

The quanta emission rate (q) was set at 42 quanta/h, corresponding to the 90th percentile for conversational activity according to REHVA [69], and represents typical emission for the early variants of SARS-CoV-2. Because the quanta emission rate includes significant uncertainty, the infection risk calculated in this study should be interpreted as a reference value, statistically corresponding to the 90th percentile of infection risk for the initial SARS-CoV-2 variants. The breathing rate of the doctor (non-infected person's): Q_{dc} is assuemed 5.21 L/min (= 3.13 × 10^{-4} m^3/s ≈ 1.13 m^3/h), as obtained from the experimental measurements in chapter 2 (see **Table 2-8**). A normalized concentration $C'_{CO_2,dc}$ = 1 indicates that the local CO_2 concentration equals the perfectly mixed concentration in the chamber..

Finally, the time until the infection probability reached 5%, denoted as $t_{5\%}$, was calculated using Eq. (4-5). A 5% infection probability was chosen following REHVA's guideline, which defines this level as an acceptably low infection risk in office environments [69]. Since the quanta emission rate (42 quanta/h) corresponds to conversational conditions for the early SARS-CoV-2 variants, the infection risks presented here represent those specific conditions.

$$t_{P\%} = -\frac{\ln(1-P)}{C_{q,dc}Q_{dc}} \quad (4-5)$$

The model assumes a well-mixed condition for the inhaled air; thus, the calculated risk represents a reference value under steady-state conditions.

4.3 Results and discussions

4.3.1 Vertical Distribution of Tracer Gas Concentration

Figure 4-7 shows the average normalized CO_2 concentration measured at the vertical poles (Pa–Pd) for each air distribution system under different ventilation rates, with and without the local exhaust hood (LEV). The normalization was performed using Eq. (4-1), where the exhaust concentration was defined as the flow-weighted average of the CO_2 concentrations at the hood and the linear exhaust outlets. A normalized concentration of 1 indicates that the local CO_2 concentration equals that of a perfectly mixed condition.

Without the hood (**Figure 4-7a–d**), both the FSDV and HFD systems exhibited nearly zero normalized concentrations up to a height of 1,500 mm, above which the concentration increased. This indicates the formation of a clear displacement ventilation flow field within the occupied zone. In contrast, the SFD system showed a well-mixed condition at 360 m^3/h and 480 m^3/h; however, when the flow rate was below the diffuser's rated range (120 m^3/h and 240 m^3/h), a displacement-like flow pattern similar to that of FSDV and HFD was observed.

With the hood installed (**Figure 4-7e–h**), a significant decrease in CO_2 concentration was observed for SFD and CD, both of which had already exhibited nearly mixed ventilation before hood operation. In contrast, under FSDV and HFD conditions—where displacement ventilation had been established even without the hood—the introduction of the hood reduced the normalized concentration to nearly zero even near the ceiling. This result demonstrates that the hood effectively prevented the dispersion of exhaled contaminants (droplets and droplet nuclei) throughout the entire room.

Figure 4-7i–l compares the four air distribution systems under identical ventilation rates with hood operation. As the ventilation rate increased, the differences between the air distribution systems became more pronounced. At 360 m^3/h and 480 m^3/h, the SFD showed the highest normalized concentration, indicating that the swirling diffusers, which were widely distributed across the floor, promoted broader mixing of exhaled air compared with the CD system.

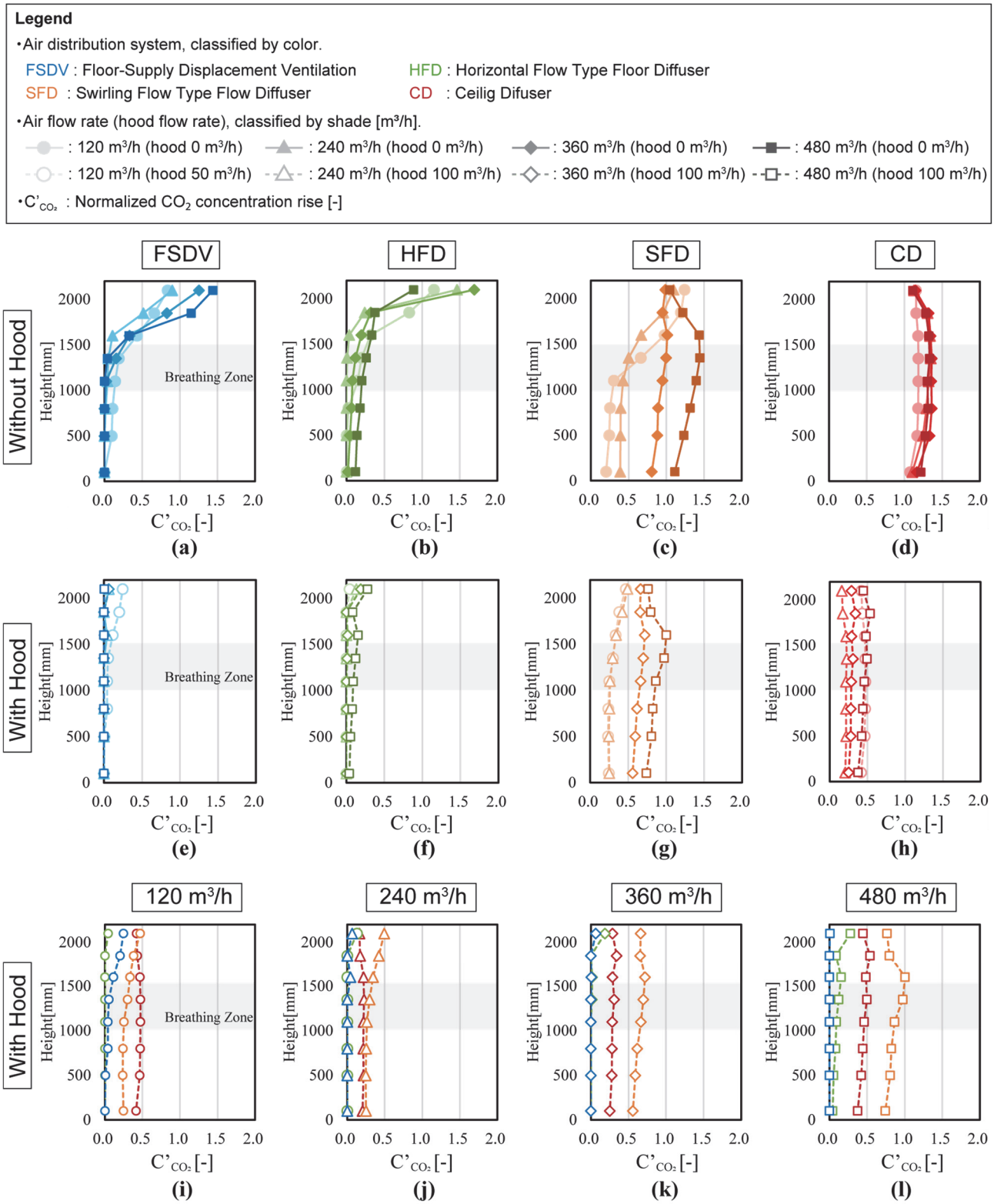


Figure 4-7. Vertical profiles of normalized CO_2 concentration rise (C'_{CO_2}) averaged over poles a–d for each air distribution system and air flow rate, with and without a local exhaust hood: (a)–(d) show results without the hood, and (e)–(h) show results with the hood, corresponding respectively to (a, e) floor-supply displacement ventilation (FSDV), (b, f) horizontal flow-type diffuser (HFD), (c, g) swirling flow-type diffuser (SFD), and (d, h) ceiling diffuser (CD). (i)–(l) show comparisons among air flow rates under the hood-installed condition:

(i) 120 m³/h, (j) 240 m³/h, (k) 360 m³/h, and (l) 480 m³/h.

4.3.2 Hood Capture Efficiency

Figure 4-8 presents the capture efficiency (η) of the local exhaust hood, calculated using Eq. (4-2).
The FSDV, HFD, and CD systems all exhibited high capture efficiencies, generally exceeding 80%. Under the lowest ventilation condition (120 m³/h, 6 h^{-1}), η remained around 80% for all systems, showing minimal variation. However, as the ventilation rate increased, the SFD system showed a pronounced decrease in capture efficiency, reaching approximately 30%. This reduction is attributed to the larger number of diffusers in the SFD configuration, which generated strong turbulent airflow between the hood and the exhalation source, thereby diminishing the hood's ability to capture contaminants.

In contrast, the HFD and CD systems demonstrated nearly identical capture efficiencies, despite having markedly different airflow characteristics prior to hood installation. As discussed in Chapter 3, this similarity is likely due to the short diffuser spacing in the HFD system (approximately 1,000 mm), where the air jets from adjacent diffusers collided at higher ventilation rates, increasing turbulence within the room.

While the HFD, SFD, and CD systems exhibited an inverse relationship between ventilation rate and capture efficiency, the FSDV system showed a direct proportionality. This result suggests that the stable upward airflow pattern characteristic of the FSDV enhanced the hood's ability to capture exhaled contaminants directly above the source as the ventilation rate increased.

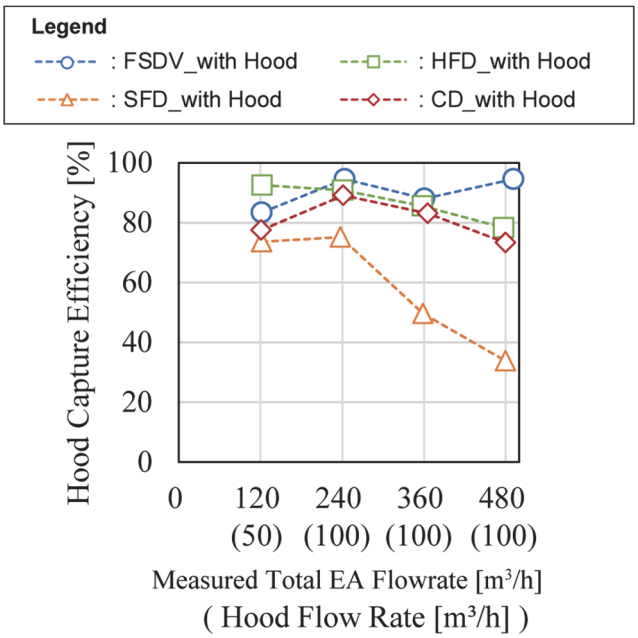


Figure 4-8. Hood capture efficiency for each air distribution system at different total exhaust air flow rates.

4.3.3 Infection Risk for the Opponent Person

Figure 4-9a shows the normalized CO_2 concentration rise ($C'_{CO_2,dc}$) measured in front of the doctor's mouth. In the CD case, $C'_{CO_2,dc}$ decreased by approximately 0.5–1.0 across all ventilation rates following the introduction of the hood, indicating a clear effect of the local exhaust system. For SFD, a significant reduction in $C'_{CO_2,dc}$ was also observed under the 360 and 480 m³/h conditions after installing the hood. However, under the lower ventilation rates of 120 and 240 m³/h, which were below the rated airflow of the diffuser, a relatively quiescent airflow field was formed, resulting in low CO_2 concentrations near the doctor's mouth even without the hood. In contrast, the FSDV system maintained $C'_{CO_2,dc}$ values close to zero under all ventilation conditions, regardless of the presence of the hood, demonstrating its superior contaminant removal performance.

Figures 4-9b and c show $t_{5\%}$, the time required for the infection probability of the doctor (the non-infected person) to reach 5%. The calculation was performed using the Wells–Riley model described in Section 4.2.6, with the quanta emission rate during speaking set to 42 quanta/h, as suggested by REHVA [69]. It should be noted that this analysis provides only a reference value, corresponding to the infection risk of the early SARS-CoV-2 variant.

The results indicate that, for both FSDV and HFD, the introduction of the hood extended $t_{5\%}$beyond 24 hours, suggesting that the infection risk for the doctor was kept sufficiently low. Conversely, for SFD and CD,

$t_{5\%}$ remained within four hours, implying that the infection risk was not negligible; however, at higher ventilation rates, the installation of the hood effectively reduced the infection risk.

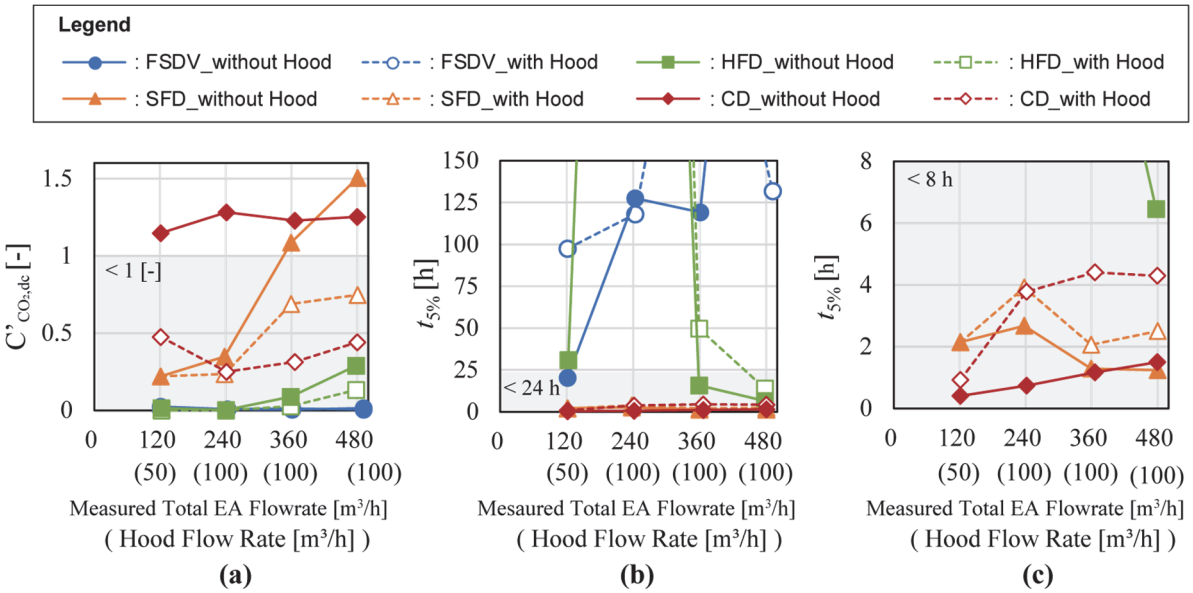


Figure 4-9. Normalized CO_2 concentration rise in front of the doctor's mouth and time required for the infection probability to reach 5%: (a) Normalized CO_2 concentration rise ($C'_{CO_2,dc}$) measured at the mouth position of the doctor (opponent person). (b) Time required for the infection probability of the doctor to reach 5% ($t_{5\%}$), calculated based on the $C'_{CO_2,dc}$. (c) Time required for the infection probability of the doctor to reach 5% ($t_{5\%}$), same data as (b), but with a different vertical axis scale (maximum 8 h instead of 150 h).

4.3.4 Summary of Key Findings

A comprehensive analysis of **Figures 4-7** to **4-9** provides several key insights into the combined effects of air distribution methods and local exhaust ventilation (LEV) on contaminant removal and infection control.

First, regarding the spatial distribution of the tracer gas, the results under the no-hood condition showed trends consistent with those observed in Chapter 3, where the exhaled human breath source was used. Even when exhalation velocity was applied to simulate breathing, the airflow and concentration distributions exhibited similar patterns to those in the exhaled human breath case. This confirms that the fundamental airflow characteristics of each ventilation system remained unchanged between the two scenarios.

When a local exhaust hood with a flow rate of 100 m³/h was installed directly above the patient's head, the contaminant plumes that previously extended above 1,500 mm in the FSDV and HFD cases were effec-

tively removed, thereby reducing the overall risk of airborne infection within the room. Removing exhaled air before it diffuses into the occupied zone is a universally beneficial strategy for minimizing exposure to any airborne infectious disease.

The capture efficiency of the hood (η) exceeded approximately 80% for the FSDV, HFD, and CD systems. At the lowest ventilation rate (120 m³/h, equivalent to 6 h^{-1}), all systems exhibited similar capture efficiencies around 80%. However, as the ventilation rate increased, a sharp decline in η (down to ~30%) was observed for SFD. This decrease can be attributed to the strong turbulent mixing generated by the numerous diffusers, which disturbed the flow between the exhalation source and the hood.

In HFD, SFD, and CD, the capture efficiency was inversely proportional to the ventilation rate, whereas in FSDV, η increased with the ventilation rate. This is because the FSDV system maintains a stable upward laminar flow that enhances the transport of contaminants toward the hood. Interestingly, HFD (a displacement-type system) and CD (a mixing-type system) showed comparable capture efficiencies despite their different airflow characteristics, while SFD—also a mixing system—exhibited the lowest efficiency. These results suggest that hood performance is strongly influenced by the local airflow structure near the source. Thus, the quantitative values presented here should be interpreted within the geometric constraints of the present setup. Nevertheless, the consistent proportional relationship between ventilation rate and capture efficiency observed in the FSDV case indicates that this combination is robust and can be effectively applied to other room configurations.

From the perspective of the doctor's exposure concentration ($C'_{CO_2,dc}$) and infection risk, a substantial reduction in $C'_{CO_2,dc}$ was observed for the CD and SFD cases at higher ventilation rates following hood installation, demonstrating the hood's effectiveness. Conversely, under low ventilation conditions (120 and 240 m³/h), HFD produced a quiescent airflow field, resulting in low exposure concentrations even without the hood. In the FSDV system, $C'_{CO_2,dc}$ remained close to zero across all ventilation rates, regardless of the presence of the hood, highlighting its superior contaminant removal capability.

The time for the infection risk to reach 5% ($t_{5\%}$) exceeded 100 hours for FSDV and 20 hours for HFD, while it remained below 4 hours for SFD and CD. Although these are indicative values based on the Wells–Riley model, they clearly show that FSDV can maintain an extremely low exposure risk within the breathing

zone (below 1,500 mm) even without a hood, and that the addition of a hood further minimizes the risk above this height (standing breathing level). As in Chapter 3, the proportional relationship between ventilation rate and infection risk reduction (or contaminant removal efficiency) was again confirmed as the most distinctive feature of FSDV.

Finally, even in environments dominated by turbulent mixing flows—such as SFD or CD—the installation of a relatively small 100 m³/h hood yielded measurable improvements in contaminant removal performance. This finding broadens the potential application of local exhaust systems, demonstrating their effectiveness as a supplementary infection control measure in various indoor environments such as clinics, consultation rooms, and medical examination spaces.

4.4 Conclusion

In this chapter, full-scale experiments were conducted for four different air distribution systems (FSDV, HFD, SFD, and CD) in combination with a local exhaust ventilation (LEV) hood. The systems were compared in terms of contaminant removal performance and infection risk reduction effectiveness.

The main findings of this chapter are summarized as follows:

Airflow characteristics and contaminant distribution

・Without the hood, similar airflow patterns to those observed in Chapter 3 were confirmed: CD and SFD produced mixed ventilation fields, whereas HFD and FSDV formed displacement-type airflow fields. When a hood with an exhaust rate of 100 m³/h was installed above the patient's head, contaminants that had previously accumulated above 1,500 mm were almost completely removed, particularly in the FSDV and HFD cases. As a result, the overall infection risk in the chamber was significantly reduced.

Relationship between hood capture efficiency and ventilation type

・The hood capture efficiency (η) exceeded approximately 80% for FSDV, HFD, and CD, whereas it decreased to around 30% for SFD at higher ventilation rates. In HFD, SFD, and CD, η exhibited an inverse rela-

tionship with ventilation rate, while in FSDV, η increased with airflow rate. This behavior is attributed to the stable upward piston flow formed in FSDV, where increased ventilation enhances the hood's capture performance. Consequently, the combination of FSDV and a hood demonstrated the most stable and efficient contaminant removal performance among all systems tested.

Evaluation of infection risk

・The normalized CO_2 concentration rise in front of the doctor's mouth ($C'_{CO_2,dc}$) and the calculated infection risk both showed that FSDV maintained nearly zero exposure levels across all ventilation rates, regardless of hood operation. The time required for the infection probability to reach 5% ($t_{5\%}$) exceeded 100 hours for FSDV and 20 hours for HFD, whereas it remained below 4 hours for SFD and CD. These results indicate that FSDV is highly effective even without a hood, and that the addition of a hood further minimizes the dispersion of exhaled air, maintaining extremely low infection risk even within the standing breathing zone (above 1,500 mm).

Design implications and further applications

・The results demonstrated that a local exhaust hood can provide meaningful infection risk reduction even at a relatively small airflow rate (100 m^3/h), regardless of the overall ventilation system. The combination of FSDV and a hood showed performance that improved with ventilation rate, confirming its suitability for high-cleanliness environments such as hospitals and cleanrooms. These findings serve as fundamental data for the integrated ventilation and local exhaust optimization model presented in the following chapter.

It should be noted that the infection risk estimations for SARS-CoV-2 presented in this study involve inherent uncertainties and should be interpreted as relative comparative indicators among different ventilation configurations rather than absolute predictions.

5 Experimental Investigation of LEV and Ventilation System Performance Using Tracer Gas and Simulated Saliva at High Ventilation Rates

5.1 Purpose of the Chapter

This chapter aims to experimentally verify the effectiveness of local exhaust ventilation (LEV) in reducing airborne infection risk during close-distance conversations. The previous CFD analysis presented in Chapter 2 demonstrated that installing a hood above the exhalation source can significantly reduce contaminant concentration under low ventilation conditions (6 ACH). However, experimental validation under controlled laboratory conditions is essential to confirm these findings and to explore the influence of surrounding airflow more precisely.

Full-scale experiments were conducted to examine the combined effects of LEV and different underfloor air distribution systems, including floor-supply displacement ventilation (FSDV), horizontal flow-type floor diffuser (HFD), and swirling flow-type floor diffuser (SFD). Both gaseous and particulate contaminants were released simultaneously to compare the dispersion characteristics of tracer gas (CO_2 + He) and artificial saliva particles. This dual-emission approach made it possible to assess infection risk more realistically by capturing the behavior of both droplets and droplet nuclei produced during human conversation, rather than relying on gas-only emissions as in Chapters 3 and 4.

An overview of the experimental configuration and key parameters is shown in **Figure 5-1**. Two representative indoor scenarios were considered: (1) a consulting room (Case A), where the infection source can be easily identified and the hood was positioned directly above the patient's head; and (2) a restaurant or meeting room (Case B), where the infection source is uncertain and the hood was installed between two occupants. In both scenarios, the ventilation system and hood flow rate were varied, as illustrated in **Figure 5-1**.

In all experiments, the overall ventilation rate of the chamber was fixed at 1,000 m^3/h (50 ACH), limited by the capacity of the air-handling unit. Although this rate exceeds the design range generally recommended

by REHVA and WHO (6–12 ACH), it enables an evaluation of hood performance under highly turbulent airflow conditions. The results presented in this chapter aim to enhance the understanding of LEV performance across different ventilation systems and to provide a practical basis for infection control in medical and semi-public indoor environments.

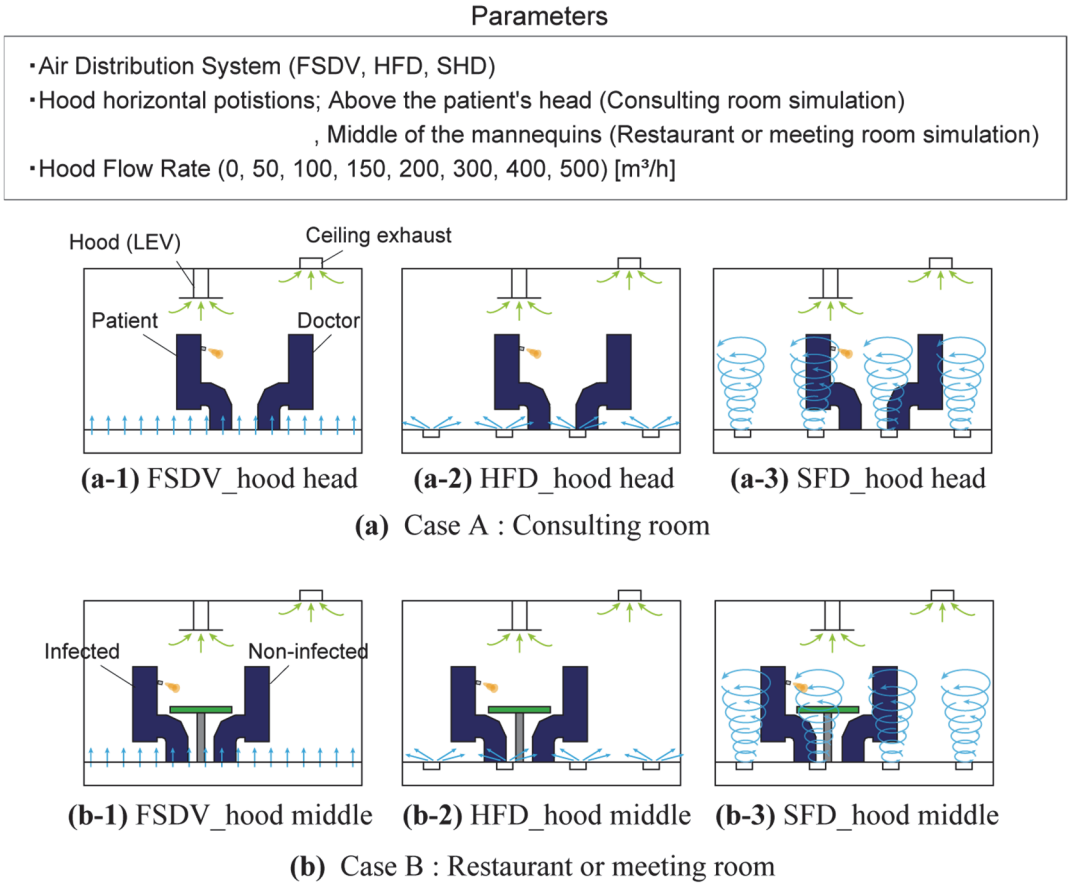


Figure 5-1. Schematic diagram of experimental parameters and test configurations. (a) Case A: Consulting room simulation, local exhaust ventilation (LEV) installed above the patient's head. (a-1) FSDV_hood head; (a-2) HFD_hood head; (a-3) SFD_hood head. (b) Case B: Restaurant or meeting room simulation, local exhaust ventilation (LEV) installed between two occupants. (b-1) FSDV_hood middle; (b-2) HFD_hood middle; (b-3) SFD_hood middle.

5.2 Methodology

5.2.1 Experimental Cases and Facilities

The full-scale experiments were conducted in a cleanroom-type test chamber owned by the University of Osaka between October 2021 and January 2022. The fundamental configuration of the facility was the same as that described in Chapters 3 and 4. A cross-sectional view of the experimental chamber is shown in **Figure 5-2a**, and an isometric view is presented in **Figure 5-2b**. The chamber dimensions were 2,400 mm (width) × 3,800 mm (depth) × 2,200 mm (height), and it included an underfloor plenum chamber through which HEPA-filtered outdoor air was supplied.

The total air supply rate was fixed at 1,000 m³/h (50 ACH), which was determined by the capacity of the outdoor air handling unit. Although this relatively high ventilation rate caused minor frictional noise as the air passed through the ducts, it did not interfere with natural conversation inside the chamber. The total exhaust airflow was set to 990 m³/h, extracted through both the local exhaust ventilation (LEV) hood and the ceiling exhaust outlets, thereby maintaining a slightly positive pressure in the room, consistent with cleanroom design principles.

Two thermal manikins were placed in the chamber to represent an infected and a non-infected person, each generating 75 W of sensible heat. The distance between their mouths was set at 1,200 mm to simulate a typical close-distance conversation. A flanged hood, previously identified as providing the highest capture efficiency under crosswind conditions [86], was employed as the LEV device (see **Figure 5-2c**).

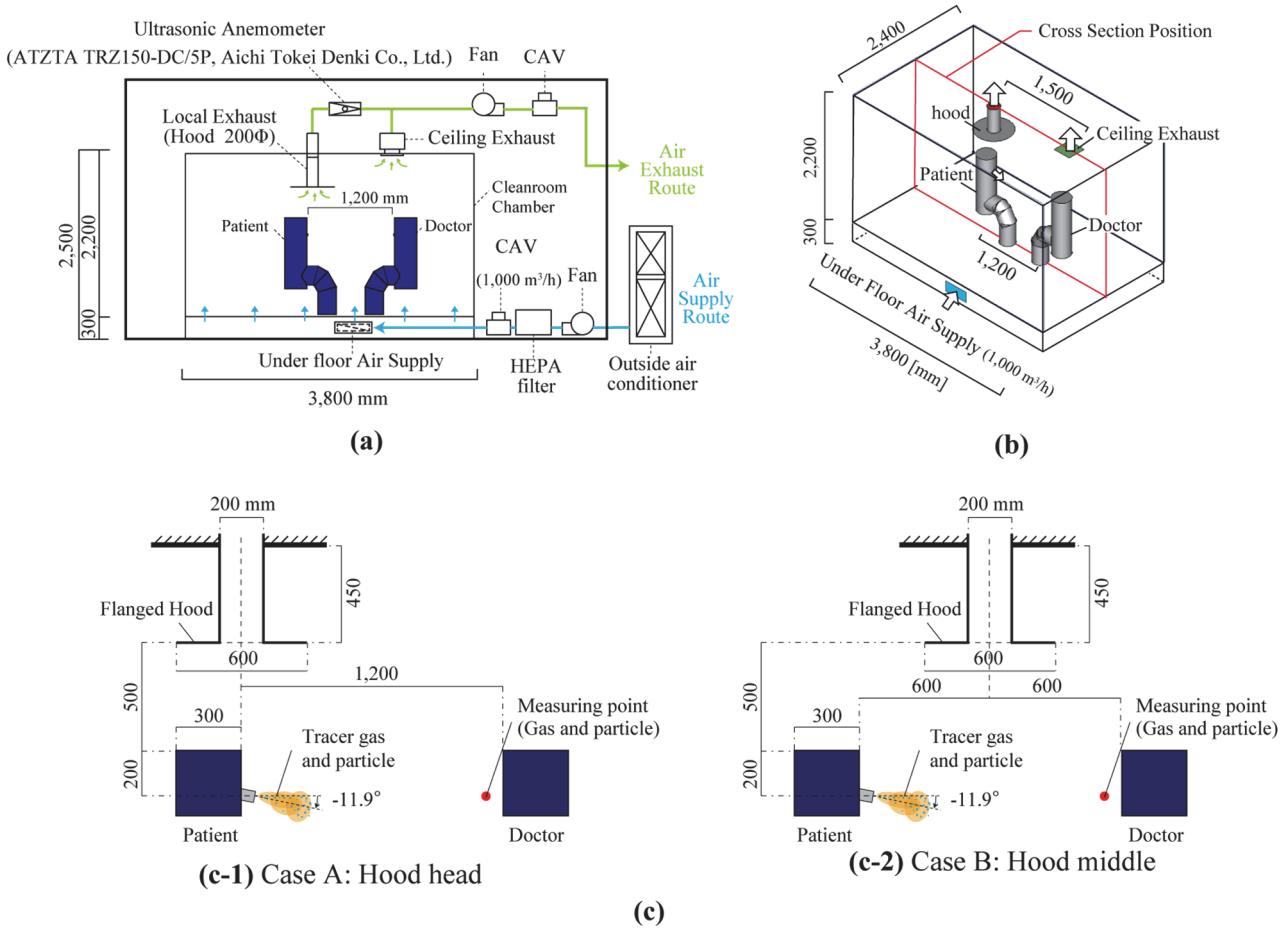


Figure 5-2. Full-scale experimental setup: (a) Cross-sectional view of the experimental chamber. (b) Isometric view of the cleanroom chamber. (c) Relationship between the emission source and the hood position. (c-1) Case A: Hood positioned above the patient's head. (c-2) Case B: Hood positioned at the midpoint between the two mannequins.

The experimental cases are summarized in **Table 5-1**. As described in the Section 5.1, the experiments were divided into two configurations: Case A, representing a consulting room, and Case B, representing a restaurant or meeting room, with the conceptual diagrams shown in **Figure 5-1**. In Case A, the hood was positioned directly above the patient's head, simulating a hospital consultation scenario. In Case B, the hood was installed at the midpoint between two mannequins to represent a situation where it is uncertain which person is infected, such as in a restaurant or meeting setting. A desk was also placed between the two mannequins to reproduce realistic indoor conditions. The spatial relationship between the emission source and the hood position is illustrated in **Figure 5-2c**. As shown in **Figure 5-1c-1**, the hood was expected to perform more effectively in Case A, where the distance between the emission source and the hood was smaller.

In each case, three types of underfloor air distribution systems were tested: floor-supply displacement

ventilation (FSDV), horizontal flow-type floor diffuser (HFD), and swirling flow-type floor diffuser (SFD). The configurations of each system are shown in **Figure 5-3**. In the FSDV system, air was uniformly supplied through a permeable carpet covering the entire floor area, whereas in the HFD and SFD systems, air was delivered through multiple diffusers. The HFD and SFD units were identical to those used in Chapters 3 and 4. According to the manufacturer's catalog, the airflow spread angle for the HFD is approximately 10–15° from the floor, while that of the SFD is approximately ±10–15° from the vertical, as described in **Figure 3-4** of Chapter 3. The air supply volume per diffuser was adjusted to remain within the standard operational range specified by the manufacturer.

As noted in Section 5.1, the FSDV was used to evaluate the fundamental capture performance of the hood under laminar flow conditions, whereas the HFD and SFD were employed to assess the effectiveness of the hood under more turbulent airflow environments. To further investigate the influence of exhaust conditions, the hood's exhaust flow rate was varied at 0, 50, 100, 150, 200, 300, 400, and 500 m^3/h for each floor air distribution system. A total of 48 experimental cases were conducted, as summarized in **Table 5-1**.

Table 5-1.
Summarization of experimental cases.

Groupe	Considered situations	Case name	Air distribution system	Hood horizontal potistions	Hood exhaust flow rate [m^3/h]
Case A	Consulting room	FSDV_hood head	FSDV	Above the patient's head	0,50,100,150,200,300,400,500
		HFD_hood head	HFD		0,50,100,150,200,300,400,500
		SFD_hood head	SFD		0,50,100,150,200,300,400,500
Case B	Restaurant or meeting room	FSDV_hood middle	FSDV	Middle of the mannequins	0,50,100,150,200,300,400,500
		HFD_hood middle	HFD		0,50,100,150,200,300,400,500
		SFD_hood middle	SFD		0,50,100,150,200,300,400,500

Abbreviation: FSDV: Floor-supply displacement ventilation; HFD: Horizontal flow-type floor diffuser;
SFD: Swirling flow-type floor diffuser.

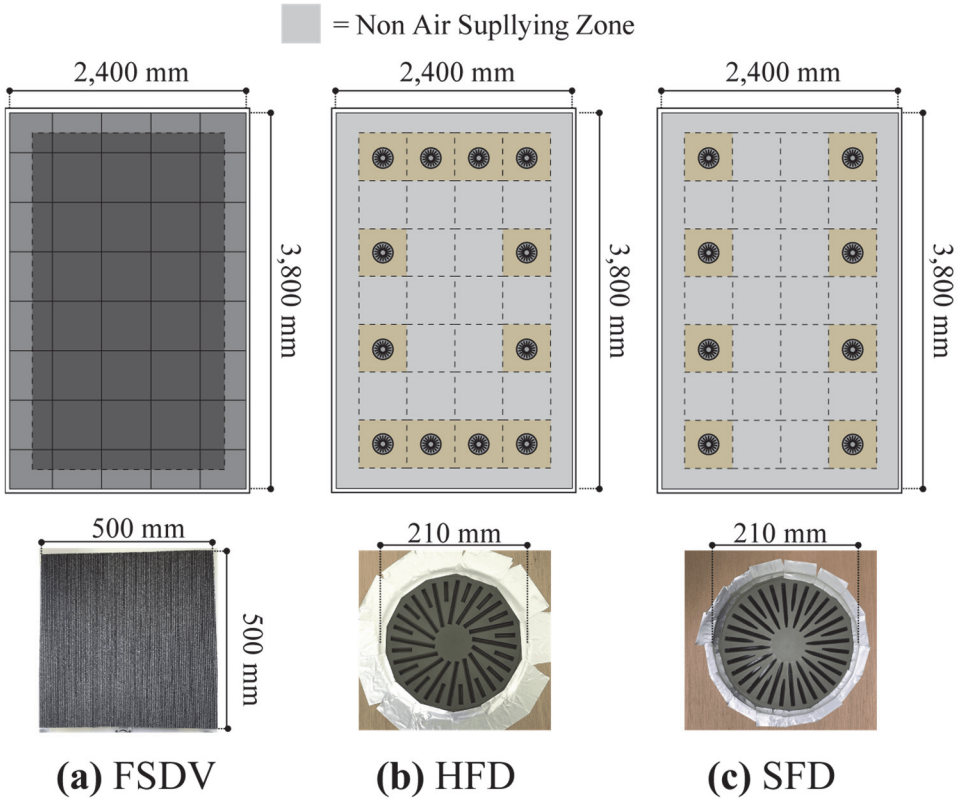


Figure 5-3. Floor layouts and diffuser details for each underfloor air distribution system: (a) Floor-supply displacement ventilation (FSDV). (b) Horizontal flow-type floor diffuser (HFD). (c) Swirling flow-type floor diffuser (SFD).

5.2.2 Conditions of Exhalation Generation

The exhaled breath of an infected person was simulated by simultaneously releasing CO_2 tracer gas and artificial saliva particles using an ultrasonic nebulizer. A schematic diagram of the exhalation generation system is shown in **Figure 5-4**. CO_2 and helium gases were mixed at a volumetric ratio of 5:3 (CO_2:He = 3.26:1.95 L/min) to achieve an overall gas density approximately equal to that of air. The gas mixture was released at the height corresponding to the infected person's mouth (1,100 mm above the floor) together with atomized artificial saliva particles.

The viscosity of the artificial saliva was adjusted following the method proposed by Ogata et al. [87], by dissolving 12 g of sodium chloride and 76 g of glycerin in 1 L of distilled water. The atomization process of the ultrasonic nebulizer (SHIN-EI INDUSTRIES, Inc., Comfort 3000 KU-500) is illustrated in **Figure 5-4b**. Particles were generated by ultrasonic vibration, driven by the mixed gas stream, and emitted through a nozzle. As this nebulizer was originally developed for medical applications rather than laboratory experiments, the

particle size distribution and number concentration were separately measured and are reported in **Appendix 5-A**.

The exhaled volume, mean exhalation velocity, and exhalation angle during conversation were derived from the authors' previous study (Chapter 2) [88] and set to 5.21 L/min, 0.30 m/s, and 11.9° downward from the horizontal, respectively. In that study, six Asian participants (three males and three females, aged 21–24, mean age 22.5) read a Japanese text aloud for one minute while their exhaled airflow velocity and vector were measured using an ultrasonic anemometer (Sonic Corporation, Model DA-700 with TR-92T 30 mm probe). The total exhaled volume was measured with a PET collection bag and quantified using a dry gas meter (SI-NAGAWA).

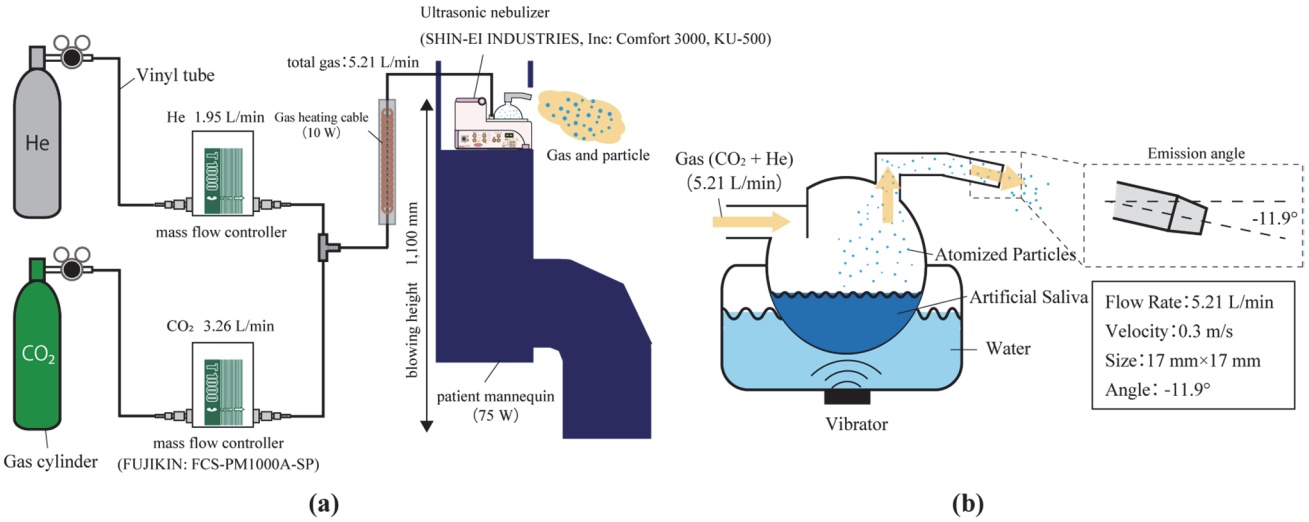


Figure 5-4. Experimental setup for simultaneous tracer gas and particle generation: (a) System configuration for CO_2 and He gas mixing with artificial saliva atomization. (b) Particle generation mechanism of the ultrasonic nebulizer (*SHIN-EI INDUSTRIES, Inc., Comfort 3000 KU-500*).

5.2.3 Measurement Points and Experimental Procedures

Following the emission of tracer gas and particles, the steady-state spatial distribution of CO_2 concentration and the particle number concentration in front of the doctor's mouth were measured. The measurement setup and locations are illustrated in **Figure 5-5**.

The CO_2 concentration was monitored using six CO_2 recorders (*RTR-576*, T&D Corporation) mounted on five vertical poles positioned along the Pa–Pe line, as shown in **Figure 5-5a–c**. The CO_2 concentration in front

of the doctor's mouth was also measured using the same type of recorder. In addition, the particle number concentration at the same location was obtained with a handheld particle counter (*Model 3888*, KANOMAX), as shown in **Figure 5-5c–d**.

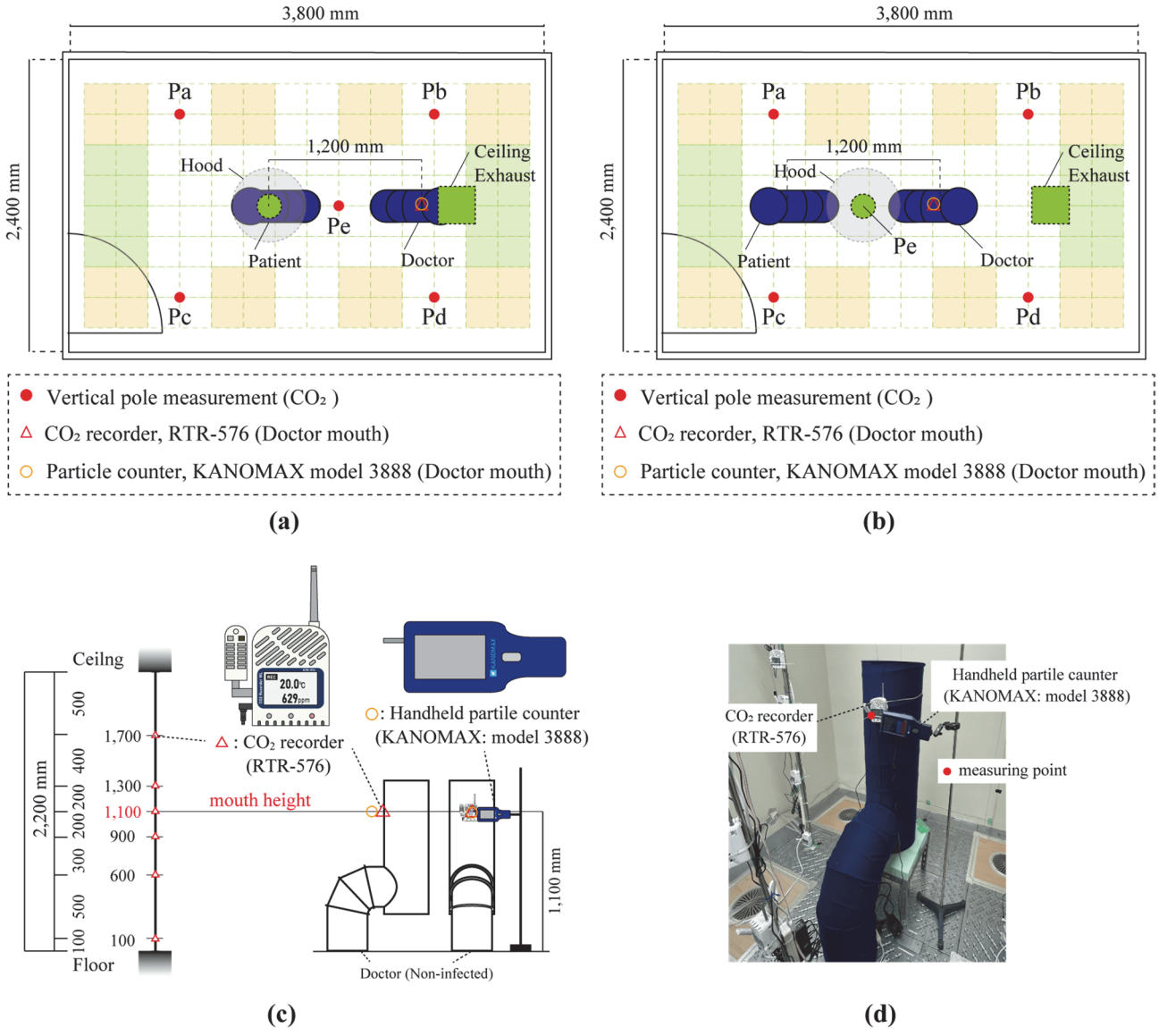


Figure 5-5. Measurement locations for CO_2 concentration and particle number concentration. (a) Plan view of Case A: hood above the patient's head. (b) Plan view of Case B: hood positioned between the mannequins. (c) Vertical pole measurement points and measurement setup at the doctor's mouth. (d) Photograph of the CO_2 and particle measurement instruments (RTR-576, T&D Corporation; handheld particle counter Model 3888, KANOMAX).

These measured values were subsequently used to calculate the quanta concentration in front of the doctor's mouth, $C_{q,dc}$ [quanta/m³], using Eqs. (5-5) and (5-8), as described in Section 5.2.5. Because of the limited number of instruments available, the spatial distribution and the local concentration in front of the doctor's mouth were measured for CO_2, whereas for particles, only the concentration in front of the doctor's mouth was recorded.

The experimental procedure is illustrated in **Figure 5-6**. The mass reduction of artificial saliva was measured before and after each experiment using an electronic balance (GX-8K, A&D Company, Ltd.) to determine the particle-based quanta concentration in front of the doctor's mouth. The calculation was performed using Eqs. (5-5) and (5-8), where M_{ab} and M_{aa} represent the saliva mass after and before the experiment, respectively.

All experiments were conducted at an air supply rate of 1,000 m³/h (50 ACH). Under these conditions, the flow field reached a steady state approximately five minutes after the start of emission. Measurements were then taken for 15 minutes under steady-state conditions. The time-averaged CO_2 concentration and particle number concentration obtained during this period were used to calculate the hood capture efficiency, the normalized CO_2 concentration, and the quanta concentration in front of the doctor's mouth, as described in Section 5.2.5. The same experimental schedule and measurement protocol were applied consistently across all 48 test cases.

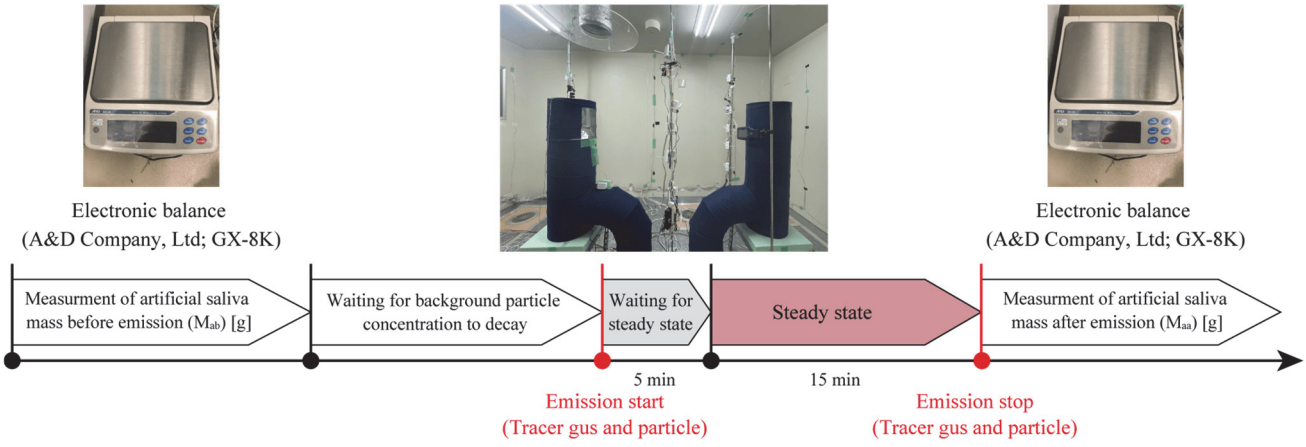


Fig. 5-6. Experimental procedure for tracer gas and particle emission tests.

5.2.4 Normalization of Tracer Gas Concentration

As described in Chapters 3 and 4, the normalized concentration rise (C'_{CO_2}) was used to evaluate the spatial distribution of the tracer gas within the test chamber. This index allows quantitative comparison of the contaminant dispersion characteristics under different air distribution systems and with or without the local exhaust ventilation (LEV) system. The normalized concentration rise expresses the relative increase in CO_2 concentration at a given location with respect to the flow-weighted exhaust concentration. the calculation method and governing equation are identical to those presented in Eq. (4-1) in Section 4.2.4.

5.2.5 Hood Capture Performance Assessment in Experiment

As described in Chapter 4, the hood capture efficiency (η) was used to evaluate the performance of the local exhaust ventilation (LEV) system. This parameter represents the proportion of tracer gas captured by the hood relative to the total amount generated within the chamber and serves as a direct indicator of the hood's ability to collect contaminants released from the source. The calculation procedure and governing equation are identical to those presented in Eq. (4-2) in Section 4.2.5.

5.2.6 Infection Risk Assessment from Particles in Experiment

As described in Section 2.3.4, the airborne infection risk during close-distance conversation was evaluated using the Wells–Riley model, incorporating the localized quanta concentration distribution derived from CFD analysis (Eqs. (2-9)–(2-10)). In this chapter, the same conceptual framework (Eq. (2-13)) was applied to estimate the total number of quanta inhaled by the non-infected person (doctor). The infection risk calculated from the tracer gas measurements was obtained using the same procedure described in Section 4.2.6, based on Eqs. (4-5) and (4-6). To ensure consistency with previous analyses, the same quanta emission rate $q = 42$ [quanta/h] and breathing rate of the doctor $Q_{dc} = 5.21$ L/min were adopted as in Chapters 2 and 4.

In this chapter, a similar approach was extended to evaluate infection risk based on particle concentration, allowing a direct comparison between gas (representing droplet nuclei) and particle (representing droplets) transmission mechanisms.

Two assumptions were made when calculating the risk of infection from particles:

(1) Although the viral density per particle may change after evaporation, the total number of viruses remains constant.

(2) The viral density during the evaporation process is assumed to be independent of particle size.

The quanta concentration in front of the doctor's mouth derived from particle concentration, $C_{q,dc}$ [quanta/m³], was calculated using Eq. (5-1):

$$C_{q,dc} = \frac{q}{Q_{pc}} \cdot \frac{V_{dp}}{V_{ep}} \quad (5-1)$$

where Q_{pc} is the sampling flow rate of the particle counter (2.81 L/min) [m³/h], V_{dp} is the total volume of particles detected in front of the doctor's mouth divided by the measurement time (15 minutes) [m³/h], and V_{ep} is the total generated particle volume divided by the emission duration (20 minutes) [m³/h]. The emission and measurement times differ by five minutes, accounting for the period required to reach steady-state conditions (see **Figure 5-6**).

The total emitted particle volume, V_{ep}, was obtained using Eq. (5-2), which incorporates the mass difference of artificial saliva solution in the nebulizer generator chamber measured before and after emission:

$$V_{ep} = \frac{(M_{ab} - M_{aa}) \cdot R_c}{\rho_{aa}} \quad (5-2)$$

The density of artificial saliva after evaporation, ρ_{aa}, was defined by Eq. (5-3):

$$\rho_{aa} = \rho_{ab} \cdot R_c / R_d^3 \quad (5-3)$$

Substituting Eq. (5-3) into Eq. (5-2) yields Eq. (5-4):

$$V_{ep} = \frac{(M_{ab} - M_{aa}) \cdot R_d^3}{\rho_{ab}} \quad (5-4)$$

where M_{ab} and M_{aa} are the masses of artificial saliva before and after emission [g], respectively, R_c is the compositional ratio of artificial saliva after evaporation to that before evaporation [-], ρ_{ab} is the pre-evaporation density of artificial saliva (1.09 g/m³), and R_d is the particle diameter ratio after evaporation to before evaporation [-]. The values of M_{ab} and M_{aa} were measured using an electronic mass balance (GX-8K, A&D Company, Ltd.) as illustrated in **Figure 5-6**.

The parameter R_d was estimated by comparing the quanta concentrations derived from gas and particle results, as discussed in Section 5.3.2.

Finally, the time required for the doctor's infection risk to reach 5% ($t_{5\%}$) was calculated using both gas-based and particle-based quanta concentrations according to Eq. (4-5) in Section 4.2.6, and therefore, the detailed calculation procedure is not repeated here.

5.3 Results

5.3.1 Results from CO_2 Gas Concentration Measurements

Figure 5-7 shows the vertical distributions of normalized CO_2 concentrations (C'_{CO_2}), calculated with respect to the flow-weighted average concentrations of the two exhaust outlets, for all 48 experimental cases. **Figures 5-7a–c** present the averaged results for measurement points Pa–Pd in Case A, where the hood was positioned above the patient's head, for each hood exhaust flow rate. Measurements at Pe, located between the two mannequins, were evaluated separately and are shown in **Figures 5-7g–l**.

In the FSDV condition, even without hood operation (Q_h = 0 m³/h, black line), the normalized CO_2 concentration remained low (**Figure 5-7a**). This result indicates that the FSDV system could effectively remove exhaled air without assistance from the hood, owing to the high overall ventilation rate of 1,000 m³/h (50 ACH). Under the HFD condition, a displacement-type airflow pattern was observed, and the normalized concentration decreased as the hood exhaust flow rate increased (**Figure 5-7b**). In contrast, under the SFD condition, where the airflow field was more mixed, the normalized concentration approached unity; however, it still showed a gradual decrease with increasing hood flow rate (**Figure 5-7c**).

Figures 5-7d–f show the average CO_2 normalized concentrations (Pa–Pd) for Case B, where the hood was located at the midpoint between two occupants. Compared with Case A (**Figures 5-7a–c**), increasing the hood exhaust flow rate did not produce a substantial decrease in normalized concentration.

Figures 5-7g–l illustrate the CO_2 normalized concentrations at Pe, located between the mannequins. The results under HFD (**Figures 5-7h** and **5-7k**) and SFD (**Figures 5-7i** and **5-7l**) conditions differed noticeably from those for Pa–Pd. Under HFD (**Figures 5-7h** and **5-7k**), the diffusion of CO_2 between the mannequins was suppressed as the hood exhaust flow rate increased, suggesting localized capture near the source. In contrast, under SFD conditions (**Figures 5-7i** and **5-7l**), higher concentrations were observed near a height of ap-

proximately 500 mm, indicating that recirculating upward vortices transported exhaled air back into the breathing zone.

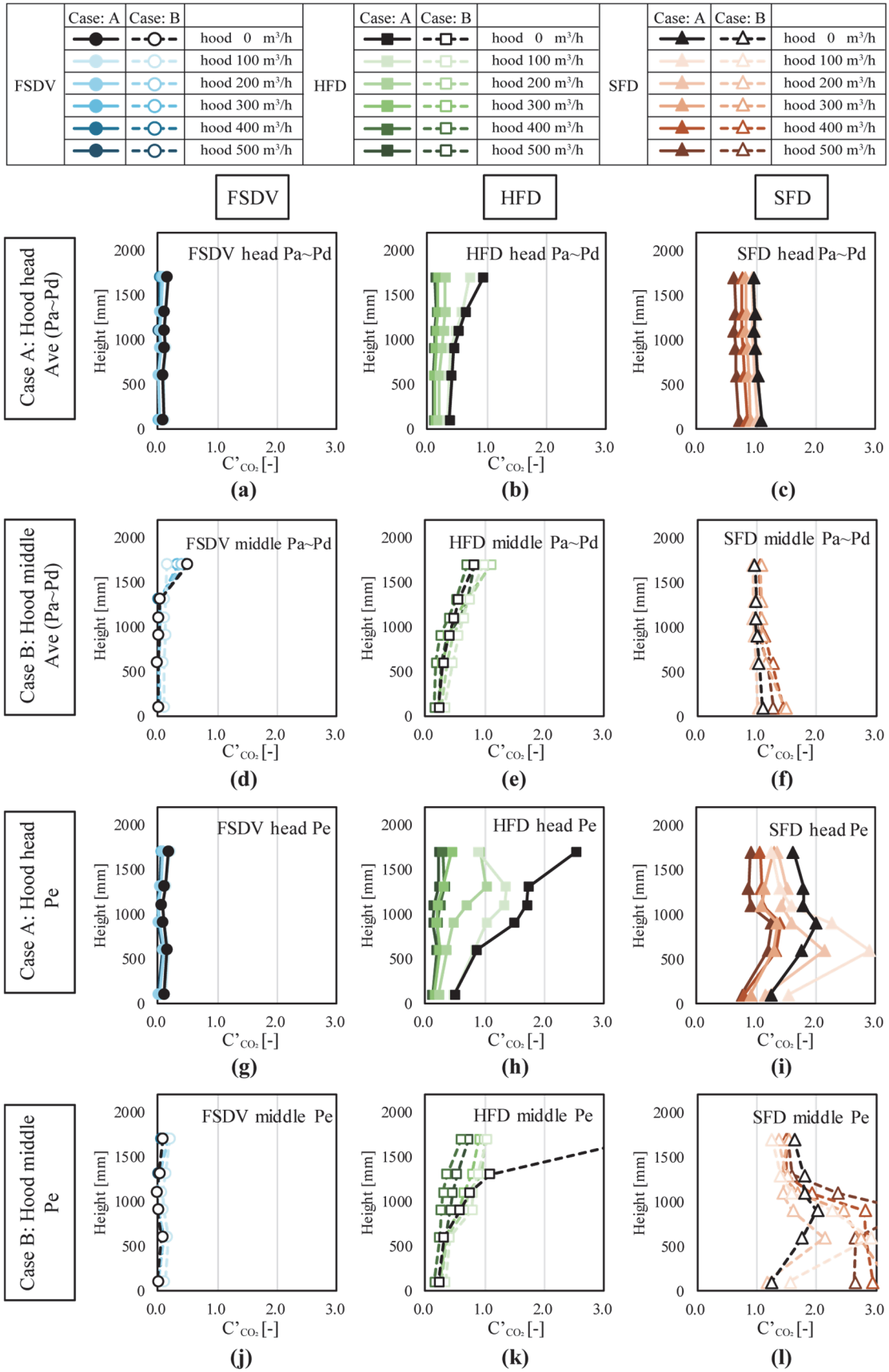


Figure 5-7. Vertical distributions of normalized CO_2 concentration (C'_{CO_2}) under different ventilation systems and hood flow rates. (a–c) Case A: Hood above the patient's head (Pa–Pd average). (a) FSDV. (b) HFD. (c)

SFD. (d–f) Case B: Hood in the middle of two occupants (Pa–Pd average). (d) FSDV. (e) HFD. (f) SFD. (g–i) Case A: CO_2 concentration at Pe (centerline). (g) FSDV. (h) HFD. (i) SFD. (j–l) Case B: CO_2 concentration at Pe (centerline). (j) FSDV. (k) HFD. (l) SFD.

Figure 5-8a presents the hood capture efficiencies (η) for tracer gas in Cases A and B, calculated from CO_2 concentration data using Eq. (4-2). A notable difference in η was observed between the two cases under the FSDV condition. In Case A, where the hood was positioned above the patient's head, η increased sharply with the hood exhaust flow rate and exceeded 90% at $Q_h \geq 300$ m³/h. In contrast, in Case B, where the hood was located between the mannequins, η remained relatively low. Nevertheless, as shown in **Figure 5-8b**, the quanta concentration in front of the doctor's mouth ($C_{q,dc}$) was sufficiently low even in Case B, indicating that the high overall ventilation rate (50 ACH) effectively diluted the contaminants.

Under the HFD condition, η in Case A showed a trend similar to that of the FSDV and reached comparable levels at higher hood exhaust flow rates (**Figure 5-8a**). In this case, $C_{q,dc}$ decreased steadily as Q_h increased, demonstrating the hood's strong local capture performance (**Figure 5-8b**). However, in Case B, the decrease in $C_{q,dc}$ with increasing Q_h was less pronounced, suggesting that lateral airflow from the diffusers disturbed the upward transport of exhaled air toward the hood.

In the SFD condition, η exhibited little difference between Cases A and B (**Figure 5-8a**), implying that only a small fraction of the exhaled air was directly captured by the hood. Instead, most of the tracer gas appeared to mix throughout the room before being exhausted through both the hood and the ceiling outlets. The $C_{q,dc}$ trend for the SFD case (**Figure 5-8b**) was generally consistent with that of the HFD: in Case A, the implementation of the hood effectively reduced the quanta concentration near the breathing zone, whereas in Case B, the influence of ambient swirling airflow was dominant, diminishing the direct capture performance.

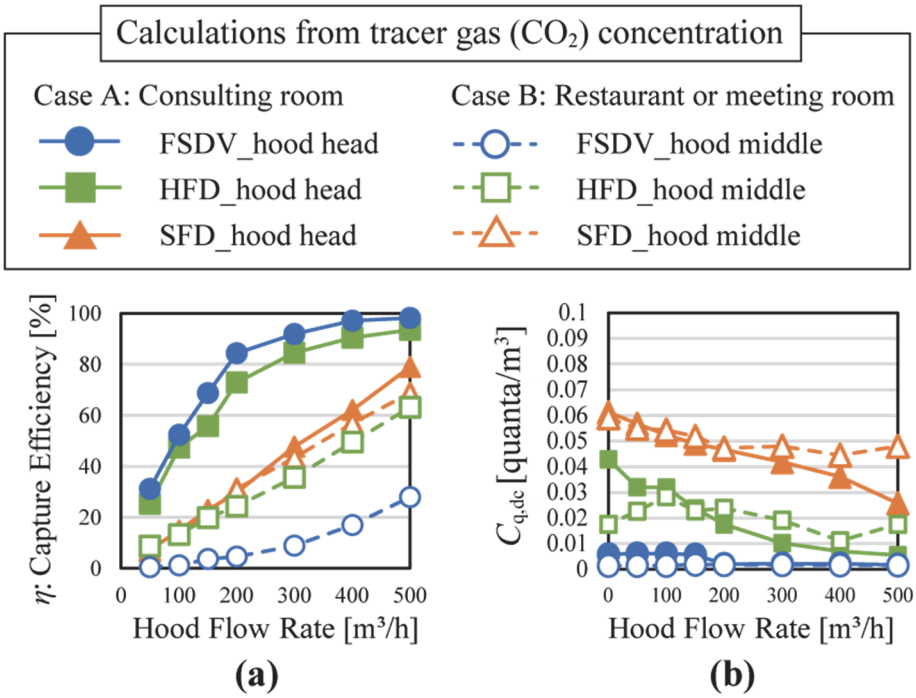


Figure 5-8. Relationship between hood exhaust flow rate and (a) hood capture efficiency η and (b) quanta concentration in front of the doctor's mouth $C_{q,dc}$ for each ventilation system (calculation results obtained from tracer gas (CO_2) concentration).

5.3.2 Results from Artificial Saliva Particles

As described in Section 5.2.6, the quanta concentration in front of the doctor's mouth ($C_{q,dc}$) derived from particles was calculated using Eqs. (5-1) to (5-4). The total volume of generated artificial saliva was determined by measuring the mass reduction before and after emission with an electronic mass balance (GX-8K, A&D Company, Ltd.), as illustrated in **Figure 5-6**. In this calculation, the density correction factor, R_d, representing the ratio of particle diameter after evaporation to that before evaporation, must be appropriately assumed.

Previous studies by Yang et al. [89], based on experimental results by Tang et al. [90] and Bagger et al. [91], reported that the final droplet size becomes approximately 0.39–0.50 times smaller at relative humidities between 10% and 90%. Although the composition of the droplets in those studies differed from that of the artificial saliva used in the present experiment, this range was adopted as a reference for selecting R_d. Accordingly, $C_{q,dc}$ was computed for R_d = 1.0, 0.50, 0.45, and 0.40, as shown in **Figure 5-9**.

Figure 5-9a compares the results obtained from gas and particles for the SFD case under different assumptions of R_d. As Rd decreased, the total generated particle volume (V_{ep}) in Eq. (5-1) decreased, resulting in

higher calculated $C_{q,dc}$ values. When R_d = 1.0, the $C_{q,dc}$ derived from particles was substantially smaller than that derived from CO_2. However, for R_d = 0.5, the two results agreed well. Further decreasing R_d to 0.45 or 0.40 caused the $C_{q,dc}$ values from particles to exceed those from CO_2. Considering particle adhesion to surfaces and gravitational settling, the actual number of particles reaching the doctor's mouth should be smaller than that of gas molecules. Therefore, R_d = 0.5 was deemed an appropriate representative value for subsequent analysis.

Under the HFD condition (**Figure 5-9b**), the calculated $C_{q,dc}$ values for R_d = 0.5 were consistent with those from the tracer gas when the hood exhaust flow rate exceeded 200 m³/h. However, at lower hood flow rates (50–150 m³/h), $C_{q,dc}$ values obtained from particles were lower than those from the gas, indicating that particle settling and local recirculation influenced the concentration near the breathing zone.

In the FSDV case (**Figure 5-9c-d**), when R_d = 0.5, the $C_{q,dc}$ values derived from both gas and particles were already small under this highly ventilated condition (50 ACH), and the comparison on a linear scale appeared to match well (**Figure 5-9c**). However, when examined on a logarithmic scale (**Figure 5-9d**), a difference of approximately 10^{-2} to 10^{-9} in magnitude was observed, demonstrating that even under strong dilution, the particle-based estimates exhibited slightly larger residual concentrations compared to those based on the tracer gas.

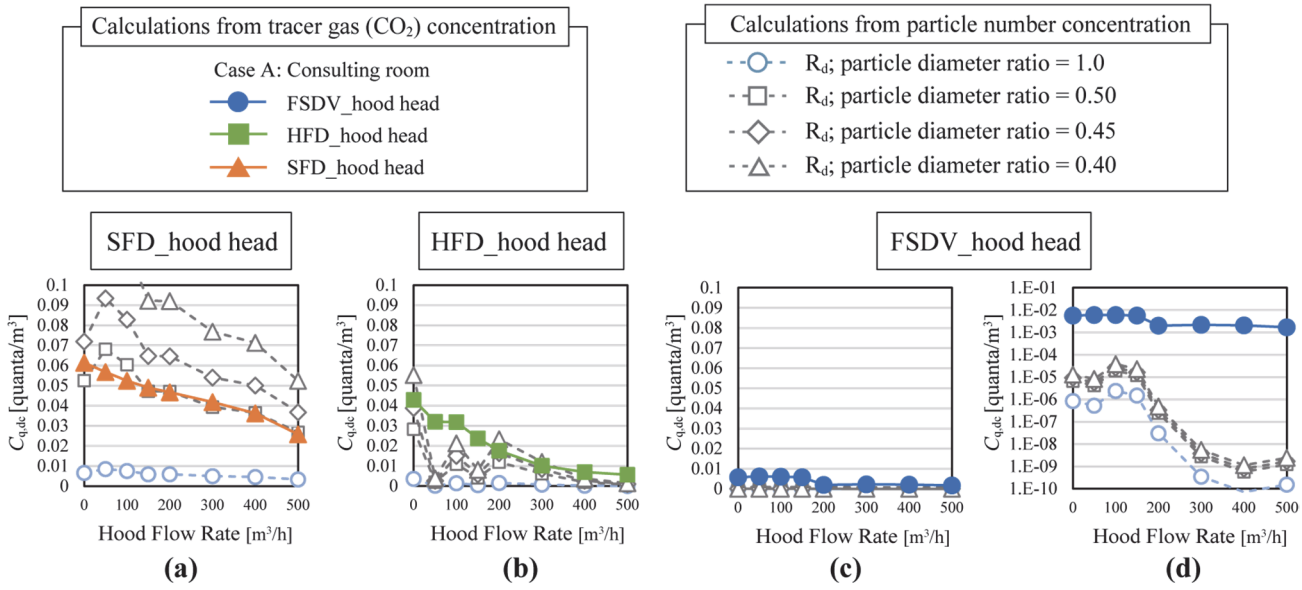


Figure 5-9. Comparison of $C_{q,dc}$ (quanta concentration in front of the doctor's mouth) calculated from tracer gas concentration and from the particle number concentration of artificial saliva, with varying particle diameter ratio after evaporation to before evaporation (R_d = 1.0–0.4). (a) SFD_hood head. (b) HFD_hood head. (c) FSDV_hood head (linear vertical axis). (d) FSDV_hood head (logarithmic vertical axis)

Figure 5-10 presents the results of $C_{q,dc}$ calculated from the quanta concentration in front of the doctor's mouth, estimated using artificial saliva particles with a particle diameter ratio of R_d = 0.5. Although the order of magnitude of $C_{q,dc}$ was comparable to or slightly smaller than that obtained from the CO_2 tracer gas, the overall trend was consistent. The risk of airborne infection followed the order FSDV < HFD < SFD, corresponding to the increasing degree of airflow turbulence among the ventilation systems.

In Case A (consulting room), the hood effectively reduced the concentration in front of the doctor's mouth as the hood exhaust flow rate increased, as shown in **Figure 5-10b**. In contrast, when the hood was positioned between the mannequins (Case B, representing a restaurant or meeting room), the influence of the hood was limited. The hood exhaust flow rate and $C_{q,dc}$ did not exhibit a clear linear relationship, indicating that in such configurations, the surrounding airflow had a dominant effect on the dispersion of exhaled particles rather than the direct suction performance of the hood.

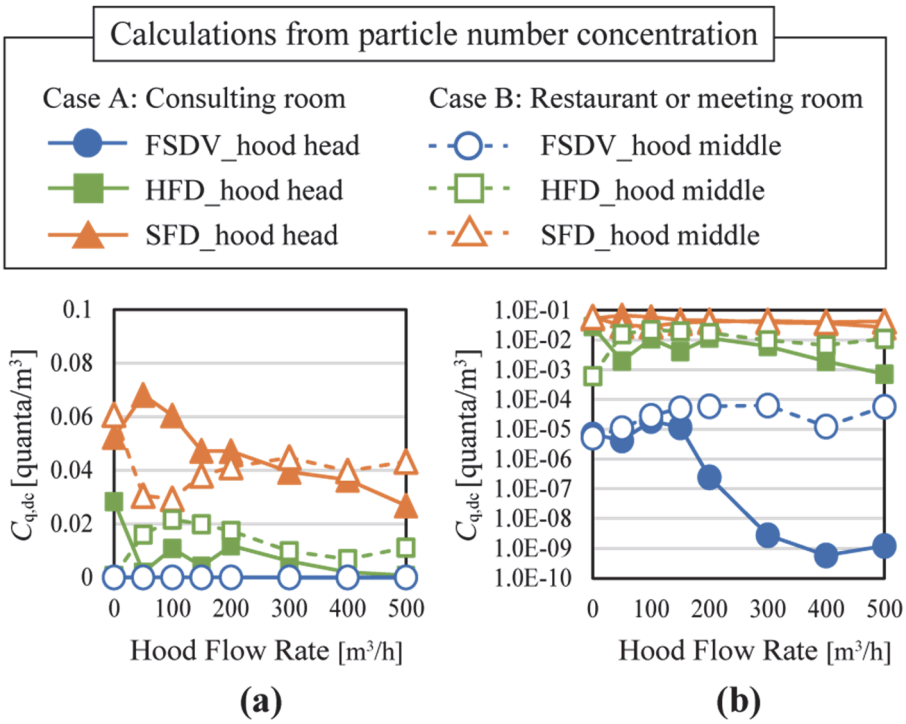


Figure 5-10. Calculation results of $C_{q,dc}$ (quanta concentration in front of the doctor's mouth) obtained from particle number concentration (R_d = 0.5). (a) $C_{q,dc}$ plotted with a linear vertical axis. (b)$C_{q,dc}$ plotted with a logarithmic vertical axis.

5.3.3 Infection Probability Estimated from Tracer Gas and Particle Concentrations

The preceding sections discussed the relationship between the local exhaust ventilation (LEV) system, exhaled airflow diffusion, and the resulting quanta concentration at the breathing zone of non-infected individuals. In this section, the infection probability for the early variants of SARS-CoV-2 is estimated using Eq. (4-7), and the effectiveness and safety of the present ventilation configurations against airborne transmission are evaluated.

Figure 5-11 illustrates the calculated results of $t_{5\%}$—the time required for the doctor's infection probability to reach 5%—derived from CO_2 tracer gas concentrations using Eq. (4-7). This estimation corresponds to infection risks associated with the initial variants of SARS-CoV-2, assuming a quanta emission rate of 42 quanta/h during conversation, as discussed in Section 5.2.6. In the FSDV, $t_{5\%}$ consistently exceeded 24 hours, indicating a sufficiently low risk of airborne infection. In the HFD, $t_{5\%}$ exceeded 8 hours when the hood exhaust flow rate was above 200 m³/h, suggesting that the risk remained low within typical working-hour durations. In contrast, under SFD conditions, $t_{5\%}$ frequently remained below 8 hours, implying that this system cannot ensure adequate protection against infection.

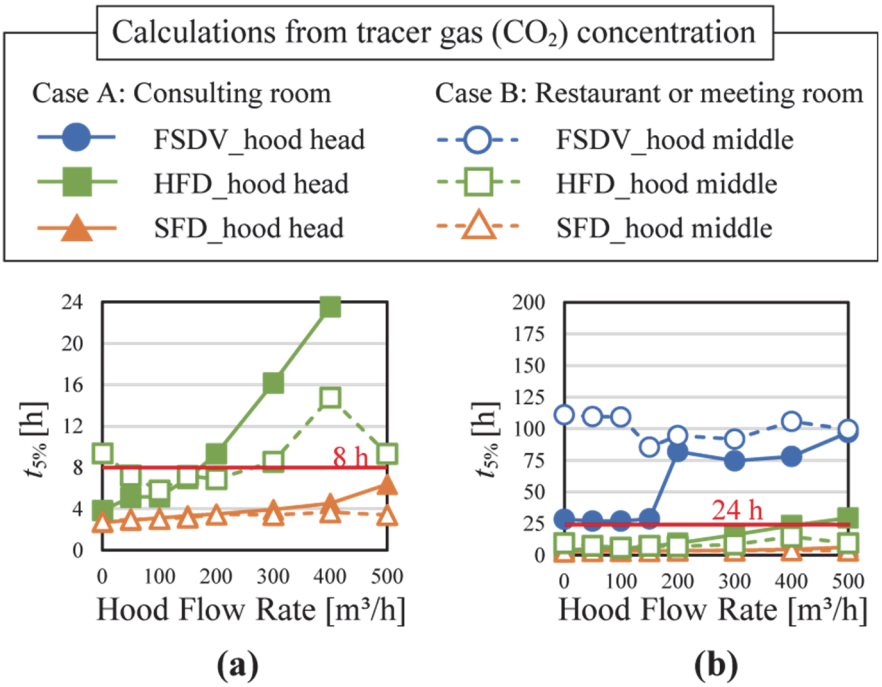


Figure 5-11. Calculation results of $t_{5\%}$, representing the time required for the doctor's infection probability to reach 5%, obtained from the tracer gas (CO_2) analysis: (a) $t_{5\%}$ plotted with a maximum vertical axis value of

24 h. (b) $t_{5\%}$ plotted with a maximum vertical axis value of 200 h.

Figure 5-12 presents $t_{5\%}$ calculated from the quanta concentration based on artificial saliva particle measurements (R_d = 0.5). The results in **Figure 5-12** were generally consistent with those obtained from tracer gas in **Figure 5-11**, demonstrating that the FSDV maintained sufficiently low infection risk even without hood operation. In the HFD, implementing LEV effectively prolonged $t_{5\%}$ beyond 8 hours, while in the SFD, $t_{5\%}$ remained below 8 hours even with hoods installed, indicating a non-negligible residual infection risk under such turbulent airflow conditions.

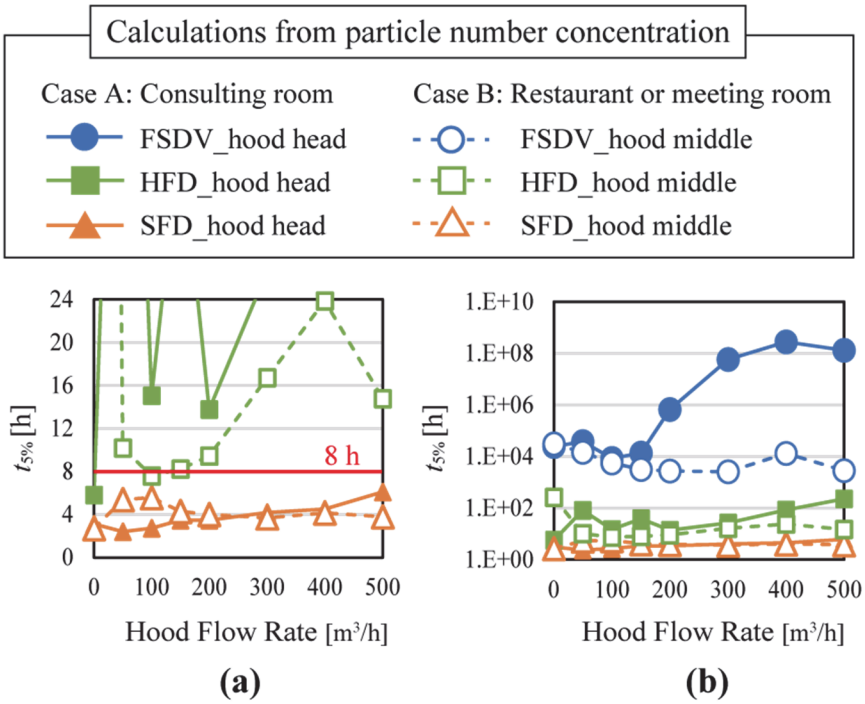


Figure 5-12. Calculation results of $t_{5\%}$, representing the time required for the doctor's infection probability to reach 5%, calculated from artificial saliva particle concentration (R_d = 0.5): (a) $t_{5\%}$ plotted with a linear vertical axis. (b) $t_{5\%}$ plotted with a logarithmic vertical axis.

5.4 Discussion

5.4.1 Summary of Key Findings

The results presented in Section 5.3 include the spatial distribution of the normalized CO_2 concentration (**Figure 5-8**), the tracer gas capture efficiency η, and the quanta concentration in front of the non-infected person's mouth ($C_{q,dc}$) calculated from CO_2 concentration (**Figure 5-9**). The corresponding results derived from artificial saliva particles are shown in **Figures 5-10** and **5-11**.

Findings from the CO_2 tracer gas results (**Figures 5-8** and **5-9**):

・The FSDV effectively exhausted the exhaled air from the infected individual without widespread diffusion, regardless of the hood flow rate.

・In the HFD, although horizontal airflow promoted a greater spread of exhaled air compared with the FSDV, increasing the hood flow rate successfully reduced the normalized CO_2 concentration to nearly zero throughout the room.

・In the SFD, the exhaled air dispersed widely due to the swirling airflow, and increasing the hood flow rate had only a minor effect on the concentration near the doctor's mouth.

・Under both the HFD and SFD conditions, the CO_2 concentration distribution between the inter-mannequin space and the overall room differed significantly. In the SFD, downward airflow between the mannequins was also suggested.

Findings from the artificial saliva particle results (**Figures 5-10** and **5-11**):

・In environments with calmer airflow, particle deposition became more pronounced, leading to smaller $C_{q,dc}$ values for particles than for CO_2 gas.

・Since CO_2-based estimation consistently yielded higher infection risk values than particle-based estimation, the tracer gas approach can be considered a conservative method for assessing airborne infection risk.

Common findings for both tracer gas and particle results:

・The performance of local exhaust hoods was strongly affected by the surrounding airflow conditions. Ventilation systems capable of maintaining a stable, upward displacement airflow—such as FSDV—are therefore optimal for effective hood operation.

・When the hood was positioned above the infector's head (Case A), it effectively reduced the quanta concentration in front of the non-infected person's mouth. In contrast, when positioned between the two mannequins (Case B), the hood exhibited limited influence on reducing $C_{q,dc}$.

5.4.2 Comparison with Previous Studies

This experiment was conducted under a ventilation rate of 50 ACH, constrained by the capacity of the experimental facility. In the study by J. Yang et al. [37], which examined the performance of personalized exhaust systems, no significant differences were observed between mixing ventilation (MV) and displacement ventilation (DV) under ordinary ventilation conditions. Their findings suggest that ambient airflow conditions can exert a substantial influence on the performance of local exhaust systems—an influence that may have been amplified in the present study due to the high ventilation rate.

In the authors' previous CFD analysis (Chapter 2) [88], the introduction of a local exhaust ventilation (LEV) system within floor-supply displacement ventilation (FSDV) at 6–12 ACH substantially reduced infection risk for the non-infected person compared to scenarios without LEV. This result indicates that LEV would likely be even more effective at lower ventilation rates (4–12 ACH) under both MV and DV conditions. A notable implication of the current findings is that, even under high ventilation volumes (50 ACH), the FSDV system can maintain a stable upward displacement airflow that minimizes horizontal dispersion of exhaled air from the patient, thereby reducing the potential for airborne infection.

These results are applicable to environments that require extremely high ventilation rates, such as superclean hospital rooms, semiconductor manufacturing facilities, and biological research laboratories. In the HFD system, when the ventilation rate was set at 50 ACH, airborne infection risks during close conversation were sufficiently reduced with hood implementation. However, in the SFD, the introduction of a hood did not adequately suppress infection risk under the same conditions. This limitation applies not only to SFD systems but also to any situation with strong local turbulence near the emission source, such as from electric fans or local air jets. Moreover, the results obtained here should be cautiously extrapolated to smaller enclosed spaces, such as consultation rooms or meeting areas, where diffuser spacing and airflow interactions are expected to differ significantly from those in large-scale chambers.

In this study, only the exhalation process of the infected person was simulated under steady-state conditions. In contrast, J. Yang et al. [37] conducted non-steady-state experiments that incorporated both exhalation and inhalation phases of the non-infected individual. In our previous research [88], the mean exhalation velocity during speech (0.30 m/s) was derived from human measurements and adopted to reproduce a time-averaged conversation. Although the inhalation phase could potentially increase the evaluated infection risk, numerical and experimental investigations of human microclimates by S. Murakami [81] have shown that approximately 90% of the air inhaled enters through the mouth region, while less than 10% is drawn in near the chest. Under the high ventilation rate of 50 ACH in this experiment, the influence of ambient airflow on infection risk assessment likely exceeds that of inhalation.

Furthermore, in a non-steady state, inhalation, exhalation, and pause phases alternate, meaning that the overall infection risk is not necessarily higher than the time-averaged steady-state condition considered here. Nevertheless, as few comparative studies have been conducted to date, future investigations should assess infection risk under lower ventilation conditions while explicitly accounting for nasal and oral inhalation dynamics.

In this study, the infection probability was expressed in terms of $t_{5\%}$ representing the time required for a 5% infection probability, thereby allowing comparison across different exposure durations. The results showed that $t_{5\%}$ exceeded 8 h for both HFD and FSDV, while it remained below 8 h for SFD. Although these values may be influenced by the initial velocity of the exhaled air from the infected person or the inhalation conditions of the non-infected individual, the overall conclusions remain valid, as the primary purpose of this study was to compare relative infection risks across ventilation strategies.

5.4.3 Limitations

This study has several limitations that should be acknowledged when interpreting the results.

・As described in Section 5.1, the ventilation rate in all experiments was fixed at 1,000 m³/h (50 ACH). Consequently, the influence of the air supply system on the airflow field was more pronounced than that of the

hood itself. Future studies should examine the effectiveness of local exhaust ventilation (LEV) under more general ventilation conditions (6–12 ACH). Under such conditions, even if the hood is positioned slightly farther from the emission source, a certain level of hood effectiveness can still be expected.

・The diameter ratio of particles after evaporation to before evaporation (R_d) was estimated by comparing experimental results with those calculated from CO_2 tracer gas (Figure 5-11). However, R_d should ideally be determined based on environmental factors such as indoor humidity and temperature. Because no direct data are available for the R_d of the artificial saliva used in this study, and in situ measurement of particle size after evaporation is technically challenging, the assumed value introduces some uncertainty.

・The motion and dispersion characteristics of particles and gases were inferred solely from concentration measurements at the breathing zone. Direct visualization of airflow and contaminant trajectories was not performed. Future work should employ Particle Image Velocimetry (PIV) or unsteady Computational Fluid Dynamics (CFD) simulations to provide more detailed insight into the dynamic behavior of exhaled flows.

・The experiments were conducted for 15 minutes under steady-state conditions. Thus, long-term cumulative effects, such as the gradual accumulation or re-suspension of particles in various parts of the chamber, were not considered. In real-world applications, additional factors—including filter clogging, duct contamination, and mechanical degradation—may reduce LEV performance over time. Since the results demonstrated that hood flow rate strongly influences infection control performance, these long-term operational effects warrant careful consideration.

・Although the particle size distribution of the artificial saliva was generally consistent with the results reported by Morawska et al. [59] (see **Appendix 5-A**), its chemical composition differed from that of actual human saliva. In particular, the use of glycerol to reproduce the viscosity of real saliva may have increased the adhesive tendency of droplets to walls and ceilings, potentially leading to an overestimation of deposition effects.

5.4.4 Implications for Future Work

Future research should address several aspects to expand upon the findings of this study and to establish a more comprehensive understanding of local exhaust ventilation (LEV) performance under practical conditions.

Under general ventilation rates of 4–12 ACH, LEV systems are expected to perform effectively even in environments where background ventilation is of the mixing type (MV). To confirm this, future experiments should systematically vary both the ventilation volume and the characteristics of the ambient airflow to evaluate their combined influence on contaminant removal and infection risk (some of these were confirmed in Chpter 4).

In this study, infection risk was evaluated using the conventional Wells–Riley model, which assumes that infection is governed solely by the balance between quanta generation and ventilation removal. However, additional physical processes such as viral inactivation and particle deposition can also influence airborne transmission. According to REHVA [69], the contribution of deposition and viral inactivation are approximately 0.30 h^{-1} [92,93] and 0.32 h^{-1} [94], respectively—values that are negligible compared with the ventilation rate applied in this study (50 h^{-1}). Therefore, neglecting these terms results in a conservative, safety-side estimation of infection risk.

Nevertheless, under more realistic conditions involving smaller ventilation rates, these additional factors may become non-negligible. Hence, future studies should employ the extended Wells–Riley framework proposed by Aganovic et al. [95] and Liu et al. [96], which explicitly incorporates deposition and viral inactivation terms to achieve higher accuracy in risk estimation.

Moreover, non-steady-state experiments that account for both exhalation and inhalation cycles of human subjects are necessary to simulate realistic breathing dynamics during close-distance interactions. Such time-dependent approaches, coupled with detailed flow visualization and unsteady CFD simulations, are expected to provide a more comprehensive understanding of transient infection pathways and the true effectiveness of LEV systems in diverse indoor environments.

5.5 Conclusion

This chapter experimentally evaluated the performance of local exhaust ventilation (LEV) systems as an airborne infection control measure during close-distance conversations. The experimental parameters included the hood exhaust flow rate and three types of underfloor air distribution systems: floor-supply displacement ventilation (FSDV), horizontal flow-type floor diffusers (HFD), and swirling flow-type floor diffusers (SFD). Two representative indoor scenarios were considered: a consulting room (Case A), where the hood was installed directly above the infected source, and a restaurant or meeting room (Case B), where the hood and a desk were positioned between two individuals.

Unlike Chapter 4, which focused solely on gaseous emissions, both CO_2 tracer gas and artificial saliva particles were employed in this study to represent exhaled contaminants, allowing direct comparison between gaseous (droplet nuclei) and particulate (droplet) transmission behaviors. In addition, while Chapter 4 examined different ventilation rates ranging from 120 to 480 m^3/h, the present experiments were conducted under a single high ventilation condition of 1,000 m^3/h (equivalent to 50 ACH), reflecting the capacity limit of the experimental facility.

The main findings of this chapter are summarized as follows:

Effect of Air Distribution Type on Infection Risk

・The vertical distribution of normalized CO_2 concentration and the quanta concentration in front of the doctor's mouth ($C_{q,dc}$) indicated that the dispersion of exhaled air and the corresponding infection risk decreased in the order of FSDV < HFD < SFD. This trend aligns with the degree of turbulence in the ambient airflow, suggesting that FSDV—with its large supply area and low average airflow velocity—is most suitable for minimizing airborne transmission risk.

Effectiveness of Hood Placement

・In Case A (consulting room), the installation of the hood effectively reduced the quanta concentration across all air distribution systems, with particularly strong effects observed in the FSDV. In contrast, in Case B (restaurant or meeting room), where the hood was positioned between two individuals, the effect on infection risk reduction was limited. These results highlight that LEV installation is most effective when the infected person's location is known, such as in clinical or diagnostic environments.

Comparison Between Gaseous and Particulate Contaminants

・Comparing infection risk estimation between gas and particles revealed that tracer gas yielded higher calculated quanta concentrations than particles, resulting in a more conservative (safety-side) assessment of infection risk. Under calm airflow conditions, especially in the FSDV, the effect of gravitational settling and particle adhesion became more pronounced, leading to lower infection risks estimated from particles than from tracer gas. These findings suggest that the influence of droplet behavior, including deposition and adhesion, increases as airflow becomes more quiescent.

Practical Implications for Ventilation Design

・Even under high ventilation rates (50 ACH), the FSDV maintained a gentle upward displacement flow that limited horizontal dispersion of exhaled air and effectively prevented airborne transmission. These results can inform ventilation design strategies for super-clean environments, such as hospital isolation rooms, semiconductor manufacturing facilities, and biological research laboratories. Furthermore, the findings can be adapted to smaller spaces, such as consultation and meeting rooms, by appropriately scaling diffuser layout and hood placement to achieve similar airflow characteristics.

This study demonstrated the importance of distinguishing between gaseous and particulate contaminant behaviors in infection risk evaluation. Whereas tracer gas simulations provide an upper-limit estimate of airborne infection potential, particle-based measurements capture more realistic droplet phenomena, including gravitational settling and surface deposition. Building upon these insights, Chapter 6 further investigates the resuspension behavior of settled particles in FSDV environments, addressing the long-term stability and resuspension of infectious aerosols under calm airflow conditions.

5.6 Appendix 5-A: Nebulizer Performance Measurement

The ultrasonic nebulizer (SHIN-EI INDUSTRIES, Inc., Comfort 3000 KU-500) used in this study was originally developed for medical applications rather than for experimental aerosol generation. Therefore, its performance was verified by measuring the particle size distribution to confirm its reproducibility in simulating human-derived droplets produced during speech.

Figure 5-A-1 illustrates the measurement setup using a light-scattering particle size analyzer (PALAS Welas Digital 2000). This instrument can measure particle concentrations up to 10^6 particles/cm³ without the need for dilution, allowing for high-fidelity measurements with minimal evaporation effects. The nebulizer was supplied with air at a flow rate of 5.21 L/min, consistent with the experimental conditions described in Section 5.2.2. Each measurement was performed three times for 60 seconds, and both particle size distribution and number concentration were recorded.

To compare the results with those reported by Morawska et al. [59], the particle size distribution was processed using Eqs. (5-A-1) and (5-A-2). The measurement range was 0.2–10 μm, divided into 32 logarithmically spaced intervals.

$$\frac{dC_{ni}}{d\,log_{10}\,D_i} = \frac{n_i}{V_m \Delta\, log_{10}\,D_i} \qquad (5-A-1)$$

$$\Delta\, log_{10}\,D_i = log_{10}\,D_{i,upper} - log_{10}\,D_{i,lower} \qquad (5-A-2)$$

where C_{ni} is the particle number concentration for each interval [m^{-3}]; D_i is the arithmetic interval width [m], n_i is the measured number of particles within the interval borders $D_{i,\,upper}$ and $D_{i,\,lower}$ [p], V_m is the measured volume [m^3], $D_{i,\,upper}$ is the diameter of the upper interval border [m], and $D_{i,\,upper}$ is the diameter of the lower interval border [m].

The total particle number concentration was obtained by summing the number concentrations for all intervals as shown in Eq. (5-A-3):

$$Sum\,(dC_{ni}) = \sum \frac{n_i}{V_m} \qquad (5-A-3)$$

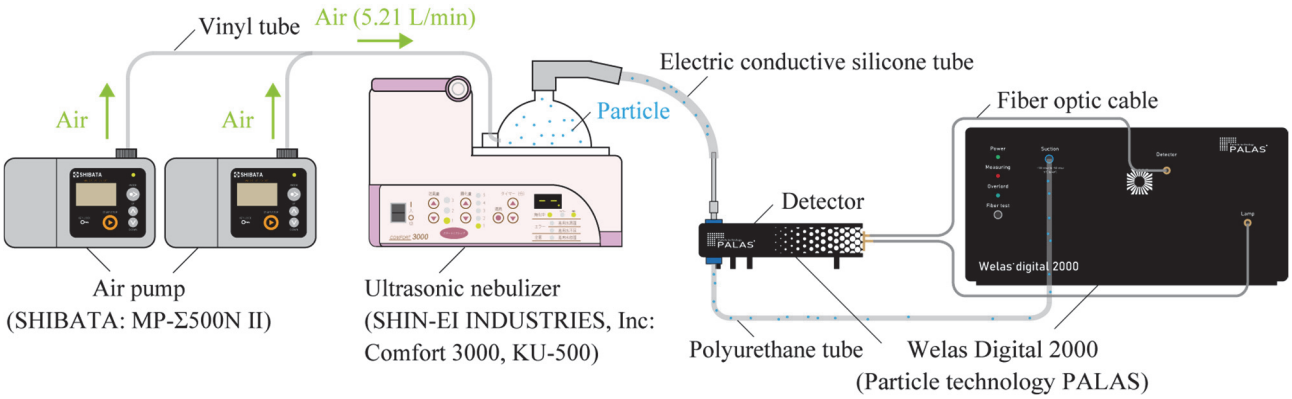


Figure 5-A-1. Measurement setup for particle size distribution and number concentration of the ultrasonic nebulizer.

The measurement results are presented in **Figure 5-A-2**. Background particle counts ranged from 10 to 100 cm^{-3} for diameters below 1 μm, which was negligibly small compared with the nebulizer-generated concentration of approximately 5×10^5 cm^{-3}. **Figure 5-A-2a** shows the averaged particle size distribution from three consecutive 60-second measurements. Two distinct peaks were observed: one at 0.2–0.3 μm and another at 1.0–1.1 μm.

Morawska et al. [59] measured human-origin aerosol particles produced during voiced counting using the Expiratory Droplet Investigation System (EDIS) and reported a single dominant peak around 0.8 μm. Their measurements were conducted after a short period of post-emission evaporation. Considering this evaporation effect, the 1.0–1.1 μm peak obtained from the ultrasonic nebulizer in this study can be regarded as comparable to the droplet sizes produced during human speech. Regarding the smaller 0.2–0.3 μm peak, it should be noted that the handheld particle counter (KANOMAX, model 3888) used in the main experiment measured particles with diameters of 0.3 μm or larger. Consequently, particles in the 0.2–0.3 μm range were likely excluded from the main experiment's measurements due to both instrument limitations and evaporation effects. However, because the particle volume of 0.2–0.3 μm droplets is only approximately 1/53 that of 1.0–1.1 μm droplets, the absence of these smaller particles is considered to have a negligible impact on infection risk assessment.

As shown in Figure **5-A-2b**, the total particle number concentration ranged from 4×10^5 to 5×10^5 particles/cm^3, confirming that the nebulizer generated a sufficient concentration of tracer particles for the full-scale experiments.

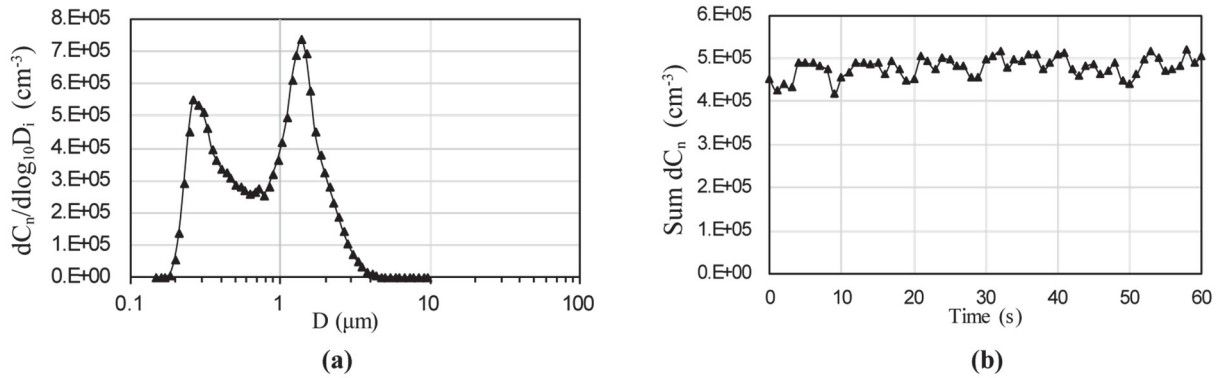


Fig. 5-A-2. Measurement results of the ultrasonic nebulizer: (a) particle size distribution averaged three times (60 seconds each time). (b) particle number concentration of the ultrasonic nebulizer (extracted one time randomly).

6 Experimental Study on Airflow-Induced Particle Resuspension under FSDV Conditions

6.1 Purpose of the Chapter

Building upon the findings of the previous chapters, this study investigates particle resuspension behavior under floor-supply displacement ventilation (FSDV) conditions. In Chapter 3, FSDV demonstrated superior contaminant removal performance compared to other air distribution systems, providing a calm upward airflow that efficiently transported exhaled contaminants away from the breathing zone. In Chapter 5, it was further revealed that in such quiescent environments, gravitational settling played a major role, causing noticeable differences between gaseous and particulate behavior. These results suggest that while FSDV is effective for removing airborne contaminants, accumulated particles on the floor surface may be more prone to resuspension depending on environmental conditions.

To address this issue, the present chapter focuses on airflow-induced particle resuspension under FSDV conditions, as a preliminary step before incorporating human walking effects in future studies. As previous research has shown, particle resuspension is influenced by the balance between aerodynamic drag and adhesive forces, both of which are affected by relative humidity. Therefore, experiments were conducted under controlled FSDV conditions using humidity and supply air velocity as key parameters (**Figure 6-1a**). For comparison, additional experiments were performed under conventional ceiling diffuser (CD) conditions using standard anemostat diffusers, with supply air velocity varied at 50% relative humidity (**Figure 6-1b**).

The objective of this chapter is to quantitatively evaluate airflow-induced particle resuspension under FSDV conditions and to identify the dominant environmental factors affecting it through direct experimental measurements.

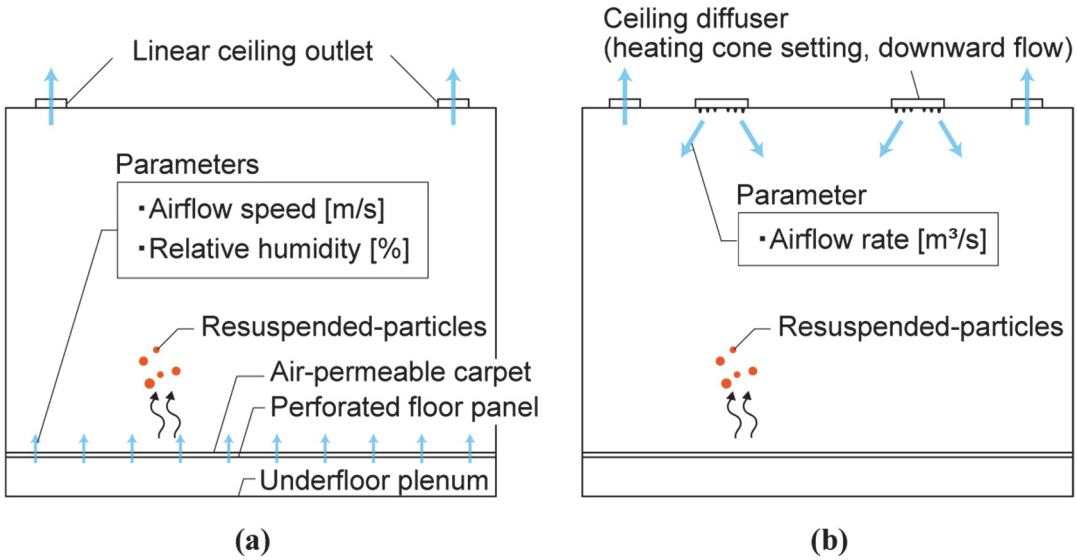


Figure 6-1. Schematic cross-section and key parameters of this study. (a) Air supply method: floor-supply displacement ventilation (FSDV). (b) Air supply method: ceiling diffuser (CD) as a comparison case.

6.2 Methodology

6.2.1 Experimental Procedures and Facilities

The layout of the laboratory and its surrounding facilities is shown in **Figure 6-2**. Experiments were conducted in a cleanroom chamber (hereafter referred to as the test chamber) owned by the University of Osaka. Supply air was introduced through a HEPA filter, and the system used 100% outdoor air without recirculation. The temperature was controllable, but humidity control was not available. The ventilation method could be switched between floor-supply displacement ventilation (FSDV) and ceiling diffuser (CD) by changing the connection of the supply duct (**Figure 6-2**). The ceiling diffuser (KUKEN Kogyo, C2 type, 200 mm φ) was operated in a heating-mode, which provides a more vertical jet compared with the cooling setup, to simulate a more conservative (i.e., higher) resuspension scenario.

The ventilation rate was adjustable from 120 to 1000 m³/h (corresponding to 6–50 air changes per hour). Both the supply and exhaust systems were equipped with constant air volume (CAV) units rated at 1000 m³/h and 990 m³/h, respectively, and were designed to maintain the test chamber at a slightly positive pressure, thereby preventing outdoor air infiltration. Because the supply and exhaust flow rates were not identical, the ventilation rate was adjusted based on the mass balance of CO_2 gas released into the exhaust duct. Therefore, in this study, the ventilation rate is defined as the exhaust airflow rate (Q_e).

A plan view and a cross-sectional view of the chamber are shown in **Figures 6-3a** and **6-3b**, respectively. The chamber floor was covered with 40 detachable air-permeable carpet tiles (each 500 mm × 500 mm). As illustrated in **Figure 6-3b**, supply air entered the underfloor plenum and was uniformly distributed into the room through perforated metal panels and the air-permeable carpet layer. The carpet consisted of alternating high- and low-loop piles, with a Nylon 6 surface and a backing composed of glass fiber and polyester nonwoven fabric (**Figure 6-3c**). The total air-supply area was 7 m², defined by the perforated panel region indicated in **Figure 6-3a**.

Note that, in the absence of internal heat sources, the airflow pattern of FSDV resembled a piston-like flow from bottom to top, rather than the conventional displacement ventilation pattern.

The experimental procedure was as follows:

1. One gram of test particles was uniformly distributed on a single carpet tile in the entrance hall.
2. The particle-loaded carpet was transferred into the test chamber (**Figure 6-3a**). Placement was completed within 2 minutes by the operator to minimize unintended particle dispersion.
3. The carpet was then exposed to airflow for a specified duration (t_e; **Table 6-1**), during which temporal variations in particle number concentration were continuously monitored using four handheld particle counters (Model 3889, Kanomax Japan Inc.) installed at fixed positions, as shown in **Figure 6-3b**.

Temperature and relative humidity were simultaneously measured at three locations: within the underfloor supply plenum (point t), inside the test chamber (point s), and in the entrance hall (point e), using a Vaisala HUMICAP® Handheld Humidity and Temperature Meter (Model MI70 with HMP75 probe) (**Figures 6-2** and **6-3b**). The saturated vapor pressure was calculated using the Wexler–Hyland equation (Eq. (6-1)) [1]. Relative humidity was then calculated using Eq. (6-2), and absolute humidity was derived using Eq. (6-3).

$$ln e_s(T) = A_1/T + A_2 + A_3 T + A_4 T^2 + A_5 T^3 + A_6\, lnT \qquad (6-1)$$

$$e = RH * e_s(T)/100 \qquad (6-2)$$

$$AH = (216.7 * e)/(T + 273.15) \qquad (6-3)$$

where e_s(T) is the saturation vapor pressure [hPa], T is the dry-bulb temperature [K], A_1-A_6 are the empirical constants ($A_1 = -0.58002206\times10^{3}$, $A_2 = +0.13914993\times10^{1}$, $A_3 = -0.48640239\times10^{-1}$, $A_4 = +0.41764768\times10^{-4}$, $A_5 = -0.14452093\times10^{-7}$, $A_6 = +0.65459673$) (reported by Hyland and Wexler (1983) [1]), e is the water vapor pressure [hPa], RH is the relative humidity [%], and AH is the absolute humidity [g/m^3].

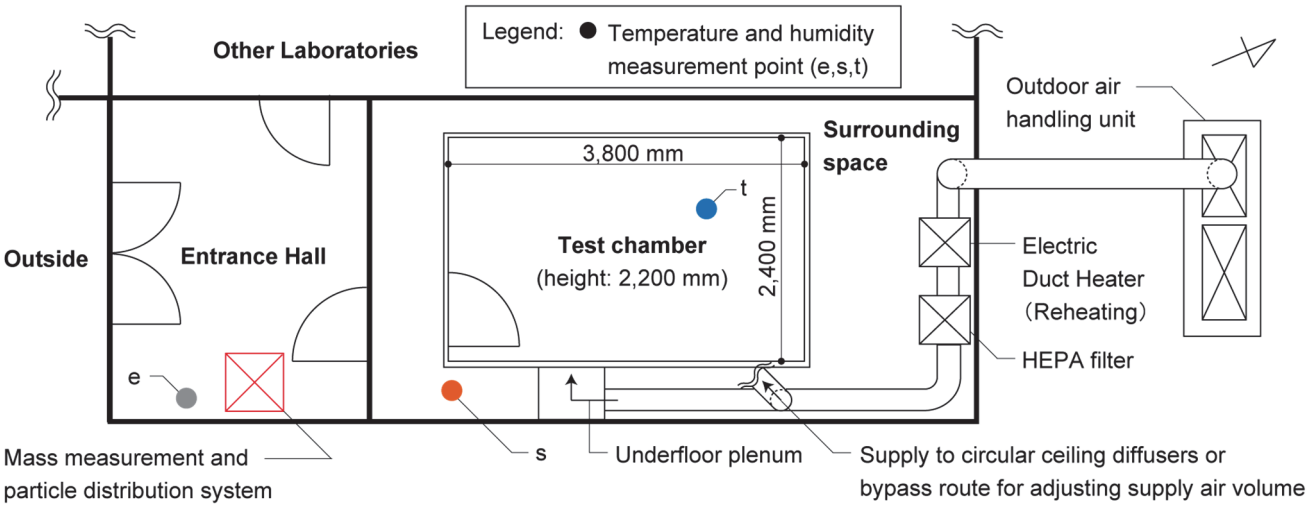


Figure 6-2. Schematic layout of the test chamber and surrounding environment.

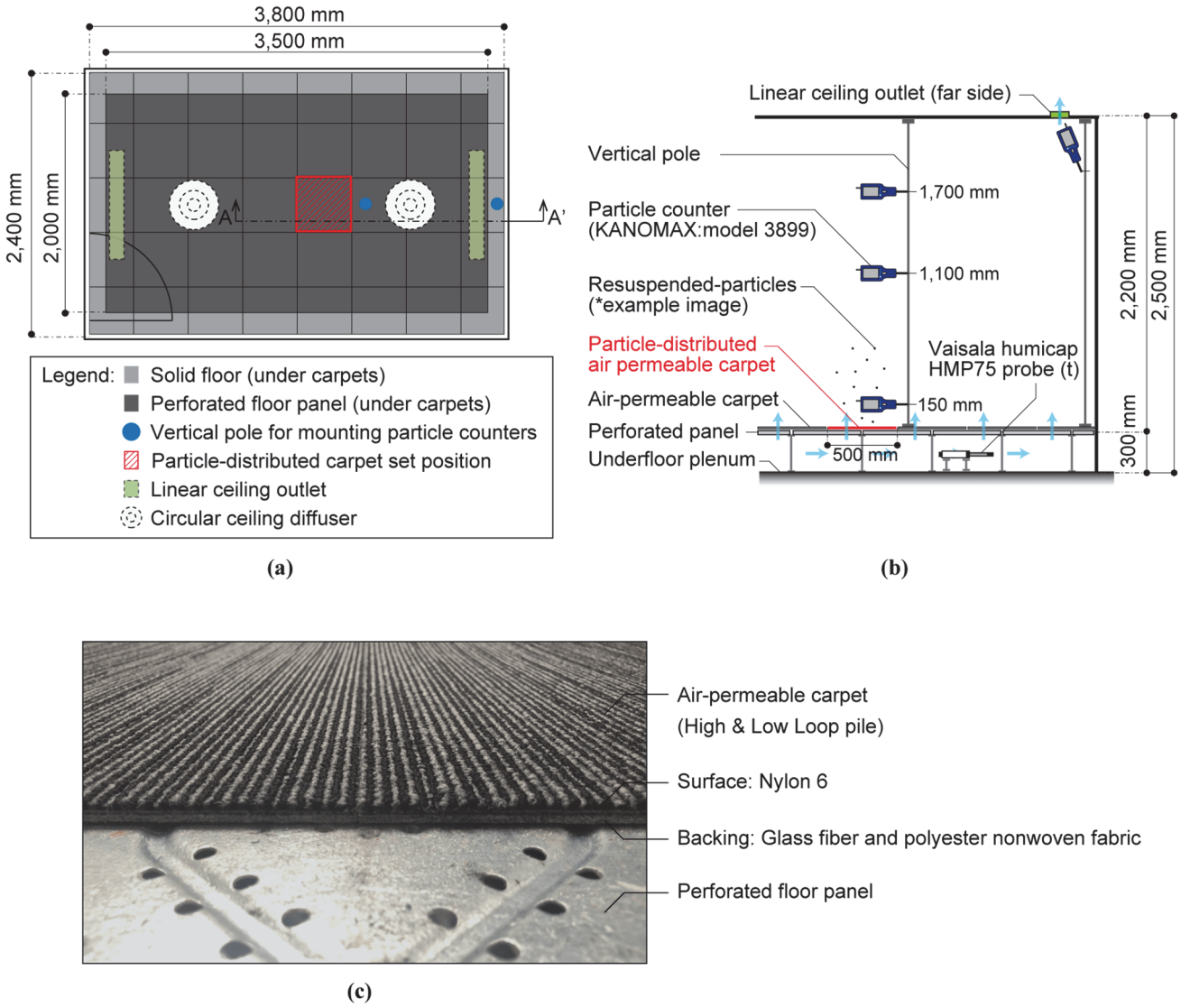


Figure 6-3. Details of the test chamber. (a) Plan view of the test chamber. A linear ceiling outlet and a ceiling diffuser are on the ceiling, displayed in dotted lines. (b) Cross-sectional view of the test chamber along line A–A′ (particle concentration measurement points). (c) Photograph of the air-permeable carpet and perforated floor panel with annotated cross-sectional details.

6.2.2 Particle Dispersion on Carpet

Details of the equipment used for mass measurement and particle dispersion, installed in the entrance hall, are shown in **Figure 6-4**. A tare plate and a carpet support made of foamed polystyrene were placed on a tuning fork-type electronic balance (RJ-620, Shinko Denshi Co., Ltd.; minimum resolution: 0.001 g). To minimize the influence of ambient airflow, the entire apparatus was enclosed within a wind shield constructed from steel

angles and vinyl sheets. A commercially available cosmetic powder sprayer was employed for particle application.

To ensure uniform spreading, the upper surface of the wind shield was divided into 16 equal sections, and particles were applied sequentially from each division point (**Figure 6-5a**). The uniformity of particle deposition was confirmed in a separate validation experiment, showing that the standard deviation among 25 divided surface sections was within 1% (**Appendix 6-A**).

An image of the carpet after the application of 1 g of powder is shown in **Figure 6-5b**. The applied mass—equivalent to 4 g/m²—was determined with reference to previous studies: 20 g/m² reported by J. Qian et al.[53] and 0.221–2.971 g/m² reported by J. Rostami et al.[97], both of which used Arizona Test Dust (ATD A1). For the test particles, a commercially available pharmaceutical powder, Ryukakusan (Ryukakusan Co., Ltd.), was selected to ensure operator safety. Ryukakusan is a finely ground mixture of herbal ingredients, most of which are insoluble in water. According to Y. Takeuchi et al. [98], its density is 2.80 g/cm³, and the volume-based median diameter (D_{50}) is 7.7 μm. These values are comparable to—but slightly larger than—those of Arizona Test Dust A1, which has a density of 2.65 g/cm³ and a mass-based median diameter (D_{50}) of 4.3 μm and has been widely used in previous studies [41].

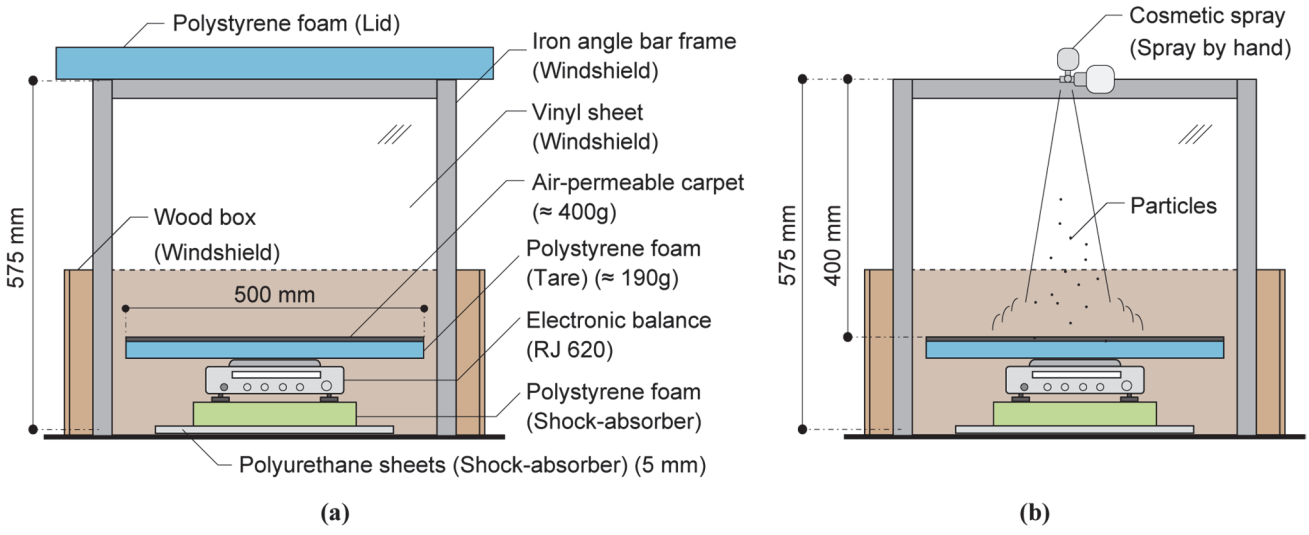


Figure 6-4. Mass measurement and particle distribution system installed in the entrance hall, shown in **Figure 6-2**. (a) Setup for carpet mass measurement. (b) Particle distribution process on the carpet.

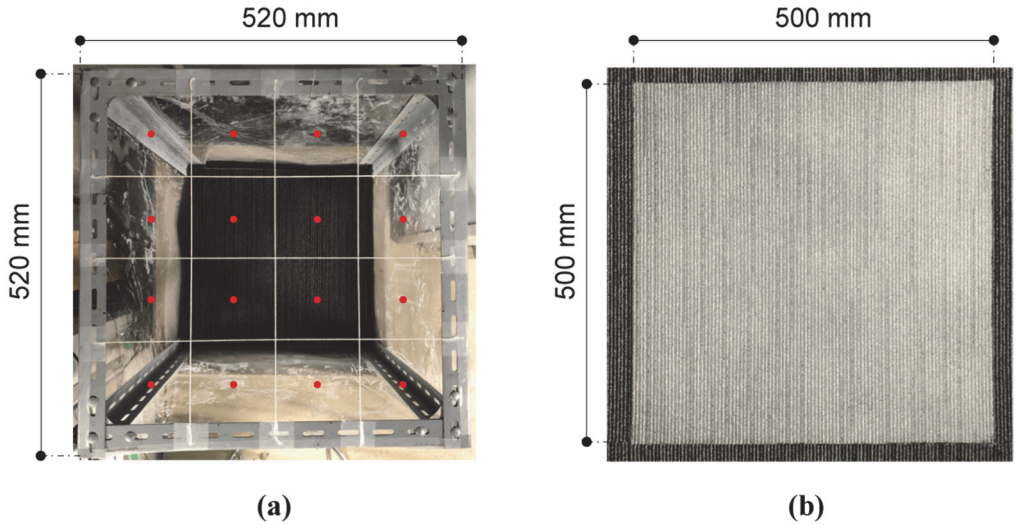


Figure 6-5. Photographs of particle dispersion. (a) Top view of particle distribution points. (b) Carpet surface after particle distribution (≈ 1.0 g).

The surface of the air-permeable carpet consisted of a nylon 6 loop pile, while the backing layer was composed of glass fiber and polyester nonwoven fabric (**Figure 6-3c**). Because nylon 6 is hygroscopic, its mass can vary depending on the ambient moisture content. Consequently, it is difficult to determine whether changes in carpet mass observed during particle application are attributable to moisture absorption or desorption, or to the adhesion of particles themselves. On average, approximately 10 minutes were required to apply 1 g of powder onto a carpet tile. Therefore, it was assumed that the rate of moisture absorption during spraying was equivalent to that occurring during the 10 minutes immediately preceding spraying.

To validate this assumption, mass changes were measured for ten individual carpet samples over a continuous 20-minute period (**Figure 6-6**). The mean absolute mass change over a 10-minute interval was 2.46 mg, with a standard deviation of 1.57 mg. This variation corresponds to less than 0.25% of the target application mass (1 g). Using this procedure, a particle application (adhesion) of 1.000 ± 0.020 g was consistently achieved under all experimental conditions summarized in **Table 6-B-1**.

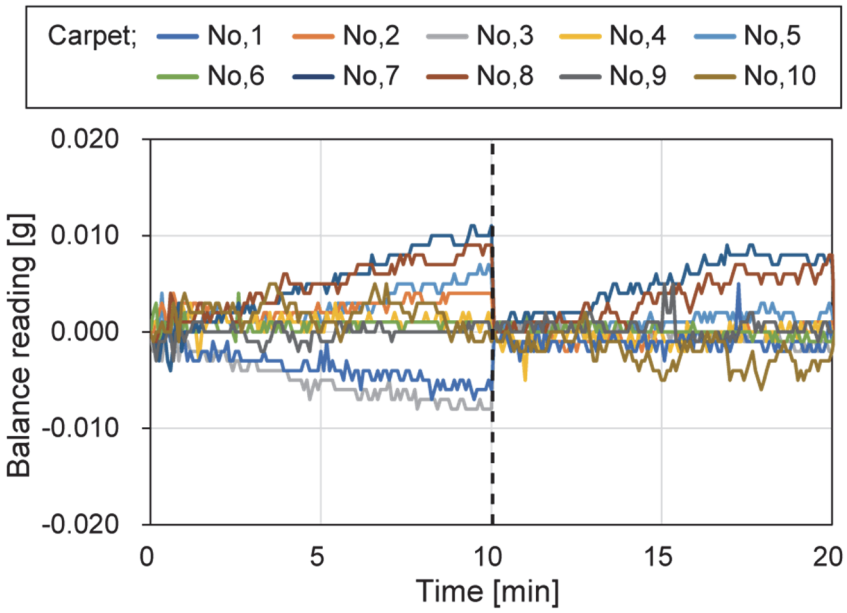


Figure 6-6. Mass change of 10 different carpets (Carpet No. 1–10) over 20 minutes (normalized to zero at 10 minutes, including tare weight).

6.2.3 Parameters and Experimental Cases

The key parameters influencing resuspension were the floor supply air velocity (v_f) and the relative humidity (RH) of the supply airflow under FSDV conditions. Experiments under CD conditions were also conducted for comparison. **Table 6-1** summarizes the experimental cases, including their naming conventions and configurations. Each test name consisted of the ventilation method, the floor supply air velocity in FSDV (or the ventilation volume in CD), and the relative humidity. **Table 6-1** also presents the relationship between the area-averaged floor supply air velocity in FSDV and other relevant parameters. Here, v_f is defined as the supply airflow rate divided by the total area of the flow-through panels shown in **Figure 6-3a**.

For comparison, control cases were established for FSDV at v_f = 0.040 m/s and RH = 20%, and for CD at 850 m³/h and RH = 50%, both without any particles applied to the carpet (non-seeded). In these control cases (FSDV_0.04_20_no and CD_850_50_no), only carpet installation and operator entry/exit were performed. No internal heat sources were present in the chamber for any test condition.

The area-averaged floor supply air velocity in FSDV was tested at three levels—0.010, 0.030, and 0.040 m/s—selected such that the corresponding dynamic pressure ratios were approximately evenly spaced. Each v_f was adjusted by varying the total supply airflow rate. A supply velocity of 0.040 m/s corresponds to 50 air changes per hour (ACH), a level typically required in hospital cleanrooms [33]. A velocity of 0.010 m/s corre-

sponds to 12.5 ACH, consistent with the HEAS-02-2022 recommendation of 12 ACH for Airborne Infection Isolation Rooms (AIIRs) [33]. According to the carpet manufacturer, the recommended operating range is below approximately 0.014 m/s; therefore, 0.010 m/s was selected to represent typical operating conditions.

In CD experiments, the supply airflow rate was varied as a parameter while maintaining RH = 50%. To match the flow condition corresponding to v_f = 0.040 m/s in FSDV, a flow rate of 990 m³/h would have been required. However, due to limitations of the outdoor air handling unit fan, the maximum achievable rate was 850 m³/h.

The experimental duration (t_e) was set to 20 times the nominal ventilation time for each condition. Relative humidity was controlled at three levels (20%, 50%, and 80%) using an outdoor air conditioner and an electric duct reheater (**Figure 6-2**). The average relative humidity in the underfloor supply plenum (**Figure 6-3b**) was maintained within ±7% of the target value under all conditions, as summarized in **Table 6-B-1**. The supply air temperatures during the measurement ranged from 17°C to 34°C (**Table B-6-1**).

Table 6-1

Test names and details of experimental conditions.

Test name	v_f [m/s]	r_d [-]	$RH(t)$ [%]	Q_e [m³/h]	n [h^{-1}]	τ_n [min]	t_e [min]	L_{total} [g] ([g/m²])
FSDV_0.04_20	0.04	16	20	990	49.3	1.2	24.3	1.00 (4.00)
FSDV_0.04_50	0.04	16	20	990	49.3	1.2	24.3	1.00 (4.00)
FSDV_0.04_80	0.04	16	20	990	49.3	1.2	24.3	1.00 (4.00)
FSDV_0.03_20	0.03	9	50	750	37.4	1.6	32.1	1.00 (4.00)
FSDV_0.03_50	0.03	9	50	750	37.4	1.6	32.1	1.00 (4.00)
FSDV_0.03_80	0.03	9	50	750	37.4	1.6	32.1	1.00 (4.00)
FSDV_0.01_20	0.01	1	80	250	12.5	4.8	96.3	1.00 (4.00)
FSDV_0.01_50	0.01	1	80	250	12.5	4.8	96.3	1.00 (4.00)
FSDV_0.01_80	0.01	1	80	250	12.5	4.8	96.3	1.00 (4.00)
CD_850_50	-	-	50	850	42.4	1.4	28.3	1.00 (4.00)
CD_750_50	-	-	50	750	37.4	1.6	32.1	1.00 (4.00)
CD_250_50	-	-	50	250	12.5	4.8	96.3	1.00 (4.00)
FSDV_0.04_20_no	0.04	16	20	990	49.3	1.2	24.3	-
CD_850_50_no	-	-	50	850	42.4	1.4	28.3	-

v_f: Area-averaged supply air velocity over flow-through panels [m/s]; r_d: Dynamic pressure ratio relative to v_f =0.010 m/s [-]; RH(t): Relative humidity in test chamber [%]; Q_e: Exhaust airflow rate [m³/h]; n: Ventilation rate [h^{-1}]; τ_n: Nominal ventilation time [min]; t_e: Duration of carpet exposure to airflow [min]; L_{total}: Total applied mass of particles on the carpet [g].

6.2.4 Calculation of Resuspension Rate

The resuspension rate (coefficient), r [h^{-1}], is defined as the fraction of particles deposited on the floor surface that are resuspended per unit time. The calculation procedure is summarized in Eqs. (6-4)-(6-10) [40,41].

Definition of the resuspension rate

First, Eq. (6-4) defines the resuspension rate r_j as the ratio of the resuspended mass per unit time (R_j) to the deposited mass (L_j) for each particle size range j:

$$r_j = R_j / L_j \qquad (6-4)$$

Calculation of R_j under FSDV conditions

Under FSDV conditions, the resuspended mass $R_{j,FSDV}$ is calculated using Eq. (6-5). A conversion factor (α) is introduced to convert the measured concentration at 150 mm above the carpet into the total resuspended amount from the entire carpet area:

$$R_{j,FSDV} = \frac{\alpha}{n\Delta t} \sum_{i=1}^{n} \left(N'_{pc,i,j} V_j \rho \right) \qquad (6-5)$$

whwer α is the conversion factor accounting for the total resuspension amount (210.2, 157.7, and 52.6 for v_f = 0.040, 0.030, and 0.010 m/s) [-], n is the total number of time steps (total number of data points) [-], Δt is the duration of each time step (constant within each test case; 6 s for flow rates of 1000, 850, and 750 m³/h, and 12 s for 250 m³/h) [s], $N'_{pc,i,j}$ is the number of particles measured at time step i for size range j, with the 10-minute average value prior to operator entry subtracted [-], ρ_p is the Particle density (2.83 for Ryukakusan [98]) [g/m^3], and V_j is the representative particle volume for size range j [m^3].

The conversion factor α is defined as the ratio of the airflow volume per carpet tile (Q_{ca}) to the suction flow rate of the particle counter (q_{pc}), as shown in Eq. (6-6):

$$\alpha = Q_{ca} / Q_{pc} \qquad (6-6)$$

wherw Q_{ca} is the airflow volume per 500×500 mm air-permeable carpet tile [m^3/h], and Q_{pc} is the suction flow rate of particle counter (0.170) [m^3/h].

The calculated α values were 210.2, 157.7, and 52.6 for v_f = 0.040, 0.030, and 0.010 m/s, respectively. This assumption is considered valid near the carpet surface, but not at greater heights where diffusion becomes dominant. Accordingly, the resuspension rate r was calculated only from the particle counter positioned 150 mm above the floor.

Background correction and observation period

To eliminate the influence of background particles, the 10-minute average concentration measured prior to operator entry was subtracted from the measured data using Eq. (6-7):

$$N'_{pc,i,j} = N_{pc,i,j} - \overline{N_{pcb,J}} \quad (6-7)$$

whwer $N_{pc,i,j}$ is the number of particles measured at time step i for size range j [-], and $\overline{N_{pcb,J}}$ is the average number of particles measured during the 10 minutes before operator entry, for size range j [-].

The total observation time ($n\Delta t$) corresponds to the period between 10 and 20 nominal ventilation times after the operator's entry, as shown in Eq. (6-8):

$$n\Delta t = 10\frac{V_r}{Q_e} \quad (6-8)$$

where V_r is the room volume (20.06) [m^3], and Q_e is the exhaust airflow rate [m^3/h].

Calculation of R_j under CD conditions

Under CD conditions, the resuspended particles from the 500 × 500 mm carpet tile were assumed to disperse uniformly throughout the chamber. The total resuspended mass was thus estimated by multiplying the particle mass concentration by the chamber volume, as expressed in Eq. (6-9):

$$R_{j,CCD} = \frac{V_r}{n\Delta t}\sum_{i=1}^{n}\left(\frac{N'_{pc,i,j}V_j\rho_p}{Q_{pc}\,\Delta t}\right) \quad (6-9)$$

To verify the assumption of complete mixing, results obtained from both the 150 mm height and the ceiling outlet were compared, confirming that the assumption was approximately valid (**Figures 6-10d** and **6-10e**).

Estimation of deposited mass L_k

The deposited mass L_j for each size range was estimated using Eq. (6-10):

$$L_j = L_{total} f_p \qquad (6-10)$$

where L_{total} is the total applied mass of particles on the carpet (1.000 ± 0.003) [g], and f_p is the mass fraction of test particles in each particle size class [–]

The particle size distribution of Ryukakusan (f_p) was obtained from Y. Takeuchi et al. [98]. This distribution was obtained using a laser diffraction particle size analyzer (LDSA-2400A, originally developed by Tohnichi Computer Applications Co., Ltd.; now managed by MicrotracBEL Corp.). Based on the mass fraction of each particle size class (**Table 6-2**), L_j was determined by multiplying the total deposited mass (1.000 ± 0.030 g) by the corresponding fraction, assuming that the reported distribution also applied to particles deposited on the carpet surface.

Table 6-2
Mass ratio of test particles (Ryukakusan) in each particle size class (f_p), estimated from Y. Takeuchi et al. [98]

0.3-0.5 μm	0.5-1.0 μm	1.0-3.0 μm	3.0-5.0 μm	5.0-10 μm	10- μm
0.01	0.01	0.09	0.19	0.4	0.3

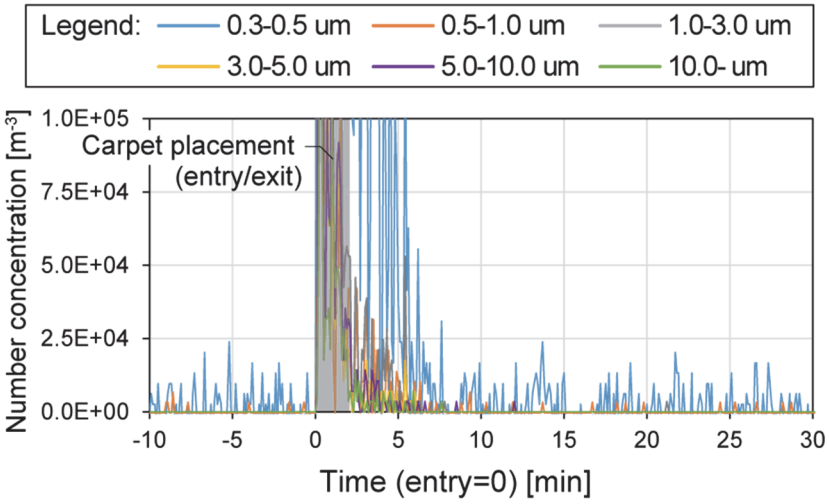
6.3 Results

6.3.1 Time Series of Indoor Particle Concentration

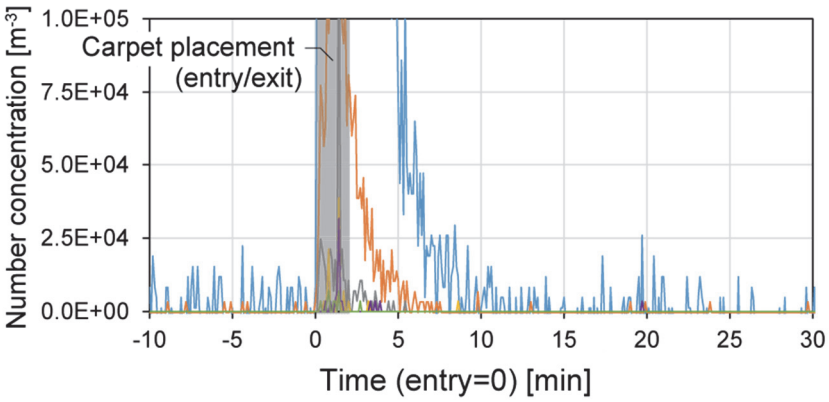
Figure 6-7 shows the time-series variation in particle number concentration by particle size at a height of 150 mm above the floor under no-particle conditions (FSDV_0.04_20_no, **Figure 6-7a**; CD_850_50_no, **Figure 6-7b**). **Figure 6-8** presents the time-series variation in particle number concentration by particle size measured by the four particle counters shown in **Figure 6-3**, under the FSDV_0.04_20 condition. In **Figures 6-7~6-9**, the average background concentration for each particle size class during the 10 minutes prior to operator entry was subtracted from the measured data (Eq. (6-7)), ensuring consistent data processing across all test conditions.

Comparing **Figures 6-7a** and **6-7b**, particle concentrations exhibited a temporary increase immediately after operator intrusion, but the subsequent decay patterns showed no substantial difference between FSDV and CD. Even when no particles were applied to the carpet, a slight particle concentration was observed—approximately 2.5×10^4 m^{-3} in the 0.3–0.5 μm size range.

Comparing **Figure 6-7a** and **Figure 6-8d**, numerous sharp peaks in particle concentration were observed at 150 mm above the floor in **Figure 6-8d**, indicating that particle resuspension occurred. Although 0.3–0.5 μm particles were dominant, distinct peaks also appeared in the 5–10 μm and >10 μm ranges, whereas no such peaks were present in **Figure 6-7a**. In contrast, the frequency and amplitude of peaks decreased with increasing height, as shown in **Figures 6-8c** (1100 mm), **6-8b** (1700 mm), and **6-8a** (exhaust concentration), confirming that resuspension effects were most pronounced near the floor surface.

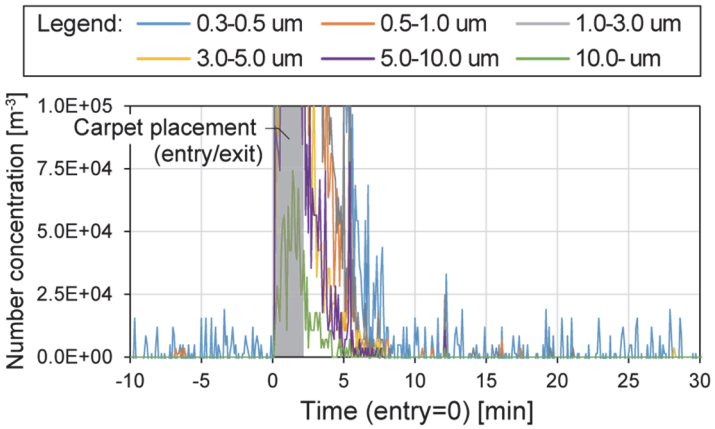


(a) FSDV_0.04_20_no, 150 mm above floor level

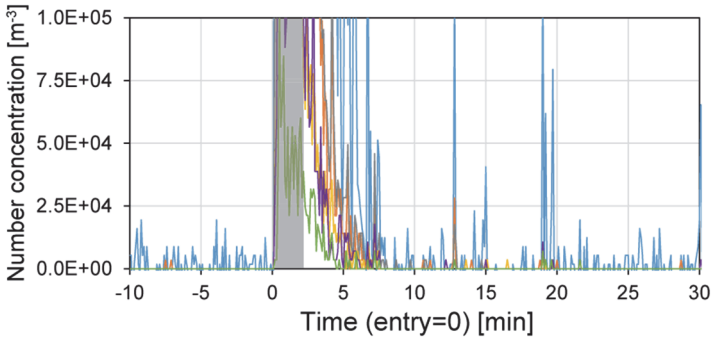


(b) CD_850_50_no, 150 mm above floor level

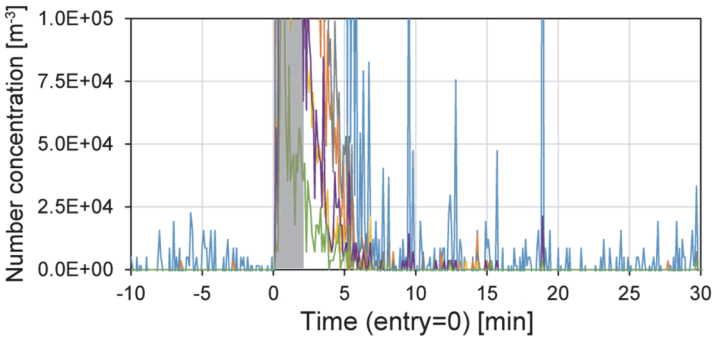
Figure 6-7. Time series of size-resolved particle number concentrations at 150 mm above the floor. (a) FSDV_0.04_20_no. (b) CD_0.04_20_no.



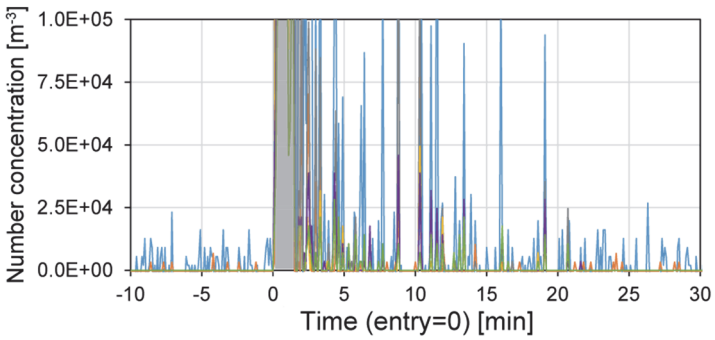
(a) FSDV_0.04_20, Linear ceiling outlet (far side)



(b) FSDV_0.04_20, 1,700 mm above floor level



(c) FSDV_0.04_20, 1,100 mm above floor level



(d) FSDV_0.04_20, 150 mm above floor level

Figure 6-8. Time series of size-resolved particle number concentrations under the FSDV_0.04_20 condition. Measurement locations of particle counters are shown in **Figure 3b**. (a) Linear ceiling outlet, located far from the entrance door. (b) 1700 mm above floor level. (c) 1100 mm above floor level. (d) 150 mm above floor level.

Figure 6-9 displays the time series of size-resolved particle number concentrations measured 150 mm above the floor under all experimental conditions. To enable comparison across different ventilation volumes, the horizontal axis was normalized by the nominal ventilation time for each condition. The interval corresponding to 10–20 normalized ventilation times was used for calculating the resuspension rate.

Among all conditions, resuspension was most pronounced under FSDV_0.04_20, as shown in **Figure 6-9a**. The influence of relative humidity is also evident: resuspension was markedly lower under the FSDV_0.04_80 condition. In contrast, under the v_f = 0.010 m/s condition (**Figures 6-9d–f**), overall resuspension levels were low, and the impact of humidity appeared minimal.

Under CD conditions, humidity was kept constant while the airflow rate was varied. At 850 m³/h and 750 m³/h, several peaks indicating measurable resuspension were observed, whereas at 250 m³/h, the number and amplitude of peaks decreased substantially. Compared with FSDV, resuspension peaks under CD were less frequent but broader, and the average particle concentration was higher, likely because resuspended particles dispersed horizontally before diffusing throughout the chamber.

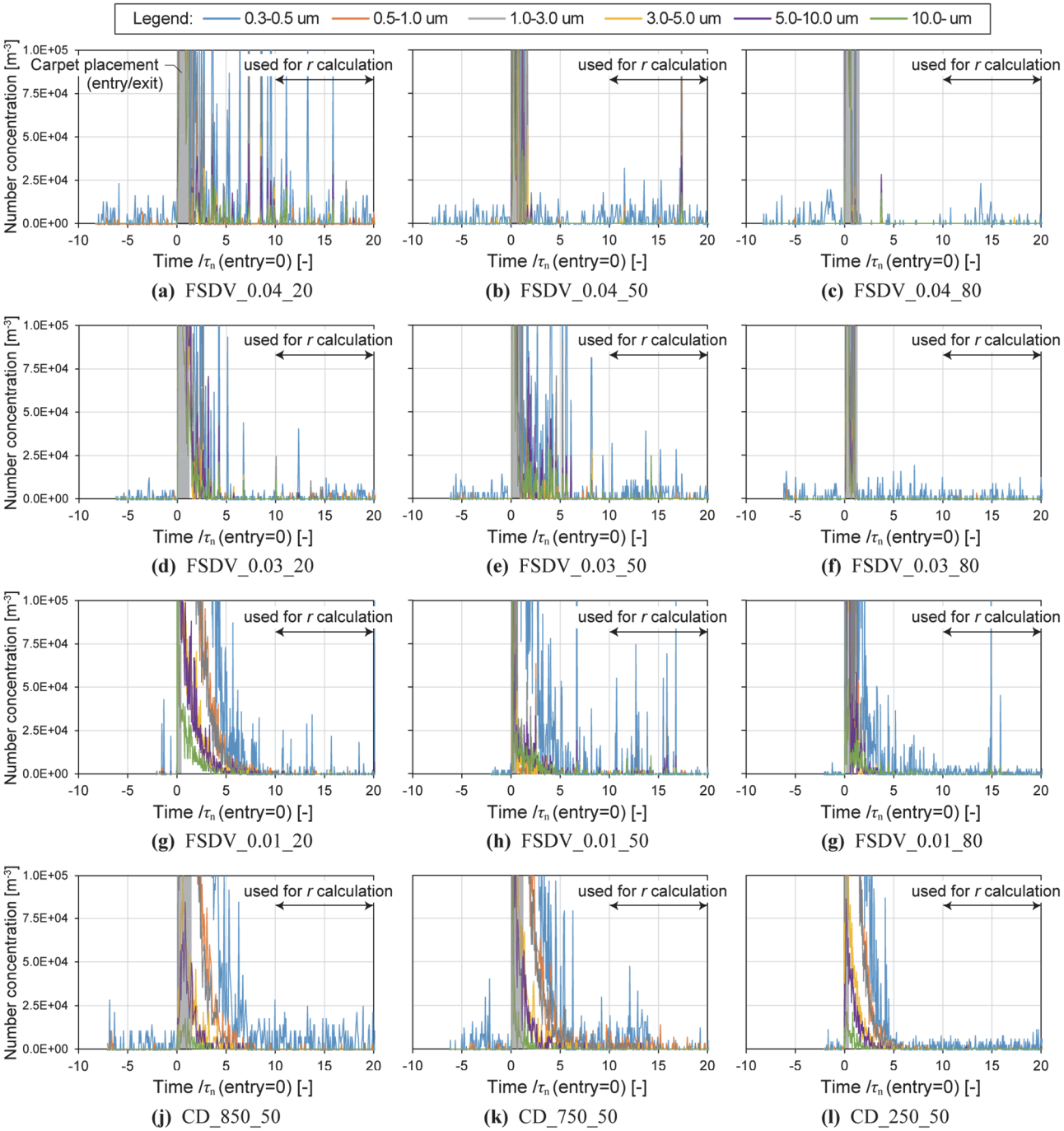


Figure 6-9. Time series of size-resolved particle number concentrations at 150 mm above the floor. The horizontal axis represents time relative to the operator's entry (entry = 0), normalized by the nominal ventilation time. Results of all experimental cases are shown in (a)–(l).

6.3.2 Resuspension Rate

Figure 6-10 shows the calculated resuspension rates [h^{-1}] for each condition, plotted as a function of particle size. Results under FSDV conditions are presented in **Figures 6-10a–c**, while those under CD conditions are shown in **Figures 6-10d** and **6-10e**. To eliminate the influence of background concentration, the 10-minute average concentration measured prior to operator entry was subtracted for each particle size range (Eq. (6-7)). As a result, some negative or zero values were obtained, which cannot be represented on a logarithmic scale; therefore, a lower panels was added below the main plot to display these data points.

Comparing **Figures 6-10a–c**, it is evident that the resuspension rate decreases with decreasing floor supply air velocity. Conversely, when comparing relative humidity at the same air velocity, the influence of humidity is more pronounced at 0.040 m/s (**Figure 6-10a**), while its effect is minimal at 0.010 m/s (**Figure 6-10c**). Regarding particle size, particles in the 5–10 μm and ≥10 μm ranges exhibited relatively higher resuspension rates at 150 mm above the floor. However, there remain significant uncertainties concerning the behavior of particles after resuspension under FSDV conditions.

Under CD conditions, assuming complete mixing, the total resuspended mass was calculated by multiplying the particle number concentration by the chamber volume. To verify this assumption, the resuspension rate was calculated separately using data from particle counters installed at 150 mm above the floor and below the linear ceiling outlet. As shown in **Figures 6-10d** and **6-10e**, the results from the two measurement heights exhibited no substantial differences in either order of magnitude or overall trend, thereby confirming the validity of the complete mixing assumption.

The resuspension rates under CD conditions ranged approximately from 10^{-5} to 10^{-3} h^{-1}, generally higher than those observed under FSDV conditions. When examined by particle size, for particles larger than 3 μm, several size classes yielded zero or negative values, and for those larger than 10 μm, the resuspension rate was zero at 150 mm above the floor for all ventilation rates.

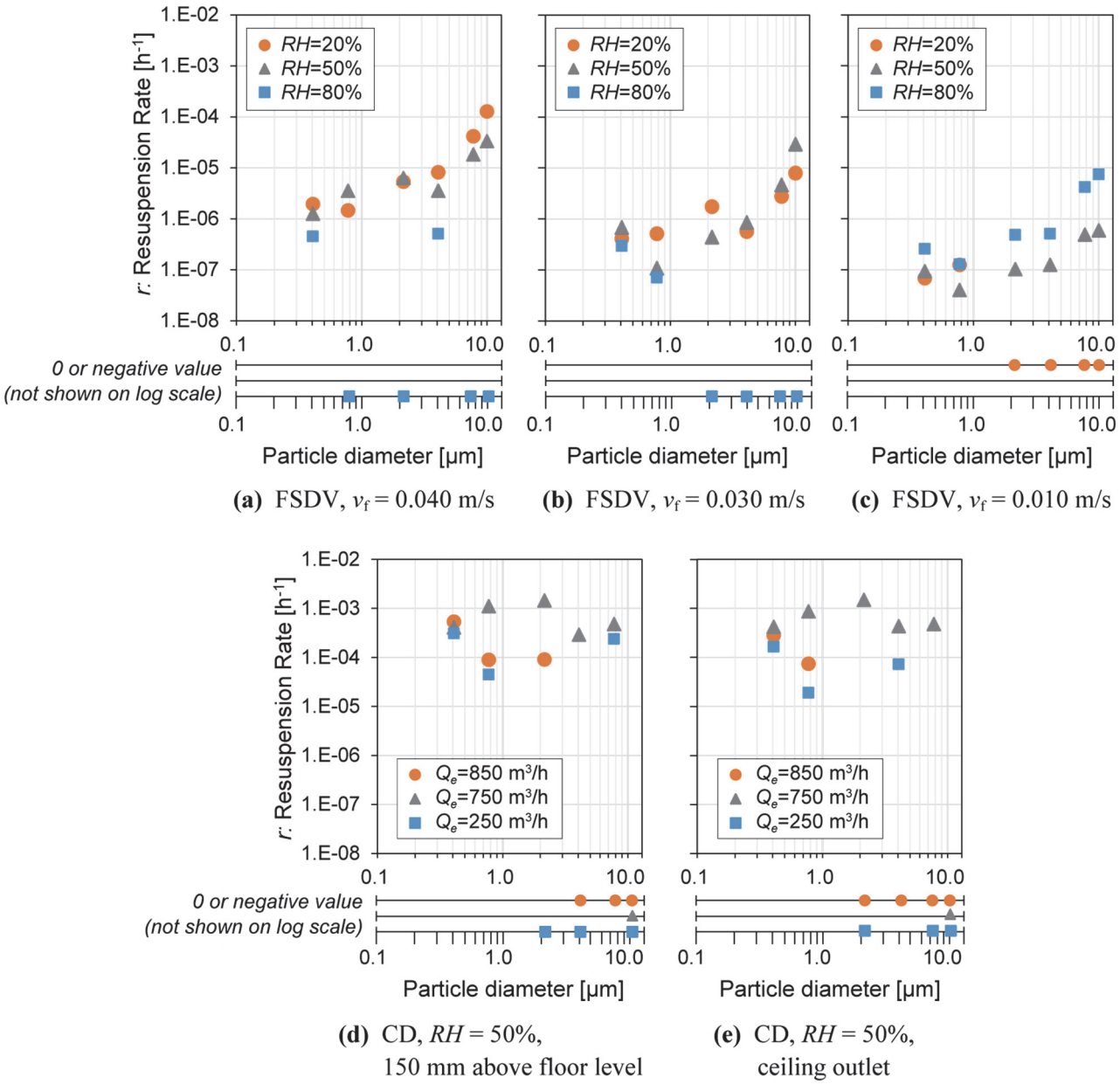


Figure 6-10. Size-resolved resuspension rates (r, [h^{-1}]) under each experimental condition (both axes in logarithmic scale). (a–c) FSDV cases with floor supply velocities (v_f) of 0.040, 0.030, and 0.010 m/s, respectively, at relative humidities (RH) of 20%, 50%, and 80%, measured 150 mm above the floor. (d, e) CD cases at RH = 50%, measured 150 mm above the floor (d) and at the ceiling outlet (e). For CD, ventilation rates Q_e were 850, 750, and 250 m³/h. The lower panels indicate data points with zero or negative values (not shown on log scale).

6.3.3 Close-Up Images of the Carpet

The carpet fibers were imaged using a Phone Micro 5 microscope (APEXEL, MS200) at 200× magnification. The camera had a resolution of 12 MP (4032 × 3024 pixels). Close-up images are shown in **Figure 6-11**. Image pairs (a) and (a′) correspond to the same locations, respectively. Images (a)–(e) were taken before airflow exposure, whereas (a′)–(e′) were taken after 30 minutes of airflow exposure. These observations were conducted under the conditions of v_f = 0.040 m/s and 50% relative humidity.

The air-permeable carpet was installed over a metal panel with evenly spaced perforations, each 6 mm in diameter, and the photographed fibers were located directly above these holes. Each perforated panel contained 328 holes (6 mm diameter), giving an open area ratio of approximately 4.5%. From the 160× images, regions showing visible changes were selected and further magnified to 800× for detailed comparison.

The pre-exposure images (**Figure 6-11a–e**) show numerous particle aggregates larger than 10 μm. Approximately 50% of Ryukakusan particles have a volume-based diameter of ≤7.7 μm [98]; however, because of image resolution limitations, the presence and condition of submicron particles could not be clearly evaluated, making it difficult to determine the adhesion ratio for each particle size. The large aggregates observed may have either been deposited as clusters during the spraying process using the cosmetic powder sprayer or coalesced on the fiber surface after deposition.

When comparing the close-up images taken after airflow exposure (**Figure 6-11a′–e′**) with those taken before exposure (**Figure 6-11a–e**), several particles in the 50–100 μm range appear to have moved or disappeared from the field of view. This phenomenon is likely attributed to the increase in aerodynamic drag with particle size, while the contact area remains nearly constant, resulting in a relatively weaker adhesive force. In **Figure 6-11b′**, a marked reduction in the number of particles on a specific fiber bundle is evident, suggesting the presence of localized high-velocity airflow. Considering that the perforated panel has an open-area ratio of about 4.5%, the local air velocity through each 6 mm hole can be estimated to be approximately 0.88 m/s under a total flow rate of 1000 m³/h.

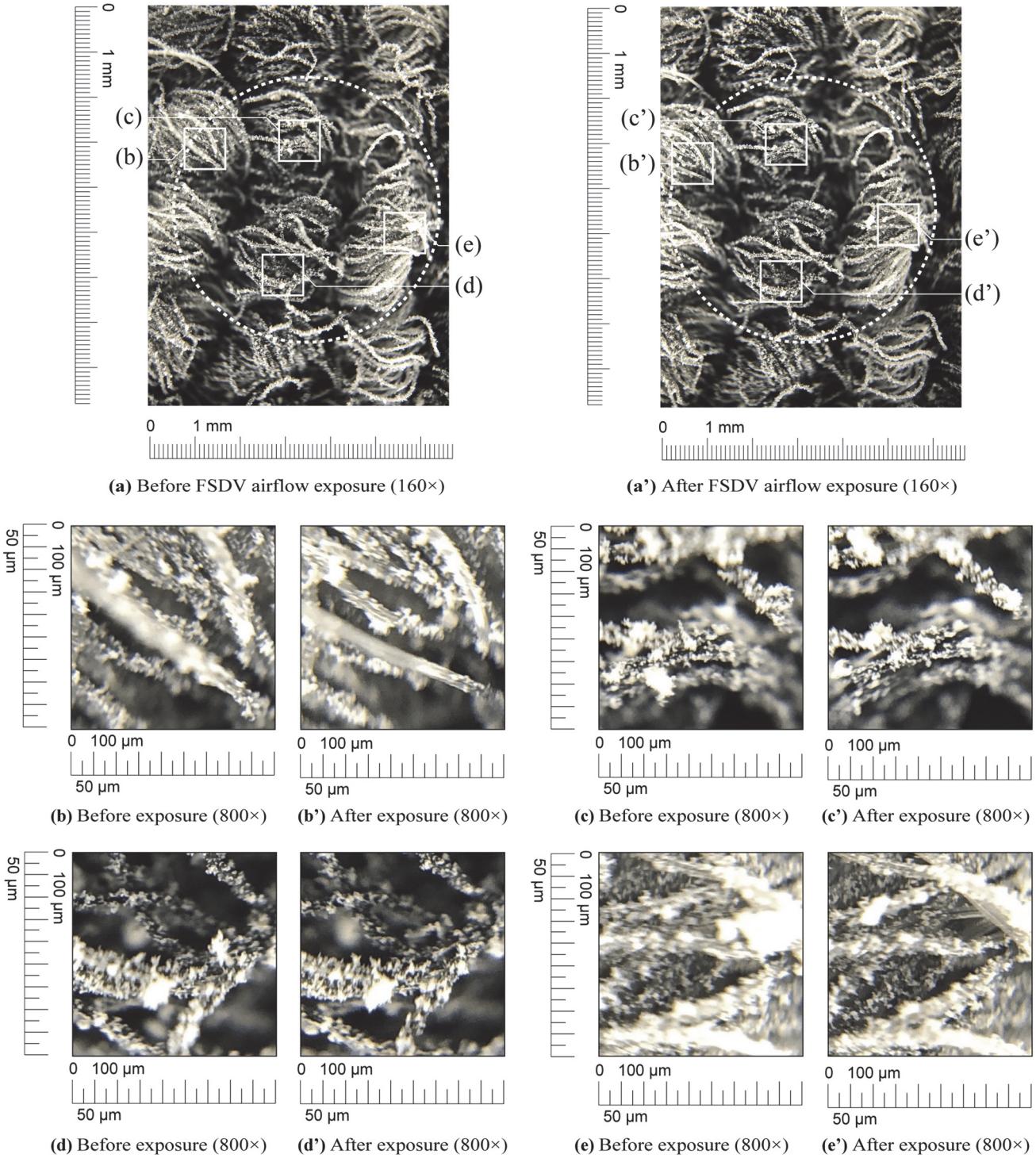


Figure 6-11. Close-up images of the carpet in Case FSDV_0.04_50. (a) Before airflow exposure (magnification: 160×); (a') After 30 min of airflow exposure (magnification: 160×). White dotted circles in (a) and (a') indicate approximate positions of the 6 mm diameter punched metal holes. (b–e) Before airflow exposure (magnification: 800×); (b'–e') After 30 min of airflow exposure (magnification: 800×). Matching alphabetical labels indicate the same locations.

6.4 Discussion

6.4.1 Estimation of Particle Behavior after Resuspension

The time series of indoor particle concentration measurements (**Figure 6-7**) confirmed that, before the carpet installation, the background particle concentration was approximately 2.5×10^4 m^{-3} for particles in the 0.3–0.5 μm range, while the concentrations of larger particles were significantly lower or nearly zero. When the carpet with deposited particles was installed, numerous peaks—interpreted as resuspension events—were observed. As the measurement height increased, both the amplitude and the frequency of these peaks decreased (**Figure 6-8**). Although the particle number concentration was dominated by smaller particles (0.3–0.5 μm), the resuspension rate, when evaluated on a mass basis, increased with particle size under FSDV conditions (**Figures 6-10a–c**). It should be noted, however, that the evaluation of resuspension rates under FSDV conditions was based on measurements obtained at 150 mm above the floor. Thus, the post-resuspension particle behavior requires further examination.

The behavior of particles after resuspension was analyzed by examining the balance between gravitational and aerodynamic drag forces—specifically, the relationship between the terminal settling velocity (v_g) and the area-averaged supply air velocity (v_u). The motion of a resuspended particle can be expressed by Newton's second law as the balance between gravitational and drag forces, as shown in Eq. (6-11):

$$m_p \frac{dv}{dt} = -F_D + F_g \qquad (6-11)$$

where m_p is the mass of a single particle [kg], F_D is the aerodynamic drag force acting on a particle [N], and F_g is the gravitational force acting on a particle [N].

The aerodynamic drag force (F_D) acting on a particle moving in air is given by Eq. (6-12):

$$F_D = C_D A_p \cdot \rho_f \, v_r^2/2 \qquad (6-12)$$

where C_D is the drag coefficient [–], A_p is the projected cross-sectional area of the particle (= $\pi D_p^2/4$) [m^2], ρ_f is the air density [kg/m^3], and v_r is the relative velocity between the particle and the surrounding airflow [m/s].

Since the particle Reynolds number (Re_p) calculated under all conditions was below 2, the drag coefficient was determined using Stokes' law, as shown in Eq. (6-13):

$$C_D = 24/Re_p : Re_p < 2 \quad (6-13)$$

where Re_p is the particle Reynolds number (= $\rho_f D_p v_r/\mu$) [–], D_p is the particle diameter [m], and μ is the dynamic viscosity of air [Pa·s].

By substituting Eq. (6-13) into Eq. (6-11) under steady-state conditions (dv/dt = 0), the terminal settling velocity v_g due to gravity can be expressed as Eq. (6-14):

$$v_g = (\rho_p - \rho_f) D_p^2 g/18\mu : Re_p < 2 \quad (6-14)$$

where ρ_p is the particle density [kg/m³] and g is the gravitational acceleration (9.81 m/s²). The relationship between gravitational and drag forces acting on particles is illustrated in **Figure 6-12a**.

The area-averaged supply air velocity v_u in the test chamber was calculated by dividing the exhaust airflow rate Q_e by the total chamber floor area A_c, as shown in (Eq. 6-15):

$$v_u = Q_e/A_c \quad (6-15)$$

Finally, the estimated time (t_c) required for a particle to reach the ceiling height (H_c) can be derived from the relative velocity between the upward supply airflow (v_u) and the terminal settling velocity (v_g), as expressed in Eq. (6-16):

$$t_c = H_c/(v_u - v_g) \quad (6-16)$$

The results of this estimation are shown in **Figure 6-12b**.

According to **Figure 6-12a**, when comparing the balance between gravitational and aerodynamic drag forces, the upward supply airflow dominates for particles smaller than approximately 10 μm. Under the 1000 m³/h and 750 m³/h conditions, corresponding to ventilation rates of approximately 50 h⁻¹ and 37 h⁻¹, respec-

tively, which are considerably higher than those in typical office environments, the upward airflow exceeds the gravitational settling velocity even for particles larger than 10 μm. In contrast, under the 250 m³/h condition (equivalent to 12.5 h^{-1}), gravitational settling becomes dominant for particles larger than about 10 μm. However, as shown in **Figure 6-8d**, particles larger than 10 μm were rarely detected near the exhaust outlet. This is likely because the measurement point represented only a very small portion of the total exhaust area. The estimated time required for resuspended particles to reach the ceiling outlet was approximately 100 s under the 1000 m³/h and 750 m³/h conditions, and about 300 s under the 250 m³/h condition (**Figure 6-12b**). These findings suggest that, although the overall amount of resuspension is limited under typical ventilation rates (around 12–13 h^{-1}), once resuspended, particles may remain suspended in the room air for approximately five minutes before being exhausted.

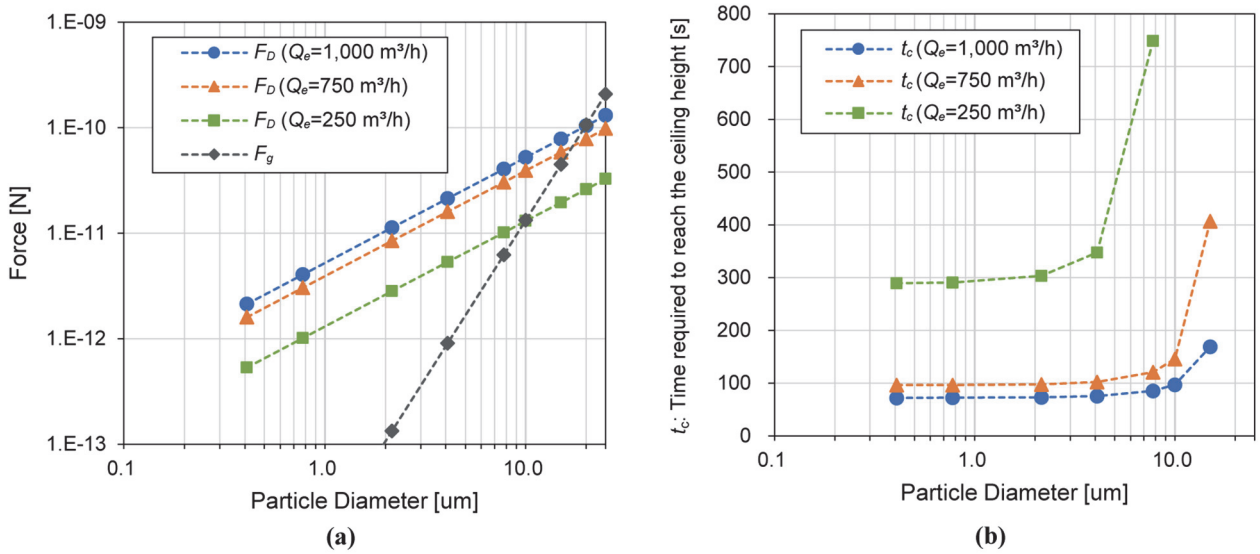


Figure 6-12. Calculations for particle movement estimation. (a) Relationship between drag force (F_d) and gravitational force (F_g). (b) t_c: Time required to reach the ceiling height [s] under each ventilation volume.

6.4.2 Summary of Key Findings

Based on the obtained results, the key findings are summarized as follows.

Peaks attributed to resuspension were dominant in the smaller particle size range (0.3–0.5 μm) in terms of number concentration (**Figure 6-8**). However, when evaluated in terms of mass, the resuspension rate tended to increase with particle size under FSDV conditions (**Figures 6-10a–c**). From the balance between gravi-

tational and aerodynamic forces, it was found that upward airflow dominated over gravity at 1000 m³/h (50 ACH) and 750 m³/h (37 ACH), whereas gravity became dominant for particles larger than approximately 10 μm at 250 m³/h (13 ACH) (**Figure 6-12a**). In **Figure 6-8a**, few peaks were detected near the ceiling outlet under the 1000 m³/h condition, likely because the resuspended particles became highly diluted before reaching the outlet and because the measurement point represented only a very small portion of the total exhaust area.

The effects of floor supply velocity (0.04, 0.03, and 0.01 m/s) and relative humidity (20%, 50%, and 80%) were pronounced. In particular, at 0.04 m/s, the resuspension rate increased significantly as relative humidity decreased, whereas at 0.01 m/s, the overall resuspension rates were small, and the influence of humidity was relatively minor (**Figures 6-10a–c**).

The ventilation mode also had a substantial impact on resuspension behavior (**Figure 6-10**). Under FSDV conditions, the resuspension rate ranged approximately from 10^{-8} to 10^{-4} h^{-1}, increasing with particle size. In contrast, under CD conditions, the resuspension rate ranged from 10^{-5} to 10^{-3} h^{-1} for smaller particles (0.3–3 μm), but was nearly zero or even negative for larger particles (≥ 10 μm). These results suggest that the dominant resuspension mechanisms differ between FSDV and CD. Under FSDV conditions, microscopic observations (**Figure 6-11**) indicated that particle agglomerates larger than 10 μm were more easily resuspended, as their exposed surface area to airflow was relatively large compared with their adhesion area, resulting in greater resuspension by the upward airflow. Conversely, under CD conditions, resuspension likely occurred primarily for smaller particles that were less influenced by adhesive or gravitational forces, driven by the shear forces generated by horizontal airflow. After resuspension, these particles dispersed uniformly throughout the chamber. For particles larger than 10 μm, surface rolling or “saltation” motion may also have occurred. However, since the calculation methods used to estimate the resuspension rate differed between the two ventilation systems, the difference in magnitude alone cannot be used to conclude that CD inherently produces greater resuspension than FSDV.

Microscopic observations further supported these findings. Noticeable changes were primarily observed in larger agglomerates exceeding 10 μm, and resuspension occurred locally in regions exposed to stronger airflow in FSDV. However, such changes were observed only in areas located directly above the 6 mm ventilation holes, whereas most other regions exhibited no noticeable change.

Regarding the order of airflow velocity, based on the opening ratio, the local air velocity through each 6 mm hole was estimated to be approximately 0.88 m/s under a total flow rate of 1000 m³/h in the FSDV condition. In the CD condition with a total flow rate of 850 m³/h, the airflow velocity was also measured using an

ultrasonic anemometer (SONIC Corporation, DA-700; probe: TR-92T, 3 cm). At a height of 50 mm above the particle-distributed carpet, the 5-minute averaged horizontal velocity was approximately 0.50 m/s, and the absolute velocity magnitude was 0.55 m/s.

6.4.3 Comparison with Previous Studies

The resuspension rates obtained in this study ranged from approximately 10^{-8} to 10^{-4} h^{-1} under FSDV conditions and from 10^{-5} to 10^{-3} h^{-1} under CD conditions. A wide range of resuspension rates has been reported in previous studies under various experimental conditions. In their review paper, Qian et al. (2014) [41] summarized numerous studies on resuspension caused by walking activities. For example, Gomes et al. (2007) [49] reported that the resuspension rate on quartz and roach-type carpets exposed to an airflow of 1.5 m/s ranged from 10^{-7} to 10^{-3} min^{-1} (equivalent to 10^{-6}–10^{-2} h^{-1}), which is comparable to the order of magnitude observed in this study. Qian et al. (2008) [53] estimated resuspension rates of 10^{-5}–10^{-2} h^{-1} during walking on carpeted floors, while Tian et al. (2014) [99] reported values in the range of 10^{-4}–10^{-1} h^{-1}.

Although the test particles and humidity conditions differed among studies, most investigations on walking-induced resuspension over carpeted floors under conventional ventilation systems reported rates within 10^{-4}–10^{-1} h^{-1} [41,42]. The values obtained in this study under FSDV conditions are therefore comparable to or lower than those induced by airflow shear or human walking, suggesting that airflow-induced resuspension under FSDV is substantially smaller than walking-induced resuspension. At the very least, it can be concluded that FSDV does not promote particle resuspension more strongly than other ventilation methods. Furthermore, many previous studies have shown that larger particles tend to exhibit higher resuspension rates, which is consistent with the results obtained under FSDV conditions in this study [53,99,100].

The resuspension mechanisms are also known to differ significantly depending on the deposition structure. Specifically, particles deposited in multilayer configurations have been found to resuspend more readily than those forming a single layer [43,56]. As shown in the microscopic images (**Figure 6-11**), most of the particles in this study formed multilayered aggregates adhering to the carpet fibers. These aggregated particle clusters —previously identified as “cluster feet” [43]— likely exhibited greater susceptibility to airflow drag forces due to their irregular shapes and exposed surface area, which may have facilitated their resuspension under FSDV conditions.

6.4.4 Limitations and Implications for Future Work

This study has several limitations that should be acknowledged:

· The mass fraction of test particles in each size class (f_p) was referenced from Y. Takeuchi et al. (2022) [98]. However, the actual particle size distribution on the carpet may have been biased toward larger diameters, as suggested by **Figure 6-11**. Higher-magnification microscopic analysis would enable a more accurate estimation of f_p.

· Although Ryukakusan exhibits a particle density and size distribution similar to—but slightly larger than—Arizona Test Dust A1 (ATD A1), which has been widely used in previous resuspension studies [53,97,101,102], further validation is required to confirm whether it behaves comparably in terms of resuspension characteristics relative to dust or infectious particles.

· Because ambient humidity during particle dispersion in the entrance hall also affects adhesive forces, improved humidity control during the dispersion process would allow for more accurate comparisons among test conditions.

· Since humidity control in this study was achieved through temperature adjustments, the temperature varied from 17 °C to 36 °C across the experimental cases (**Table 6-B-1**). Maintaining a uniform temperature across all test conditions could further enhance the reliability of comparative analysis.

· Under conditions with a floor supply velocity of 0.010 m/s, the overall resuspension was extremely low. Consequently, adhesive forces and temperature variations may have exerted relatively strong influences, potentially reducing the reproducibility of the results.

· To provide more statistically robust data, each experimental condition should ideally be repeated multiple times. However, due to resource constraints, this was not feasible in the present study, and reproducibility could not be fully assessed.

In future studies, it will be important to clarify the quantitative relationship between particle resuspension and infection risk. Additionally, experimental investigations should be conducted to evaluate resuspension rates under FSDV airflow when external disturbances such as walking or falling objects are present.

6.5 Conclusion

This chapter experimentally investigated the resuspension behavior of fine particles deposited on an air-permeable carpet under floor-supply displacement ventilation (FSDV) airflow. The focus was on understanding the aerodynamic resuspension mechanisms in calm airflow conditions, where gravitational settling was found to be dominant in Chapter 5. For comparison, additional experiments were conducted under conventional ceiling diffuser (CD) conditions. The study aimed to clarify how supply air velocity and relative humidity affect particle resuspension, which represents a critical factor in maintaining indoor cleanliness in spaces where FSDV is applied for airborne infection control.

The main findings of this chapter are summarized as follows:

Effect of airflow velocity and humidity

・Under FSDV conditions with a floor supply velocity of v_f = 0.040 m/s (equivalent to 50 ACH), the resuspension rate ranged from 10^{-7} to 10^{-4} h^{-1}. Increasing relative humidity markedly suppressed resuspension, with negligible re-entrainment at 80% RH. When the velocity was reduced to vf = 0.010 m/s (12 ACH), the resuspension rate decreased to 10^{-8}–10^{-5} h^{-1} and showed minimal dependence on humidity.

Comparison with previous studies

・The resuspension rates observed under FSDV airflow (10^{-8}–10^{-4} h^{-1}) were comparable to those reported under 1.5 m/s swirling diffuser flow [49] and substantially lower than those associated with human walking on conventional floors [41,42]. This indicates that FSDV does not promote excessive resuspension, even at relatively high ventilation rates.

Results under ceiling diffuser conditions

・Under CD airflow, smaller particles (0.3–3 μm) showed resuspension rates of 10^{-5}–10^{-3} h^{-1}, while larger particles (≥ 10 μm) exhibited nearly zero or even negative rates. However, due to differences in flow structure and calculation assumptions, these values cannot be directly compared to those obtained under FSDV conditions.

Particle size dependency

・However, under FSDV, larger particles contributed more significantly to the total resuspended mass, likely due to stronger aerodynamic lift acting on their relatively larger exposed surface area.

Microscopic observations

・Microscopic images of the carpet surface revealed multilayer clusters of particles larger than 10 μm adhering to fibers. Some of these “cluster feet” were displaced under FSDV airflow at v_f = 0.040 m/s and 50% RH, confirming the localized nature of resuspension near the ventilation holes.

Spatial characteristics of resuspension

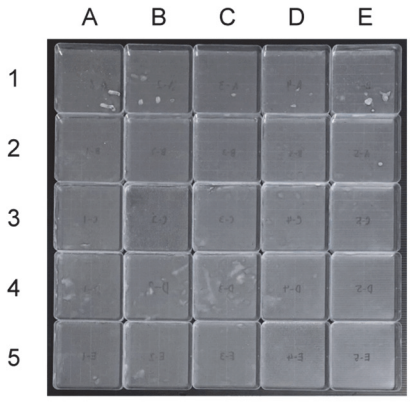
・Resuspension primarily occurred in localized regions directly above the 6 mm perforations beneath the carpet, where upward airflow was most concentrated.

In summary, this study demonstrated that airflow-induced particle resuspension under FSDV is not excessive and remains within a manageable range for indoor environments. Particularly under the recommended operational condition of 12 ACH, the system maintains both high contaminant removal efficiency and low resuspension potential. Although further investigation is required to account for mechanical disturbances such as human walking, the present study successfully established a quantitative experimental framework for evaluating resuspension under FSDV airflow. These results provide a foundation for future studies on dynamic resuspension phenomena and offer valuable insights for HVAC design and infection control strategies in calm, displacement-ventilated environments.

6.6 Appendix 6-A: Validation of Uniform Particle Distribution

An experiment was conducted to verify the uniformity of particle distribution from the powder-spraying device shown in **Figure 6-4**. The test conditions were identical to those used in the main experiment, including the spraying height and device. Twenty-five Petri dishes (100 × 100 mm each) were arranged in a 5 × 5 grid on the deposition surface, and the increase in mass of each dish was measured using a tuning fork-type electronic balance (RJ-620, Shinko Denshi Co., Ltd.; minimum resolution: 0.001 g). The upper opening of the wind shield was divided into sixteen equal sections (**Figure 6-5a**). From each section, fifteen sprays were applied sequentially in rotation, rather than repeatedly at the same point, to prevent localized accumulation. Each spraying cycle required approximately ten minutes to complete, and the entire procedure was repeated three times.

Photographs taken after spraying, the measured mass increases, and their relative spatial distributions are presented in **Figure 6-A-1**, while the total and statistical results (mean and standard deviation) are summarized in **Table 6-A-1**. As seen in **Figure 6-A-1a, d, g**, the visual appearance differed noticeably between the first and the second/third trials. This variation is attributed to differences in ambient relative humidity between test days, which likely altered the surface condition of the Petri dishes. In the ideal case, each of the twenty-five dishes would account for 4 % of the total mass increase. The experimental results (**Figure 6-A-1c, f, i**) showed that all dishes fell within 4 ± 0.5 %. According to **Table 6-A-1**, the total mass increase across all dishes was 0.971 ± 0.097 g, corresponding to an average increase of 0.339 ± 0.004 g per dish. The ratio of the standard deviation to the mean for individual dishes was 0.091, confirming that the particle distribution achieved uniformity within approximately 1 %.



(a)

	A	B	C	D	E
1	0.034 g	0.032 g	0.031 g	0.034 g	0.031 g
2	0.033 g	0.035 g	0.036 g	0.035 g	0.030 g
3	0.032 g	0.034 g	0.037 g	0.039 g	0.033 g
4	0.037 g	0.038 g	0.040 g	0.038 g	0.033 g
5	0.035 g	0.038 g	0.036 g	0.034 g	0.033 g

(b)

	A	B	C	D	E
1	3.9 %	3.7 %	3.6 %	3.9 %	3.6 %
2	3.8 %	4.0 %	4.1 %	4.0 %	3.5 %
3	3.7 %	3.9 %	4.3 %	4.5 %	3.8 %
4	4.3 %	4.4 %	4.6 %	4.4 %	3.8 %
5	4.0 %	4.4 %	4.1 %	3.9 %	3.8 %

(c)



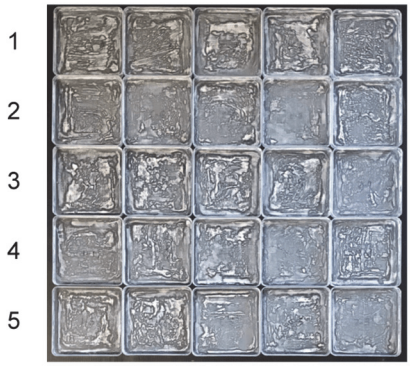
(d)

	A	B	C	D	E
1	0.043 g	0.041 g	0.041 g	0.049 g	0.044 g
2	0.034 g	0.043 g	0.045 g	0.048 g	0.044 g
3	0.039 g	0.047 g	0.048 g	0.051 g	0.042 g
4	0.038 g	0.042 g	0.042 g	0.047 g	0.040 g
5	0.034 g	0.039 g	0.040 g	0.041 g	0.039 g

(e)

	A	B	C	D	E
1	4.1 %	3.9 %	3.9 %	4.6 %	4.1 %
2	3.2 %	4.1 %	4.2 %	4.5 %	4.1 %
3	3.7 %	4.4 %	4.5 %	4.8 %	4.0 %
4	3.6 %	4.0 %	4.0 %	4.4 %	3.8 %
5	3.2 %	3.7 %	3.8 %	3.9 %	3.7 %

(f)



(g)

	A	B	C	D	E
1	0.037 g	0.036 g	0.041 g	0.044 g	0.038 g
2	0.034 g	0.036 g	0.039 g	0.040 g	0.039 g
3	0.035 g	0.043 g	0.044 g	0.044 g	0.037 g
4	0.033 g	0.039 g	0.040 g	0.037 g	0.038 g
5	0.039 g	0.044 g	0.045 g	0.046 g	0.035 g

(h)

	A	B	C	D	E
1	3.8 %	3.7 %	4.2 %	4.5 %	3.9 %
2	3.5 %	3.7 %	4.0 %	4.1 %	4.0 %
3	3.6 %	4.4 %	4.5 %	4.5 %	3.8 %
4	3.4 %	4.0 %	4.1 %	3.8 %	3.9 %
5	4.0 %	4.5 %	4.6 %	4.7 %	3.6 %

(i)

Figure 6-A-1. Results of spraying powder onto Petri dishes from a height of 400 mm using the device shown in **Figure 6-4b** (240 sprays). (a, d, g) Photographs after spraying; (b, e, h) Increase in dish weight [g]; (c, f, i) Relative contribution of each dish to the total weight increase [%]. (a–c) First trial; (d–f) Second trial; (g–i) Third trial.

Table 6-A-1

Deposited powder mass on Petri dishes in three spraying trials (240 sprays per trial).

Trial	Total [g]	Average [g]	SD_p [g]	CV [-]
1	0.868	0.035	0.003	0.077
2	1.061	0.042	0.004	0.102
3	0.983	0.039	0.004	0.094
Mean ± SD	0.971 ± 0.097	0.039 ± 0.004	0.004	0.091

The average mass increase per Petri dish was calculated as the total divided by 25. SD_p: Standard deviation of the mass increase among the 25 Petri dishes; CV: Coefficient of variation (SD_p / Average). The bottom row presents the mean ± SD_p across the three trials. For SD_p and CV, only the mean values are shown.

6.7 Appendix 6-B: Temperature and Relative Humidity during the Experiments

Details of the temperature, relative humidity, ventilation rate, and mass of the dispersed powder during the experiments are summarized in **Table 6-B-1**.

Table 6-B-1

Details of experimental conditions measured in each test.

Test name	$RH(t)$ [%]	$T(t)$ [℃]	$AH(t)$ [g/m^3]	$RH(s)$ [%]	$T(s)$ [℃]	$AH(s)$ [g/m^3]	$RH(e)$ [%]	$T(e)$ [℃]	$AH(e)$ [g/m^3]	Q_e [m^3/h]	L_{Total} [g]
FSDV_0.04_20	19.2 ± 0.4	28.1 ± 0.1	5.23 ± 0.11	36.2 ± 0.3	20.3 ± 0.1	6.37 ± 0.03	38.2 ± 0.4	19.3 ± 0.1	6.34 ± 0.06	990	1.001
FSDV_0.04_50	53.2 ± 5.3	18.7 ± 0.6	8.54 ± 0.97	52.9 ± 0.8	19.9 ± 0.0	9.08 ± 0.14	54.1 ± 0.1	19.9 ± 0.1	9.30 ± 0.06	990	1.014
FSDV_0.04_80	82.3 ± 0.8	17.3 ± 0.2	12.11 ± 0.05	69.0 ± 0.9	18.7 ± 0.0	11.08 ± 0.14	66.8 ± 0.4	18.3 ± 0.1	10.46 ± 0.04	990	0.992
FSDV_0.03_20	19.3 ± 0.5	33.3 ± 0.1	6.97 ± 0.20	35.9 ± 0.3	25.4 ± 0.1	8.45 ± 0.07	40.3 ± 0.6	23.2 ± 0.1	8.40 ± 0.13	748 ± 4	1.019
FSDV_0.03_50	49.8 ± 1.1	21.6 ± 0.3	9.47 ± 0.16	60.4 ± 0.4	19.7 ± 0.0	10.25 ± 0.04	60.3 ± 0.4	19.7 ± 0.1	10.27 ± 0.06	757 ± 9	1.002
FSDV_0.03_80	79.2 ± 0.5	17.7 ± 0.1	11.93 ± 0.09	69.8 ± 0.3	18.8 ± 0.0	11.24 ± 0.05	70.3 ± 0.3	18.2 ± 0.1	10.94 ± 0.09	740 ± 7	1.009
FSDV_0.01_20	16.7 ± 0.5	28.0 ± 0.4	4.55 ± 0.14	39.8 ± 1.5	18.7 ± 0.1	6.37 ± 0.22	42.7 ± 0.7	17.1 ± 0.2	6.23 ± 0.17	241 ± 1	1.001
FSDV_0.01_50	43.0 ± 6.3	19.1 ± 0.7	7.04 ± 0.82	45.2 ± 1.8	22.1 ± 0.1	8.84 ± 0.37	44.8 ± 0.8	22.2 ± 0.4	8.77 ± 0.24	246 ± 1	0.999
FSDV_0.01_80	73.3 ± 3.9	21.6 ± 0.1	13.90 ± 0.69	73.4 ± 0.8	22.1 ± 0.0	14.35 ± 0.15	73.5 ± 0.5	22.0 ± 0.3	14.17 ± 1.31	246 ± 1	0.986
CD_850_50	46.4 ± 0.7	36.5 ± 0.1	19.88 ± 0.25	58.8 ± 0.5	33.0 ± 0.1	20.98 ± 0.14	57.0 ± 0.8	33.1 ± 0.1	20.44 ± 0.17	848 ± 10	1.024
CD_750_50	45.4 ± 1.6	27.9 ± 0.2	12.28 ± 0.35	62.4 ± 0.6	24.7 ± 0.1	14.13 ± 0.11	64.6 ± 0.4	24.3 ± 0.0	14.31 ± 0.07	756 ± 6	1.003
CD_250_50	46.3 ± 0.8	23.9 ± 0.2	10.00 ± 0.16	48.8 ± 0.8	25.1 ± 0.2	11.32 ± 0.12	48.2 ± 0.5	25.7 ± 0.1	11.58 ± 0.09	254 ± 1	1.024
FSDV_0.04_20_no	21.0 ± 0.6	27.0 ± 0.4	5.42 ± 0.11	35.9 ± 1.6	20.1 ± 0.6	6.24 ± 0.07	36.7 ± 1.1	18.8 ± 0.1	5.90 ± 0.21	990	-
CD_850_50_no	49.1 ± 1.1	35.4 ± 0.2	19.88 ± 0.29	60.7 ± 0.6	32.3 ± 0.2	20.80 ± 0.05	60.0 ± 0.3	32.3 ± 0.1	20.64 ± 0.02	848 ± 10	-

Measurement locations are shown in **Figure 6-2**. (t): Test chamber; (s): Surrounding space; (e): Entrance hall. Values are expressed as mean ± standard deviation over the experimental duration, except for L_{total}. AH is calculated from RH and T using Eqs. (6-1)~(6-3). Q_e is calculated from the CO_2 balance measured in exhaust duct. Q_e = 990 m^3/h indicates the set value of the constant air volume system (CAV); the ventilation volume was automatically adjusted.

7 General Conclusions

7.1 Summary of Each Chapter

A summary of each chapter is provided as follows:

Chapter 2: CFD Analysis of Local Exhaust Ventilation for Close-Contact Conversation

This chapter examined the performance of a combined local exhaust ventilation (LEV) and floor-supply displacement ventilation (FSDV) system through steady-state CFD analysis, using experimentally measured exhalation data during Japanese speech as boundary conditions.

The measured mean exhalation velocity, flow rate, and angle were 0.30 m/s, 5.21 L/min, and 11.9°, respectively, providing a realistic representation of close-distance conversation. The simulations revealed that the hood exhaust flow rate (Q_h) and the balance between hood and ceiling exhaust were the dominant factors influencing capture efficiency (η). When the hood's capture region completely covered the source, cross-contamination between the infector and the doctor's breathing zone was effectively prevented.

At lower ventilation rates (6 ACH), the FSDV alone could not sufficiently suppress airborne contaminants; however, introducing an LEV hood directly above the source reduced the quanta concentration in front of the doctor's mouth by over two orders of magnitude, demonstrating a substantial reduction in infection risk. These findings are validated and confirmed in the following Chapters 4 and 5.

Chapter 3: Experimental Evaluation of Different Underfloor Air-Distribution Systems without LEV

This chapter presented full-scale experimental comparisons of four air distribution systems—floor-supply displacement ventilation (FSDV), horizontal flow-type floor diffuser (HFD), swirling flow-type floor diffuser (SFD), and ceiling diffuser (CD)—to evaluate their contaminant removal efficiency and thermal comfort at various ventilation rates (6–24 ACH).

Distinct airflow patterns were observed among the systems. The CD and SFD generated mixed flow fields, while the HFD and FSDV produced displacement-type airflow. Among them, the FSDV exhibited the most stable vertical concentration profile, maintaining the lowest contaminant levels across all airflow conditions. This confirmed the superior capability of FSDV in limiting the upward spread of exhaled human breath.

The contaminant removal efficiency (ε_{OZ}) of the FSDV increased with airflow rate and exceeded that of other systems, demonstrating its dominant removal performance. In contrast, the HFD and SFD were more sensitive to airflow rate, showing efficiency reduction at higher supply volumes.

Regarding thermal comfort, all floor-supply systems maintained vertical temperature differences of less than 2 °C between head and foot levels, satisfying the ASHRAE 55 criteria.

Overall, the FSDV achieved both high contaminant removal efficiency and thermal comfort stability, making it the most promising system for environments requiring strict air cleanliness control. These findings provide a fundamental reference for the subsequent experimental investigation (Chapter 4), which examines the synergistic effect of combining LEV with general ventilation systems for reducing infection risk.

Chapter 4: Experimental Evaluation of LEV Performance under Different Ventilation Systems

This chapter presented full-scale experimental evaluations of local exhaust ventilation (LEV) performance under four air distribution systems: FSDV, HFD, SFD, and CD, at various ventilation rates (6–24 ACH).

Without the hood, airflow patterns were consistent with those in Chapter 3: CD and SFD exhibited mixed ventilation, while HFD and FSDV formed displacement-type airflow patterns. When an LEV hood (100 m^3/h) was placed above the patient's head, contaminants previously accumulated above 1.5 m were almost eliminated, particularly in the FSDV and HFD cases, demonstrating a substantial reduction in infection risk. The hood capture efficiency (η) exceeded 80% for FSDV, HFD, and CD but fell to around 30% for SFD at higher ventilation rates. While η decreased with ventilation rate for HFD, SFD, and CD, it increased for FSDV, owing to its stable upward piston airflow. This indicates that FSDV + LEV provides the most consistent and effective contaminant removal performance.

The infection risk assessment revealed that FSDV maintained near-zero exposure levels, with the time for infection probability to reach 5% ($t_{5\%}$) exceeding 100 h, even without the hood. The LEV further minimized quanta concentration in the doctor's breathing zone, confirming its strong synergistic effect.

Overall, the combination of FSDV and LEV achieved superior contaminant removal, energy efficiency, and infection risk suppression, validating its applicability to high-cleanliness environments such as consulting rooms, hospitals, and cleanrooms.

Chapter 5: Experimental Investigation of Droplet and Droplet Nuclei Behavior at High Ventilation Rates

This chapter experimentally evaluated the performance of local exhaust ventilation (LEV) systems as an airborne infection control measure under high ventilation conditions (1,000 m^3/h, 50 ACH). Three underfloor air distribution types (FSDV, HFD, and SFD) were tested in two scenarios: Case A, where the hood was positioned above the infector's head, and Case B, where the hood was installed between two individuals. Unlike Chapter 4, both CO_2 tracer gas and artificial saliva particles were used to represent droplet nuclei and droplets, respectively, allowing for a direct comparison between gaseous and particulate transmission behaviors.

The dispersion and infection risk followed the trend FSDV < HFD < SFD, consistent with the increasing turbulence of ambient airflow. The FSDV achieved the lowest quanta concentrations in front of the doctor's mouth, demonstrating its superior performance in suppressing exhaled contaminant spread. The hood placement had a strong influence on effectiveness: in Case A, LEV installation substantially reduced the infection risk across all systems, whereas in Case B, the effect was limited due to greater ambient flow interference.

Comparing gas and particle results, tracer gas consistently produced higher quanta concentrations than particles, representing a safety-side estimate. Under calm FSDV airflow, gravitational settling and adhesion further reduced airborne particle concentrations. Even under high ventilation, the FSDV maintained gentle, upward airflow, thereby minimizing horizontal dispersion and reducing the risk of airborne infection. These findings clarify the distinct behaviors of droplets and droplet nuclei, forming the basis for Chapter 6, which investigates particle resuspension phenomena under FSDV conditions.

Chapter 6: Airflow-Induced Particle Resuspension under FSDV Conditions

This chapter experimentally examined airflow-induced particle resuspension under floor-supply displacement ventilation (FSDV), focusing on calm airflow environments where gravitational settling was shown to dominate in Chapter 5. Fine particles (D_{50} = 7.7 μm) were uniformly deposited on an air-permeable carpet, and resuspension behavior was evaluated under varying supply air velocities (v_f = 0.010–0.040 m/s) and relative humidity levels (20–80%). For comparison, additional experiments were conducted under ceiling diffuser (CD) conditions.

Under FSDV, resuspension rates ranged from 10^{-8} to 10^{-4} h^{-1}, showing strong suppression with increasing humidity and minimal dependence below 12 ACH (v_f = 0.010 m/s). Even at 50 ACH, resuspension remained limited, confirming that FSDV does not promote excessive particle resuspension. The results were

comparable to those reported for 1.5 m/s swirling diffuser flows [49] and much lower than rates induced by human walking [41,42]. Microscopic observations revealed localized resuspension near 6 mm ventilation holes, where upward airflow was concentrated, and identified multilayer particle clusters (>10 μm) adhering to carpet fibers. Larger particles contributed more significantly to the total resuspended mass due to their greater aerodynamic lift relative to the adhesion area.

Overall, the study confirmed that particle resuspension under FSDV remains within a manageable range, maintaining both high contaminant removal performance and low resuspension potential under standard operational conditions (12 ACH). These findings establish the first quantitative framework for evaluating resuspension under FSDV airflow and provide foundational data for future research on dynamic disturbances, such as human walking, in displacement-ventilated environments.

7.2 Overall Conclusions and Future Perspectives

This dissertation systematically investigated ventilation strategies for reducing the risk of airborne infections during close-contact conversations, with a focus on the combined performance of local exhaust ventilation (LEV) and floor-supply displacement ventilation (FSDV) systems. Through a combination of computational, experimental, and microscopic analyses, the study clarified how ventilation type, hood configuration, contaminant phase (gas or particle), and airflow characteristics influence the risk of infection and indoor cleanliness.

The results from Chapter 2 demonstrated through CFD analysis that combining LEV with FSDV substantially enhanced contaminant capture and infection control efficiency, particularly at low ventilation rates typical of consulting rooms. The measured human exhalation parameters provided realistic boundary conditions, and the optimized hood flow balance effectively separated contaminated and clean airflow paths.

In Chapter 3, full-scale experiments comparing FSDV, HFD, SFD, and CD systems showed that FSDV produced the most stable displacement flow, achieving both the lowest contaminant concentration and the highest removal efficiency. These findings established FSDV as the most promising base ventilation system for infection control.

Chapter 4 verified experimentally that introducing LEV further enhanced infection risk reduction across all ventilation types. The combination of FSDV and LEV maintained nearly zero quanta concentration in the breathing zone and prolonged the infection probability threshold time ($t_{5\%}$) far beyond typical exposure durations. This hybrid system thus provides a practical solution for hospitals and cleanrooms that require high cleanliness and low energy consumption.

In Chapter 5, experiments under high ventilation conditions (50 ACH) were conducted to compare the infection risks estimated using tracer gas and particles. Both showed that infection risk decreased in the order FSDV < HFD < SFD. However, gas-based assessments yielded higher quanta concentrations than particles due to the effects of gravitational settling and adhesion. This clarified that gas-based methods provide conservative, safety-side estimates for infection risk.

Finally, Chapter 6 quantified particle resuspension under FSDV airflow, revealing that resuspension rates (10^{-8}–10^{-4} h^{-1}) remained extremely low under typical operating conditions (12 ACH). Although localized resuspension occurred near ventilation holes, the overall effect was negligible compared to walking-induced resuspension. These results demonstrated that FSDV can maintain both low infection risk and long-term cleanliness stability.

In conclusion, this study provides a comprehensive scientific basis for the optimal design and application of local exhaust ventilation (LEV) and floor-supply displacement ventilation (FSDV) systems, contributing to the development of ventilation design guidelines for medical and high-cleanliness environments. The results demonstrated that, unlike other floor-supply systems, the contaminant removal performance of FSDV increases with ventilation rate, highlighting its superior scalability. Moreover, due to its calm and stable airflow, combining FSDV with LEV effectively captured exhaled air during close conversations even under moderate ventilation rates (6–12 ACH), without promoting undesirable dispersion.

From the perspective of practical application, FSDV faces several challenges, including high installation costs, the structural difficulty of constructing a raised floor, maintenance issues such as cleaning water spills, and the risk of thermal discomfort caused by cool air supplied near the feet or by large vertical temperature gradients. Unlike ceiling diffusers, FSDV is difficult to implement in existing buildings and is therefore primarily adopted in newly constructed facilities. Furthermore, in highly clean environments such as hospitals

and cleanrooms, adoption remains rare due to concerns about particle resuspension and the lack of precedent, and ceiling-supply–floor-exhaust unidirectional airflow systems are generally preferred.

In contrast to this current state, the findings of this thesis demonstrate that FSDV enhances contaminant removal performance and reduces infection risk as ventilation rates increase, thereby providing a rational basis for its implementation in hospitals and cleanrooms where high airflow rates and high cleanliness are required. Similar benefits can also apply to office environments, and several office buildings have already implemented FSDV, indicating the possibility of broader adoption in future projects.

With regard to applying LEV beyond consulting rooms, the performance of LEV is highly dependent on its relative position to the contaminant source. The installation of hoods between individuals—such as in restaurants or meeting rooms—was found to be less effective in reducing infection risk. However, under high-ventilation conditions, even in mixed-flow environments such as CD and SFD, introducing a 100 m^3/h hood substantially reduced infection risk, confirming the potential applicability of LEV in various indoor settings.

In terms of energy efficiency, the introduction of LEV can reduce the required outdoor air volume, resulting in notable energy savings. Furthermore, when LEV effectively captures exhaled air, the remaining exhaust air can be filtered and safely reused as recirculated air (RA), contributing further to the reduction of required outdoor air supply. FSDV itself has been adopted in energy-efficient buildings such as the Taisei Sapporo Building (Super Eco Building No. 1, 2006) and the Maekawa MFG Headquarters Building (2008), both of which achieved CASBEE S-rank ratings. These examples demonstrate that FSDV enables highly energy-efficient designs in laboratories and offices. Taken together with the findings of this study, the hybrid use of FSDV and LEV represents a ventilation strategy capable of achieving both infection control and energy efficiency.

Regarding the concern of particle resuspension, the results showed that airflow-induced resuspension under FSDV was significantly lower than that caused by typical walking activity, indicating its suitability for clean environments. However, because FSDV also exhibited larger gravitational settling (Chapter 5) and higher resuspension of coarse particles compared to ceiling supply, further studies using complementary evaluation metrics—such as experiments involving actual walking or converting resuspension rates into infection risk—are required to fully assess the resuspension characteristics of FSDV.

This study also has several limitations, including insufficient consideration of unsteady behaviors such as coughing or body movement during close conversations, uncertainties inherent in infection-risk assessment, incomplete evaluation from an energy-consumption perspective, and the fact that resuspension was assessed

only in terms of particle counts and not converted into infection risk. Nevertheless, future research that quantitatively demonstrates the advantages of FSDV and LEV relative to their installation costs will contribute to the development of systematic design guidelines and promote wider implementation in practice. As an initial contribution toward this goal, this thesis has shown the superior contaminant removal and infection-risk reduction performance of LEV and floor-supply unidirectional airflow compared with other ventilation systems. It is expected that the findings of this study will serve as a valuable reference for HVAC engineers and facility designers, helping them select appropriate ventilation strategies that ensure both infection control and energy-efficient indoor environmental quality.

7.3 List of Publications (Original paper)

The original paper I published during my doctoral program is as follows:

(a) Original paper

i. Yoshihara J, Yamanaka T, Kobayashi T, Choi N, Kobayashi N. Performance of combination of local exhaust system and floor-supply displacement ventilation system as prevention measure of infection in consulting rooms. Japan Architectural Review, Volume 6, Issue 1, 02 November 2023

Note: The above paper was originally submitted as an *Original Paper*, but due to an oversight by the author during the publication process, it was mistakenly published as a *Review Paper*. Therefore, the following correction notice was issued through *Jpn Archit Rev* on 15 April 2024:

Correction to "Performance of combination of local exhaust system and floor-supply displacement ventilation system as prevention measure of infection in consulting room"
(https://onlinelibrary.wiley.com/doi/10.1002/2475-8876.12444)

ii. Yoshihara J, Yamanaka T, Choi N, Kobayashi T, Kobayashi N, Fujiwara A. Infection-prevention performance of local exhaust ventilation under three different underfloor air distribution systems during a face-to-face conversation. Building and Environment, Volume 265, 1 November 2024, 111911

ACKNOWLEDGEMENT

This dissertation stands upon the generous support of many people and the accumulated pursuit of knowledge by countless researchers before me. I wish to express my deepest gratitude to all of them.

First and foremost, I extend my profound appreciation to my academic advisor, Professor Emeritus **Toshio Yamanaka**, who supervised me from my undergraduate studies through the first year of my doctoral course and continued to supervise my research even after his retirement. Thanks to him, the experimental facility (clean room chamber) used in this dissertation was constructed. From the initial concept of using a local exhaust device to reduce infection risks to identifying the lack of understanding concerning resuspension in FSDV, his insights and generous support made this research possible. His words of encouragement inspired me to pursue a doctoral degree, and every seminar with him was intellectually enriching and enjoyable. The flexible way of thinking and academic curiosity I learned from him will remain a cornerstone of my life. I hope to pass on the same spirit of generosity and knowledge to my future students.

I would like to express my profound appreciation to Professor **Tomohiro Kobayashi**, Division of Global Architecture, The University of Osaka, the chief examiner of this dissertation. As both a scholar and a person, he has been a role model whose guidance has profoundly shaped my academic and personal growth. His encouragement, constructive criticism, and patience have guided me through every challenge. I am sincerely grateful for the freedom he entrusted to me and for always believing in my potential. Without his mentorship, my doctoral journey would not have been possible. I wholeheartedly wish him continued health and success.

I would like to express my sincere gratitude to **Professor Yoshiyuki Shimoda**, Department of Environmental and Energy Engineering, The University of Osaka, for kindly serving as a sub-examiner despite his busy schedule.

I would like to express my sincere gratitude to **Associate Professor Nare Choi**, who engaged in meaningful discussions with us from my undergraduate years through the first year of my doctoral course. During our seminars, she offered valuable insights, and her unique and intelligent

perspectives greatly contributed to the progress of my research. Moreover, her brightness and kindness have always been a source of encouragement and strength for me. I deeply admire her character and aspire to become a person as strong and compassionate as she is.

This study was financially supported by the **JSPS KAKENHI Grant-in-Aid for Scientific Research (B) (No. 21H01492, Principal Investigator: Toshio Yamanaka)** for Chapters 2, 3, 4, and 5; **the Grant-in-Aid for Challenging Research (Exploratory) (No. 19K22011, Principal Investigator: Toshio Yamanaka)** for Chapter 2; **the Osaka University Faculty of Medicine COVID-19 Research and Development Grant (FY2020)** for Chapters 2 and 5; **JST SPRING (Grant Number JPMJSP2138,** Principal Investigator: Jun Yoshihara**)** for Chapter 6.

I would also like to express my gratitude to **Mrs. Nagata**, **Dr. Okamoto**, and all the members of **Tohata Architects & Engineers, Inc.**, for their valuable support and collaboration on Chapters 3, 4, and 6. Their insights from a practical engineering perspective were extremely valuable and greatly contributed to the advancement of this research. I sincerely hope that the findings of this study will be of practical use in future engineering applications and design practices.

My heartfelt appreciation goes to **Assistant Professor Haruna Yamasawa** for her thoughtful guidance during our seminars. When I was an undergraduate student, she was in the doctoral program, and I learned a great deal from her—many of those lessons are reflected in the findings presented in Chapter 2. I sincerely wish her continued health, happiness, and success in her future professional career across the world.

I wish to express my sincere gratitude to **Dr. Noriaki Kobayashi**, a technical staff member in our laboratory, for his invaluable ideas and expertise. His technical insight and practical knowledge helped me overcome numerous challenges during every stage of experimental setup and equipment operation. I sincerely wish his continued health and success, and I would be delighted if we could have the opportunity to work together again in the future.

I am thankful to **Mrs. Naoko Onmae**, the administrative staff of our laboratory, for her cheerful and kind-hearted support. Thanks to her assistance with a wide range of administrative procedures, I was able to procure essential equipment and participate in academic conferences without difficulty. Furthermore, her bright personality was a source of comfort and joy, and her kindness during my most difficult times is something I will never forget.

I wish to express my gratitude to **Ms. Zhang Ren**, who collaborated with me on the studies pre-

sented in Chapter 2 during 2021–2022. Though we were inexperienced at the time, working together through trial and error remains an unforgettable and formative experience for me. I sincerely wish her continued success in her future endeavors and would be delighted if we could collaborate again someday.

My sincere appreciation is extended to **Mr. Aoi Fujiwara**, who collaborated on the experiments described in Chapters 3, 4, and 6 between 2022 and 2023. His intelligence and kindness made our collaboration deeply enjoyable. Without his efforts, this dissertation would not have been completed, and the research outcomes would surely have been far more limited. As my first junior colleague, he holds a special place in my memory, and I sincerely wish him continued success and progress in the future.

I would like to express my deep gratitude to **Dr. Shaoyu Sheng**, my senior colleague in the laboratory. When I was an undergraduate student, he was in the doctoral program, and thanks to the detailed knowledge of CFD that he generously taught me, I was able to complete my bachelor's thesis. He taught me many other things as well, always without hesitation or reserve. I sincerely hope that we will have opportunities to collaborate again in the future.

I would like to express my heartfelt appreciation to **Dr. Aya Essa**, also a senior colleague in the laboratory. Her kind words praising my English gave me the confidence to continue improving. Our conversations about life abroad were truly precious and enjoyable experiences that deepened my interest in the world beyond Japan. I sincerely wish her continued success and hope that our paths will cross again in the future.

I would like to express my sincere gratitude to **Dr. Zitao Jiang**, another senior colleague in the laboratory. I greatly enjoyed our many discussions about research, which were always stimulating and insightful. We also traveled together twice for international conferences, creating unforgettable memories for which I am truly thankful. I hope that I will have the chance to work with Dr. Jiang again as he continues to build his career on the global stage.

I would like to thank my **laboratory peers—past and present—as well as my friends from university and my hometown** for their companionship and support. True value is often realized only after parting. I have learned that it is friends who stand by you in the most difficult times, and I am sincerely thankful to everyone who treated me with warmth despite my shortcomings. I hope to accomplish much in the future so that I can give back to all of you.

Finally, I am especially grateful to my parents, **Takeshi and Misae**, for their unwavering encouragement, perseverance, and unconditional love. Their optimism has always been my greatest source of strength, and I am deeply thankful for their patience throughout my long academic journey. I am also sincerely grateful to my late **grandparents** and hope that they will continue to watch over my path with warmth.

I extend my heartfelt gratitude to everyone who has supported me. Although I still have much to learn, I aspire to become someone who can give back to others as generously as I have received.

REFERENCES

[1] R.W. Hyland, A. Wexler, Formulations for the thermodynamic properties of dryair from 173.15 K to 373.15 K, at pressures to 5 MPa., ASHRAE Transactions (1989).

[2] T. Greenhalgh, J.L. Jimenez, K.A. Prather, Z. Tufekci, D. Fisman, R. Schooley, Ten scientific reasons in support of airborne transmission of SARS-CoV-2, The Lancet 397 (2021) 1603–1605. https://doi.org/10.1016/S0140-6736(21)00869-2.

[3] C.J. Heneghan, E.A. Spencer, J. Brassey, A. Plüddemann, I.J. Onakpoya, J.L. Oke, D.H. Evans, J.M. Conly, T. Jefferson, N.H.L. Leung, H. Kong, M. Yao, SARS-CoV-2 and the role of airborne transmission: a systematic review [version 3; peer review: 1 approved with reservations, 2 not approved], (2021). https://doi.org/10.12688/f1000research.52091.1.

[4] L. Morawska, D.K. Milton, It Is Time to Address Airborne Transmission of Coronavirus Disease 2019 (COVID-19), Clinical Infectious Diseases 71 (2020) 2311–2313. https://doi.org/10.1093/CID/CIAA939.

[5] S. Tang, Y. Mao, R.M. Jones, Q. Tan, J.S. Ji, N. Li, J. Shen, Y. Lv, L. Pan, P. Ding, X. Wang, Y. Wang, C.R. MacIntyre, X. Shi, Aerosol transmission of SARS-CoV-2? Evidence, prevention and control, Environ. Int. 144 (2020). https://doi.org/10.1016/J.ENVINT.2020.106039.

[6] Y. Li, H. Qian, J. Hang, X. Chen, P. Cheng, H. Ling, S. Wang, P. Liang, J. Li, S. Xiao, J. Wei, L. Liu, B.J. Cowling, M. Kang, Probable airborne transmission of SARS-CoV-2 in a poorly ventilated restaurant, Build. Environ. 196 (2021) 107788. https://doi.org/10.1016/J.BUILDENV.2021.107788.

[7] World Health Organization, Coronavirus disease (COVID-19): How is it transmitted?, (2021). https://www.who.int/emergencies/diseases/novel-coronavirus-2019/question-and-answers-hub/q-a-detail/coronavirus-disease-covid-19-how-is-it-transmitted (accessed September 10, 2025).

[8] National Institute of Infectious Diseases, Current Situation of Infection, October 26, 2022; Measures to be taken, 6. Effective ventilation, (2022). https://www.niid.go.jp/niid/en/2019-ncov-e/11615-covid19-ab104th-en.html (accessed November 17, 2022).

[9] World Health Organization, Transmission of SARS-CoV-2: implications for infection prevention precautions, World Health Organization (2020).

[10] J.W. Tang, W.P. Bahnfleth, P.M. Bluyssen, G. Buonanno, J.L. Jimenez, J. Kurnitski, Y. Li, S. Miller, C. Sekhar, L. Morawska, L.C. Marr, A.K. Melikov, W.W. Nazaroff, P. v. Nielsen, R. Tellier, P. Wargocki, S.J. Dancer, Dismantling myths on the airborne transmission of severe acute respiratory syndrome coronavirus-2 (SARS-CoV-2), Journal of Hospital Infection 110 (2021) 89–96. https://doi.org/10.1016/J.JHIN.2020.12.022.

[11] W.H. Seto, Airborne transmission and precautions: facts and myths, Journal of Hospital Infection 89 (2015) 225–228. https://doi.org/10.1016/J.JHIN.2014.11.005.

[12] D.K. Milton, A Rosetta Stone for Understanding Infectious Drops and Aerosols, J. Pediatric Infect. Dis. Soc. 9 (2020) 413–415. https://doi.org/10.1093/JPIDS/PIAA079.

[13] M. Zhang, P. Shrestha, X. Liu, T. Turnaoglu, J. DeGraw, D. Schafer, N. Love, Computational fluid dynamics simulation of SARS-CoV-2 aerosol dispersion inside a grocery store, Build. Environ. 209 (2022). https://doi.org/10.1016/j.buildenv.2021.108652.

[14] P. v Nielsen, Aalborg Universitet Displacement Ventilation, (1993).

[15] X. Yuan, Q. Chen, L.R. Glicksman, A Critical Review of Displacement Ventilation, AIVC 4101 (1998) 1–13. https://www.aivc.org/resource/critical-review-displacement-ventilation (accessed November 26, 2022).

[16] E. Bjørn, P. V. Nielsen, Dispersal of exhaled air and personal exposure in displacement ventilated rooms, Indoor Air 12 (2002) 147–164. https://doi.org/10.1034/j.1600-0668.2002.08126.x.

[17] R.K. Bhagat, P.F. Linden, Displacement ventilation: A viable ventilation strategy for makeshift hospitals and public buildings to contain COVID-19 and other airborne diseases: Ventilation strategy for COVID-19, R. Soc. Open Sci. 7 (2020). https://doi.org/10.1098/RSOS.200680.

[18] J. Wei, Y. Li, Airborne spread of infectious agents in the indoor environment, Am. J. Infect. Control 44 (2016) S102–S108. https://doi.org/10.1016/J.AJIC.2016.06.003.

[19] N. Rajaratnam, Turbulent jets, Elsevier Science Ltd (1976). https://books.google.co.jp/books?id=g3R4gFObzloC (accessed February 25, 2023).

[20] H. Yamasawa, T. Kobayashi, T. Yamanaka, N. Choi, M. Cehlin, A. Ameen, Effect of supply velocity and heat generation density on cooling and ventilation effectiveness in room with impinging jet ventilation system, Build. Environ. 205 (2021) 108299. https://doi.org/10.1016/J.BUILDENV.2021.108299.

[21] Y.J.P. Lin, P.F. Linden, A model for an under floor air distribution system, Energy Build. 37 (2005) 399–409. https://doi.org/10.1016/J.ENBUILD.2004.07.011.

[22] K. Zhang, X. Zhang, S. Li, X. Jin, Review of underfloor air distribution technology, Energy Build. 85 (2014) 180–186. https://doi.org/10.1016/J.ENBUILD.2014.09.011.

[23] F. Bauman, T. Webster, UC Berkeley HVAC Systems Title Outlook for underfloor air distribution Publication Date, ASHRAE J. 43 (2001) 18–27.

[24] K.J. Loudermilk, Underfloor Air Distribution Solutions for Open Office Applications, ASHRAE Trans. (1999) 605–613. https://www.aivc.org/resource/underfloor-air-distribution-solutions-open-office-applications (accessed November 28, 2022).

[25] C.H. Cheong, B. Park, S.R. Ryu, Effect of under-floor air distribution system to prevent the spread of airborne pathogens in classrooms, Case Studies in Thermal Engineering 28 (2021) 101641. https://doi.org/10.1016/J.CSITE.2021.101641.

[26] N. Gao, J. Niu, L. Morawska, Distribution of respiratory droplets in enclosed environments under different air distribution methods, Building Simulation 2008 1:4 1 (2008) 326–335. https://doi.org/10.1007/S12273-008-8328-0.

[27] A. Melikov, A. Li, R. Kosonen, X. Li, Occupant targeted ventilation brings clean air to occupants,

The REHVA European HVAC Journal (2022). https://www.researchgate.net/publication/358915595.

[28] D. Lewis, Is the coronavirus airborne? Experts can't agree, Nature 580 (2020) 175. https://doi.org/10.1038/D41586-020-00974-W.

[29] W. Su, B. Yang, A. Melikov, C. Liang, Y. Lu, F. Wang, A. Li, Z. Lin, X. Li, G. Cao, R. Kosonen, Infection probability under different air distribution patterns, Build. Environ. 207 (2022). https://doi.org/10.1016/j.buildenv.2021.108555.

[30] J. Yoshihara, T. Yamanaka, N. Choi, T. Kobayashi, H. Yamasawa, N. Kobayashi, H. Nagata, S. Okamoto, S. Yasui, K. Sugita, A. Fujiwara, Performance of Local Exhaust System as Prevention Measure of Infection in Consulting Room. (Part 11) The Effect of Air Flow Rate on Infection Risk in Various Under floor Air Supply Systems (in Japanese), 2024.

[31] P. V Nielsen, Displacement Ventilation - theory and design, Aalborg University, 1993. https://vbn.aau.dk/ws/portalfiles/portal/36323578/Displacement+Ventilation+-+theory+and+design+%28gul+serie%29.pdf (accessed May 24, 2024).

[32] J. Yoshihara, T. Yamanaka, N. Choi, T. Kobayashi, N. Kobayashi, A. Fujiwara, Infection-prevention performance of local exhaust ventilation under three different underfloor air distribution systems during a face-to-face conversation, Build. Environ. 265 (2024). https://doi.org/10.1016/j.buildenv.2024.111911.

[33] Healthcare Engineering Association of Japan (HEAJ), Hospital Facilities Design Guidelines (Air conditioning volume), HEAS-02-2022, Tokyo, 2022.

[34] S. Executive, Controlling airborne contaminants at work: A guide to local exhaust ventilation (LEV) HSG258, Health and Safety Executive (2017). https://books.hse.gov.uk/ (accessed December 5, 2022).

[35] J. Liu, S. Zhu, M.K. Kim, J. Srebric, A Review of CFD Analysis Methods for Personalized Ventilation (PV) in Indoor Built Environments, MDPI : Sustainability 11 (2019) 1–33. https://doi.org/10.3390/su11154166.

[36] A.K. Melikov, Personalized ventilation, Indoor Air 14 (2004) 157–167. https://doi.org/10.1111/J.1600-0668.2004.00284.X.

[37] J. Yang, S.C. Sekhar, K.W.D. Cheong, B. Raphael, Performance evaluation of a novel personalized ventilation-personalized exhaust system for airborne infection control, Indoor Air 25 (2015) 176–187. https://doi.org/10.1111/ina.12127.

[38] J.R. Allison, C. Dowson, K. Pickering, G. Červinskytė, J. Durham, N.S. Jakubovics, R. Holliday, Local Exhaust Ventilation to Control Dental Aerosols and Droplets, J. Dent. Res. 101 (2022) 384–391. https://doi.org/10.1177/00220345211056287/ASSET/IMAGES/LARGE/10.1177_00220345211056287-FIG1.JPEG.

[39] T. Akimoto, T. Nobe, S. Tanabe, K. Kimura, Experimental study on indoor thermal environment and ventilation performance of floor-supply displacement ventilation system, Journal of Architecture and Planning (Transactions of AIJ) 62 (1997) 17–25. https://doi.org/10.3130/AIJA.62.17_3.

[40] G.A. Sehmel, PARTICLE RESUSPENSION: A REVIEW, Environ. Int. 4 (1980) 107–127.

[41] J. Qian, J. Peccia, A.R. Ferro, (Review) Walking-induced particle resuspension in indoor environments, Atmos. Environ. 89 (2014) 464–481. https://doi.org/10.1016/j.atmosenv.2014.02.035.

[42] F. Yuan, R. Yao, W. Yu, S. Sadrizadeh, H. Awbi, P. Kumar, Dynamic characteristics of particulate matter resuspension due to human activities in indoor environments: A comprehensive review, Journal of Building Engineering 79 (2023). https://doi.org/10.1016/j.jobe.2023.107914.

[43] C. Henry, J.P. Minier, Progress in particle resuspension from rough surfaces by turbulent flows, Prog. Energy Combust. Sci. 45 (2014) 1–53. https://doi.org/10.1016/j.pecs.2014.06.001.

[44] Y. Kubota, H. Higuchi, Aerodynamic particle resuspension due to human foot and model foot motions, Aerosol Science and Technology 47 (2013) 208–217. https://doi.org/10.1080/02786826.2012.742486.

[45] E. Abt, H.H. Suh, P. Catalano, P. Koutrakis, Relative contribution of outdoor and indoor particle sources to indoor concentrations, Environ. Sci. Technol. 34 (2000) 3579–3587. https://doi.org/10.1021/es990348y.

[46] J. Ren, M. Wade, R.L. Corsi, A. Novoselac, Particulate matter in mechanically ventilated high school classrooms, Build. Environ. 184 (2020). https://doi.org/10.1016/j.buildenv.2020.106986.

[47] G. Pei, J.D. Freihaut, D. Rim, Long-term application of low-cost sensors for monitoring indoor air quality and particle dynamics in a commercial building, Journal of Building Engineering 79 (2023). https://doi.org/10.1016/j.jobe.2023.107774.

[48] R. Shaughnessy, H. Vu, Particle loadings and resuspension related to floor coverings in chamber and in occupied school environments, Atmos. Environ. 55 (2012) 515–524. https://doi.org/10.1016/j.atmosenv.2012.04.008.

[49] C. Gomes, J. Freihaut, W. Bahnfleth, Resuspension of allergen-containing particles under mechanical and aerodynamic disturbances from human walking, Atmos. Environ. 41 (2007) 5257–5270. https://doi.org/10.1016/j.atmosenv.2006.07.061.

[50] M.P. Buttner, P. Cruz-Perez, L.D. Stetzenbach, P.J. Garrett, A.E. Luedtke, Measurement of airborne fungal spore dispersal from three types of flooring materials, 2002.

[51] H. Zhang, H. Liu, A.R. Ferro, Vivian, A.C.K. Lai, Effects of triboelectric charging, flooring materials, relative humidity, and shoe sole materials on human walking-induced particle resuspension, Build. Environ. 244 (2023). https://doi.org/10.1016/j.buildenv.2023.110838.

[52] S.Y. Yang, H.H. Zhang, T.C. Hsiao, A.R. Ferro, A.C.K. Lai, Evaluation of human walking-induced resuspension of bacteria on different flooring materials, Build. Environ. 235 (2023). https://doi.org/10.1016/j.buildenv.2023.110218.

[53] J. Qian, A.R. Ferro, Resuspension of dust particles in a chamber and associated environmental factors, Aerosol Science and Technology 42 (2008) 566–578. https://doi.org/10.1080/02786820802220274.

[54] H.K. Hyytiäinen, B. Jayaprakash, P. V. Kirjavainen, S.E. Saari, R. Holopainen, J. Keskinen, K. Hämeri, A. Hyvärinen, B.E. Boor, M. Täubel, Crawling-induced floor dust resuspension affects the microbiota of the infant breathing zone, Microbiome 6 (2018). https://doi.org/10.1186/s40168-018-0405-8.

[55] T. Wu, M. Täubel, R. Holopainen, A.K. Viitanen, S. Vainiotalo, T. Tuomi, J. Keskinen, A. Hyvärinen,

K. Hämeri, S.E. Saari, B.E. Boor, Infant and Adult Inhalation Exposure to Resuspended Biological Particulate Matter, Environ. Sci. Technol. 52 (2018) 237–247. https://doi.org/10.1021/acs.est.7b04183.

[56] B.E. Boor, J.A. Siegel, A. Novoselac, Monolayer and multilayer particle deposits on hard surfaces: Literature review and implications for particle resuspension in the indoor environment, Aerosol Science and Technology 47 (2013) 831–847. https://doi.org/10.1080/02786826.2013.794928.

[57] C. Henry, J.P. Minier, S. Brambilla, Particle resuspension: Challenges and perspectives for future models, Phys. Rep. 1007 (2023) 1–98. https://doi.org/10.1016/j.physrep.2022.12.005.

[58] K. Hayato, T. Yasunobu, K. Yu, K. Toshiki, Y. Toshio, N. Hisako, O. Shigeru, Y. Saori, Verification of Particles Behavior due to Differences in Air Conditioning Methods (in Japanese), Transactions of the Society of Heating, Air-Conditioning and Sanitary Engineers of Japan 47 (2022) 1–11.

[59] L. Morawska, G. Johnson, Z. Ristovski, M. Hargreaves, K. Mengersen, S. Corbett, C. Chao, Y. Li, D. Katoshevski, Size distribution and sites of origin of droplets expelled during expiratory activities, 2009. http://eprints.qut.edu.au/.

[60] Z. Ai, C.M. Mak, N. Gao, J. Niu, Tracer gas is a suitable surrogate of exhaled droplet nuclei for studying airborne transmission in the built environment, Build. Simul. 13 (2020) 489–496. https://doi.org/10.1007/s12273-020-0614-5.

[61] E. Bjørn, P. v. Nielsen, Dispersal of exhaled air and personal exposure in displacement ventilated rooms, Indoor Air 12 (2002) 147–164. https://doi.org/10.1034/j.1600-0668.2002.08126.x.

[62] D.T. Pritchard, J.A. Currie, Diffusion of coefficients of carbon dioxide, nitrous oxide, ethylene and ethane in air and their measurement, Journal of Soil Science 33 (1982) 175–184.

[63] R. Kosonen, N. Lastovets, P. Mustakallio, G.C. da Graça, N.M. Mateus, M. Rosenqvist, The effect of typical buoyant flow elements and heat load combinations on room air temperature profile with displacement ventilation, Build. Environ. 108 (2016) 207–219. https://doi.org/10.1016/j.buildenv.2016.08.037.

[64] ANSI/ASHRAE, Standard 140–2017—Standard Method of Test for the Evaluation of Building Energy Analysis Computer Programs, ASHRAE (2017).

[65] M. Komori, T. Yamanaka, T. Kobayashi, N. Choi, N. Kobayashi, Development of a Design of Local Exhaust Hood with High Capture Efficiency (Part5) Prediction of Airflow under Exhaust Hood by Modeling under Passing Airflow, Techinical Papers of Annual Meeting the Society of Heating, Air-Conditioning and Sanitary Engineers of Japan 4 (2022) 69–72.

[66] New Edition “Factory Ventilation,” SHASE of Japan (2009). http://www.shasej.org/tosho/M-14.html (accessed July 24, 2023).

[67] World Health Organization, Natural Ventilation for Infection Control in Health-Care Settings, World Health Organization (2009). (accessed November 13, 2022).

[68] T. Yamanaka, Natural Ventilation and Prediction of Infection Risk, The Society of Heating, Air-Conditioning and Sanitary Engineers of Japan 95 (2021) 11–17.

[69] Federation of European Heating Ventilation and Air Conditioning Associations, COVID-19 guidance document Version 4.0; How to operate HVAC and other building service systems to prevent the

spread of the coronavirus (SARS-CoV-2) disease (COVID-19) in workplaces, 2020.

[70] W.F. Wells, Airborne Contagion and Air Hygiene: An Ecological Study of Droplet Infections - William Firth Wells -, University of Michigan Libraries, 1955. (accessed July 10, 2023).

[71] Riley EC, Murphy G, Riley RL, Airborne spread of measles in a suburban elementary school., Am. J. Epidemiol. 107 (1978) 421–432.

[72] T. Watanabe, T.A. Bartrand, M.H. Weir, T. Omura, C.N. Haas, Development of a dose-response model for SARS coronavirus, Risk Analysis 30 (2010) 1129–1138. https://doi.org/10.1111/j.1539-6924.2010.01427.x.

[73] G. Buonanno, L. Stabile, L. Morawska, Estimation of airborne viral emission: Quanta emission rate of SARS-CoV-2 for infection risk assessment, Environ. Int. 141 (2020). https://doi.org/10.1016/j.envint.2020.105794.

[74] H. Kobayashi, S. Kato, S. Murakami, Scales for Evaluating Ventilation Efficiency as Affected by Supply and Exhaust Openings Based on Spatial Distribution of Contaminant by Means of Numerical Simulation, The Society of Heating, Air-Conditioning Sanitary Engineers of Japan 68 (1998) 29–36.

[75] J.K. Gupta, C.H. Lin, Q. Chen, Characterizing exhaled airflow from breathing and talking, Indoor Air 20 (2010) 31–39. https://doi.org/10.1111/j.1600-0668.2009.00623.x.

[76] J. Hang, Y. Li, R. Jin, The influence of human walking on the flow and airborne transmission in a six-bed isolation room: Tracer gas simulation, Build. Environ. 77 (2014) 119–134. https://doi.org/10.1016/j.buildenv.2014.03.029.

[77] J.M. Villafruela, I. Olmedo, M. Ruiz de Adana, C. Méndez, P. V. Nielsen, CFD analysis of the human exhalation flow using different boundary conditions and ventilation strategies, Build. Environ. 62 (2013) 191–200. https://doi.org/10.1016/j.buildenv.2013.01.022.

[78] T. Hayashi, S. Kato, S. Murakami, J. Yang, CFD analysis on rising stream around human body and its effect on inhalation air quality, ASHRAE Trans. 108(2) (2002).

[79] X. Li, K. Inthavong, Q. Ge, J. Tu, Numerical investigation of particle transport and inhalation using standing thermal manikins, Build. Environ. 60 (2013) 116–125. https://doi.org/10.1016/J.BUILDENV.2012.11.014.

[80] S. Hyun, C. Kleinstreuer, Numerical simulation of mixed convection heat and mass transfer in a human inhalation test chamber, Int. J. Heat Mass Transf. 44 (2001) 2247–2260. www.elsevier.com/locate/ijhmt (accessed August 3, 2023).

[81] S. Murakami, Analysis and design of micro-climate around the human body with respiration by CFD, Indoor Air 14 (2004) 144–156. https://doi.org/10.1111/J.1600-0668.2004.00283.X.

[82] M. Magnus, On the efficiency of displacement ventilation, with particular reference to the influence of human physical activity, doctoral dissertation of University of Gavle, University of Gavle, 1990.

[83] REHVA, Ventilation Effectiveness: REHVA Guidebooks, Federation of European Heating, Ventilation and Air-Conditioning Associations, 2004.

[84] REHVA, Displacement Ventilation: REHVA Guidebooks, Federation of European Heating, Ventilation and Air-Conditioning Associations, 2017.

[85] ASHRAE, ASHRAE Standard 55; Thermal Environmental Conditions for Human Occupancy., Atlanta, 2004.

[86] M. Komori, T. Yamanaka, T. Kobayashi, N. Choi, N. Kobayashi, Y. Suzuki, Study on capture performance of local exhaust hood under passing airflow (in Japanese), Journal of Environmental Engineering (Japan) 88 (2023) 587–596. https://doi.org/10.3130/aije.88.587.

[87] M. Ogata, M. Ichikawa, H. Tsutsumi, T. Ariga, S. Hori, S.I. Tanabe, Measurement of cough droplet deposition using the cough machine (in Japanese), Journal of Environmental Engineering (Japan) 83 (2018) 57–64. https://doi.org/10.3130/aije.83.57.

[88] J. Yoshihara, T. Yamanaka, T. Kobayashi, N. Choi, N. Kobayashi, Performance of combination of local exhaust system and floor-supply displacement ventilation system as prevention measure of infection in consulting room, Japan Architectural Review 6 (2023). https://doi.org/10.1002/2475-8876.12413.

[89] W. Yang, L.C. Marr, Dynamics of Airborne influenza A viruses indoors and dependence on humidity, PLoS One 6 (2011). https://doi.org/10.1371/journal.pone.0021481.

[90] I.N. Tang, A.C. Tridico, K.H. Fung, Thermodynamic and optical properties of sea salt aerosols, Journal of Geophysical Research Atmospheres 102 (1997) 23269–23275. https://doi.org/10.1029/97jd01806.

[91] H.L. Bagger, C.C. Fuglsang, P. Westh, Hydration of a glycoprotein: Relative water affinity of peptide and glycan moieties, European Biophysics Journal 35 (2006) 367–371. https://doi.org/10.1007/s00249-005-0035-5.

[92] T.L. Thatcher, A.C.K. Lai, R. Moreno-Jackson, R.G. Sextro, W.W. Nazaroff, Effects of room furnishings and air speed on particle deposition rates indoors, 2002.

[93] E. Diapouli, A. Chaloulakou, P. Koutrakis, Estimating the concentration of indoor particles of outdoor origin: A review, J. Air Waste Manage. Assoc. 63 (2013) 1113–1129. https://doi.org/10.1080/10962247.2013.791649.

[94] N. van Doremalen, T. Bushmaker, D.H. Morris, M.G. Holbrook, A. Gamble, B.N. Williamson, A. Tamin, J.L. Harcourt, N.J. Thornburg, S.I. Gerber, J.O. Lloyd-Smith, E. de Wit, V.J. Munster, Aerosol and Surface Stability of SARS-CoV-2 as Compared with SARS-CoV-1, New England Journal of Medicine 382 (2020) 1564–1567. https://doi.org/10.1056/nejmc2004973.

[95] A. Aganovic, Y. Bi, G. Cao, F. Drangsholt, J. Kurnitski, P. Wargocki, Estimating the impact of indoor relative humidity on SARS-CoV-2 airborne transmission risk using a new modification of the Wells-Riley model, Build. Environ. 205 (2021). https://doi.org/10.1016/j.buildenv.2021.108278.

[96] W. Liu, L. Liu, C. Xu, L. Fu, Y. Wang, P. V. Nielsen, C. Zhang, Exploring the potentials of personalized ventilation in mitigating airborne infection risk for two closely ranged occupants with different risk assessment models, Energy Build. 253 (2021). https://doi.org/10.1016/j.enbuild.2021.111531.

[97] J.A. Rosati, J. Thornburg, C. Rodes, Resuspension of particulate matter from carpet due to human activity, Aerosol Science and Technology 42 (2008) 472–482. https://doi.org/10.1080/02786820802187069.

[98] Y. Takeuchi, T. Nakatsubo, A. Fukui, R. Fujii, K. Tahara, H. Takeuchi, Design of a Medicine Spoon for an Herbal Powder and Evaluation of the Powders Flowability―In a Case of an Herbal Powder Formulated as an Antitussive and Expectorant―(in Japanese), Journal of Pharmaceutical Science and Technology, Japan 77 (2017) 164–176.

[99] Y. Tian, K. Sul, J. Qian, S. Mondal, A.R. Ferro, A comparative study of walking-induced dust resuspension using a consistent test mechanism, Indoor Air 24 (2014) 592–603. https://doi.org/10.1111/ina.12107.

[100] A. Benabed, A. Boulbair, PM10, PM2.5, PM1, and PM0.1 resuspension due to human walking, Air Qual. Atmos. Health (2022). https://doi.org/10.1007/s11869-022-01201-3.

[101] A.C.K. Lai, Y. Tian, J.Y.L. Tsoi, A.R. Ferro, Experimental study of the effect of shoes on particle resuspension from indoor flooring materials, Build. Environ. 118 (2017) 251–258. https://doi.org/10.1016/j.buildenv.2017.02.024.

[102] H.Y. Jhang, S. Yang, D. Licina, Resuspension of inhalable particles from clothing: A manikin-based chamber study, Build. Environ. 267 (2025). https://doi.org/10.1016/j.buildenv.2024.112157.